Microscope Mode Secondary Ion Mass Spectrometry Imaging



Yifeng Jia

Linacre College

University of Oxford

A thesis submitted for the degree of

Doctor of Philosophy

Michaelmas 2025

Acknowledgements

First and foremost, I would like to express my deepest gratitude to my supervisor, mentor, and group leader, Professor Mark Brouard. Without him, this thesis would not have been possible, and there might have been one fewer DPhil. I am truly grateful that he accepted me into his group, even though I initially knew little about chemical dynamics or mass spectrometry imaging. I would give him a perfect score as a supervisor: 100 out of 100. He guided me patiently and systematically, training me to become a meticulous and self-critical physicist/chemist. Beyond being an outstanding scientist, he is also a remarkable mentor and educator. During times when I felt lost, he was always patient and insightful, gently pointing me toward the right direction. I deeply appreciate his constant support, guidance, and encouragement throughout my DPhil journey.

My sincere thanks also go to Dr. Felicia Green, who has always supported and guided me through many challenges during my research. She patiently instructed me step by step in real experiments, and whenever I encountered tricky problems, she helped me find the right path to a solution. I am deeply grateful for her openness and encouragement, she always said yes to my naive ideas and requests. I truly appreciate all her help and admire her greatly as an inspiring female scientist.

I would also like to thank Dr. Elena Castellani, who has been a wonderful colleague and a true friend. She was always there to listen when I faced difficulties and never failed to encourage me. I deeply appreciate her kindness, support, and friendship throughout my DPhil journey.I would also like to thank Dr. Michael Burt for his support and for patiently answering my many questions during the early stages of my DPhil. His guidance helped me settle into the research smoothly and build a solid foundation for my work.

I would like to thank Dr. Josh Featherstone, my coding tutor, for his patience in answering my endless coding questions. I am also grateful for his company during our trip to Los Angeles, where we shared a truly enjoyable journey. I would like to thank Dr. Natasha Smith, who guided me in the MALDI experiments and simulations, both of which were essential in building the foundation of my work. I would also like to thank Dr. Chow-shing (Martin) Lam, who has been like a mentor to me within the group. He always encouraged my spontaneous ideas, whether in science or in life. He taught me a great deal about optics and spectroscopy, and helped me broaden my perspective on scientific research.

Special thanks to Joe, Max, and Kieran, who helped me greatly with coding, algorithms, and simulations. Without your support, my DPhil would have been much more

difficult. I would also like to thank Tai-Che (Jerry) Chou, a good friend whose company and conversations about life and science I have truly enjoyed. I admire your unique scientific perspectives, which have broadened my own way of thinking. Thanks also to other group members — Matt, Yuanyuan Pu, Yuting Su, Weiyu (Frank) Kan, Mukhtar, Frederic, Harryson, and Prof. Li Che. It has been my honor and pleasure to work with all of you and to be a member of the Brouard group. I sincerely hope that you enjoy great success and happiness in your future work and life.

My special thanks go to the PTCL workshop team, especially Phil, who taught me a great deal and provided invaluable help with electronics. I would also like to thank IONOPTIKA, particularly Dr. Paul Blenkinsopp and Dr. Robert Bianchini, for their generous support and guidance with the instruments.

I wish to express my deepest gratitude to my parents, who have supported me every step of the way since I was a toddler. You have always respected my personal choices, from attending Hengshui High School, deciding to pursue a Master's degree in Manchester, to continuing my DPhil studies at Oxford. You are enlightened and supportive parents, and I am deeply grateful for the love and care you have given me since childhood, a debt I can never fully repay.

Most importantly, I wish to thank one of the most important people in my life, my wife, Yuanyuan (Nina) Cheng. I have never sincerely thanked you before, as I am a person who finds it hard to express feelings in words face to face. One of the greatest achievements of my DPhil is marrying you. You have always listened to me share my dreams, even when they seemed far-fetched or like daydreams. You have never disappointed me, you always understand and support me. I know that in supporting and following me, you have made compromises in your own dreams, and no words can ever fully express my gratitude. What I can do is always support and stand by you, as I vowed in our marriage. I truly hope and wish that all your dreams come true.

Finally, I would like to thank myself for never giving up on chasing my dreams and career. True to the name I gave myself — Leo — I remind myself to stay brave and keep moving forward.

请允许我用我的母语致谢我博士期间最重要的人：

首先，我要向我的导师Mark Brouard 教授致以最诚挚的感谢。没有他细致的指导与悉心的培养，我无法完成我的博士学业。时至今日，我依旧衷心感谢他在四年前接纳我加入课题组，尽管当时我对组内的研究方向以及即将开展的课题几乎一无所知。他不仅是一位杰出的科学家，更是一位令人敬佩的教育家。师者，传道、授业、解惑也。他不仅是一位优秀的老师，更是一位真正意义上的导师。他教会了我如何进行批判性思考，如何以认真与诚实的态度对待科研；他一步步地将我培养成一名合格的物理化学家；他也在我迷茫与压力重重的时刻，给予我方向与鼓励。无论未来如何，我都由衷地感激Brouard 教授，是他带领我踏入了科学的大门。

我还要由衷地感谢我的家人，特别是我的父母。我深感幸运，能够出生在一个开明、有爱、总是给予全力支持的家庭。我来自一个普通的工薪家庭，但我的父母始终竭尽所能，为我提供能够给到的最好的教育与生活条件。我非常感激他们对我出国留学的理解与支持，更感激他们塑造和培养了我坚韧、勇敢的人格，这些无疑都是我前进道路上重要的奠基石。托举是恩，感恩父母始终默默鼓励我追逐自己的梦想。能成为家族中第一个博士生，我感到无比荣幸。养育之恩，铭记于心，终生难报。

我最要感激的人，也是我人生中最重要的人——我的妻子，成源媛。自2018年相识相爱以来，我们经历了近四年异地、异国。那些岁月里数不清的火车票与视频通话，承载着我们对彼此始终如一的信任与支持。我难以想象，当我决定继续留在英国攻读博士学位时，她内心的复杂与不舍；而我更感激她毫不犹豫地选择来到英国，与我相伴、共同生活。妻子对我的爱与包容，我对她的亏欠与感激，并非寥寥数语所能表达。往后人生，我依旧会怀揣初心和爱意，像结婚誓词所说的，“永远爱你，尊重你，陪伴你，做你的人生挚友和爱人”。博士求学期间，我们能够结为夫妻，是我此生最大的幸运与幸福。这个博士学位，有她一半的功劳。

Abstract

Mass spectrometry imaging (MSI) is a powerful, label-free technique for visualizing the spatial distribution of chemical species on surfaces, with spatial resolution reaching the micron or sub-micron scale. Among various MSI modalities, secondary ion mass spectrometry (SIMS) stands out for its superior spatial resolution and capability to analyze metal multilayer (such as semiconductors) with high depth sensitivity. However, SIMS typically offers a more limited mass range compared to matrix-assisted laser desorption ionization (MALDI). Improving acquisition speed and throughput is critical to expanding the application scope of SIMS. To address this, a defocused C_{60}^{+} primary ion (PI) beam was employed to irradiate a sample area of approximately $4\,mm^2$. A time- and position-sensitive detector was used to record an image in each acquisition cycle without the need to raster the PI beam. This configuration, commonly referred to as *microscope mode* imaging (in contrast to the conventional *microprobe mode*), substantially increases imaging throughput.

This thesis investigates and optimizes key parameters in microscope mode SIMS imaging, including mass resolution, spatial resolution, and the accessible mass range. A fundamental limitation in spatial resolution arises from the inherent velocity and angular distributions of the generated secondary ions (SIs), which are influenced by the sputtering and ionization mechanisms. To analyze these distributions, velocity map imaging (VMI) is employed, leveraging a TimePix3-based camera with a time resolution of 1.56 ns to reconstruct full three-dimensional SI velocity distributions.

We present a novel approach to 3D surface velocity map imaging using a TimePix3 detector to probe the ionization and sputtering processes of both organic and metallic materials. This method provides high-precision 3D velocity measurements and enables detailed examination of secondary ion dynamics. By calibrating the system and tuning ion optical settings, we capture both angular and velocity distributions of ions produced by 20 keV and 40 keV $C_{60}{}^{+}$ bombardment. The results reveal distinct differences in the sputtering behavior of organic and metallic species, reflecting underlying differences in their kinetic energy transfer and ionization mechanisms.

These accurate measurements of velocity distributions contribute to a deeper understanding of spatial resolution limits and allow for the informed design of next-generation microscope-mode SIMS instruments. This thesis advances a transformative approach

to MSI, aimed at advancing both scientific research and clinical diagnostics. The transition from microprobe to microscope-mode SIMS, combined with intensified CCD and TimePix3-based detection, enables gains in throughput, resolution, and acquisition speed.

Further advancements include the implementation of a novel bunching scheme and a time-dependent Post-Extraction Differential Acceleration (PEDA) strategy, which significantly enhance mass resolution. A detailed study of spatial resolution dynamics reveals the interplay between magnification, signal fidelity, and distortion, guiding strategies for resolution optimization. The concurrent application of time-of-flight imaging with the TimePix3-based detector demonstrates high temporal and spatial precision, with prospects for even greater performance using future upgrades such as the TimePix4.

Contents

List of Abbreviations **xiii**

1 Introduction **1**
1.1 Overview . . . 1
1.2 History of Mass Spectrometry . . . 3
1.3 Ion Sources . . . 3
1.3.1 Secondary Ion Mass Spectrometry (SIMS) . . . 5
1.3.2 Matrix-Assisted Laser Desorption/Ionization (MALDI) . . . 9
1.3.3 Electrospray Ionization (ESI) . . . 12
1.4 Mass Analyser . . . 14
1.4.1 Time-of-Flight analyser . . . 15
1.5 Mass Spectrometry Imaging . . . 21
1.5.1 Previous work on Microscope mode ToF-MSI . . . 26
1.6 Aberration . . . 28
1.7 Secondary Ions' Velocity Distribution . . . 30
1.8 Velocity Map Imaging . . . 33
1.8.1 Applications of VMI . . . 36
1.9 Summary . . . 40

2 Modeling and Simulation **43**
2.1 SIMION . . . 43
2.1.1 Potential Arrays . . . 43
2.1.2 Electrostatic Field and Ion Trajectory Calculation . . . 45
2.1.3 Define Ions . . . 46
2.1.4 Workbench . . . 48
2.1.5 LUA file . . . 49
2.2 Output Results and Calculation . . . 49
2.2.1 Mass resolution calculation . . . 50
2.2.2 Spatial resolution calculation . . . 51
2.3 Genetic Algorithm . . . 53
2.3.1 Strength and Weakness . . . 55
2.3.2 Optimize mass and spatial resolution . . . 56
2.4 Summary . . . 58

3 Experiment Methods **61**
3.1 Introduction . . . 61
3.2 Primary Ion Beam . . . 63
3.3 Ion Optics . . . 67
3.4 Detector Assembly and Data Process . . . 70
3.4.1 Faraday Cup . . . 70
3.4.2 Everhart-Thornley detector . . . 72
3.4.3 Microchannel plates . . . 73
3.4.4 Fast scintillator . . . 75
3.4.5 Photomultiplier tube . . . 78
3.4.6 CCD and CMOS camera . . . 80
3.4.7 The Pixel Imaging Mass Spectrometry Sensor (PImMS) . . . 82
3.4.8 TimePix3-based camera . . . 84
3.4.9 Data processing . . . 86
3.5 Sample Preparation . . . 89
3.6 Experiment Workflow . . . 91
3.7 *m/z* Calibration . . . 94
3.8 Spatial Resolution Definition . . . 96
3.9 Summary and aims . . . 101

4 Three Dimensional Mass Spectrometry-Velocity Map Imaging **103**
4.1 Introduction . . . 104
4.2 Experimental Methods . . . 105
4.3 Velocity Focus . . . 109
4.4 Imaging Centering . . . 117
4.5 Determining the ToF origin . . . 120
4.6 3D velocity calibration . . . 122
4.7 VMI with TimePix3-based camera . . . 124
4.7.1 multi-mass VMI . . . 124
4.7.2 3D VMI with TimePix3-based camera . . . 126
4.7.3 Primary ion beam energy impact . . . 130
4.8 Summary . . . 135

5 High-resolution Secondary Ion Mass Spectrometry Imaging **137**
5.1 Introduction . . . 137
5.2 Post-Extraction Differential Acceleration (PEDA) . . . 139
5.2.1 Theory of Time-Variable PEDA . . . 139
5.2.2 Ion Trajectory Simulation . . . 141
5.2.3 Experimental method . . . 143
5.2.4 Triggering . . . 145

5.2.5 Post-extraction differential acceleration (PEDA) 145
5.2.6 Sample preparation 146
5.2.7 Data Processing 146
5.3 Results and discussion 147
5.3.1 Post-extraction differential acceleration 147
5.3.2 The impact of scintillator rise time on the mass resolution . . . 155
5.3.3 Spatial resolution enhancement 157
5.3.4 PEDA with TimePix3 162
5.3.5 High-throughput rat brain tissue mass imaging 167
5.4 Conclusion 170

6 Depth Profile **173**
6.1 Statement of Contributions 173
6.2 Introduction 174
6.3 Experimental Methods 174
6.3.1 Instrument setup 174
6.3.2 Samples 176
6.4 Analysis Algorithm Software 176
6.4.1 Image frame number identification 177
6.4.2 Region of Interest (ROI) capability 180
6.5 Results and Discussions 181
6.5.1 Single layer depth profile 181
6.6 Conclusion and Future Work 184

7 Conclusions and Outlooks **185**

Appendices

A Appendices **193**

References **197**

List of Abbreviations

MSI . . . . . Mass Spectrometry Imaging.

SIMS . . . . . Secondary Ion Mass Spectrometry.

MALDI . . . . . Matrix-assisted laser desorption/ionisation.

DESI . . . . . Desorption electrospray ionisation.

ESI . . . . . Electrospray ionisation.

PEDA . . . . . Post-extraction differential acceleration.

PEISI . . . . . Post-extraction inversion slice imaging.

PImMS . . . . . Pixel Imaging Mass Spectrometry.

CCD . . . . . Charge-coupled device.

CMOS . . . . . Complementary Metal-Oxide-Semiconductor.

PMT . . . . . Photomultiplier tube.

ToF . . . . . Time of flight.

ToA . . . . . Time of arrival.

ToT . . . . . Time of threshold.

VMI . . . . . Velocity map imaging.

GA . . . . . Genetic Algorithm.

PA . . . . . Potential array.

ROI . . . . . Region of interest.

1 Introduction

1.1 Overview

Mass spectrometry (MS) is a powerful analytical technique used to determine the mass-to-charge ratio (m/z) of ions. Here, m denotes the mass of the ion, and z represents its charge number, which is, by definition, unitless. The mass is typically expressed in unified atomic mass units (u), where 1 u is defined as 1.66054×10^{-27} kg. The charge of an ion is expressed as $z = q/e$, where q is the ion's charge and e is the elementary charge (1.602×10^{-19} C).

In a typical mass spectrum, the x-axis corresponds to the m/z values, while the y-axis represents either ion counts or relative abundance. This capability allows MS to be employed for both qualitative and quantitative analyses, enabling the identification of unknown compounds, structural elucidation, and determination of chemical composition across a wide range of molecules.

Owing to its high sensitivity, rapid analysis time, and broad applicability, MS has become indispensable in both academic research and industrial applications. In recent decades, the life sciences have increasingly relied on MS for the analysis of lipids [1–8], proteins [9–14], and metabolites [15–19].

In pharmaceutical research, MS plays a crucial role in pharmacokinetics [20, 21], drug metabolism [18, 22], and drug discovery [23–25]. Beyond biological and medical

sciences, MS also finds widespread use in semiconductor analysis [26, 27], environmental monitoring [28], molecular reaction dynamics [29, 30], thermodynamic parameter determination [31, 32], and geochronology [33, 34].

A mass spectrometer typically comprises the essential components illustrated in Figure 1.1. These include: a *sample inlet*, which introduces the compound under analysis—such as a gas chromatograph (GC) or a direct insertion probe; an *ionisation source*, which converts neutral sample molecules into ions; one or more *mass analysers*, which separate ions based on their mass-to-charge ratio (m/z); a *detector*, which quantifies the ions transmitted through the analyser(s); and a *data processing system*, which transforms raw ion signals into interpretable spectra or images.

In certain configurations, particularly in advanced systems, multiple mass analysers are employed. For instance, in tandem mass spectrometry (commonly abbreviated as MS/MS), a precursor ion is first selected by the initial mass analyser and then subjected to either spontaneous or induced fragmentation. The resulting product ions are subsequently analysed by a second mass analyser, enabling detailed structural elucidation and enhanced specificity in compound identification.

It is also worth noting that some instrument designs integrate the sample inlet and ionisation source into a single unit, whereas others may combine the mass analyser and detector. Signal processing is typically carried out using an oscilloscope or, more commonly, a computer system equipped with specialised software to generate high-resolution, readable mass spectra or ion images.

In general, a mass spectrometer operates through the following sequence:

1. Ions are generated from the sample in the ionisation source.

2. The ions are separated by their m/z in the mass analyser.

3. The ions are detected and their abundance measured by the detector.

4. The detector signals are transmitted to the computer for processing and interpretation.

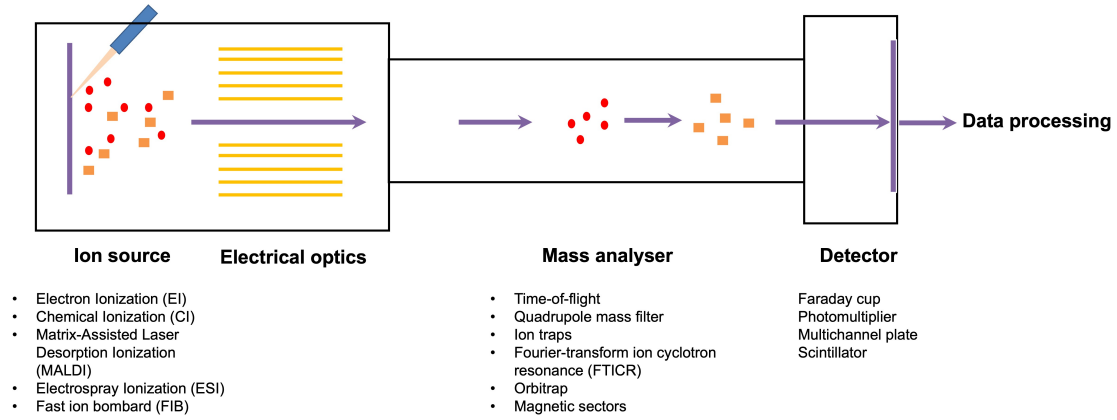


Figure 1.1: Basic mass spectrometer diagram: samples are ionised, separated by their mass-to-charge ratio, and detected to generate a mass spectrum.

1.2 History of Mass Spectrometry

Mass spectrometry is a historical and foundational analytical technique that has evolved over more than a century. The following timeline highlights some of its most significant discoveries, technological advancements, and pioneering contributions. Figures and references are included to illustrate key developments in the field.

1.3 Ion Sources

The ion source is one of the most critical components of a mass spectrometer, as it is responsible for vaporising and ionising neutral analytes before they enter the mass analyser, without ionisation the analytes can't easily be manipulated and detected. Ionisation techniques vary in the amount of internal energy imparted to the analyte molecules. Techniques that induce extensive fragmentation are referred to as *hard* ionisation methods, such as secondary ion mass spectrometry (SIMS). In contrast, *soft* ionisation techniques generate predominantly intact molecular ions with minimal fragmentation. Electron ionisation (EI), chemical ionisation (CI), and field ionisation (FI) are generally limited to gas-phase and are therefore only suitable for analytes that are volatile, thermally stable, and of relatively low molecular mass (typically below 1000 Da). In contrast, matrix-assisted laser desorption ionisation (MALDI) and electrospray ionisation (ESI) are applicable to condensed-phase samples and are

Table 1.1: Key milestones in mass spectrometry and related discoveries.

Year	Scientist(s)	Contribution / Notes
1886	Eugen Goldstein	Discovered anode rays (canal rays) in cathode ray tubes (Figure 1.2(a)) [35]; foundation for MS
1897	J. J. Thomson	Discovered the electron and determined mass-to-charge ratio [36]; Nobel Prize in Physics 1906
1898	Wilhelm Wien	Analysed anode rays using magnetic deflection; confirmed positive ions [37]; Nobel Prize 1911
1901	Walter Kaufmann	Studied cathode rays under parallel electric and magnetic fields [38]; evidence for relativistic mass increase
1909	Millikan, Fletcher	Oil drop experiment; measured electron charge -1.592×10^{-19} C [39, 40]
1912	J. J. Thomson	First mass spectrometer (parabola spectrograph) [41]; mass-to-charge separation
1919	Francis W. Aston	First MS with velocity focusing (Figure 1.2(b)) [42]; Nobel Prize 1922
1934	R. Conrad	Applied MS to organic chemistry
1942	Consolidated Eng. Corp.	First commercial MS (CEC Model 21-101, Figure 1.2(c)) [43]
1946	W. Stephens	Proposed linear ToF analyser [44]
1948	Cameron, Eggers	First operational linear ToF MS [45]
1952	R. A. Marcus	Quasi-equilibrium theory (QET) and RRKM theory [46, 47]; Nobel Prize 1992
1953	W. Paul et al.	Quadrupole MS [48]; Nobel Prize 1989 (Paul)
1956	McLafferty, Gohlke	First GC–MS [49]
1966	Munson, Field	Chemical ionisation (CI) [50]
1967	McLafferty, Jennings	Collision-induced dissociation (CID) [51, 52]
1972	Karataev, Mamyrin, Smirnov	Reflectron; enhanced ToF MS resolution [53]
1974	Horning et al.	APCI; soft ionisation for liquid-phase samples [54]
1974	McLafferty et al.	HPLC–MS [55]
1974	Comisarow, Marshall	FT-ICR MS [56]
1977	Cooks, Kruger	Kinetic method for thermochemical analysis [57]
1981	Barber et al.	Fast atom bombardment (FAB) ion source [58]
1987	Tanaka et al.	MALDI [59]; Nobel Prize 2002
1988	Fenn	Electrospray ionisation (ESI) [60]; Nobel Prize 2002
1991	Spengler, Kirsch, Kaufmann	MALDI-ToF with PSD and reflection mode [61]
1999	A. A. Makarov	Orbitrap mass analyser [62]
2000	Badman and Cooks	Miniature mass analyzers [63]
2004	Luxembourg et al.	Microscope mode MSI with position-sensitive detector [64]
2006	Pringle et al.	Ion mobility spectrometry (IMS) platform [65, 66]
2006	R. G. Cooks et al.	Ambient mass spectrometry [67]
2011	Graham et al.	distance-of-flight (DOF) mass spectrometry [68]
2013	Leo et al.	peptide-peptide interactions with mass spectrometry [69]
2014	Walton et al.	Ion soft landing characterized by deposition of intact species on surfaces [70]
2023	Zhou et al.	High-throughput Echo-LESA-MS [71]

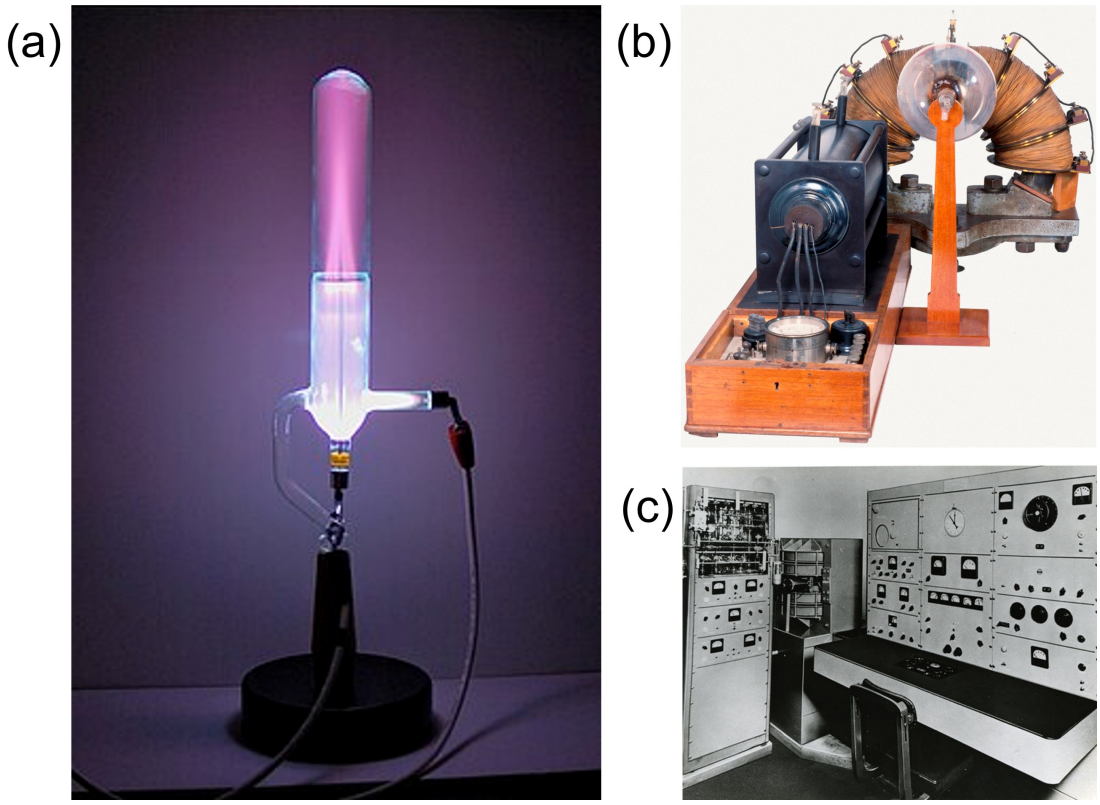


Figure 1.2: (a) Canal rays: An anode ray tube showing positively charged ions passing through the perforated cathode and producing a pink glow. Image adapted from Wikipedia. (b) The first mass spectrometer developed by Aston, featuring velocity focusing. (c) CEC Model 21-101 mass spectrometer: the first commercial mass spectrometer, developed by the Consolidated Engineering Corporation.

widely used for larger and less volatile molecules. Depending on the nature of the sample and the desired degree of fragmentation, the choice of ion source must be made carefully. In the following sections, the principles and applications of secondary ion mass spectrometry, matrix-assisted laser desorption ionisation, and electrospray ionisation are discussed in detail.

1.3.1 Secondary Ion Mass Spectrometry (SIMS)

Secondary Ion Mass Spectrometry (SIMS) is a type of mass spectrometry that utilises a focused, energetic primary ion beam to bombard the sample surface. The impact causes the ejection of material, including neutral particles and secondary ions, from the top layers of the sample. These secondary ions are then analysed by the mass spectrometer to determine their mass-to-charge ratios.

Under low primary ion fluence conditions, only the uppermost atomic or molecular layers (typically a few nanometres thick) are sputtered and analysed. Importantly, at such low doses, the bulk topographical features of the sample remain largely undisturbed. This enables SIMS to be used for depth profiling and three-dimensional chemical analysis of complex surfaces.

Over the past few decades, various types of primary ion beams have been developed and optimised for SIMS. Among these, atomic ion beams and cluster ion beams are the most commonly used. Each has its own advantages and trade-offs:

- **Atomic primary ion beams** (e.g., Ga^+, Cs^+) typically provide superior lateral (spatial) resolution, making them ideal for high-resolution imaging. However, they tend to produce smaller secondary ion yields and less molecular information due to stronger fragmentation.
- **Cluster primary ion beams** (e.g., C_{60}^+, gas cluster ion beams (GCIB)) are comparatively "softer", meaning they cause less fragmentation of larger molecules. This results in higher molecular ion yields and improved mass range, especially for organic and biological samples. However, their lateral resolution is generally lower due to beam broadening effects.

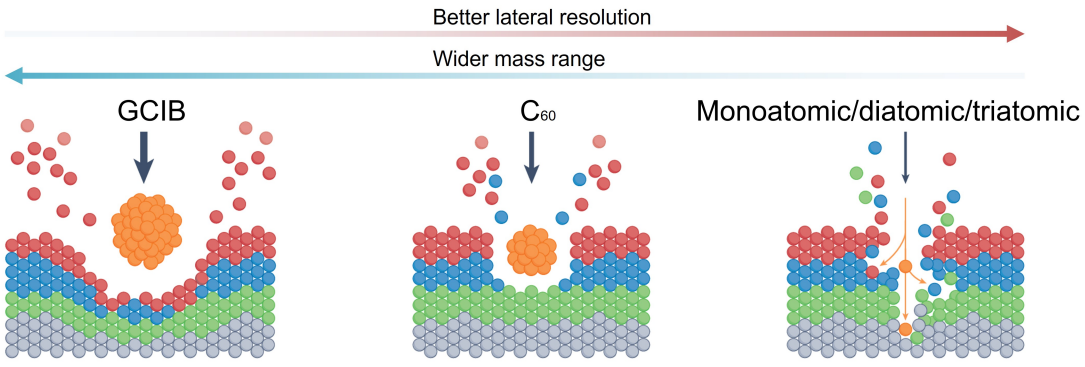


Figure 1.3: Comparison of different primary ion sources in SIMS. Larger cluster beams (GCIB and C_{60}^+) offer broader mass range detection but lower lateral resolution compared to atomic ion sources. Adapted from ref. [72].

Figure 1.3 illustrates the trade-off between mass range and lateral resolution across different types of primary ion sources. In general, larger primary ion clusters (e.g.,

GCIB $>$ C_{60}^{+} $>$ atomic) allow for the analysis of a broader mass range but at the cost of spatial resolution.

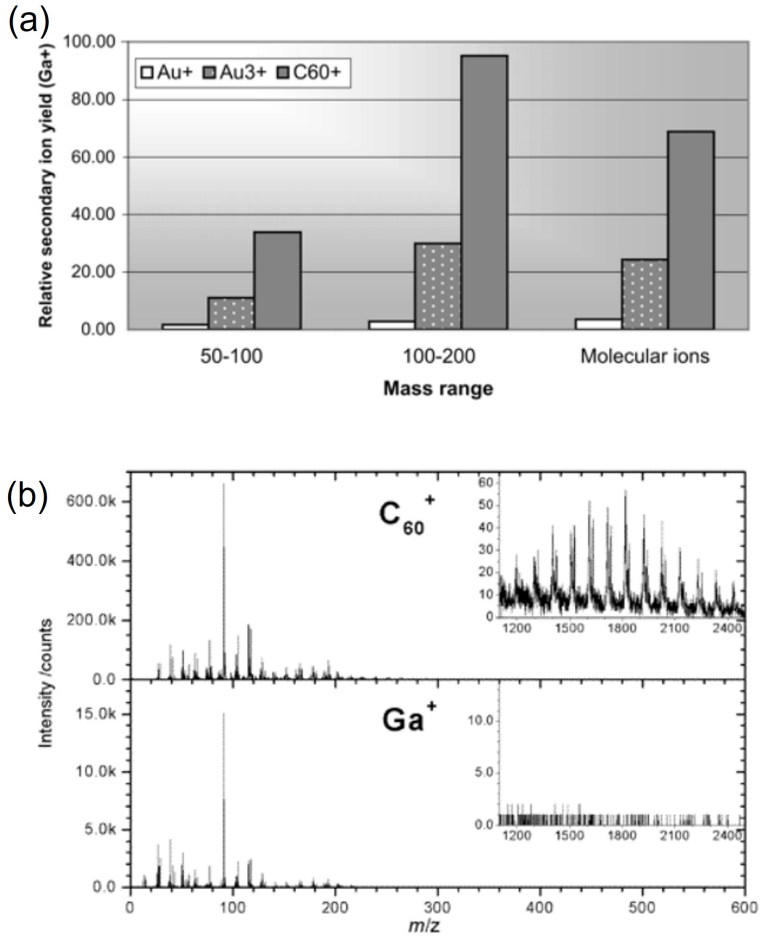


Figure 1.4: (a) Comparison of positive secondary ion yields during analysis of PET using Au^{+}, Au^{3+}, and C_{60}^{+} primary ions at 10 keV impact energy; (b) Positive TOF-SIMS spectrum of PS-2000 obtained using 10 keV impact energy from C_{60}^{+} and Ga+ beams. Dose (ions): C_{60}^{+}, 4.05×10^{8}; Ga^{+}, 4.3×10^{8}. Adapted from ref. [73].

The C_{60}^{+} primary ion (PI) beam, as employed in the SIMS instrumentation at the University of Oxford, has undergone substantial development over the past two decades. Current ion optical designs enable spatial resolutions down to approximately 3 µm, as demonstrated by the imaging of a 150-mesh copper grid using a 100 µm beam-forming aperture and a 0.1 nA C_{60}^{+} beam current. The 25 keV power supply is capable of delivering a smaller beam diameter—potentially below 1 µm—further improving spatial resolution [73].

Typically, primary ions can be accelerated to energies of up to 120 keV [74]. Increasing the impact energy of C_{60}^+ enhances the secondary ion (SI) yield due to the greater energy deposition upon the sample surface. However, this enhancement is not uniform across the mass range. At an impact energy of 120 keV, an increase in the intensity of high-mass fragments is observed, accompanied by a corresponding reduction in the signal of low-mass fragments [74].

When compared with monoatomic primary ion sources such as Ga^+, Au^+, Au^{3+}, C_{60}^+ primary ions can increase ion yields by a factor of 3 to 20, depending on the sample matrix and experimental conditions. This improvement is particularly advantageous for the analysis of high-molecular-weight species. For instance, peaks at around 2000 m/z can be clearly observed in C_{60}^+-induced TOF-SIMS spectra, whereas they may be absent or poorly resolved using monoatomic ion beams [73], as Figure 1.4 shows.

Gas cluster ion beams (GCIBs) consist of thousands of atoms or molecules—typically argon, CO_2, or H_2O—that are aggregated into clusters and accelerated towards the sample surface. These clusters can sputter larger, intact analyte molecules while causing minimal or no residual subsurface damage. Due to this advantage, GCIBs are particularly well suited for the analysis of high molecular weight compounds, such as proteins and lipids.

Hua Tian *et al.* demonstrated the application of a water-based GCIB (H_2O-GCIB) in SIMS, successfully acquiring frozen tissue images at a spatial resolution of 1 μm [75]. Furthermore, they achieved single-cell level multi-omics profiling—including proteomics—in breast cancer tissue [76]. Compared with C_{60}^+-based SIMS, H_2O-GCIB-SIMS provided enhanced molecular sensitivity, making it a powerful tool for high-content tissue analysis. A schematic of the experimental workflow, along with representative overlay and single-ion images, is shown in Figure 1.5.

Typically, atomic and diatomic primary ion beams are employed for inorganic analysis, whereas polyatomic and cluster primary ions are more suitable for organic analysis. Gas cluster ion beams (GCIBs) and low-energy atomic primary beams offer optimal depth resolution for organic and inorganic materials, respectively.

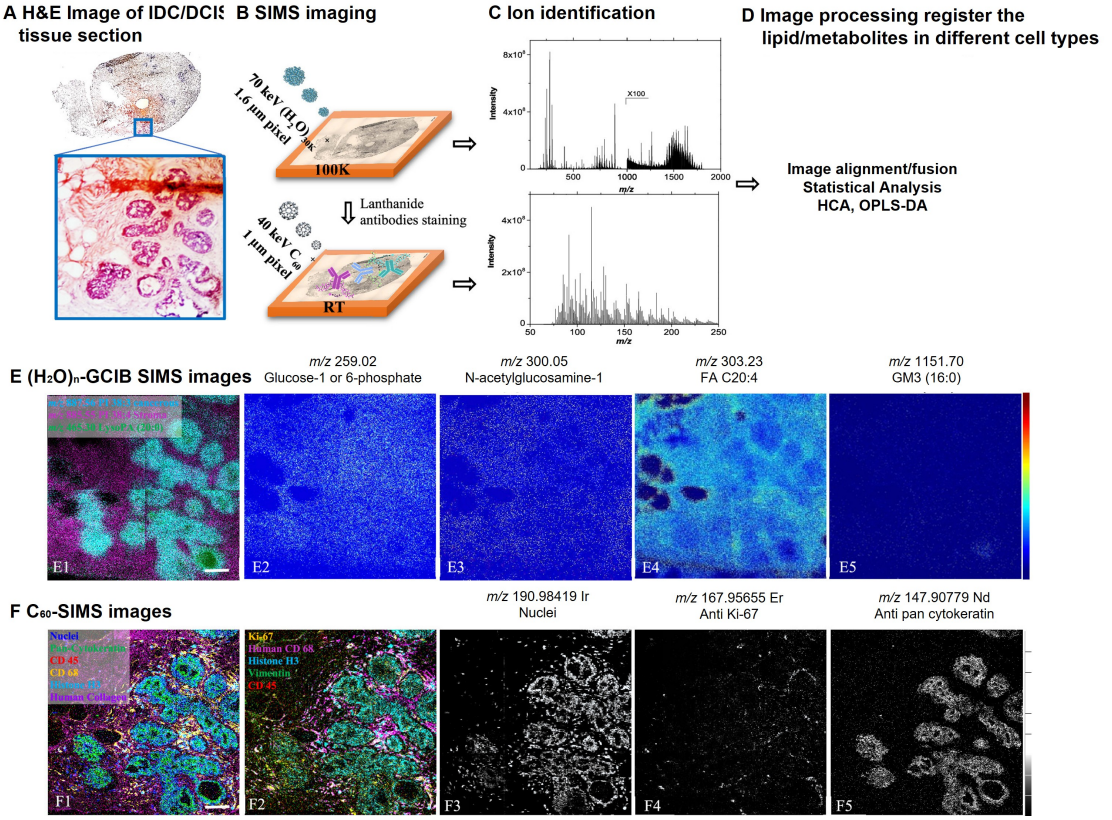


Figure 1.5: Schematic of the workflow for cell-type-specific profiling of multi-omics on IDC/DCIS breast cancer tissue sections at the single-cell level. Selected overlay and single-ion images obtained using H_2O-GCIB-SIMS and C_{60}^+-SIMS, adapted from [76].

Atomic primary ions such as O^+, O_2^+, Ar^+, and Cs^+ have been extensively tested on inorganic surfaces, including As/GaAs [77], metals, metal oxides, and alloy multi-layers [78]. GCIBs have also been successfully applied in imaging and depth profiling of various materials [79], achieving three-dimensional imaging of polymer multilayers with depth resolutions as fine as 5 nm [80].

In recent decades, SIMS has demonstrated its powerful capability for 3D imaging of biological specimens, including single cells [81, 82] and tissue sections [83], enabling molecular-level insights into spatial organisation and composition.

1.3.2 Matrix-Assisted Laser Desorption/Ionization (MALDI)

Matrix-assisted laser desorption/ionisation (MALDI) is one of the most widely used soft ionisation techniques for the analysis of intact biomolecules, peptides, synthetic polymers, and large inorganic compounds. Unlike direct laser desorption ionisation,

MALDI involves co-crystallising the analyte with a matrix—small organic molecules dissolved in a volatile solvent—that strongly absorbs energy at the laser wavelength.

The sample is prepared by mixing the analyte with the matrix in solution, then depositing the mixture onto a target plate. Because MALDI typically operates under high vacuum, the sample must be air-dried prior to analysis to remove all residual solvent. Once placed in the instrument, ionisation occurs under vacuum through the interaction with an intense laser pulse.

Upon laser irradiation, a bulk volume of the matrix-analyte mixture is simultaneously desorbed and ionised. Commonly used ultraviolet (UV) lasers include nitrogen lasers ($\lambda = 337\,\text{nm}$) and Nd:YAG lasers (wavelengths of 266 or 355 nm). Infrared (IR) lasers, such as Er:YAG lasers ($\lambda = 2.94\,\mu\text{m}$) and CO_2 lasers ($\lambda = 10.6\,\mu\text{m}$), are also employed, though less frequently.

Typical laser fluences for UV-MALDI are around $20\,\text{mJ/cm}^2$ with pulse durations in the nanosecond range. IR-MALDI, on the other hand, usually requires laser fluences that are approximately one order of magnitude higher than those used in UV-MALDI.

However, the exact mechanism of the MALDI process is not completely elucidated. Here two models are listed:

1. **Photo-ionisation model** [84, 85]: The most widely accepted model involves a combination of solid-phase and gas-phase processes. In the solid phase, proton transfer may occur between matrix and analyte molecules prior to desorption. Upon laser irradiation, matrix molecules are photo-ionised, and in the subsequent laser-generated plume, proton transfer or electron transfer reactions may occur in the gas phase. A schematic representation of the photo-ionisation mechanism is shown in Figure 1.6.

2. **Thermal proton transfer model**[86]: In this model, the energy from the laser pulse is converted into thermal energy, leading to a rapid temperature increase in the matrix-analyte mixture. This causes the sample to melt and desorb. Proton transfer reactions occur in this transient liquid phase before desorption into the gas phase. Both neutral and ionic species are emitted into the expanding plume. As

the plume expands, the concentration of reactive species decreases rapidly, and the chemical reactions eventually cease.

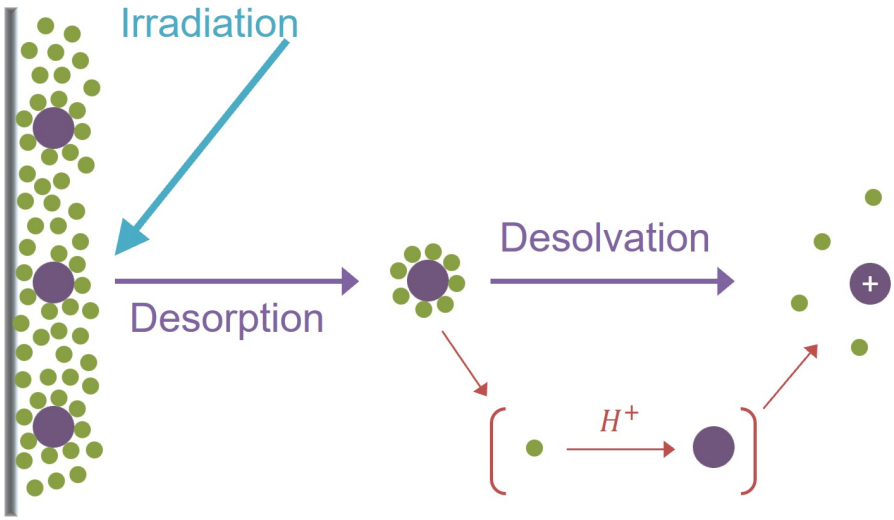


Figure 1.6: Schematic of the MALDI photo-ionisation mechanism.

MALDI is a complex process, there are several other models were proposed to explain it, which are listed in ref.[87–91].

Matrix selection and optimisation is one of the most critical steps in MALDI sample preparation. The choice of matrix depends on both the laser wavelength and the class of analyte to be studied. An ideal matrix must satisfy several criteria: strong absorbance at the laser wavelength, sufficiently low molecular weight to allow sublimation, stability under vacuum, the ability to promote analyte ionisation, solubility in solvents compatible with the analyte, and minimal chemical reactivity. Based on these principles, several commonly used UV-MALDI matrices and their properties are summarised in Table 1.2.

In 2000, the atmospheric pressure matrix-assisted laser desorption/ionization (AP-MALDI) source was developed. Its underlying principle is similar to that of conventional vacuum MALDI. The same sample matrices and preparation techniques used in vacuum MALDI are generally compatible with AP-MALDI.

The key difference lies in the ionization environment: AP-MALDI generates ions under atmospheric pressure, whereas traditional MALDI operates under high vacuum. To analyze the ions in the mass spectrometer, a heated capillary or ion transfer tube is used

Table 1.2: Commonly used UV-MALDI matrices and their applications.

Compound	**Other Names**	**Wavelength (nm)**	**Applications**
2,5-Dihydroxybenzoic acid	DHB, Gentisic acid	337, 355, 266	Peptides, nucleotides, oligonucleotides, oligosaccharides
3,5-Dimethoxy-4-hydroxycinnamic acid	Sinapinic acid (SA)	337, 355, 266	Peptides, proteins, lipids
4-Hydroxy-3-methoxycinnamic acid	Ferulic acid	337, 355, 266	Proteins
α-Cyano-4-hydroxycinnamic acid	CHCA	337, 355	Peptides, lipids, nucleotides
Picolinic acid	PA	266	Oligonucleotides
3-Hydroxy picolinic acid	HPA	337, 355	Oligonucleotides

to transport the ions from the atmospheric region into the vacuum of the mass analyzer. A schematic illustration of an AP-MALDI source is shown in Figure 1.7.

The ions are transferred into the vacuum system through an atmospheric pressure interface (API). To facilitate ion transport into the lower-pressure region, a high voltage (typically 2–3 kV) is applied to the surface of the target plate, and a stream of dry nitrogen gas is directed at the sample area. It is important to note that ion transmission into the mass spectrometer is relatively inefficient under atmospheric conditions; therefore, AP-MALDI generally consumes more sample than conventional vacuum MALDI.

Although the ionization mechanism of AP-MALDI is similar to that of conventional MALDI, the rapid and efficient thermalization of internal energy at atmospheric pressure results in even softer ionization. As a result, AP-MALDI tends to cause less fragmentation than vacuum MALDI, and in some cases, it can be even softer than infrared MALDI (IR-MALDI).

1.3.3 Electrospray Ionization (ESI)

In this thesis, electrospray ionization (ESI) is used for sample preparation and is therefore introduced briefly.

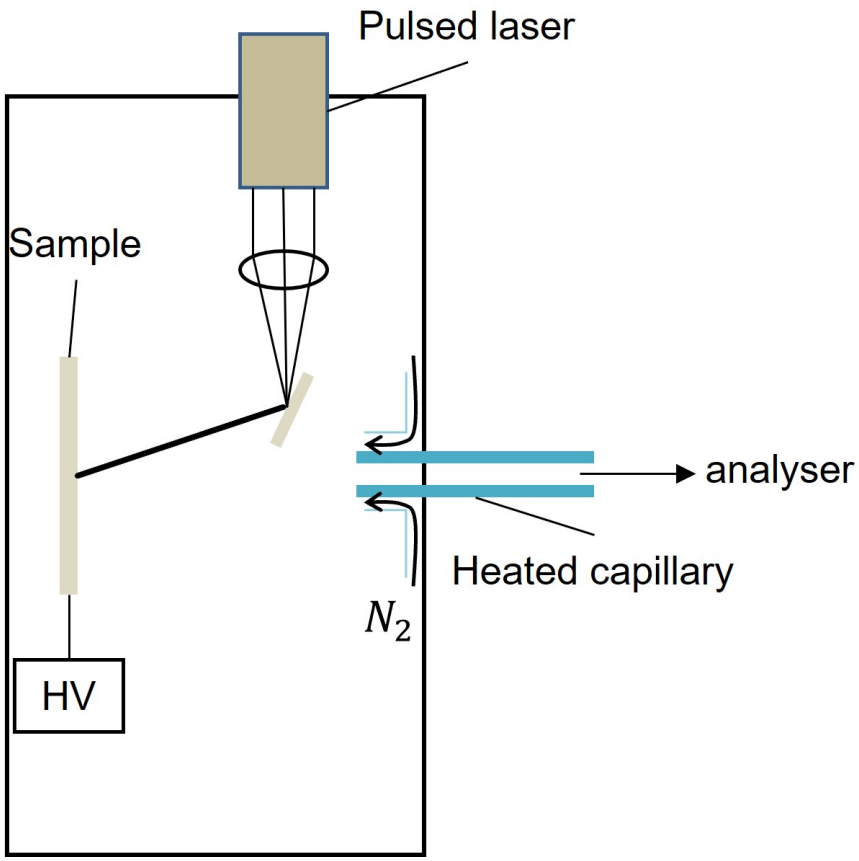


Figure 1.7: Diagram of an AP-MALDI (atmospheric pressure MALDI) ion source.

As another soft ionization technique, ESI has proven highly effective for ionizing non-volatile, labile, and large biological molecules[92]. In ESI, a strong electric field is applied under atmospheric pressure to a liquid flowing through a capillary at a low rate (typically 1–10 µl min^{-1}). This electric field, generated by a potential difference of 2–6 kV between the capillary and a counter-electrode, induces charge accumulation at the liquid surface. The resulting electrostatic forces cause the liquid to disperse into highly charged droplets.

These charged droplets are then directed through a curtain of heated inert gas—most commonly nitrogen—or through a heated capillary to assist in solvent evaporation, ultimately producing gas-phase ions. A schematic of the ESI source is shown in Figure 1.8.

ESI is known for its high sensitivity, allowing detection of analytes at the picomolar level. Furthermore, ESI can produce multiply charged ions from biomolecules, enabling very large molecules to be detected at relatively low m/z values.

A derivative technique based on ESI, called desorption electrospray ionization (DESI),

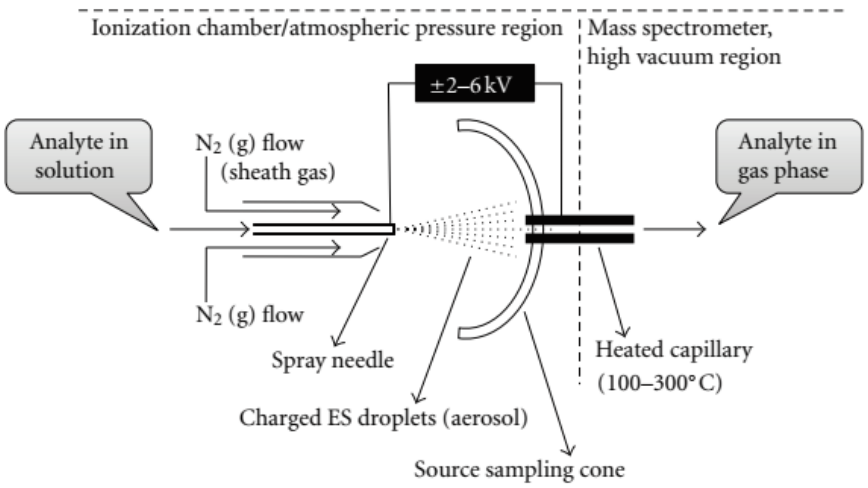


Figure 1.8: Schematic representation of the ESI ion source. Adapted from ref. [93].

has gained popularity since its introduction by Takats *et al.* in 2004[94]. In DESI, an aerosol of charged droplets generated by ESI is directed onto a sample surface. From this surface, small organic and macromolecules are desorbed, ionized, and transferred into the mass spectrometer as desolvated ions under ambient conditions, this allows for ambient sampling of solid analytes.

1.4 Mass Analyser

Apart from the ion sources, the mass analyser is another key part of a mass spectrometer. Once the gas-phase ions are generated, they are sent to a mass analyser to separate them by their different masses. The physical property of ions is measured by their mass-to-charge ratio m/z, rather than their masses. Therefore, for multiply charged ions, the apparent m/z values are fractional parts of their actual masses.

Like ion sources, several types of mass analyzers have been developed, each with unique characteristics and applications. Table 1.3 summarizes the key properties of eight widely used mass analyzers: quadrupole, ion trap, time-of-flight (ToF), ToF reflectron, Qq-ToF, magnetic sector, Fourier-transform ion cyclotron resonance (FT-ICR), and Orbitrap.

The most important parameters of the mass analysers listed in Table 1.3 are mass resolution, mass accuracy, and mass limit.

Table 1.3: Comparison of common mass analyzers. Adapted from ref.[81, 95–101].

Property	**Quad**	**Ion Trap**	**ToF**	**ToF Refl.**	**Qq-ToF**	**Mag. Sect.**	**FT-ICR**	**Orbitrap**
Mass Limit(Th)	4k	6k	$>10^6$	10k	10k	20k	10k	6-8k
Resolution(at 1kDa)	2k	4k	5k	20k	$<6\times10^4$	10^5	10^6–10^7	10^6
Accuracy (ppm)	100	100	2–5	5–10	<5	<1–5	0.1-0.6	<1
Ion Sampling	Cont.	Cont.	Pulsed	Pulsed	Pulsed	Cont.	Pulsed	Pulsed
Pressure (Torr)	1e-5	1e-5	1e-6	1e-6	1e-6	1e-7	1e-8	1e-10

Mass resolution, also known as mass resolving power, is defined as the mass difference at which adjacent spectral peaks can be distinctly resolved. It is typically expressed as $m/\Delta m$, where m is the mass of the ion peak and Δm is the full width at half maximum (FWHM) of that peak.

Mass accuracy refers to the deviation between the experimentally measured m/z value and the true or theoretical value. It is usually expressed in parts per million (ppm).

Mass limit indicates the upper bound of the mass range the analyser can detect reliably.

A detailed method for calculating both mass resolution and mass accuracy is provided in Chapter 3. As this thesis exclusively utilises a time-of-flight (ToF) analyser, its fundamental principles and operations are outlined in detail in the following sections.

1.4.1 Time-of-Flight analyser

Time-of-Flight (ToF) is one of the earliest and most historically significant types of mass analyser. The concept was first described by Stephens in 1946 [102], and a practical design for a linear ToF mass spectrometer was later published by Wiley and McLaren in 1955 [103], which subsequently led to the development of the first commercial ToF instrument.

A schematic diagram of a linear ToF instrument coupled with a MALDI ion source is shown in Figure 1.9. The illustration depicts operation to detect negatively charged ions, the polarity of the applied grid potentials must be inverted accordingly. Once ions are generated by the MALDI source, they are accelerated by an electric potential in the acceleration region. The ions are accelerated to the same kinetic energy and are directed into the drift region.

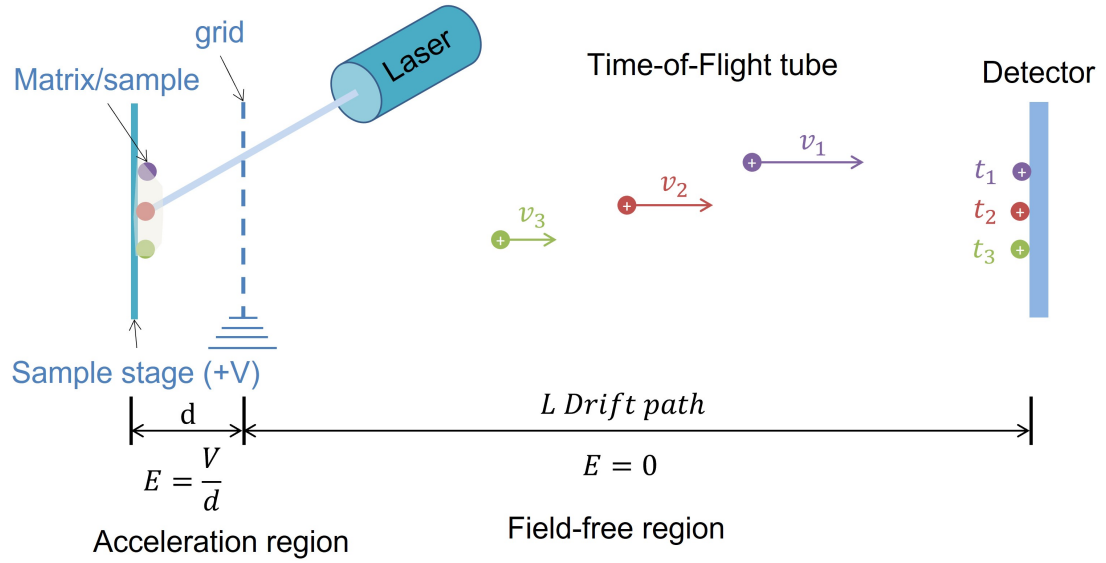


Figure 1.9: Illustration of a linear ToF instrument configured for positive-mode MALDI. Ions are accelerated by electric potentials and separated in the field-free drift region. Ions with different m/z values travel at different velocities, resulting in different arrival times at the detector.

In this field-free region, the ions travel at constant velocity. Since ions with the same energy (E), but with different mass-to-charge (m/z) ratios attain different velocities, they arrive at the detector at different times. This separation in arrival time enables mass analysis.

In principle, Time-of-Flight (ToF) mass analysers do not possess an intrinsic upper mass detection limit, allowing them to be coupled with a wide range of ion sources. For instance, when integrated with matrix-assisted laser desorption/ionisation (MALDI), ToF analysers can detect ions with masses exceeding 100 kDa [104]. One of the key advantages of ToF analysers is their high-speed acquisition capability: they can generate a full mass spectrum over a broad mass range within microseconds, significantly faster than many other types of mass analysers. Additionally, ToF instruments are characterised by high ion transmission efficiency, which results in excellent sensitivity.

The resolution R of a ToF mass spectrometer can be derived from the relationship between the ion flight time and its mass-to-charge ratio. Starting from Equation A.6, reproduced here for clarity:

$$m/z = 2eV_{\text{rep}}t^2/L^2, \tag{1.1}$$

one can differentiate both sides with respect to time t to obtain an expression relating small changes in mass to changes in time:

$$\mathrm{d}_m/z = \left(2eV_{\mathrm{rep}}/L^2\right) t\, \mathrm{d}_t \tag{1.2}$$

Rearranging this in terms of relative quantities gives:

$$m/\mathrm{d}_m = t/2\,\mathrm{d}_t \tag{1.3}$$

Hence, the mass resolution R of a ToF instrument can be defined as:

$$R = \frac{m}{\Delta m} = \frac{t}{2\Delta t} \tag{1.4}$$

where Δm is the full width at half maximum (FWHM) of the mass peak and Δt is the corresponding FWHM in the time domain. The resolution is therefore directly proportional to the ion's flight time and inversely proportional to the temporal width of its arrival distribution.

The dominant factors contributing to Δt include the temporal spread of ion velocities as they exit the ion source and the initial spatial and kinetic energy distributions of ions in the desorption plume. While the detector's response time contributes slightly to Δt, it is usually negligible compared to the spread caused by initial energy and position distributions.

As velocity spread is a primary contributor to the mass resolution in Time-of-Flight (ToF) mass spectrometry, strategies have been developed to minimise this effect and enhance resolution. One such method is *Delayed Pulsed Extraction* (DPE), introduced by Wiley and McLaren in the 1950s [103], which enables time-focusing of ions with the same mass-to-charge ratio but different initial kinetic energies. The concept is illustrated schematically in Figure 1.10.

In static extraction mode (Figure 1.10(a)), ions formed in the source region are immediately extracted by a constant electric field. Ions with the same m/z but higher initial velocities reach the detector earlier than slower ions, leading to temporal dispersion and peak broadening.

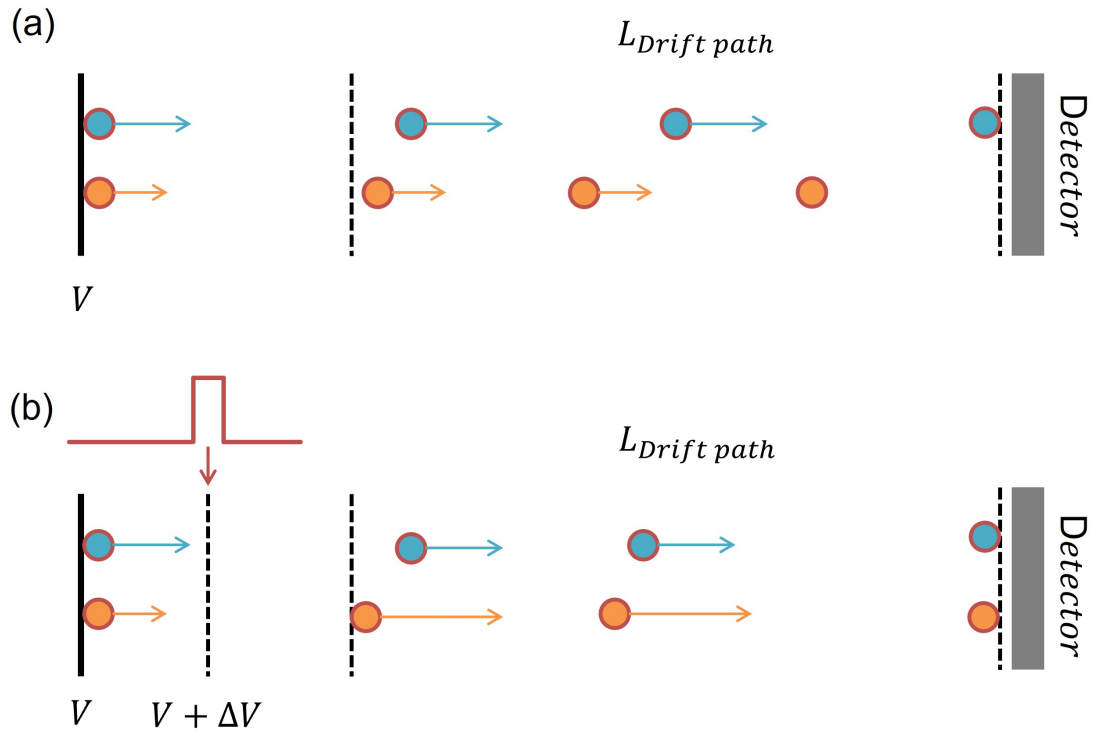


Figure 1.10: Schematic representation of (a) static extraction and (b) delayed pulsed extraction (DPE). In both cases, two ions with the same m/z but different initial velocities are shown. Arrow length indicates ion velocity. In static extraction, ions retain their velocity difference throughout the drift region, resulting in temporal dispersion. In DPE, the slower ion receives a greater acceleration during the delayed pulse, allowing it to catch up with the faster ion, thus reducing arrival time spread and sharpening the peak.

In contrast, in the delayed pulsed extraction mode (Figure 1.10(b)), a pulsed electric field is applied after a short delay following ion formation. During this delay, ions with different initial velocities spatially separate; faster ions move further from the source, while slower ones lag behind. When the extraction pulse is applied, the spatial separation enables differential acceleration: slower ions receive a greater acceleration than faster ones. With careful tuning of the pulse delay and extraction potential, ions of the same m/z can be made to converge temporally at the detector. This results in reduced arrival time spread and significantly improved mass resolution through time focusing. DPE is especially beneficial in where initial velocity distributions are broad due to the desorption process. Time-focusing methods like DPE thus play a crucial role in achieving high resolution in ToF mass spectrometry.

Recently, a technique known as post-extraction differential acceleration (PEDA) has

been developed for MALDI systems [105, 106]. Conventional post-extraction approaches generally optimise only a very narrow mass range. Guo *et al.* first introduced a double-field PEDA method to optimise two distinct mass ranges simultaneously [105]. For the home-built mass spectrometer described here, the mass ranges achieving $m/\Delta m \geq 1000$ were 65 and 165 Da, corresponding to single-field PEDA at 410 Da and double-field PEDA at 360 and 480 Da, respectively. Different laser dyes are used to test the PEDA performance across various mass ranges. The corresponding spectra and images are shown in Figure 1.11(a) and (b), respectively.

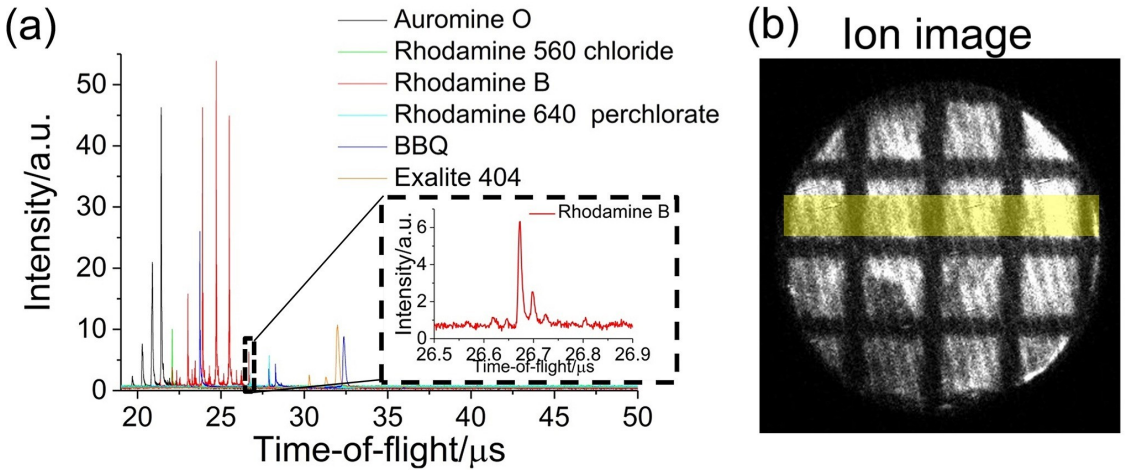


Figure 1.11: Laser dye mass spectra (a) and ion images (b) are respectively used to characterize the mass and spatial resolution dependence over a 500 Da range of both single- and double-field PEDA. Adapted from Ref. [105]

Furthermore, a time-dependent PEDA has been implemented to achieve high mass resolution across a continuously wider mass range. In this approach, a linearly rising potential is applied to the ion extraction electrode, subjecting sequential m/z ratios to a varying electric field and thereby aligning their foci at the detector. Using this method, at least 75% of the maximum mass resolution was obtained over a 300–600 Da range when the ion microscope was focused around 450 Da, representing more than a ten-fold improvement compared with the conventional single-field PEDA method.

Another effective approach for improving mass resolution in Time-of-Flight (ToF) mass spectrometry is the use of an electrostatic reflector, commonly referred to as a *reflectron*. The reflectron is positioned at the end of the field-free drift region and functions as an ion mirror. After entering the reflectron, ions are decelerated, turned

around, and then re-accelerated towards a detector that is typically located on the same side as the ion source.

The primary function of the reflectron is to correct for the kinetic energy dispersion among ions of identical mass-to-charge ratio (m/z). This energy spread is a key source of peak broadening in linear ToF instruments. As illustrated in Figure 1.12, ions with the same m/z but differing kinetic energies will penetrate the reflectron to different depths: ions with higher kinetic energy (and therefore higher velocity) travel deeper into the reflectron before being reflected. Consequently, these faster ions experience a longer flight path and spend more time in the reflectron than their slower counterparts. With careful tuning of the reflectron voltage gradient and path length, the time delay compensates for the first order initial energy spread, allowing ions with the same m/z to arrive at the detector simultaneously. This results in significantly enhanced mass resolution. More ion trajectory calculations are shown in the appendices A.

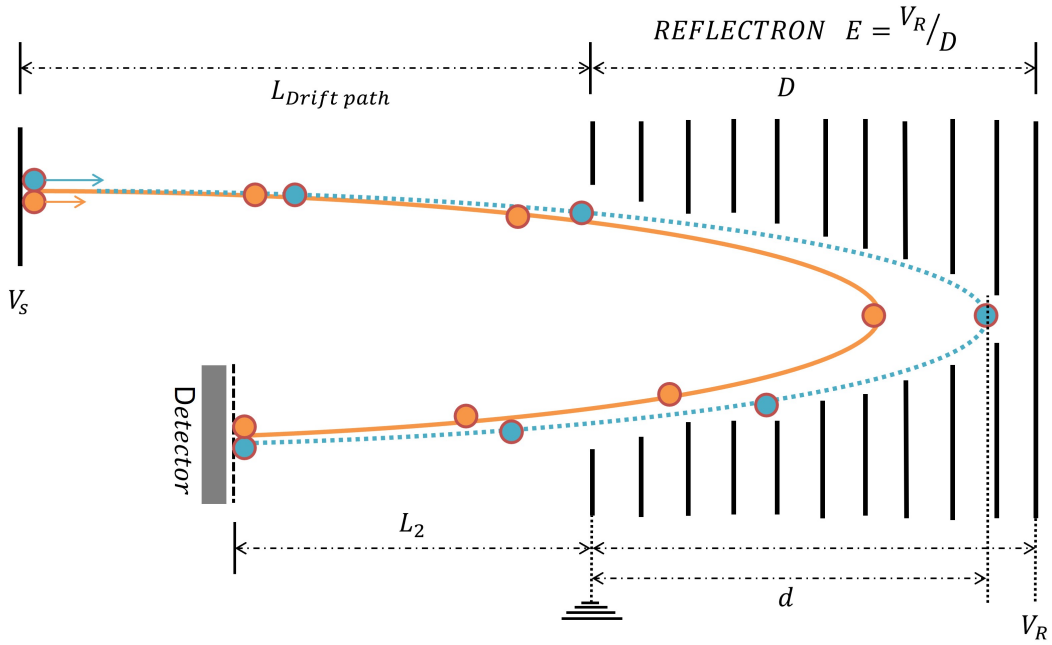


Figure 1.12: Schematic representation of a ToF instrument equipped with a reflectron. The two circles represent ions with identical m/z values but different kinetic energies. By carefully adjusting the reflectron voltage and length, the ions are time-focused to reach the detector simultaneously.

Reflectron ToF (re-ToF) instruments can achieve resolutions of up to 20,000 or higher, depending on the design and operating conditions. In addition to improving resolution,

reflectrons also help reduce the effects of long-term drift and mechanical imperfections in the instrument by acting as a secondary time-focusing stage. This makes reflectron-based ToF analysers particularly advantageous for high-accuracy mass measurements and complex mixture analyses.

1.5 Mass Spectrometry Imaging

Mass spectrometry imaging (MSI) is a powerful label-free analytical technique that enables the investigation of the spatial distribution of chemical species across a diverse array of samples. It facilitates the simultaneous imaging of thousands of molecular entities—including lipids, metals, metabolites, peptides, proteins, and glycans—within a single experiment, often achieving micrometre or even sub-micrometre spatial resolution. By combining the molecular specificity of mass spectrometry with spatial visualisation in thin tissue sections, MSI has emerged as a highly valuable tool for the chemical characterisation of biological specimens.

Owing to rapid technological advancements in recent years, MSI is increasingly finding applications in clinical diagnostics, pathology, and the pharmaceutical sciences. These developments include improvements in sample preparation protocols to enhance reproducibility and data reliability, as well as innovations in instrument design that have significantly improved spatial resolution and data acquisition speed. With these enhancements, MSI is now capable of achieving single-cell resolution in some cases.

Furthermore, the high dimensionality and complexity of MSI datasets have driven the integration of advanced statistical methods and machine learning algorithms. These computational tools facilitate the efficient handling, interpretation, and visualisation of large-scale imaging data, thereby expanding the scope and impact of MSI in modern biomedical research and clinical applications.

One of the most emerging applications is the biological tissue analysis. MSI acquisition time is usually hours and done under vacuum, therefore the tissue samples need to be fixed to halt enzyme activity to reduce degradation and delocalization (e.g., diffusion across the tissue) of the molecules[107]. This is typically done by flash-freezing the sample for MSI. The tissue samples are thinly sectioned with a thickness of

6-20 µm to keep the conductivity and ensure the ion's extraction. Figure1.13 shows N-glycans images in Formalin-Fixed Paraffin-Embedded (FFPE) colon carcinoma sections obtained with a MALDI-MSI[108].

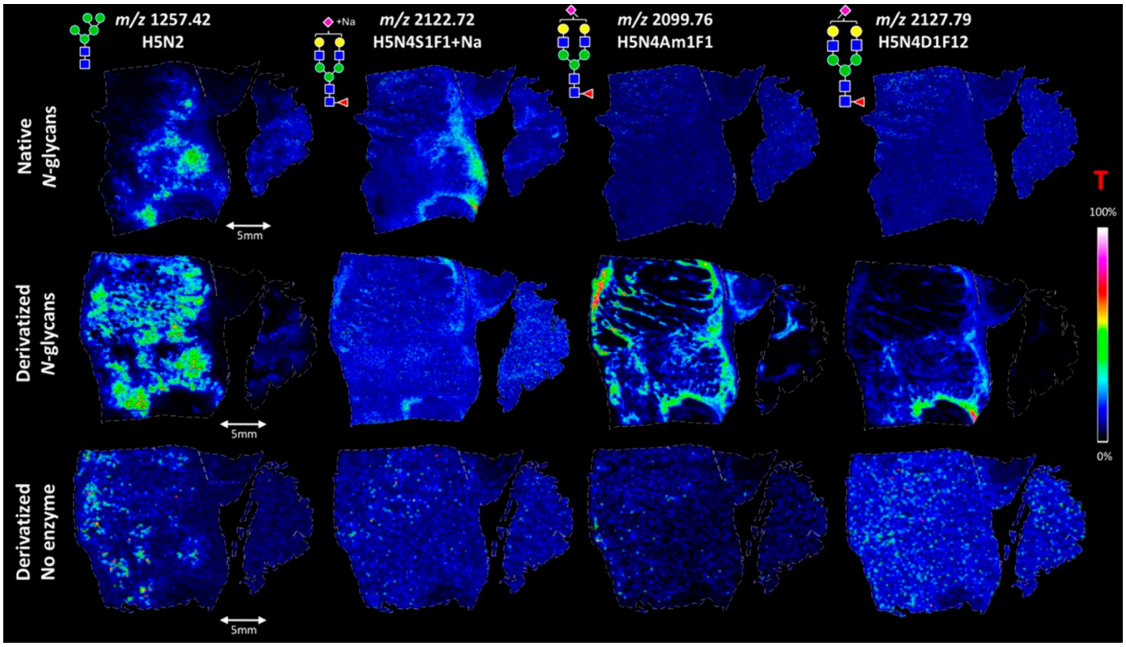


Figure 1.13: MSI comparison of digestion and derivatization of N-glycans in FFPE colon carcinoma sections. Adapted from ref.[108].

As MSI is typically employed for surface analysis, it is most commonly coupled with ionisation techniques such as matrix-assisted laser desorption/ionisation (MALDI), secondary ion mass spectrometry (SIMS), and desorption electrospray ionisation (DESI). Different ion sources have their different detection mass ranges, and their spatial resolution is usually limited by the focusing capability of their primary ion beam in the conventional microprobe mode MSI. A comparison of different MSI is shown in the table1.4.

MALDI and DESI are commonly employed for the direct analysis of biomolecules such as lipids and metabolites, due to their soft ionization characteristics, which minimize fragmentation during ionization. In contrast, SIMS utilizes a hard ionization method, making it more suitable for the detection of inorganic species or small biomolecules. However, SIMS offers a significant advantage in spatial resolution. The ion beam used in SIMS can be precisely focused, some atomic ion beams can achieve spot sizes as small as 50-200 nm[110, 111], enabling sub-cellular imaging capabilities that surpass those of MALDI and DESI.

Name	Ionisation source	Type of ionisation	Analytes	Spatial Resolution	Mass range
SIMS	Ion gun	Hard	Elemental ions, small molecules, lipids	50 nm – 10 µm	0 – 1000 Da
DESI	Solvent spray	Soft	Small molecules, lipids, peptides	100 µm	0 – 2000 Da
nano-DESI	Solvent bridge	Soft	Small molecules, lipids, peptides	10 µm	0 – 2000 Da
MALDI	UV Laser beam	Soft	Lipids, peptides, proteins	2.5 – 20 µm	0 – 10^5 Da
LAESI	mid-IR Laser beam, solvent spray	Soft	Small molecules, lipids, peptides, proteins	200 µm	0 – 2000 Da
LA-ICP-MS	UV Laser beam	Hard	Elemental ions	10 – 100 µm	0 – 250 Da

Table 1.4: Comparison of typical parameters among MSI techniques. Adapted from ref. [109].

There are two principal modes of mass spectrometry imaging (MSI): microprobe mode and microscope mode. Among these, microscope mode has become the most widely adopted approach in contemporary MSI applications. In this mode, a focused primary ion or laser beam is rastered across the sample surface in a pixel-by-pixel fashion, with the spatial resolution primarily determined by the diameter of the focused beam. The operating principle of microprobe mode MSI is illustrated in Figure 1.14(A).

Advancements in mass analyser technology—such as improvements in mass resolution, mass accuracy, and sensitivity—can be directly incorporated into MSI instruments, significantly enhancing their analytical performance. Furthermore, unlike other imaging techniques such as fluorescence microscopy or radioimmunoassays, MSI generally does not require labelling, making it an inherently label-free technique. This provides a distinct advantage when analysing complex or poorly characterised biological systems.

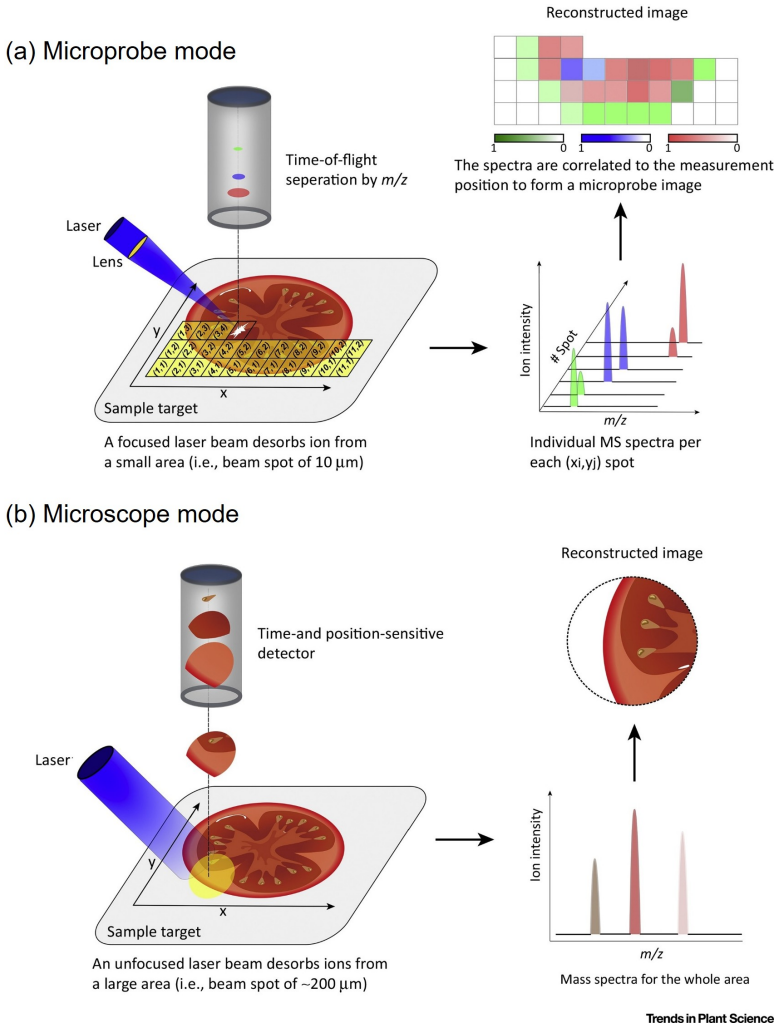


Figure 1.14: Schematic overview of microprobe (A) and microscope (B) mode mass spectrometry imaging (MSI), demonstrated on a matrix-assisted laser desorption/ionisation (MALDI) time-of-flight (ToF)/MS platform. Adapted from Ref. [112].

Microscope mode MSI offers the potential to acquire high-resolution ion images more rapidly than the microprobe mode. In this approach, the sample surface is illuminated using a defocused laser or primary ion beam, allowing for the simultaneous desorption and ionisation of molecules across a broad area. Unlike the microprobe mode, which scans point by point, microscope mode captures spatial information in parallel.

The position of the resulting ions is recorded using a position-sensitive imaging detector located at the end of a time-of-flight (ToF) analyser. This configuration enables the reconstruction of spatially resolved ion images from the detected ion trajectories. The operational principle of microscope mode MSI is illustrated in Figure 1.14(B).

This process is analogous to stigmatic optical microscopy and offers the advantage of decoupling spatial resolution from the size of the probe beam, while still achieving resolutions in the range of 1–20 µm.

Microscope mode MSI was initially limited by its reliance on conventional CCD cameras, which are only capable of detecting a single ion image corresponding to one m/z value at a time. This significant limitation prevented widespread application of the technique for several decades, until the development of CMOS-based imaging detectors. Unlike CCDs, CMOS cameras are capable of recording both the arrival time and spatial position of each ion. In principle, this allows for the simultaneous detection of all resolved m/z values within a defined mass range in a single experiment [113–116].

The earliest implementations of microscope mode MSI were coupled with electrostatic analysers (ESAs), which help to minimise flight time dispersion resulting from variations in the initial kinetic energy of ions. These instruments typically featured a field of view of approximately 300 µm, with image resolutions between 1–5 µm. A mass resolution of approximately 15,000 $m/\Delta m$ was achieved for $C_2F_5^+$ secondary ions [117]. Using a similar configuration, R. M. A. Heeren and co-workers reported the first macromolecular ion microscope images in 2004, performing MALDI on a modified commercial TRIFT II (triple focusing time-of-flight) mass spectrometer [64].

In 2022, Heeren's group further advanced the technique by integrating a TimePix3 camera and a C_{60}^+ primary ion beam with the BioTrift instrument—an upgraded platform based on the TRIFT II mass microscope. This configuration enabled the acquisition of gigapixel-scale images from rat brain tissue within just 34 minutes, achieving a spatial resolution of approximately 2 µm [118]. However, under this setup, the achievable mass resolution was limited to approximately 100 $m/\Delta m$.

To overcome such limitations, a multi-turn time-of-flight (TOF) mass analyser, MULTUM-IMG, was developed by Toyoda *et al.* in 2008 [119]. As illustrated in Figure1.15, MULTUM-IMG comprises four toroidal electric sectors, allowing ions to circulate in a closed orbit along a figure-eight trajectory for hundreds of turns. In principle, if the instrument satisfies the *perfect focusing* condition, ions with identical m/z values

entering the multi-turn section simultaneously will exit it at the same time and position, irrespective of their initial velocities or incident angles.

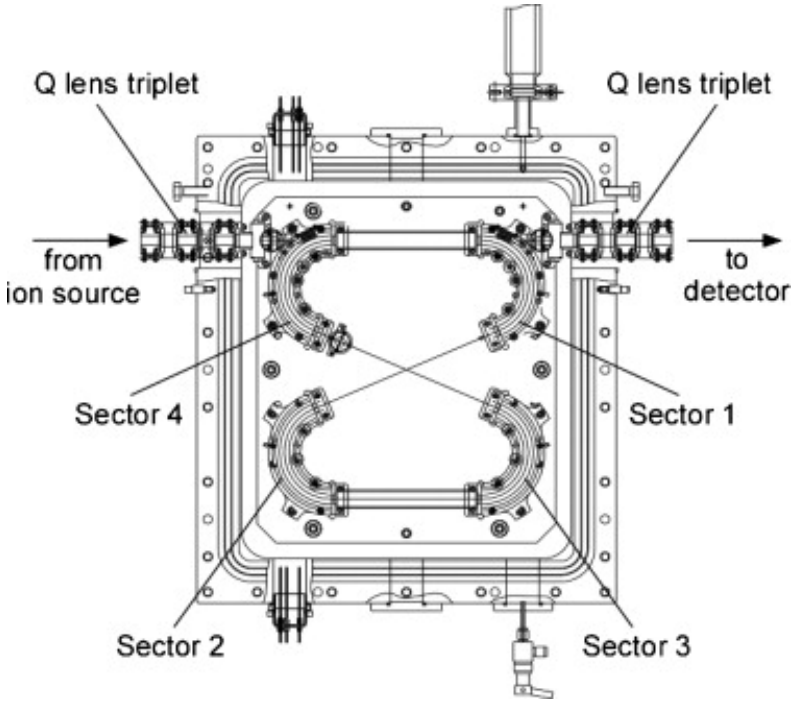


Figure 1.15: Factory drawing of the multi-turn TOF mass analyzer (MULTUM-IMG). Adapted from ref.[119].

This design enables enhancement of the TOF resolution by increasing the number of turns, as the temporal width of the TOF peaks remains constant while the flight time increases. Using the MULTUM instrument, a mass resolution of 130,000 $m/\Delta m$ was achieved after 500 turns. Positional information of the ions can also be retained throughout multiple cycles. However, significant image distortion was observed: after just one turn, the ion images projected onto the detector were already noticeably deformed, and became increasingly blurred after three turns.

1.5.1 Previous work on Microscope mode ToF-MSI

Brouard *et al.* developed a mass spectrometry imaging (MSI) instrument based on modifications to a conventional velocity map imaging (VMI) setup. Using this instrument, microscope mode MSI experiments were performed with a Pixel Imaging Mass Spectrometry (PImMS) camera [113]. In the first design iteration, the microscope mode

MALDI-MSI system was capable of analysing a spatial area of $5 \times 5\,\text{mm}^2$ using a 355 nm Nd:YAG laser. The mass resolution achieved was $m/\Delta m = 67$ using a photomultiplier tube (PMT), and $m/\Delta m = 48$ using the PImMS camera. The spatial resolution was 23 µm with a CCD camera, and approximately 99 µm with the PImMS system.

The higher mass resolution observed with the PMT is attributed to its shorter time response compared to the PImMS camera. In contrast, the improved spatial resolution achieved with the CCD camera results from its higher pixel count relative to the PImMS detector.

To further enhance the mass resolution of the instrument, post-extraction differential acceleration (PEDA) [105, 106] and a reflectron [120] have been incorporated into the MALDI setup. The configuration of this system is illustrated in Figure 1.16.

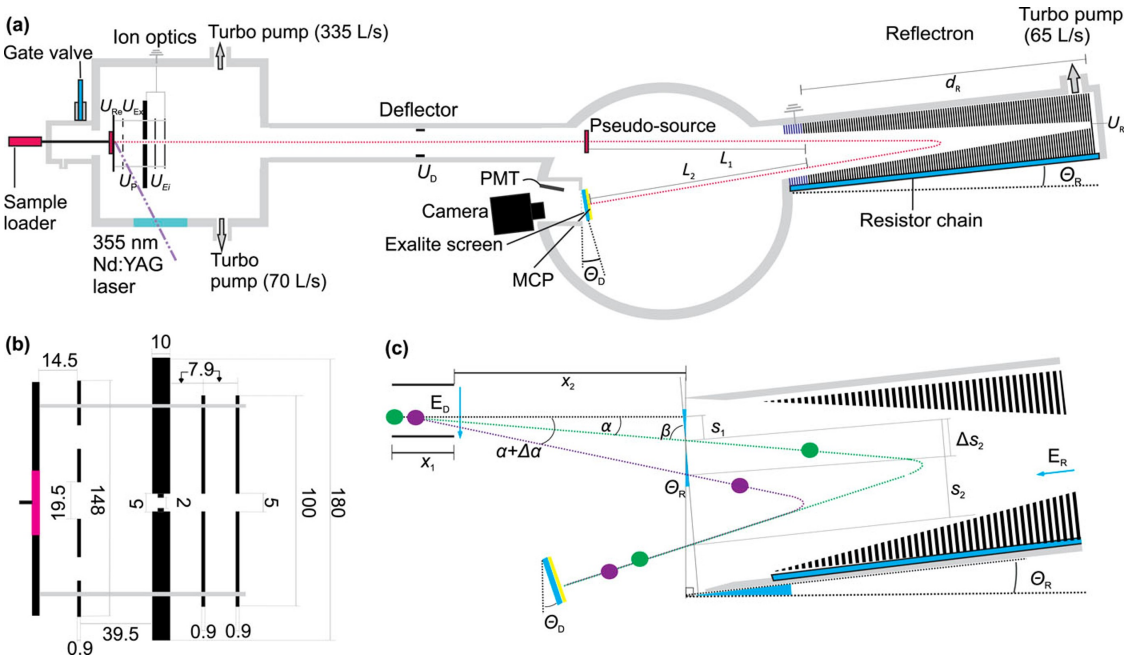


Figure 1.16: A schematic of the microscope imaging mass spectrometer. The red trace represents a typical ion trajectory that originates following laser-induced ionization of a sample. The ions are focused by an ion microscope, deflected through a single-stage gridless reflectron, and projected onto a position-sensitive detector. Ion images and mass spectra are recorded using an event-triggered imaging sensor or using a photomultiplier tube (PMT) and CCD camera. Adapted from ref.[120].

Using the single-field PEDA technique, which applies a single-step electric pulse, an optimised mass resolution of approximately 4,000 $m/\Delta m$ was achieved at around 420 m/z.

However, the conventional post-extraction method is highly limited in applicability, functioning effectively only within a very narrow mass range (typically <70 m/z)[105].

To overcome this limitation, Guo and Brouard developed a double-field PEDA method in 2018, employing two pulsed electrodes to simultaneously focus ions of two different m/z values. This approach extended the usable mass window to approximately 165 m/z, while maintaining a mass resolution exceeding 3,000 $m/\Delta m$[105].

Subsequently, an electrodynamic PEDA approach was introduced, enabling dynamic optimisation of ion trajectories across a broader mass range. With this configuration, a mass window spanning 300–600 m/z was effectively focused, yielding mass resolutions of approximately 4,000 $m/\Delta m$ across the range[106].

To further increase the mass resolution of MALDI-MSI systems, a reflectron time-of-flight (ToF) analyser was integrated into the setup [120]. This configuration enabled imaging of mass-resolved ions from a 270 µm diameter sample area. By employing pulsed extraction differential acceleration for ion optical focusing, a pseudo-source plane was generated, allowing for efficient use of a single-stage, gridless reflectron.

With this approach, simultaneous mass and spatial resolutions of $8{,}100 \pm 700\, m/\Delta m$ and 18 ± 6 µm, respectively, were achieved. The limiting factor for the obtainable mass resolution was primarily the response time of the position-sensitive detector. According to simulation results, the system has the potential to reach a mass resolution of up to $30{,}200 \pm 2{,}900\, m/\Delta m$.

1.6 Aberration

Technically, the spatial resolution of mass spectrometry imaging (MSI) is constrained by several factors, including the ion optical focusing performance, the size of individual ion clusters upon impact, and the pixel count of the imaging detector. Theoretically, the ultimate limitations on spatial resolution in MSI systems are governed by optical aberrations inherent to the ion optics. These include spherical aberration, chromatic aberration, and Petzval field curvature, all of which can distort ion trajectories and degrade image quality.

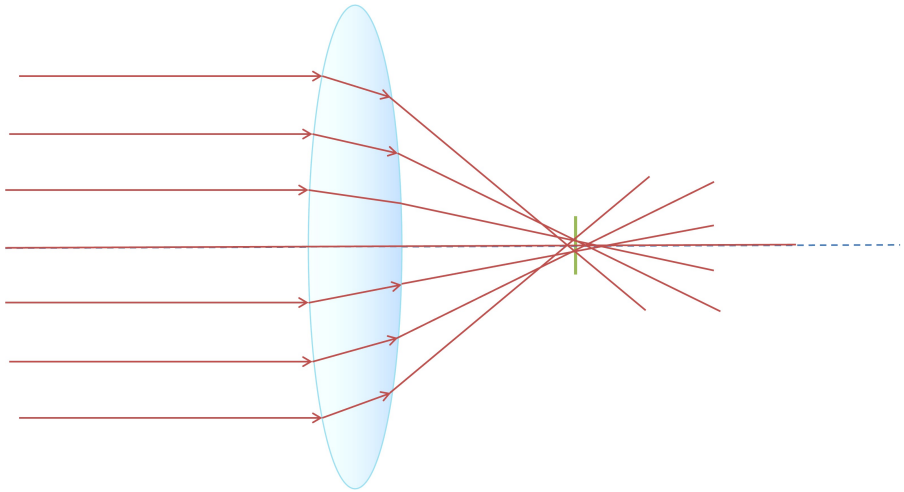


Figure 1.17: Schematic illustration of spherical aberration. Light rays entering different regions of the lens are focused at different points, leading to image blur.

Spherical aberration is a common optical imperfection that occurs when rays passing through different regions of a spherical lens or mirror fail to converge at a single focal point. This effect results in image blurring and reduced resolution, as illustrated in Figure 1.17. A similar phenomenon occurs in ion lens systems, where electrodes create approximately spherical electric field lines that act as "electric lenses" to focus ions. In such systems, a spherical ion lens has an aplanatic point—where spherical aberration is absent—only at a lateral distance from the optical axis equal to the radius of the spherical surface divided by the refractive index of the lens material. Spherical aberration degrades the focus of telescopes, mass spectrometers, and other precision instruments. This limitation is particularly significant because spherical components are much easier and more cost-effective to manufacture than aspherical ones. In many practical designs, it is more economical to use a combination of spherical elements to correct for spherical aberration rather than to fabricate a single aspherical lens.

Another factor that negatively impacts spatial resolution is chromatic aberration, also referred to as chromatic distortion in optics. This phenomenon occurs when light composed of multiple wavelengths passes through a lens; due to wavelength-dependent refraction, the different wavelengths are focused at different positions along the optical axis, as illustrated in Figure 1.18. A similar effect occurs in ion optical systems. In this case, ions with varying kinetic energies behave analogously to light rays of different

wavelengths—ions with higher or lower energies are focused at different points by the ion lens. This energy-dependent focusing results in image blur and a reduction in spatial resolution.

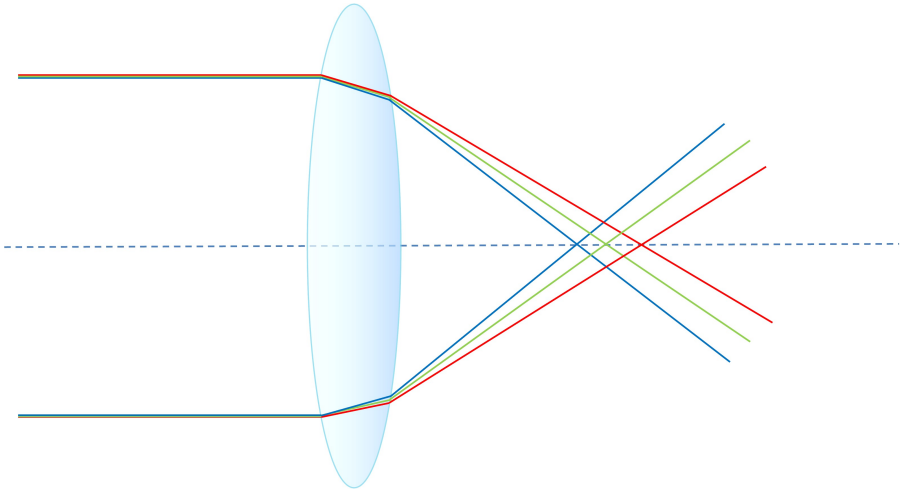


Figure 1.18: Schematic illustration of chromatic aberration. Light rays with different wavelengths entering the same region of a lens are focused at different points, leading to image blur.

Petzval field curvature, named after Joseph Petzval [121], refers to an optical aberration in which a flat object perpendicular to the optical axis cannot be brought into focus on a flat image plane. Instead, the best focus occurs on a curved surface, known as the Petzval surface. As a result, parts of the image near the edges may appear out of focus when the center is sharp, and vice versa. This is especially problematic in imaging systems that require a flat detector or recording medium.

Field curvature can be corrected by introducing a field flattener lens element, or by designing the optical system to match the curvature of the image plane—such as in the case of the human eye, where the retina approximates a curved surface. In mass spectrometry imaging systems, similar distortions can arise in ion optics, particularly when position-sensitive detectors are assumed to lie on a flat plane, but the ion trajectories focus onto a curved surface.

1.7 Secondary Ions' Velocity Distribution

As discussed in the previous section on aberrations, ions possessing different kinetic energies are challenging to focus onto a common point, which fundamentally limits

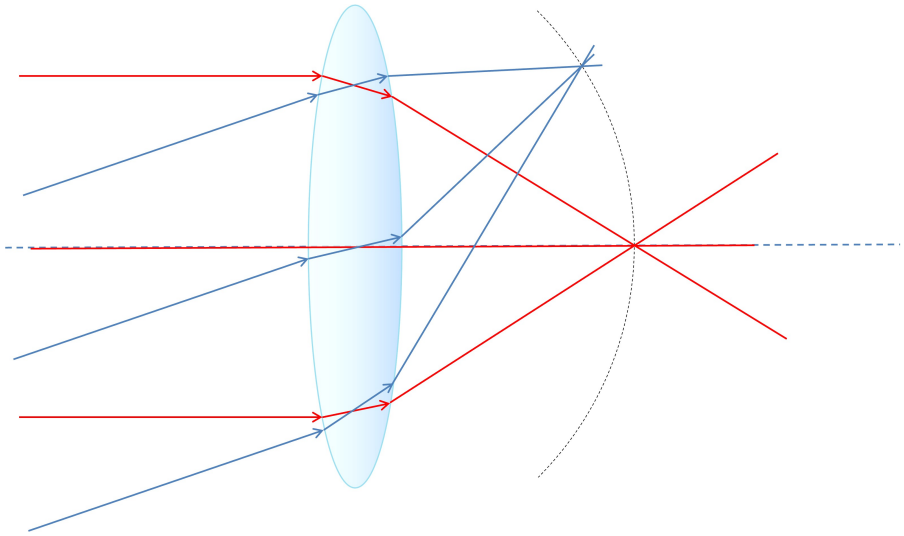


Figure 1.19: Illustration of Petzval field curvature. The image "plane" (curved arc) deviates from an ideal flat detector surface (vertical dashed line), leading to focus errors across the field.

the achievable spatial resolution. Furthermore, the kinetic energy spread among ions of the same mass-to-charge ratio (m/z) adversely affects the mass resolution of the time-of-flight (ToF) mass spectrometry spectrum.

To improve both mass and spatial resolution simultaneously, PEDA techniques are employed in this work. PEDA enhances the focusing of ions in both energy and space domains. However, determining the optimal acceleration voltages and trigger timings for such systems requires detailed simulations, which are described comprehensively in Chapter 2. These simulations are carried out using the SIMION ion optics software, and their accuracy relies heavily on realistic and precise input parameters, particularly the velocity distributions of the ions.

Matrix-assisted laser desorption/ionisation (MALDI) is a well-established technique that has been extensively applied in biological analysis for decades. The velocity distributions of various ion species produced by MALDI are well characterised and available in the literature [122]. In contrast, gas-cluster ion beam secondary ion mass spectrometry (GCIB-SIMS), though promising, is a relatively recent development in the context of biological applications. Consequently, the kinetic energy and angular distributions of secondary ions generated in GCIB-SIMS systems are not yet thoroughly studied or well understood, which poses challenges for accurate simulation and instrument optimisation.

Experimental measurements of the velocities of sputtered species have been pivotal in advancing the theoretical understanding of the sputtering process, particularly in the context of monoatomic primary ions (PIs). Sputter yields resulting from ion beam bombardment are influenced by several parameters, including the mass, energy, and angle of incidence of the incoming ions, as well as the chemical composition and structure of the sample surface. For cluster PI beams interacting with organic materials, an optimal incidence angle of approximately 45° has been identified, with this effect becoming increasingly pronounced as the energy per atom decreases [123]. While the velocity distributions—comprising both kinetic energy and angular spread—of sputtered ions are well characterised for monoatomic PIs on metallic surfaces, significantly less is known about their behaviour under cluster ion impact, particularly on organic substrates.

Numerous molecular dynamics (MD) and experimental studies have focused on gas cluster ion beams (GCIBs) impinging on metallic surfaces, due to their extensive use in industrial applications such as surface cleaning and polishing. These studies have shown that, under normal incidence, sputtered particles can acquire substantial lateral momentum—an effect not typically observed with monoatomic ion beams. This lateral component is influenced by the atomic number of the incident PIs and the crystallinity of the sputtered substrate [124]. Comparable results have been reported for organic surfaces subjected to GCIB bombardment [125].

Previous investigations of C_{60}^+ primary ions, as employed in this study, have predominantly utilised MD simulations. Comparative studies indicate that C_{60}^+ ions yield lower ejection energies for silver (Ag) compared to monoatomic or small cluster PIs [126–128], although broader kinetic energy distributions (KEDs) have been observed for the ejection of Ag dimers [128]. Experimental work has supported these findings.

Research on organic materials [124, 129–131] has suggested the existence of two distinct sputtering mechanisms, each contributing differently to the angular and kinetic energy distributions of the emitted particles. The first mechanism involves molecules ejected at near-normal angles with low translational kinetic energy (KE) but elevated internal energy. The second mechanism is characterised by particles emitted at off-normal angles, possessing high translational KE and low internal excitation. Delcorte [129]

referred to these as the "spring" and "washing" mechanisms, respectively, based on studies of gold (Au) and polystyrene (PS). Alternative interpretations, however, attribute these differences to the relative location of the sputtered molecules within the impact zone: molecules originating from the periphery of the primary ion's impact "crater" are believed to exhibit off-normal trajectories [129, 130].

1.8 Velocity Map Imaging

Several techniques have been developed to measure the angular distributions of ions. Common approaches include the use of planar retarding field analysers [132] and varying the position of the detector within a time-of-flight mass spectrometer (ToF-MS). However, these methods typically provide only coarse statistical information regarding ion angular distributions. They either suffer from limited angular resolution or are incapable of recording the full angular information simultaneously.

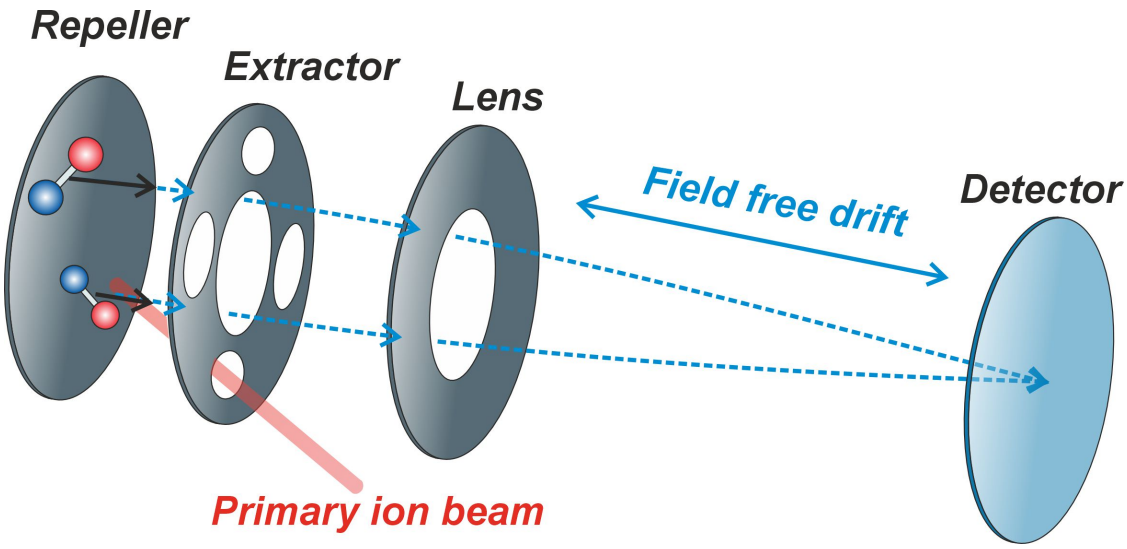


Figure 1.20: Schematic diagram of the ion optics for VMI. Fragment cations are generated at the repeller and focused onto the detector in such a manner that the impact position of each ion reflects its initial velocity vector, rather than its point of origin.

A significant advancement came with the development of the Velocity-Map Imaging (VMI) technique by Eppink and Parker[133], which allows for direct visualisation of ions' velocity and angular distributions. In conventional VMI setups, the ion optics typically consist of a repeller, an extractor, and a grounded lens. Ions formed on or

near the repeller are accelerated through this configuration and subsequently enter a field-free drift region. Within this region, ions possessing the same velocity vector are focused onto the same point on the position-sensitive detector. Crucially, the final impact position on the detector is determined by the ions' initial velocity vectors rather than their point of origin, thus enabling velocity-space imaging. This configuration is illustrated schematically in Figure 1.20.

VMI was first employed to record imaging of O^+ ions and electrons by Eppink and Parker [133], as shown in Figure 1.21. The figure presents the velocity distribution of O^+ ions produced by the photodissociation of molecular oxygen following two-photon excitation at approximately 225 nm.

A comparison between Figures 1.21(a) and (b) reveals that replacing the fine mesh grid with an open extractor electrode significantly enhances the imaging resolution, thereby improving velocity precision. This early application demonstrated the power of VMI to resolve fine details of ion and electron angular distributions, and laid the foundation for its broader adoption across various fields of molecular dynamics and reaction imaging.

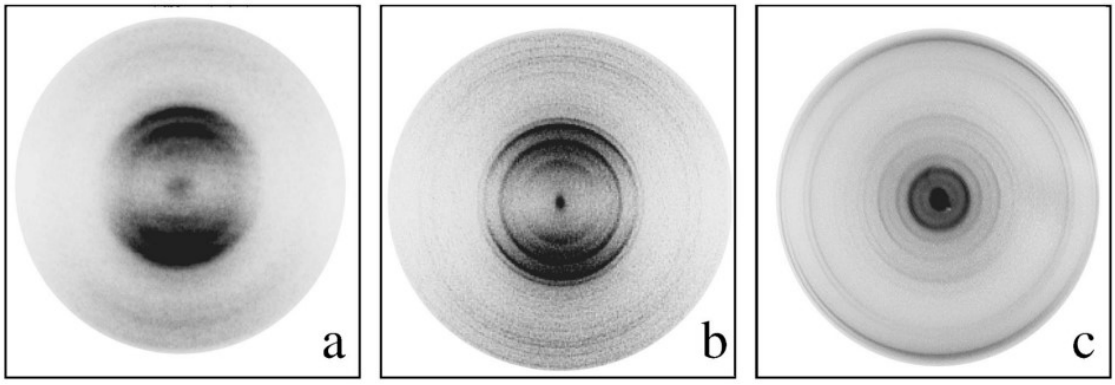


Figure 1.21: O^+ ion and electron images resulting from O_2 excitation to the $3d\pi(3\Sigma_1 g^+)$ Rydberg state around 225 nm. (a) O^+ ion image measured using a fine mesh grid; (b) image obtained with an imaging lens (open extractor electrode); (c) electron image acquired under similar conditions. Adapted from Ref.[133].

Initially, the Velocity-Map Imaging (VMI) technique was employed in the study of molecular photodissociation and crossed molecular beam scattering experiments. Conventional ion detection in VMI typically utilises multichannel plates (MCPs) coupled with a phosphor screen and a CCD camera. However, several limitations inherent to this

detection method have led to VMI being most commonly implemented in a 'crushed' or 'projected' imaging mode, in which the component of the ion velocity along the time-of-flight (ToF) axis remains unresolved. The principle of two-dimensional (2D) ion imaging is illustrated in Figure 1.22(a), while an example of an unsliced Cl^+ ion image resulting from the photofragmentation of Cl_2 at 355 nm is shown in Figure 1.22(d)[134].

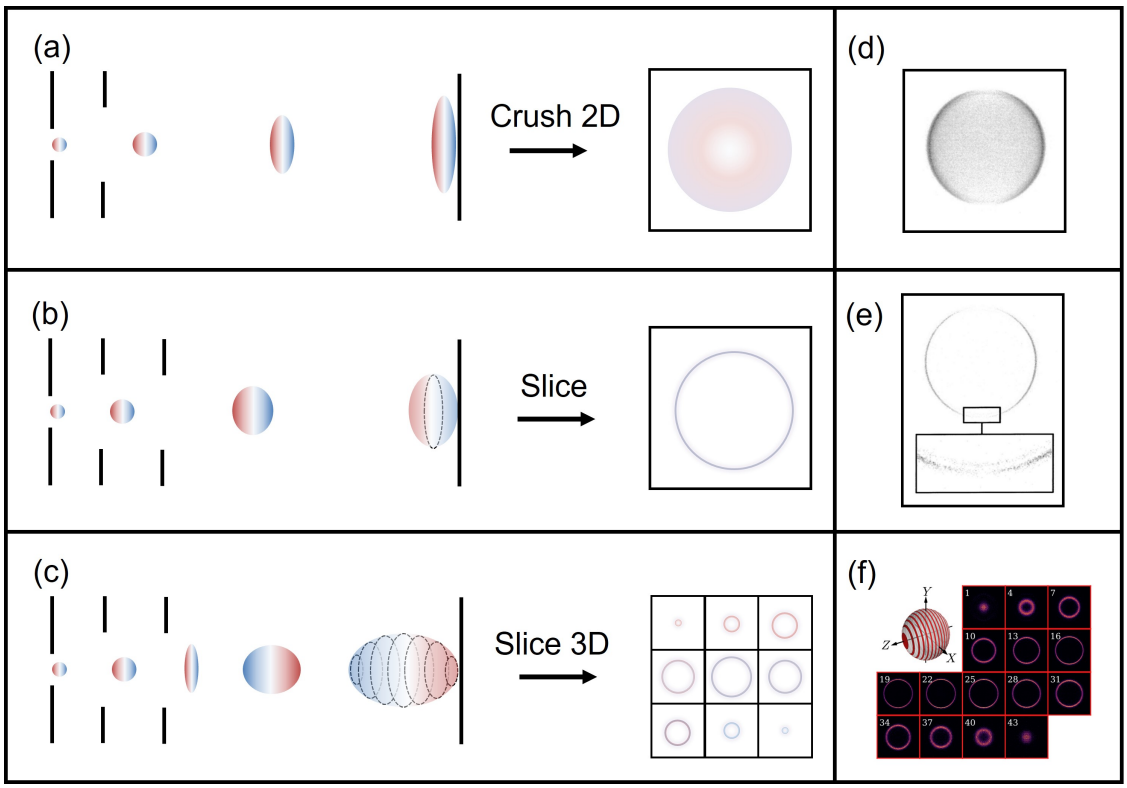


Figure 1.22: Schematic representation of ion imaging techniques. (a) Conventional two-dimensional (2D) projected VMI compresses the entire ion signal into a single image, losing time-of-flight (ToF) resolution. (b) Slice ion imaging isolates a central section of the ion cloud to enhance velocity resolution. (c) Three-dimensional (3D) ion imaging reconstructs the full Newton sphere through time-resolved acquisition using fast detectors. (d) Example of an unsliced Cl^+ ion image from the photodissociation of Cl_2, adapted from ref. [134]. (e) Corresponding sliced Cl^+ ion image recorded with a 40 ns detector gate. (f) Time-sliced images of CO ($J = 50$) fragments following the photodissociation of OCS, each slice corresponding to a 25 ns time bin, adapted from ref. [135].

To achieve more precise measurements with improved velocity resolution, sliced ion imaging techniques have been developed. In particular, direct current (DC) slice imaging has been widely adopted over the past two decades[134]. The concept of slice imaging is depicted in Figure 1.22(c). In the first demonstration of DC slice imaging, additional ion-optical lenses were introduced to expand the Cl^+ ion Newton sphere. This

expansion increased the ion time-of-flight from 40 ns to 190 ns using a single lens, and further to 400 ns with a dual-lens configuration. A narrow detector gate of 40 ns was then used to capture the central slice of the ion cloud, achieving a velocity resolution of $\Delta v/v = 2.8\%$, as illustrated in Figure 1.22(e).

In principle, slice imaging ion optics enable the reconstruction of the full three-dimensional (3D) Newton sphere of ions, provided that the detector possesses sufficiently high data acquisition rates and precise timing resolution. For this reason, 3D VMI typically employs MCPs coupled with phosphor screens and high-speed CMOS-based detectors, such as PImMS or TimePix3 cameras, or alternatively, delay-line detectors. Pulsed extraction techniques—such as post-extraction inversion slice imaging (PEISI)[135]—can also be employed to further stretch the ion clouds, thereby increasing the number of slices achievable while maintaining moderate timing requirements.

1.8.1 Applications of VMI

Owing to its ability to directly measure ion velocities, VMI has become a powerful technique for studying the momentum distributions of charged particles, such as electrons and ions, thereby providing detailed insights into molecular dynamics and reaction outcomes.

VMI's primary applications include the investigation of chemical reaction dynamics, such as photodissociation and bimolecular collisions, enabling the characterisation of product internal energies, translational energy distributions, and scattering angles. For example, a hexapole state-selected scattering system developed at Oxford has been used to investigate the three-vector correlation dynamics of end-on and side-on oriented NO molecules colliding with argon atoms. In these experiments, rotationally excited NO molecules are detected following collisions, with three well-defined vectors: the initial NO bond-axis vector $\mathbf{r}$, and the initial and final relative velocity vectors, $\mathbf{k}$ and $\mathbf{k}'$, as shown in Figure 1.23.

In the area of photoinduced dynamics, particularly in Coulomb explosion imaging and femtosecond reaction dynamics, VMI has numerous applications. For example, by coupling VMI with a PImMS 2 camera, the femtochemistry of nitrobenzene following excitation at 240 nm has recently been investigated [137]. Photochemical channels

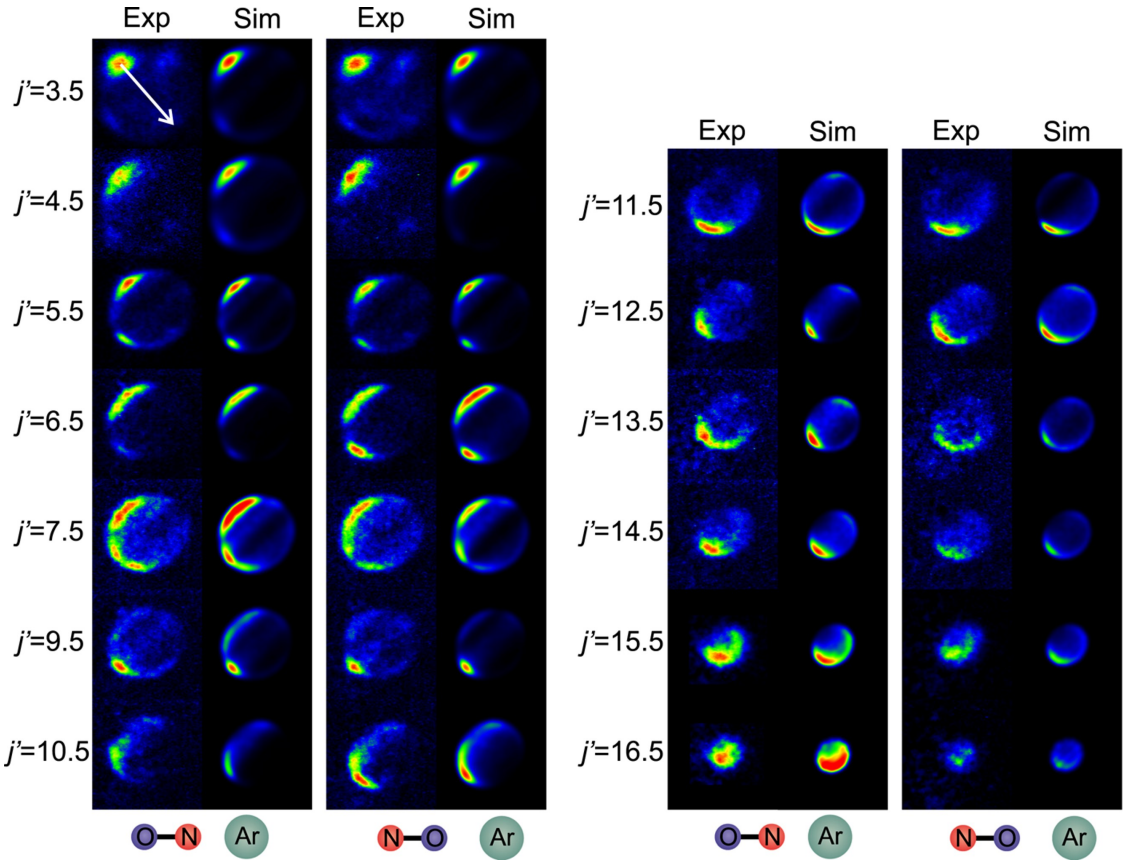


Figure 1.23: Experimental and quantum-mechanical (QM) simulated ion images for spin–orbit conserving transitions into the *e* Λ-doublet level. The first and third columns show images for collisions with the nitrogen ("N") end, while the second and fourth columns display images for collisions with the oxygen ("O") end. The white arrow in the top-left panel indicates the direction of the relative velocity. Adapted from Ref. [136].

were assigned by observing correlations between the molecular fragment ions of the corresponding product pairs, enabling the time-resolved dynamics of channels leading to NO, NO_2, and C_6H_5NO to be fully characterised.

Beyond the gas phase, VMI has also been widely applied in solid surface scattering [138–142], gas-liquid interface studies [143, 144]. Depending on the nature of the surface, as well as the type, energy, and orientation of the incident atom or molecule, a wide range of processes can occur at the gas–surface interface. These include direct scattering (H/Au (111) [145], NO/Ag (111) [146], N_2/Au (111) [147]), trapping–desorption (CO/Pt (111) [148]), dissociative adsorption (CH_4/Pt (111) [149], H_2O/Ni (111), and HCl/Au (111) [150]), and associative desorption (H_2/Cu (111) [151]). To investigate such processes, Harding *et al.* developed a new instrument (Figure 1.24(a))

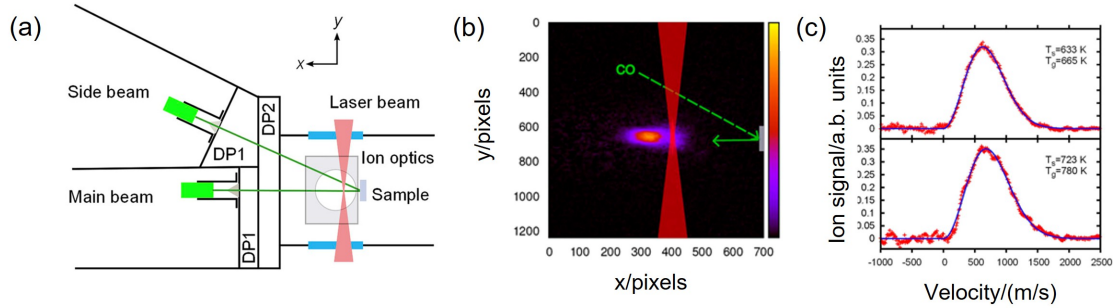


Figure 1.24: (a) Schematic of the source and main chambers of the instrument. The speeds of desorbing CO molecules are obtained by spatial ion imaging with non-resonant multiphoton ionisation. (a) Composite ion image of CO desorbing from a Pd(111) surface, showing the positions of the molecular beam, laser beam, and surface. (b) Speed distributions at two surface temperatures (T_s), obtained by taking a narrow 20-pixel-wide slice in the x-direction through the centre of the feature (at y = 680 pixels). Figures adapted from Ref. [138].

that employs ion imaging to study molecular beam–surface scattering and surface desorption kinetics, enabling the independent determination of both surface residence times and scattering velocities of desorbing molecules.

VMI has also been extensively applied to studies of gas–liquid interfaces. Roman *et al.* developed a configuration to investigate the inelastic scattering of OH radicals from a liquid perfluoropolyether (PFPE) surface, as shown in Figure 1.25(a) and (b). This arrangement is conceptually similar to the instrument described by Harding *et al.* [138], in which the VMI ion optics are positioned perpendicular to the scattering surface. In this configuration, when scattered particles leave the liquid surface, they are ionised by a laser pulse, after which the VMI electric field accelerates the resulting ions towards the detector. The time-of-flight (ToF) measurement provides access to the component of the ions' velocity along the flight axis, while their angular distributions can be reconstructed by determining their relative positions with respect to the surface plane and the surface normal.

With this configuration, a pulsed molecular beam of OH radicals, with a kinetic energy distribution peaking at 35 kJ mol^{-1}, was directed at a continually refreshed PFPE surface. The OH molecules were detected in a state-selective manner with both spatial and temporal resolution, using pulsed planar laser-induced fluorescence. Analysis of the scattered speed distributions revealed that they were strongly superthermal, independent of the incidence angle, whether normal (0° (Figure 1.25(c)) or oblique (45°(Figure 1.25(d)).

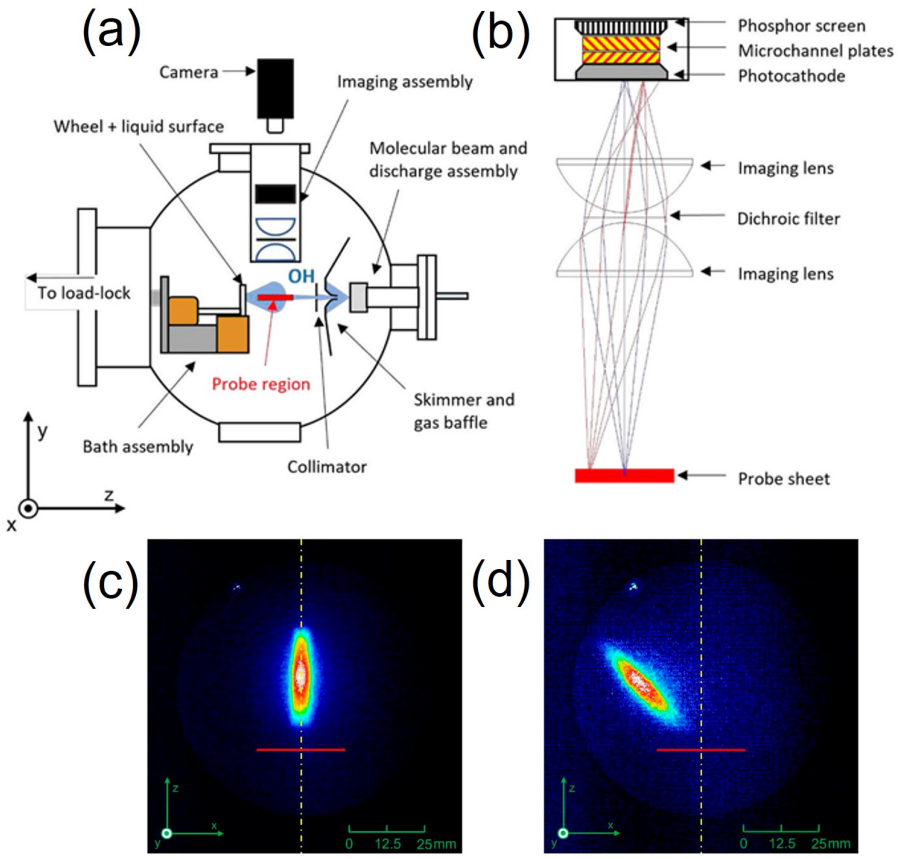


Figure 1.25: (a) Schematic of the main chamber (not to scale). (b) Close-up of the imaging assembly, showing indicative paths of fluorescence photons collected by the imaging lenses. The laser sheet lay in the *xz* plane and propagated into the plane of the page (*x* direction). The liquid-coated wheel was positioned in the *xy* plane and rotated about an axle aligned with the z-direction. The molecular beam (MB) propagated either along the surface normal (z) or at 45° to the surface normal in the *xz* plane. (c) Selected frame (discharge–probe delay of 94 µs) from a raw image sequence of OH (N = 3, $\theta_i = 0°$) scattering from the PFPE surface. (d) Selected frame (discharge–probe delay of 94 µs) from a raw image sequence of OH (N = 3, $\theta_i = 45°$, in the xz plane) scattering from the PFPE surface. Figures adapted from Ref. [143].

In surface-scattering studies, obtaining the full three-dimensional velocity distribution is essential for analysing the angular distributions of secondary ions. As discussed in previous work [138, 143], while the velocity component along the ToF axis can be measured, it is recorded separately from the velocity components in the detector plane. Consequently, conventional approaches to three-dimensional VMI at surfaces are largely 'statistical' in nature, relying on the reconstruction of the 3D velocity distribution from many ion events, rather than directly measuring the true three-dimensional velocity of each individual ion. In contrast, a novel approach employing a TimePix3-based camera

enables the precise measurement of 3D VMI for multiple masses simultaneously. This method will be introduced and discussed in detail in Chapter 4.

1.9 Summary

Mass spectrometry is a powerful analytical technique for characterising the chemical composition of complex samples. When integrated with spatially resolved detection systems, mass spectrometry imaging (MSI) emerges as a label-free method capable of simultaneously identifying molecular species and mapping their spatial distributions within a sample. In contrast to microprobe mode MSI, which relies on a tightly focused primary ion beam rastered across the sample, microscope mode MSI employs a defocused, wide-area primary beam combined with position-sensitive detectors to image larger surface areas (on the order of millimetres) in a single acquisition. This approach significantly enhances experimental throughput and reduces analysis time.

However, due to the necessity of preserving the spatial origin of the ions emitted from the sample surface, several performance-enhancing techniques commonly employed in conventional time-of-flight (ToF) mass spectrometers cannot be directly adapted to the microscope mode MSI configuration. Consequently, microscope mode MSI faces three principal challenges: (1) limited effective mass range, (2) reduced mass resolution, and (3) decreased mass accuracy.

Microscope mode matrix-assisted laser desorption/ionisation (MALDI) MSI has been under active development in the Brouard group. Through the implementation of PEDA, mass resolution has been improved to over 3,000 $m/\Delta m$ across a mass range exceeding 165 m/z. When further combined with a reflectron, the Oxford MALDI MSI instrument is capable of achieving simultaneous mass and spatial resolutions of 8100 $\pm$ 700 $m/\Delta m$ and 18 $\pm$ 6 µm, respectively.

Given the intrinsic three-dimensional (3D) imaging capability of Secondary Ion Mass Spectrometry (SIMS), the integration of SIMS with microscope mode MSI presents a promising avenue for high-throughput, label-free chemical imaging with spatial and depth resolution. In this work, we report the development of a next-generation microscope mode

SIMS imaging system. By incorporating an electrodynamic PEDA, we achieve enhanced mass resolution across a broad mass range—details of which are presented in Chapter 5.

Despite these advances, the velocity distributions of secondary ions emitted during the SIMS process remain insufficiently characterised. To address this, we introduce a novel approach employing a Timepix3 camera in conjunction with velocity-map imaging (VMI) optics to directly measure the three-dimensional velocity distributions of secondary ions. This methodology, which provides deeper insight into the kinetic characteristics of sputtered species, is discussed in detail in Chapter 4. This technique also shows potential benefits for other fields, such as gas–surface scattering, where it can provide a time precision of 1.56 ns.

2 Modeling and Simulation

2.1 SIMION

SIMION is a commercially available software package widely employed for the calculation of electric fields and the simulation of charged particle trajectories within those fields. It operates based on a defined configuration of electrodes and associated voltages, along with user-specified initial conditions for the particles. The software also supports optional features such as quasi-static radio-frequency (RF) fields, external magnetic fields, and collisional dynamics [152, 153].

In this work, SIMION 2020 is used for the design and optimisation of ion optical elements, the assignment of potential distributions, and the computation of ion trajectories through the instrument.

2.1.1 Potential Arrays

In SIMION, electrostatic and magnetic fields are represented as *potential arrays* (PAs). A PA is a two- or three-dimensional grid composed of equally spaced points, where each point defines both the potential (e.g., voltage) and the type of the spatial location (e.g., electrode, magnetic pole, or a non-electrode/non-pole region). For points designated as electrodes or poles, the assigned potential values serve as boundary conditions for the numerical solution of the field distribution across the array.

Electrode geometries in SIMION can be created either by importing CAD drawings or by defining them programmatically using a geometry (GEM) file. In a GEM file, electrodes are described by their origin (*X, Y, Z*), shape, dimensions (length, width or radius), symmetry, and orientation (elevation and azimuth angles).

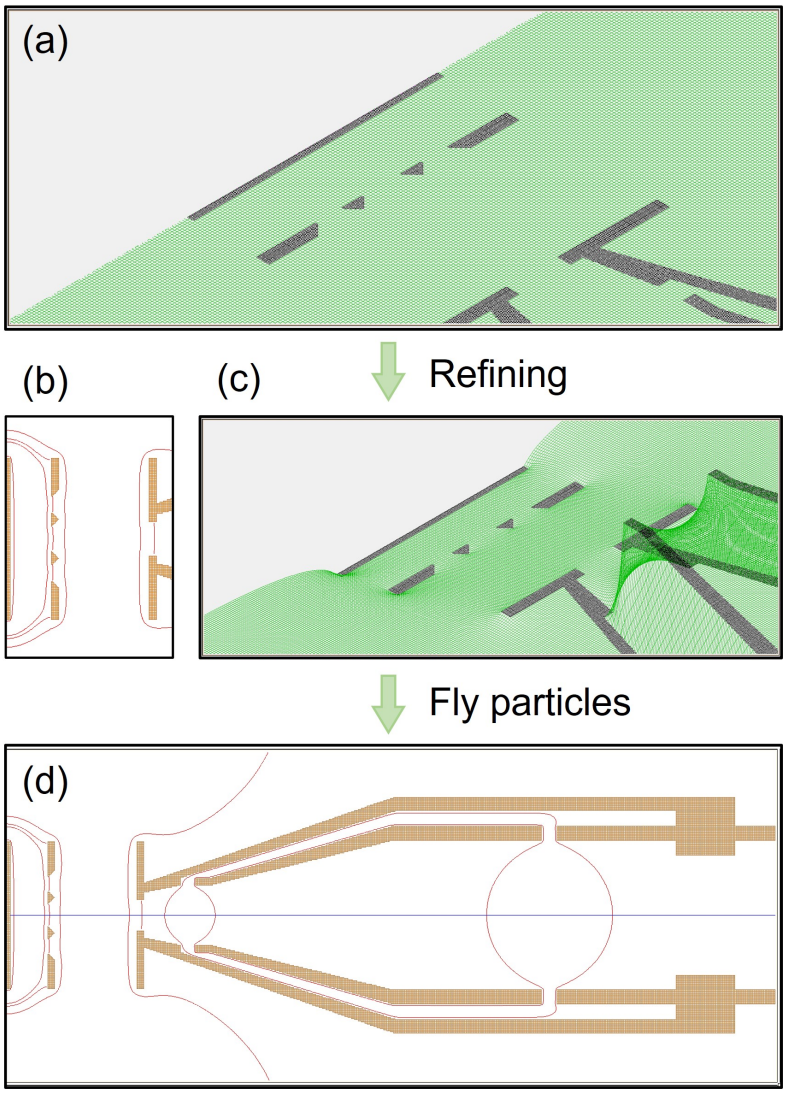


Figure 2.1: Construction of an ion optics workbench in SIMION: (a) definition of electrodes using a GEM file, (b) refinement of the potential array, (c) visualisation of the resulting 3D potential array, and (d) particle trajectory simulation and recording of ion parameters.

Increasing the resolution of the potential array (PA) grid—i.e., decreasing the spacing between grid points—results in smoother and more accurate representations of electrode boundaries. However, this increased precision comes at a computational cost: each grid point occupies approximately 10 bytes of RAM. Consequently, a three-dimensional

PA of size $100 \times 100 \times 100$ requires roughly 10 megabytes of memory. To mitigate the computational burden while maintaining spatial fidelity, SIMION offers support for symmetry-based optimisation, including planar, cylindrical, and mirror symmetries. These options enable simulation over a reduced spatial domain, from which the full geometry can be reconstructed computationally.

The simulation workflow in SIMION is illustrated in Figure 2.1. Electrode geometries are first defined in a plain text geometry file with a '.GEM' extension, as shown in Figure 2.1(a). Once the geometry is established, the electrostatic potentials at each point in the array are calculated or refined. The movement of charged particles through the resulting field is governed by Newton's second law, allowing SIMION to compute the trajectory of each ion under the influence of the calculated electric potential.

After refinement, the resulting electric field and potential distributions can be visualised using the potential energy (PE) view, as illustrated in Figures 2.1(b) and (c), respectively. Particle trajectories are then simulated and tracked within this defined field. The flight path of each ion, such as the example shown by the blue trajectory in Figure 2.1(d), provides insight into the dynamics of ion transport through the system.

2.1.2 Electrostatic Field and Ion Trajectory Calculation

To determine the electrostatic field in the vacuum regions between electrode points, Laplace's equation is employed. This partial differential equation governs the behaviour of the electric potential in regions devoid of free charge. The solution of Laplace's equation is subject to boundary conditions that define the domain of the function. Two types of boundary conditions are commonly used:

- **Dirichlet boundary conditions**, which specify the electric potential on the surfaces of the electrodes. These values serve as fixed boundary inputs during the refinement process.

- **Neumann boundary conditions**, which define the normal derivative of the potential at a boundary, corresponding physically to the electric flux through that surface.

In SIMION, Dirichlet conditions are typically applied to the electrode surfaces by assigning them specific voltages, while Neumann conditions are often set to zero on external simulation boundaries to represent a zero-flux constraint. The ion trajectories within the simulation are determined from Laplace's equation. Laplace's equation is solved during the refinement process, which determines the electrostatic potential at each point in space based on the potentials of all surrounding points. This is calculated prior to the introduction of charged particles into the ion optics, under the assumption of zero charge density.

The electrostatic field, $\mathbf{E}$, can be derived from the potential field, V, through the relation $\mathbf{E} = -\nabla V$. Laplace's equation states that the divergence of the gradient of the electric potential is zero:

$$\nabla \cdot \mathbf{E} = \nabla^2 V = 0, \tag{2.1}$$

which, in Cartesian coordinates, is expressed as:

$$\frac{\partial^2 V}{\partial x^2} + \frac{\partial^2 V}{\partial y^2} + \frac{\partial^2 V}{\partial z^2} = 0. \tag{2.2}$$

This equation implies that the potential field cannot exhibit local maxima or minima in free space; the potential is fully determined by the boundary conditions.

There are two principal types of boundary conditions associated with Laplace's equation: Dirichlet and Neumann. In SIMION, Dirichlet boundary conditions are used to define the voltages on electrode surfaces. Neumann boundary conditions, on the other hand, are derived from the first derivative of the potential and describe the electric flux across boundaries. For the simulations presented in this thesis, Neumann boundary conditions are set to zero, indicating that there is no normal component of electric flux across the outer boundaries of the simulation domain.

2.1.3 Define Ions

Within SIMION, the initial conditions of particles can be defined in a FLY2 file. Serial parameters can be defined in this file, including ion number, ion charge polarity, ion birth position, initial velocity (speed and angular distribution), time of birth (TOB). The

initial velocity of a particle is defined by specifying its source position and the desired directional distribution. This distribution can take various forms, such as a conical emission pattern or a set of predefined azimuthal and elevation angles that determine the trajectory of the particle upon emission (Figure 2.2).

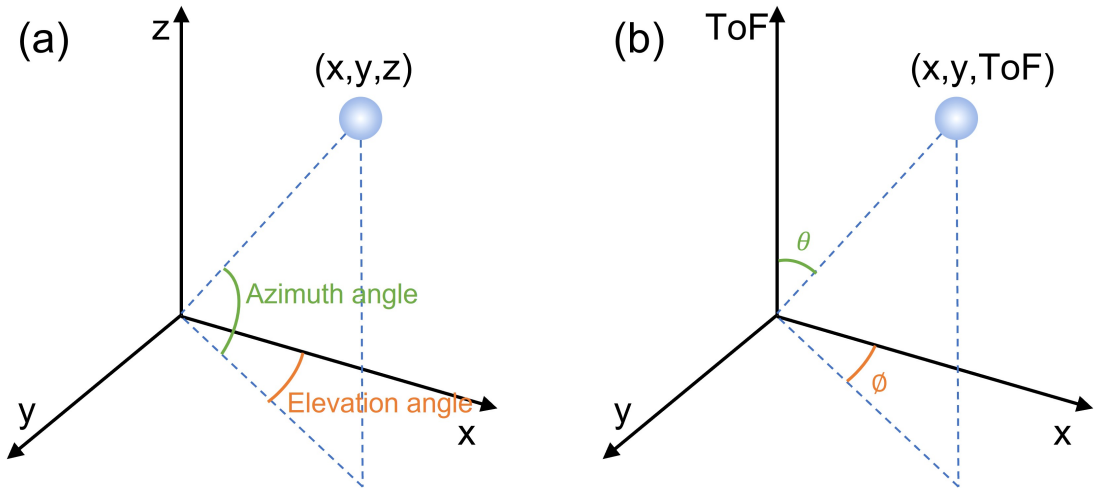


Figure 2.2: (a) SIMION coordinate axes used to define the ion position. (b) Corresponding position axes in the real experimental system.

In the SIMS system, the ionisation mechanism differs significantly from that in MALDI. Most secondary ions are generated through a sputtering process, where kinetic energy (KE) transfer plays the dominant role in ionisation. Consequently, different organic ions often exhibit similar kinetic energies. Previous research has investigated the bombardment of Benzo[a]pyrene (b[a]p) and Ni{001} using a 20 keV C_{60}^{+} beam at normal incidence (0°) [154]. In this study, the KE distribution of b[a]p featured a peak around 0.63 eV, with an optimal energy separation threshold at approximately 3.8 eV.

Regarding the angular distribution, the energy-integrated polar angle profile of b[a]p, shown in Figure 2.3(c), reveals a peak emission angle near 30°, superimposed on an approximately cosine-like background. This approximate velocity distribution is used as an initial condition in the simulation for calibration purposes. A more detailed analysis and calibration of 3D velocity distributions of secondary ions are presented in the chapter on three-dimensional velocity map imaging (VMI) from surfaces.

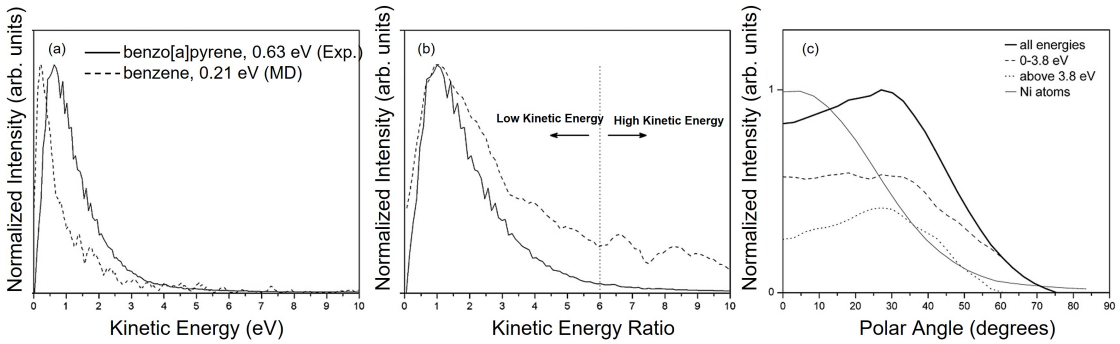


Figure 2.3: (a) and (b) show the experimental and simulated kinetic energy distributions of b[a]p, while (c) illustrates its angular distribution[154].

2.1.4 Workbench

To simulate a complex system, multiple Potential Arrays (PAs) are required to adjust the parameters of instrument components. Each component can be defined and simulated independently, which facilitates the design of various symmetries and configurations for different components.

Once all PAs have been refined, they are loaded into an ion optics workbench. SIMION's ion optics workbench (commonly referred to as the workbench) is a conceptual three-dimensional rectangular volume of space—up to 8 cubic kilometres in size—within the simulated environment. Up to 200 PA instances can be assembled within this workbench.

The workbench configuration is saved as an `.IOB` file, which functions as a central hub linking PAs, ion trajectory files, and LUA scripting files. All associated files can be mobilised and simulated simply by executing the `.IOB` file.

Within the `.IOB` file, each PA can be manipulated—moved, rotated, or scaled, allowing for convenient tuning of the relative positions and dimensions of different components. Furthermore, the voltage on each electrode can be quickly adjusted directly within the `.IOB` file, although this is suitable primarily for simple voltage settings. For more complex voltage profiles, such as time-dependent potentials, a LUA script is required to achieve accurate voltage control.

2.1.5 LUA file

A LUA script is employed to enable accurate and complex voltage control. While various programming languages such as Python and C++ can be used for similar purposes, LUA was chosen for its computational efficiency and simplicity in integration with SIMION.

In our LUA implementation, several tasks are carried out to support the simulation process. LUA facilitates the initialisation of variables and the definition of control functions, and it also serves to initialise the overall system state. As outlined in the previous discussion on the workbench, electrode voltages can be adjusted manually for simple configurations. However, for more complex, time-dependent potential settings, LUA scripting provides the necessary control.

For example, in Chapter 5, the PEDA is applied to time-focus an ion cluster. This requires the application of a time-dependent voltage to the extractor electrode. Using LUA, such a voltage can be programmed to trigger after a specific delay time, synchronised with the ion flight path.

Another critical capability of the LUA script is its ability to record and compute simulation output data. Parameters such as ion position, ToF, velocity, kinetic energy, and others can be logged during the simulation. Based on these outputs, further calculations can be performed, including magnification, mass resolution, and spatial resolution, enabling comprehensive post-processing and analysis.

2.2 Output Results and Calculation

As ions travel through the electric fields, their physical parameters can be calculated and recorded under the influence of the Potential Arrays (PAs). In theory, quantities such as kinetic energy, velocity, position, time-of-flight (ToF), and other variables can be recorded at any point along their trajectories. However, capturing such comprehensive data across all spatial positions would require substantial computational memory.

In the simulations conducted for this thesis, most information is recorded when the ions reach the detector plane, represented as a *'splat'* in SIMION. Key parameters, including positions (X, Y, Z) and ToF, are extracted at this point. These outputs are

used to calculate important performance metrics such as magnification, mass resolution, and spatial resolution.

The initial ion distribution in the simulation is defined as three discrete point sources, equally spaced along the y-axis. The central group of ions is positioned at the centre of the repeller electrode, while the other two are symmetrically distributed along the y-axis. Given that the ion optics system is designed with cylindrical symmetry, the ion distribution along the y-axis is representative of the complete two-dimensional radial distribution.

2.2.1 Mass resolution calculation

One of the key performance parameters in mass spectrometry imaging (MSI) is the mass resolution. To evaluate it, the time-of-flight (ToF) of each ion is statistically analysed to compute the mean arrival time ($\bar{t}$) and the standard deviation of the arrival time distribution (σ_{ToF}).

In time-of-flight mass spectrometry (ToF-MS), there exists a well-established relationship between mass resolution and temporal resolution, as expressed by the following equation:

$$\frac{m}{\Delta m} \approx \frac{\bar{t}}{2\Delta t} = \frac{\bar{t}}{2 \cdot 2\sqrt{2\ln 2} \cdot \sigma_{\mathrm{ToF}}} \approx \frac{\bar{t}}{4.71\sigma_{\mathrm{ToF}}}, \tag{2.1}$$

where Δt is the full width at half maximum (FWHM) of the arrival time distribution. Assuming a normal distribution, the relationship $\Delta t / \sigma_{\mathrm{ToF}} = 2\sqrt{2\ln 2}$ holds.

A further assumption underlying the validity of this expression is that the detector response time must not be a limiting factor; that is, it must be negligible in comparison with Δt.

Up to this point, the simulation has been conducted under idealised conditions. However, in practical applications, the temporal resolution of the mass spectrum is also constrained by the response characteristics of the scintillator screen—particularly its rise time—which will be discussed in detail in Chapter 3.

In the simulation, the scintillator's temporal behaviour is modelled as a Gaussian-like distribution and is convolved with the intrinsic time-of-flight (ToF) distribution. This

convolution accounts for the additional temporal broadening introduced by the detector's finite response time. The resulting overall time spread, σ_t, is given by:

$$\sigma_t = \sqrt{\sigma_{\mathrm{ToF}}^2 + \sigma_{\mathrm{det}}^2}, \tag{2.2}$$

where σ_{ToF} represents the intrinsic spread in ion flight times, and σ_{det} denotes the standard deviation of the scintillator's temporal response.

Accordingly, the mass resolution with convoluted broadening becomes:

$$\frac{m}{\Delta m} \approx \frac{\bar{t}}{4.71\,\sigma_t} = \frac{\bar{t}}{4.71\sqrt{\sigma_{\mathrm{ToF}}^2 + \sigma_{\mathrm{det}}^2}}, \tag{2.3}$$

where σ_{det} is the standard deviation of the detector's temporal response.

As a result of the detector's inherent temporal spread, a fundamental limit on the achievable mass resolution exists. When the intrinsic spread σ_{ToF} approaches zero, the limiting value of the full width at half maximum (FWHM) is determined solely by the detector:

$$\lim_{\sigma_{\mathrm{ToF}} \to 0} \Delta t = 2\sqrt{2\ln 2} \cdot \sigma_{\mathrm{det}} = 2.355\,\sigma_{\mathrm{det}}. \tag{2.4}$$

2.2.2 Spatial resolution calculation

Another key performance parameter in mass spectrometry imaging (MSI) is the spatial resolution, which is also determined through simulation. In the spatial resolution calculation, the magnification factor, M_i, serves as an intermediate variable.

Magnification is defined as the ratio between the separation of ion impact positions on the detector plane and the corresponding initial spacing between ion sources. Specifically, it is calculated as:

$$M_i = \frac{Y_i - Y_1}{(i-1)d} \quad (i = 2, 3), \tag{2.5}$$

where Y_i is the centre position of the i-th ion spot on the detector, Y_1 is the centre position of the reference (first) ion spot, and d is the physical distance between adjacent

point sources in the initial ion distribution. The magnified ion trajectories and spatial distributions are illustrated in Figure 2.4.

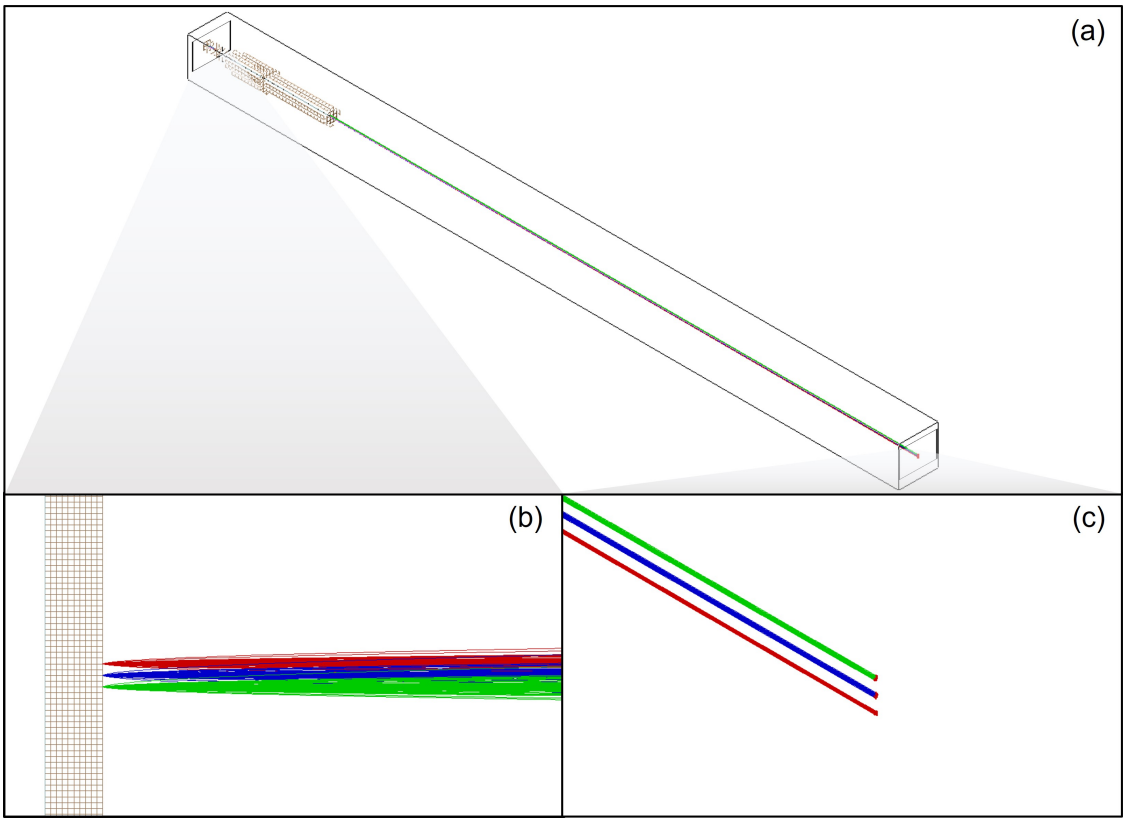


Figure 2.4: (a) The complete ion trajectories through the ion optical system. (b) The initial positions and spatial distribution of ions on the repeller. (c) The corresponding distribution of ions upon reaching the detector plane.

The spatial resolution can then be calculated using the information obtained from the simulation. It is defined as the full width at half maximum (FWHM) of the ion distribution—referred to as the `splat`—on the detector plane. For the i-th ion spot, the spatial resolution, denoted as $\Delta R_{i,50\%}$, is given by:

$$\Delta R_{i,50\%} = 2\sqrt{2\ln 2}\cdot\sigma_{i,y} \approx 2.355\,\sigma_{i,y} \quad (i = 1,2,3), \tag{2.6}$$

$$\Delta r_{i,50\%} = \Delta R_{i,50\%}/M_i \quad (i = 1,2,3,4,5), \tag{2.7}$$

where $\sigma_{i,y}$ is the standard deviation of the i-th ion spot's y-coordinate distribution on the detector. This approximation assumes a Gaussian distribution of the ion impact positions. The spatial resolution of the instrument is $\Delta r_{i,50\%}$.

In the experimental setup, preparing a sample with a sufficiently small spot size is technically challenging. As an alternative, a grid-patterned sample is used. In this context, the spatial resolution is defined as the distance over which the signal intensity rises from 20% to 80%, a method that will be discussed in detail in Chapter 3.

2.3 Genetic Algorithm

In computer science and operations research, a *genetic algorithm* (GA) is a metaheuristic inspired by the process of natural selection. It belongs to the broader class of *evolutionary algorithms* (EAs) [155]. Genetic algorithms are widely employed to generate high-quality solutions to complex optimisation and search problems, utilising biologically inspired operators such as selection, crossover, and mutation.

Typical applications of GAs include optimising decision trees to enhance performance, solving constraint-based puzzles such as Sudoku [156], hyperparameter tuning in machine learning models, and causal inference tasks in data analysis [157].

In this thesis, to achieve optimal mass resolution and spatial resolution across a wide mass range, the PEDA method is employed, as will be discussed in detail in Chapter 5. Implementing PEDA requires simultaneous optimisation of multiple parameters, including six electrode voltages and a trigger delay time.

To efficiently explore this high-dimensional parameter space, a genetic algorithm (GA) is used to reduce the search field and guide the optimisation process. The process of the GA is shown in the Figure2.5

The first step in the genetic algorithm is *initialisation*, where a set of minimum and maximum values is defined as the boundary for each variable. An initial population is then generated by randomly selecting values for each variable within these bounds—these sets of values represent the chromosomes.

The second step is *selection*. In this phase, each chromosome in the population is evaluated using a fitness function that quantifies the quality of the solution it represents. Chromosomes with higher fitness scores are more likely to be selected to reproduce and form the next generation.

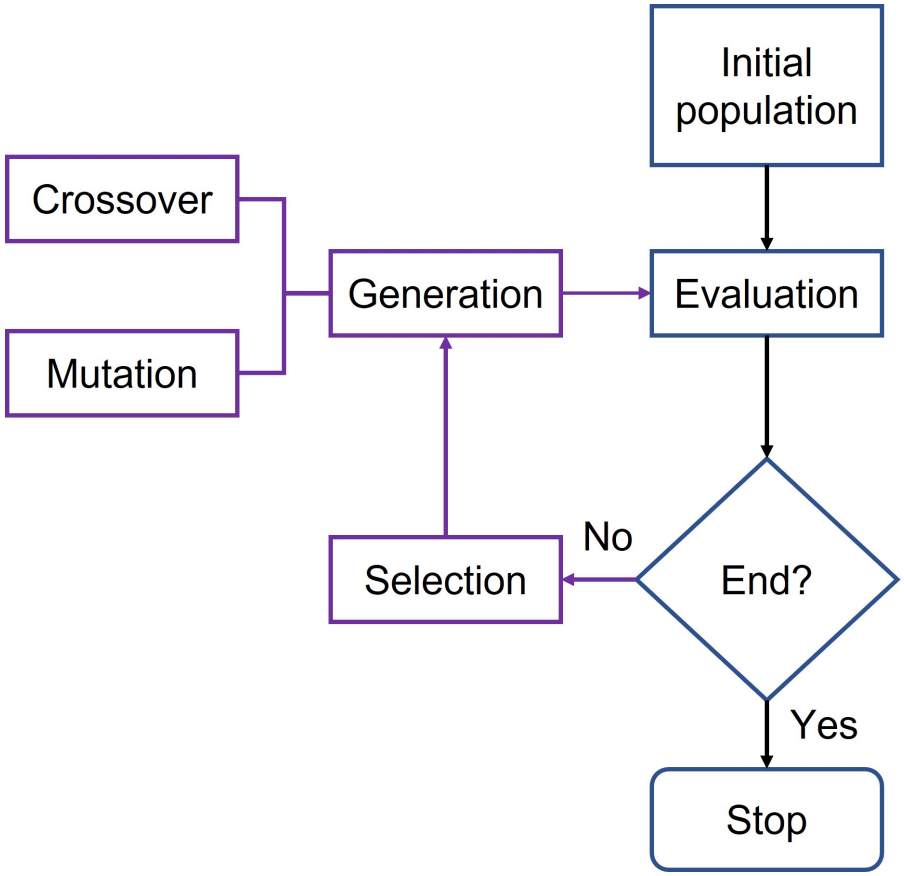


Figure 2.5: Genetic algorithm procedure.

Once the entire population has undergone the selection process, the next step is to generate a new population through *crossover* and *mutation*. Mimicking natural evolutionary mechanisms, pairs of "parent" chromosomes are selected based on their fitness to produce new "child" chromosomes.

Each variable within a chromosome is referred to as a *gene*, and offspring are generated using a uniform crossover method. In this approach, each gene has an equal probability of being inherited from either parent. Genes are selected independently during the crossover phase, resulting in child chromosomes composed of a randomised combination of genes from both parents.

To prevent convergence towards local minima and to maintain genetic diversity within the population, a *mutation* operator is applied to the child chromosomes. The mutation operator defines the probability that each gene will undergo mutation. For each gene, a random number is generated; if this number falls within the defined mutation probability,

the gene is altered to a new random value within the permissible parameter range. If the random number lies outside the mutation threshold, the gene remains unchanged, inherited directly from the parent chromosome.

Parent chromosomes are selected in a semi-random manner, with a higher probability of selection given to those with superior fitness scores. This combination of probabilistic selection and random mutation helps prevent premature convergence of the population and increases the likelihood of escaping local optima, thereby improving the chances of finding the global optimum.

This iterative process continues until a predefined termination condition is met. Typically, this is defined as reaching a maximum number of generations, but alternative stopping criteria may include convergence of the best fitness values, achievement of a target solution, or stagnation in fitness improvements over successive generations.

2.3.1 Strength and Weakness

As a global optimisation method, the genetic algorithm (GA) is often compared with more conventional approaches such as the gradient descent algorithm. Gradient descent is an iterative optimisation algorithm for finding a local minimum of a function. To locate the minimum, steps are taken proportional to the negative of the gradient of the function at the current point. Conversely, if steps are taken in the direction of the positive gradient, the algorithm instead converges towards a local maximum; this procedure is known as gradient ascent, as illustrated in Figure 2.6(b).

A limitation of gradient-based methods is their reliance on derivative information, which makes them poorly suited for problems with multiple local optima. As illustrated in Figure 2.6(a), the process can be visualised as descending through a mountainous landscape, where the walker progresses through four positions: the initial peak (1), the first valley (2), the second peak (3), and finally the global minimum (4). Following a gradient descent strategy, the walker becomes trapped at the first valley (point 2), unable to reach the global minimum.

In contrast, GAs do not require derivative information and have a high probability of locating the global minimum without becoming trapped in local minima. They are

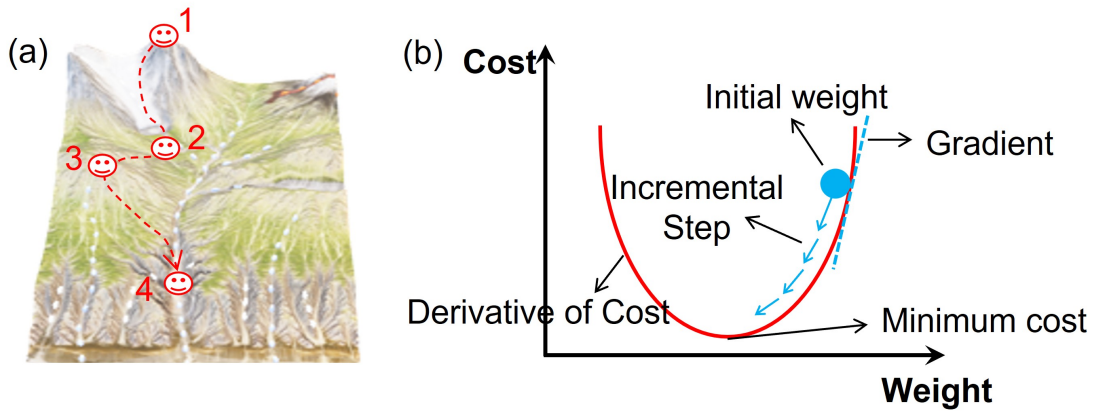


Figure 2.6: Schematic of the gradient descent algorithm. (a) An analogy illustrating gradient descent as the process of finding the lowest point in a hilly landscape. The walker passes through four points (1–4) while descending. (b) Illustration of the algorithmic steps: the gradient (slope), i.e. the first-order derivative of the function at a given point, is computed. A step is then taken in the direction opposite to the gradient, with the step size determined by α times the gradient at that point.

therefore particularly well suited for optimisation problems characterised by multiple local optima, non-smooth objective functions, large parameter spaces, or noisy and stochastic conditions.

However, genetic algorithms (GAs) also have limitations. They are computationally expensive, as the algorithm must explore a large search space and evaluate multiple permutations and combinations before converging towards a solution. While GAs are highly effective for tackling complex optimisation problems, they can be inefficient or even counterproductive when applied to relatively simple problems. Although the underlying concept of GAs is straightforward, their practical implementation can be challenging and is often regarded as more of an art than a rigid procedure. Without careful parameter tuning and appropriate design, the algorithm may converge prematurely to a non-optimal solution. In this thesis, it is crucial to identify the global minimum; therefore, a genetic algorithm (GA) is employed to optimise the PEDA settings.

2.3.2 Optimize mass and spatial resolution

In the simulation, five voltages and one trigger time are configured. Static voltages are applied to the repeller and ion lens, while a time-dependent voltage is used for the

extractor. This requires the specification of three voltage levels and one trigger time. Further details regarding the PEDA methodology are discussed in Chapter 5.

The voltage limitations of the physical power supplies are 10 kV for both the repeller and extractor, and 20 kV for the ion lens. Consequently, the maximum voltage values used in the simulation are constrained accordingly, with the genetic algorithm (GA) operating within a voltage range of approximately 5 kV.

The GA adopts a principle of minimisation in numerical optimisation. That is, among the candidate voltage configurations, the one yielding the minimum value of the defined optimisation equation is selected as the optimal setting. The optimisation criterion is given by:

$$\text{Optimise} = \frac{SR^2}{(MR/1000)^2}, \tag{2.8}$$

where SR represents the spatial resolution and MR denotes the mass resolution. In both simulation and experimental conditions, a typical mass resolution (MR) is approximately 10,000 m/Δm, whereas the spatial resolution (SR) is around 10 µm. Therefore, MR is normalised by a factor of 1000 to bring it to a comparable order of magnitude with SR and to improve numerical stability during optimisation.

As the objective is to achieve higher mass resolution and finer spatial resolution, the optimisation function is constructed such that lower values indicate improved performance. The GA therefore seeks to minimise the value of Equation (2.8), thereby favouring configurations that maximise MR and minimise SR.

Table 2.1: The optimised voltages for the different mass ranges within the GA.

Parameter	**400-800**m/z	**600-1200**m/z
Repeller	7500V	7500V
Extractor	3992V	4827V
Einzel lens	-15337V	-14822V
PEDA	4417V	5151V
PEDA ramp	5256V	7019V
PEDA delay time	391ns	570ns

In the simulations, a time-dependent PEDA is applied to extend high-resolution performance across a wide mass range. As an illustrative example, two mass ranges

(400–800 m/z and 600–1200 m/z) are optimised using a fixed repeller voltage of 7500 V with the GA. The optimised voltage settings are summarised in Table 2.1, while the corresponding resolutions are presented in Figure 2.7. Further details of both the simulation and experimental results are discussed in Chapter 5.

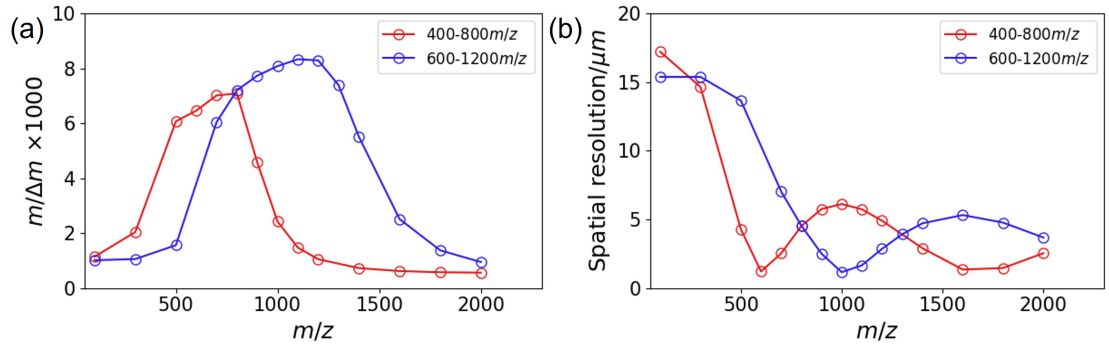


Figure 2.7: Within the GA result, simulated mass resolutions cross two mass ranges are shown in (a), while (b) represents the spatial resolution.

Across the optimised mass range, a mass resolution of approximately 7500 $m/\Delta m$ can be achieved with a convolution time of 1.5 ns, which represents the limitation imposed by the detector, while the spatial resolution reaches between 1 and 5 µm.

2.4 Summary

SIMION was employed to model various aspects of our experimental setup, including velocity calibration for surface velocity-map imaging (surface-VMI) and the enhancement of both spatial and mass resolution in spatial imaging mode. Given a defined configuration of electrodes with specified voltages and initial particle conditions, SIMION is capable of accurately simulating the resulting electric fields and the trajectories of charged particles within them.

The fundamental components of a SIMION simulation workbench are well established. Potential arrays define the electrode geometries and the electric potentials at discrete points in space. Ion definition files describe key properties of the ions, such as mass-to-charge ratio, initial position, and initial velocity. Additionally, user programming functionality allows automation of complex simulation tasks, such as dynamic voltage adjustments and result analysis, greatly enhancing simulation efficiency.

SIMION employs robust and efficient numerical methods to compute electric fields and simulate ion trajectories with high precision. As a result, it provides significantly greater accuracy and flexibility compared to traditional analytical techniques, such as the transfer matrix method. Owing to its reliability and versatility, the majority of the simulation and design work presented in this thesis was conducted using SIMION.

3
Experiment Methods

3.1 Introduction

The modeling and simulation methods in prior chapter assists in the development of the ideas to improve the performance of microscope mode SIMS Imaging and calibration of the 3D velocity map imaging. Each section of this chapter will cover a key aspect of the mass spectrometry used to achieve this, including the ion source, ion optics, detector, sample preparation, clock synchronization, data acquisition (DAQ) system, and time-of-fight (ToF) to m/z calibration.

The microscope-mode SIMS imaging instrument was designed in collaboration between Oxford University Chemistry Department, the Rosalind Franklin Institute (RFI), and Ionoptika Ltd, with more detailed information available in prior work [158]. The instrument features a C_{60}^+ ion beam, which can operate at either 20 or 40 keV as the primary ion energy. It includes a sample stage, extraction optics, a time-of-flight (ToF) tube, and a detector assembly, all housed within a high-vacuum system. A camera is mounted in the atmosphere above the phosphor screen.

Details of the instrument's ion source and extraction design are shown in Figure 3.1(a). The C_{60}^+ ion beam is oriented at an angle of 50 degrees to the sample surface to optimise ion yield [159, 160]. This configuration is preferred because, at glancing incidence, ejected ions are more likely to be reabsorbed or obstructed by surface features. In

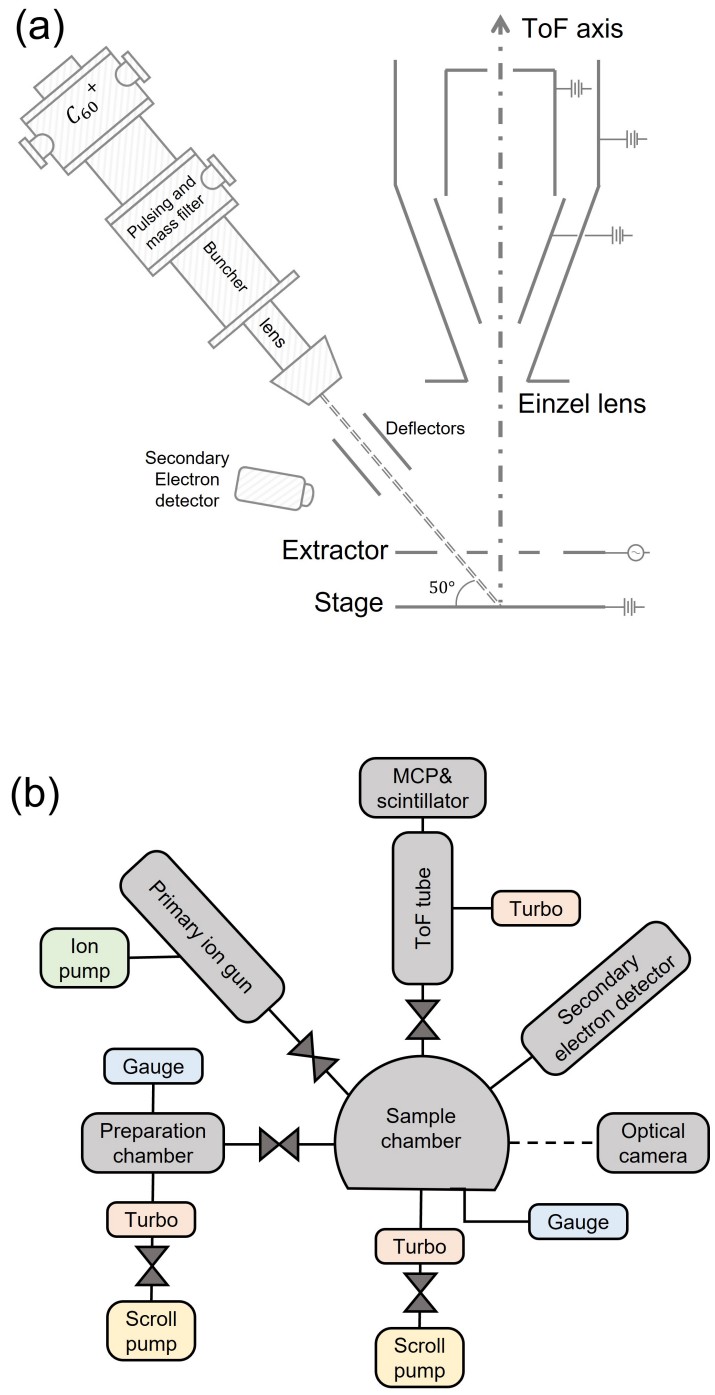


Figure 3.1: Simplified schematic showing the basic components making up the microprobe SIMS instrument. (a) is an overview of the primary ion beam column and ion extraction assembly. Adapted from ref. [158]. (b) shows the schematic of the complete SIMS instrument.

contrast, when the incidence angle is reduced to around 45 degrees, this blocking effect is diminished, resulting in a significant enhancement in ion yield [161].

The instrument is also equipped with a secondary electron detector (SED), which

is used to analyse surface topography and to verify the focusing performance of the C_{60}^+ ion beam. The SED collects secondary electrons emitted from the surface during ion bombardment, providing complementary imaging information. Secondary electron imaging (SEI) in this context is performed using microprobe mode, where the primary ion beam rasters across the surface on a pixel-by-pixel basis. In this mode, the spatial resolution of the resulting SEI is primarily limited by the spot size of the primary ion beam, thus the spatial resolution of SEI can represent the primary ion beam spot size.

The system comprises three vacuum chambers: a preparation chamber, a primary ion beam chamber, and a sample chamber. A schematic of the entire system layout is shown in Figure 3.1(b). The detector region and the preparation chamber are each isolated from the main sample chamber using gas-gate valves, while the primary ion beam chamber is separated from the sample chamber by a manually operated valve. These valves allow independent operation and maintenance of each section without compromising the vacuum integrity of the adjacent chambers.

The primary ion beam chamber is maintained at an ultra-high vacuum (UHV) pressure of approximately 1.2×10^{-8} mbar using a dedicated ion pump. The preparation and sample chambers are evacuated using a multi-stage pumping system. Initially, scroll pumps reduce the pressure in each section to around 10^{-5} mbar. Subsequently, Leybold Trivac D40V turbomolecular pumps further reduce the pressure to the experimental operating level of approximately 10^{-8} mbar. This ultra-vacuum environment is essential for minimising ion scattering, maintaining beam stability, and ensuring accurate and reproducible mass spectrometry measurements.

Further details of each component of the instrument are provided in the following sections.

3.2 Primary Ion Beam

The C_{60}^+ ion beam is generated using an electron impact ionization source (Ionoptika Ltd.), where sublimed fullerite (C_{60}^+) was heated to approximately 380–390 °C under vacuum to produce a vapor stream. The vapor was then ionized by 70 eV electrons, yielding predominantly C_{60}^+ ions. These ions were subsequently mass-selected using a

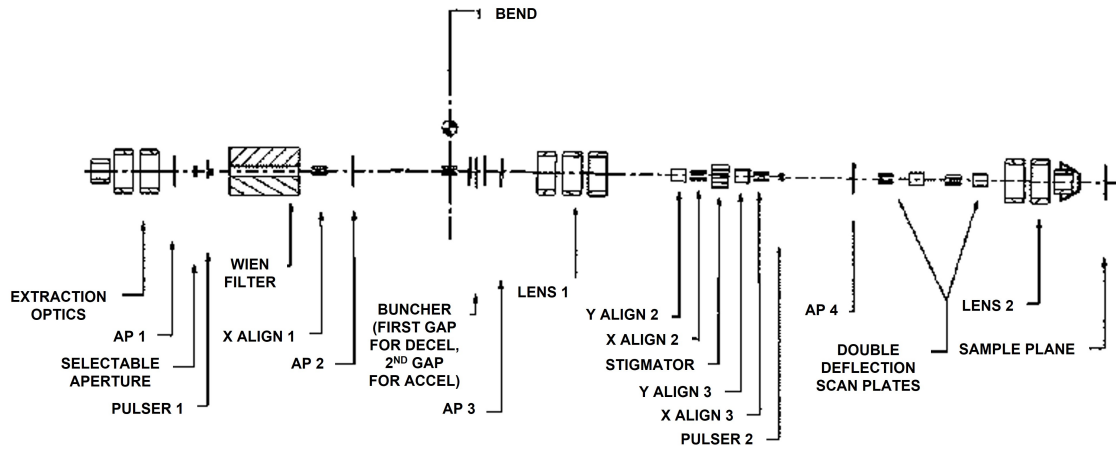


Figure 3.2: Schematic of 40 kV C_{60} system. Adapted from Ref. [162].

Wien filter[163] to ensure the purity of the cluster beam. The initial beam pulse duration is set between 70 and 200 ns; in this thesis, a duration of 100 ns is used. However, although increasing the pulse duration can enhance the C_{60}^{+} ion amount, it can also negatively impact the mass resolution.

To mitigate temporal dispersion of the primary ion beam, a voltage-pulsed buncher is implemented within the ion gun assembly. This buncher is located downstream of the Wien filter and upstream of the focusing lenses. Upon arrival of the filtered cluster beam, the buncher applies a time-focusing pulse that compresses the temporal width of the ion packet. This process reduces the initial pulse duration from approximately 100 ns to below 6 ns without compromising the beam current.

Temporal focusing of the primary beam is crucial for achieving high spectral resolution. However, direct measurement of the pulse duration after the buncher is challenging. To indirectly assess the temporal focusing, we examine the rise edge of the detected H^{+} peak, since hydrogen ions, owing to their low mass, exhibit minimal intrinsic time dispersion. As a result, their peak width provides a reliable proxy for the compressed pulse duration.

The performance of the buncher was evaluated by varying both the applied voltage and the trigger timing of the pulsed potential. Two buncher voltage settings were investigated: 3.5 kV and 1.4 kV. Figure 3.3 shows the resulting H^{+} peaks under these conditions. In both cases, scanning the buncher trigger timing allowed the H^{+} peak to be temporally

focused to a duration of approximately 6 ns, corresponding to the rise time of the peak. The optimally focused peaks are highlighted in purple in Figures 3.3(a) and (b). If the buncher pulse timing is not correctly adjusted, the C_{60}^+ beam will be misfocused, or even defocused in time. For example, as shown in Figure 3.3, when the trigger time is set 40 ns earlier than the optimum, only part of the C_{60}^+ beam is properly focused while the remainder is not, resulting in a double-peaked pulse.

However, the rise time is limited by the rise time of the P 47 phosphor screen, as introduced later in Chapter 5. To mitigate the impact of this limitation, a BC-408 scintillator, which has a rise time of approximately 1 ns, is also employed to measure the bunched C_{60}^+ pulse width. The H^+ peaks collected with both the P 47 (red line) and BC-408 (blue line) detectors are compared in Figure 3.4. When the C_{60}^+ beam is well time focused, the true beam time duration can be determined from the BC-408 detector measurements, yielding a rise time of about 2-3 ns.

An aperture is positioned downstream of the extraction optics to control the spatial focus or spot size of the primary ion beam. A range of aperture diameters is available (1.0, 0.3, 0.1, 0.07, and 0.03 mm), enabling fine control over the beam diameter, which can be adjusted from approximately 2 µm to 100 µm, depending on the selected aperture size. In microscope-mode mass spectrometry imaging (MSI), a defocused ion beam is preferred to illuminate a broader sample area, and a 1.0 mm aperture is typically employed. The primary ion beam is accelerated to either 20 or 40 keV and subsequently focused using two electrostatic lenses, designated as lens 1 and lens 2 within the system. By adjusting the lens voltages and aperture configuration, the beam spot diameter can be tuned across a range from approximately 1-10 µm (focused) to over 2 mm (defocused). To ensure precise beam positioning, four deflector electrodes are located between the two lenses. These electrodes steer the beam laterally, allowing accurate alignment and targeting of the sample surface.

Ion current measurements are conducted using a Faraday cup, with typical currents ranging from 100 pA to 1.5 nA. The primary ion beam is incident normal to the sample surface, which is located within an ultra-high vacuum (UHV) chamber maintained at a base pressure of approximately 1.2×10^{-8} mbar. For sample irradiation, raster scanning

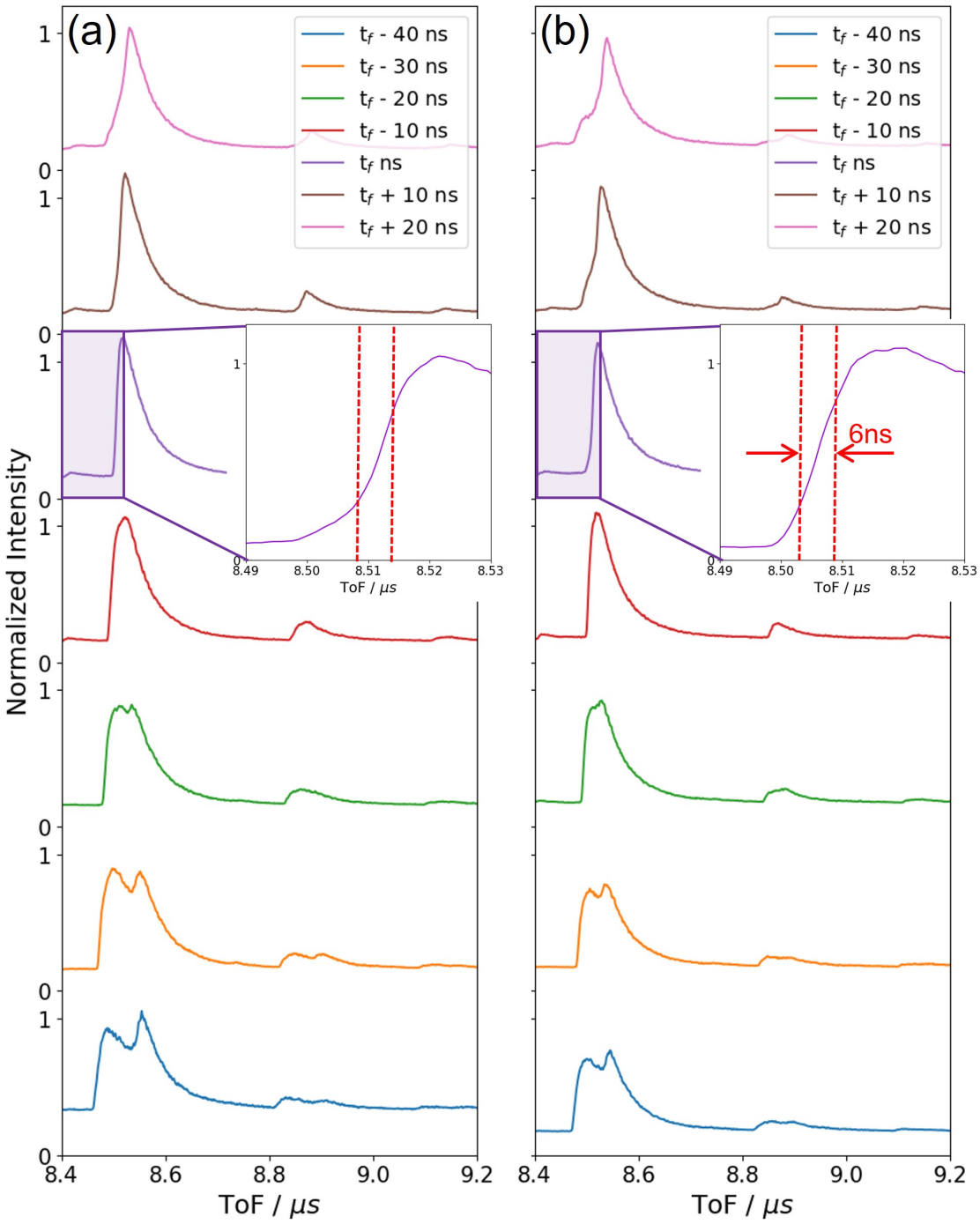


Figure 3.3: H^+ peak obtained by varying the buncher pulse trigger timing at (a) 3.5 kV and (b) 1.4 kV. The optimally focused peaks are indicated by the shaded purple regions.

is implemented via the beam deflection plates to ensure uniform exposure across the defined imaging area.

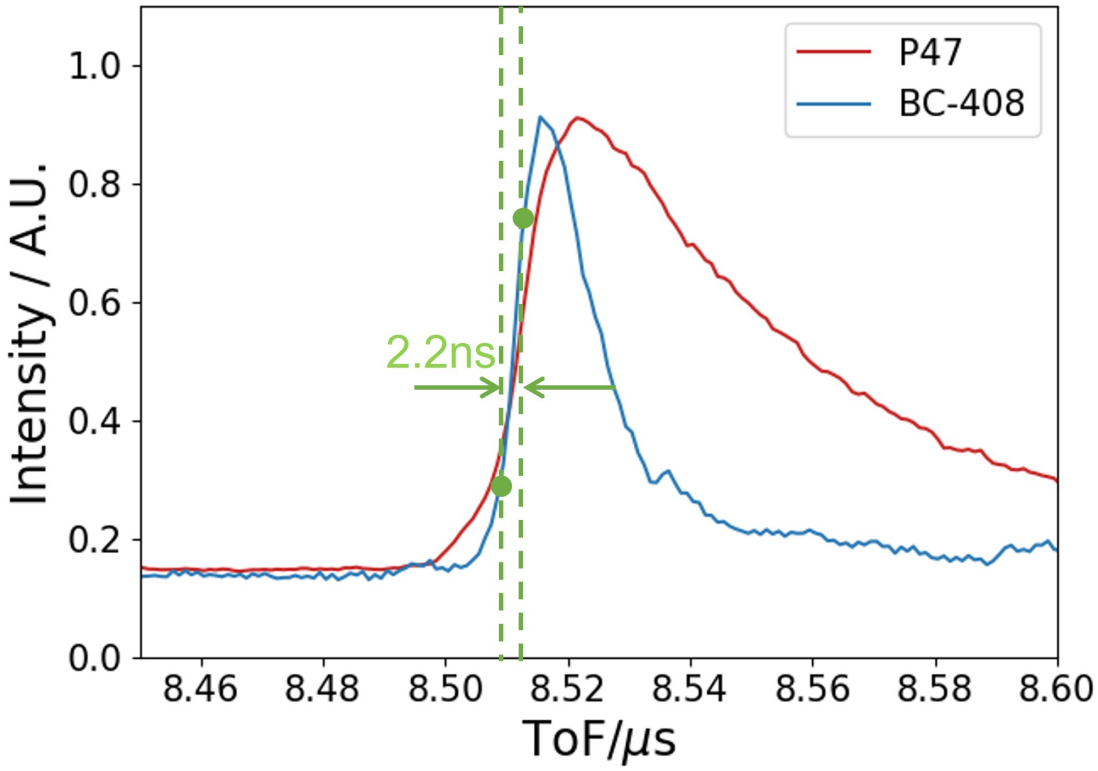


Figure 3.4: Comparison of H^+ ToF spectra collected using the P 47 detector (red) and the BC-408 detector (blue) under focused buncher settings.

3.3 Ion Optics

Figure 3.5(a) shows the 3D model of the ion optics assembly, which comprises three main components: a repeller electrode (E1), an extractor electrode (E2), and an einzel lens system (E4), all positioned between two grounded electrodes (E3 and E5). For clarity, the corresponding 2D cross-sectional view along the central axis, including detailed dimensions, is presented in Figure 3.5(b). To ensure uniform electric field distribution and optimal ion transmission, both the extractor and einzel lens are designed with cylindrical symmetry.

The sample is mounted on a conductive copper sample stage, which also functions as the repeller electrode (E1). This stage is controlled by a motorised translation stage capable of sub-micrometer precision, enabling fine alignment of the sample surface with respect to the ion optics. The repeller can be biased with either a high positive or negative potential, depending on whether cations or anions are to be accelerated

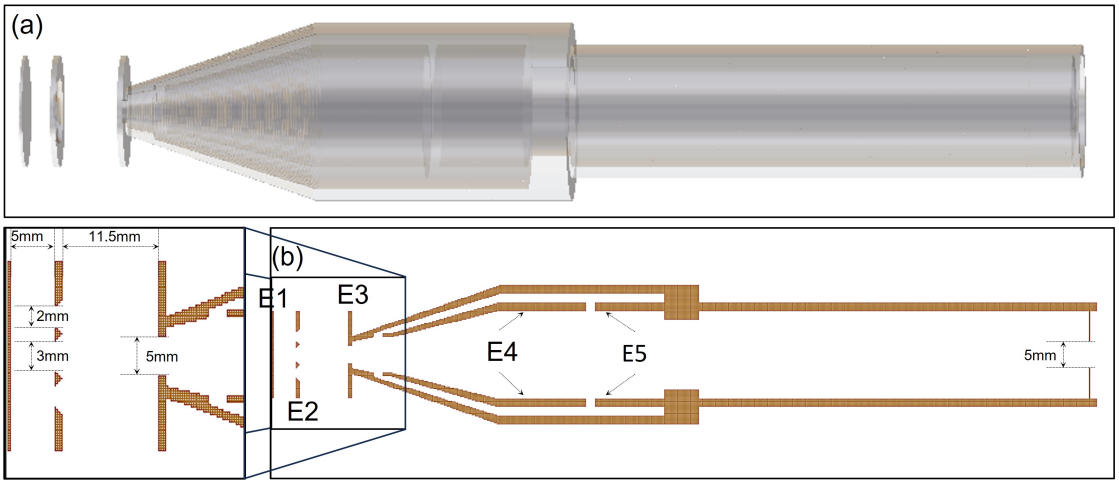


Figure 3.5: (a) 3D structure of the ion optics assembly; (b) 2D cross-sectional view with detailed electrode dimensions along the central axis. (All the images are made using the SIMION software.

along the time-of-flight (ToF) axis.

The extractor electrode (E2) is positioned 5 mm above the sample stage and is designed with five apertures: one central hole, 3 mm in diameter, aligned with the time-of-flight (ToF) axis for efficient secondary ion extraction, and four symmetrically arranged side holes, each 2 mm in diameter. One of these side holes allows the primary ion beam to pass through and impact the sample mounted on the repeller. A detailed view of the extractor plate structure is shown in Figure 3.6(a).

In positive ion mode, the repeller is applied with a high positive voltage to accelerate secondary cations. In the simulation setup, a potential of 10 kV is applied to the repeller. Under these conditions, the trajectory of the primary ion beam is observed to bend due to the electrostatic field, causing it to deviate from the central axis. Figures 3.6(b) and 3.6(c) illustrate the beam path through the extractor plate before and after deflection correction, respectively. To compensate for this deviation, deflector voltages of -500 V and $+500$ V are applied to the beam steering electrodes, effectively restoring the beam to its desired central trajectory.

Conversely, in negative ion mode, the polarity of the electric field is reversed. The repeller is held at a high negative voltage, which causes the primary ion beam to bend in the opposite direction. In this case, the polarity of the deflector voltage must also be inverted to accurately align the primary beam with the target on the sample surface.

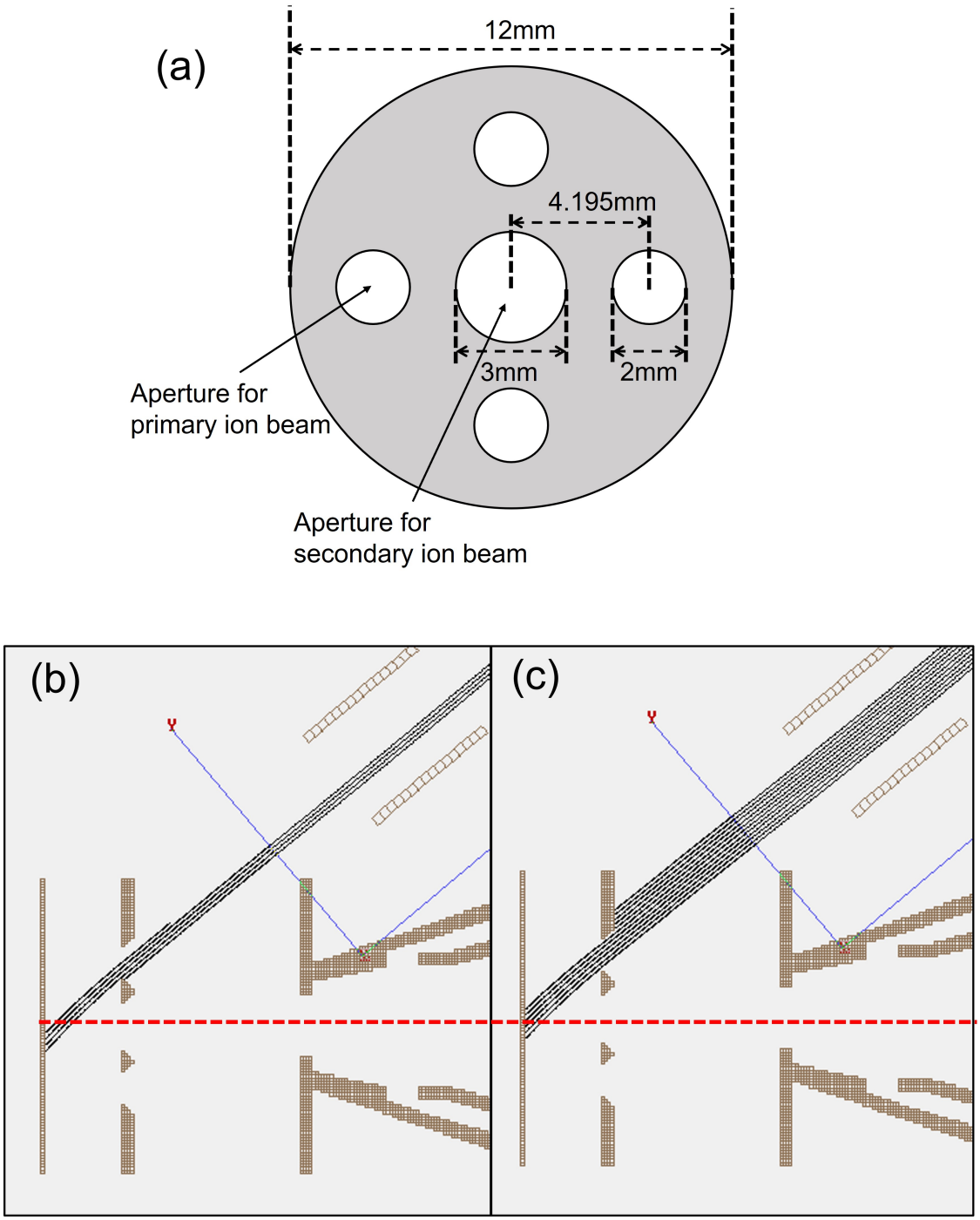


Figure 3.6: (a) Structure of the extractor plate. (b) and (c) show the simulated trajectories of the primary ion beam passing through the extractor plate without and with deflection correction, respectively.

The einzel lens assembly consists of three cylindrical electrodes. The first electrode (E3) is grounded and located 11.5 mm above the extractor. It features a circular head and a tapered cylindrical body for smooth field transition. The middle electrode (E4) is

electrically isolated and can be biased with a variable high voltage to operate in either spatial-focusing or velocity-focusing mode, depending on the experimental requirement. The final electrode (E5) is grounded and has a 5 mm diameter aperture to allow the focused secondary ions to pass through toward the detector.

This ion optics design enables fine control of secondary ion trajectories, allowing the system to be optimised for different imaging modes in time-of-flight secondary ion mass spectrometry (ToF-SIMS).

3.4 Detector Assembly and Data Process

Multiple detectors are employed in this instrument to monitor both the primary ion beam and the secondary ion signal. A Faraday cup and a secondary electron detector (SED) are utilised to measure the current and assess the focused spot size of the primary ion beam.

At the terminal end of the field-free drift region lies the secondary ion detector assembly, where the incident secondary ions are transformed into detectable signals. The detector consists of two microchannel plates (MCPs) arranged in a chevron geometry, followed by a fast-response scintillator or phosphor screen. This arrangement significantly amplifies the incoming ion signal: the MCPs multiply the electrons generated by each ion impact, and the scintillator subsequently converts the electron cascade into visible photons. These photons are then recorded using a camera or photodetector, enabling time-resolved or spatially resolved ion detection.

3.4.1 Faraday Cup

A Faraday cup is typically constructed from a metal cup or cylindrical enclosure with a small orifice. This orifice is electrically connected to ground via a resistor. When charged particles—such as ions—enter the cup, they are neutralised upon striking the inner walls by either donating or accepting electrons. This neutralisation induces a current through the resistor, which is then amplified and measured. By detecting this discharge current, the number of impinging ions can be quantified.

The measured electric current, defined as the flow of electrons per unit time, directly corresponds to the number of incident charges. For a continuous beam of singly charged

ions or electrons, the number of particles N hitting the cup per unit time t (in seconds) can be expressed as:

$$\frac{N}{t} = \frac{I}{e}$$

where I is the measured current (in amperes), and e is the elementary charge (1.60×10^{-19} C). Consequently, a current of one nanoampere (10^{-9} A) corresponds to approximately six billion singly charged particles striking the Faraday cup each second.

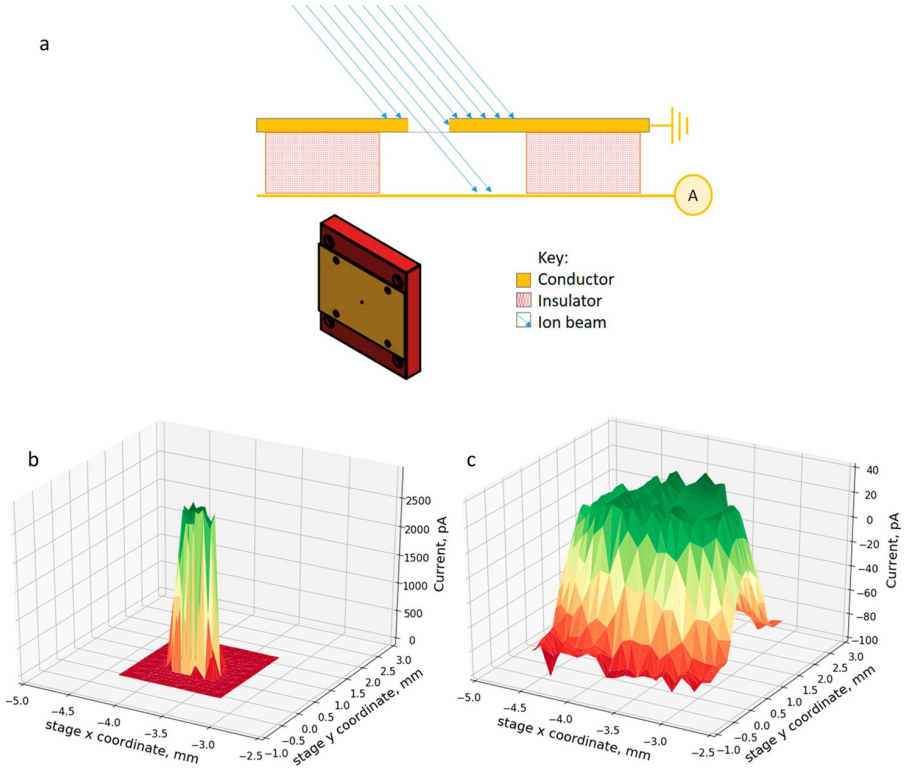


Figure 3.7: (a) Schematic of a device based on a Faraday cup for measuring beam flux at a given position. Current beam profiles for a C_{60}^{+} primary ion beam when (b) focused (0.18 mm wide) and (c) defocused (1.8 mm wide). Adapted from ref.[158]

However, charge counting in detectors such as the Faraday cup is not perfectly accurate, and is subject to two primary sources of error: (1) the emission of low-energy secondary electrons from the surface upon impact by the incident charged particle, and (2) backscattering of the incident particle, often at angles close to 180°, which may cause the particle to temporarily or permanently escape the collecting surface. These effects reduce the net current measured and lead to undercounting. The problem is

especially pronounced with electron beams, where it becomes fundamentally impossible to distinguish between a newly incident electron, a backscattered primary electron, or a fast secondary electron generated upon surface interaction.

In the Oxford microscope-mode SIMS imaging instrument, a Faraday cup is utilized to measure the primary ion beam current and evaluate its spatial uniformity. A schematic of the modified Faraday cup configuration is shown in Figure 3.7. In Figure 3.7(a), the Faraday cup is integrated into the sample holder. The top layer consists of a conductive sample plate, typically held at high voltage, while the bottom layer is the grounded Faraday cup, which collects and measures the ion beam current. An insulating layer is positioned between the conductive plate and the Faraday cup to ensure electrical isolation and maintain a stable electric field. Figures 3.7(b) and (c) illustrate the measured current distributions of the C_{60}^{+} primary ion beam under focused (0.18 mm) and defocused (1.8 mm) beam conditions, respectively.

3.4.2 Everhart-Thornley detector

The Everhart–Thornley detector (E–T detector or ET detector) is commonly used in scanning electron microscopes (SEMs) to detect secondary electrons (SE) and, in some configurations, backscattered electrons (BSE). It is named after its inventors, Everhart and Thornley. Secondary electrons are emitted from the sample surface when it is bombarded by a primary ion or electron beam. These secondary particles typically have significantly lower energy than the primary beam—on the order of a few electron volts.

As shown in Figure 3.8, when the primary beam strikes the sample surface, it generates secondary electrons. A positive bias is applied to a collector grid to attract and direct these electrons toward the detector. This collection potential can be tuned to optimize the efficiency of electron capture.

Once collected, the electron signal is amplified using a channeltron multiplier or a photomultiplier tube (PMT)—components that will be introduced in a later section. When electrons strike the wall of the dynode, multiple secondary electrons are produced per collision. The amplification factor depends on the applied accelerating voltage; for example, a gain of approximately 5×10^7 can be achieved at an accelerating voltage

of 2000 V. The final result is a pulse of electrons at the detector output. This signal is further amplified by an electronic amplifier to produce a voltage signal suitable for display on a monitor or for digital image acquisition.

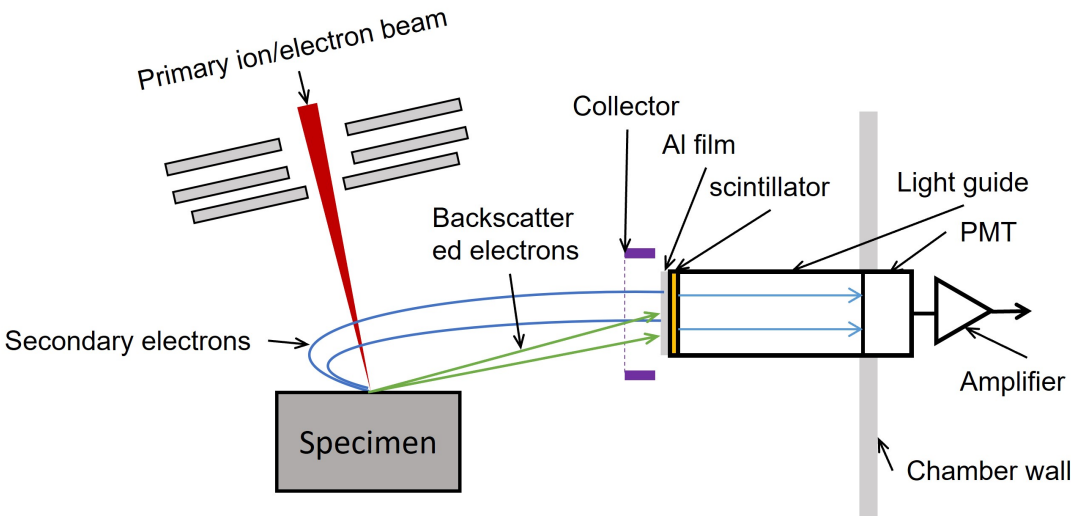


Figure 3.8: Schematic of a secondary electron detector. A primary ion/electron beam (red) is focused and accelerated by a series of electrodes. Upon bombardment of the specimen by the primary beam, secondary electrons are emitted from the surface. These secondary electrons are subsequently collected and directed towards a photomultiplier tube for detection.

3.4.3 Microchannel plates

Microchannel plates (MCPs) are used to amplify the detected secondary ion signals. An MCP is a circular glass slab containing a regular array of parallel cylindrical open pores (microchannels) (see Figure 3.9). Two MCPs are stacked in an inverted chevron configuration, where the microchannels are arranged in a V-shape to enhance signal amplification. MCPs are well-suited for position-sensitive detection due to their relatively large surface area and the spatial isolation of individual channels, which ensures that the spatial pattern of electrons emitted at the rear surface preserves the image of the incident particles on the front surface. The MCPs used in our system have an outer diameter of 40 mm. The open area of the MCP—defined as the combined cross-sectional area of the microchannels—is critical for evaluating its efficiency. Our MCPs feature densely packed microchannels with a pore diameter of 25 µm and a pitch size of 32 µm.

An important characteristic of an MCP is the open area ratio (OAR), defined as the ratio of the pore area to the total surface area of the plate. The OAR directly limits the detection efficiency (η). A close-packed arrangement of pores typically results in OAR values between 50–60%, whereas our MCPs have a minimum OAR of 45%. The probability of detecting n particles in coincidence is given by η^n. For example, if $\eta = 0.45$, the probability of detecting two particles in coincidence is $\eta^2 = 0.45^2 = 0.2025$ (or 20.25%).

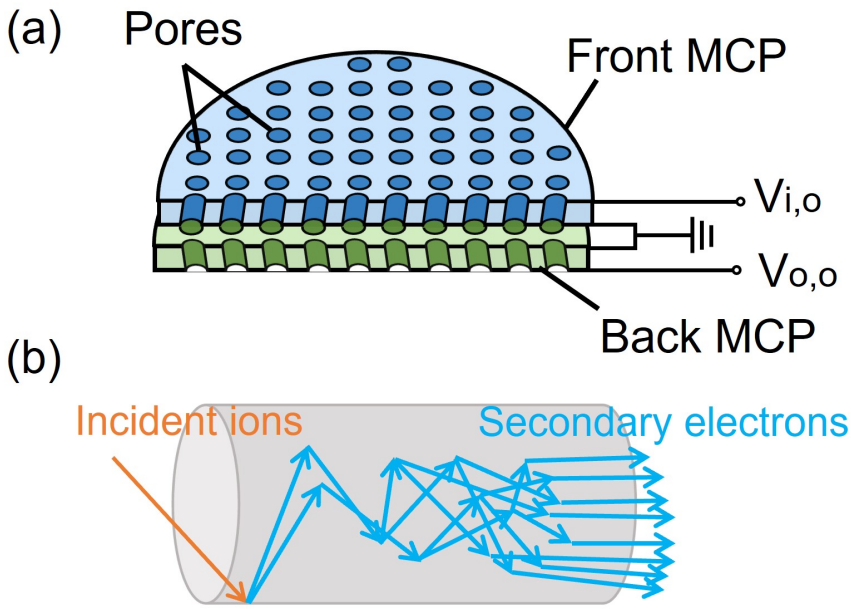


Figure 3.9: (a) illustrates the cross section of the MCPs in negative mode, while (b) shows the signal transformation and amplification process in a single pore. The sizes and numbers or pores and MCP are not to scale.

As shown in Figure 3.9(b), incident ions are amplified by each MCP pore and converted into electron signals. The amplification factor depends on the electric field across the microchannel. A single MCP can sustain a maximum potential difference of 1 kV. When the front face is grounded and the rear face is held at 1 kV, the maximum gain of the MCP is approximately 10^4.

In the dual-MCP configuration, the system operates in positive mode: the front face of the first MCP is held at $V_{i,o}$ a maximum of -1 kV, while its rear face (which is also the front face of the second MCP) is grounded. The back face of the second MCP is then biased $V_{o,o}$ up to $+1$ kV. In negative mode, the front face of the first MCP is grounded, the

back face of the second MCP is held at a voltage $V_{o,o}$, and the intermediate connection between the two plates is biased at $V_{o,o}/2$.

The main advantage of stacking MCPs is increased gain, as the electron avalanche from the first MCP is further amplified by the second. However, this configuration introduces the risk of positive ion feedback—an undesirable phenomenon that limits the effective channel length and overall gain. As the electron cascade intensifies while traversing the channel, residual gas atoms or adsorbed molecules on the channel walls may become ionised by electron impacts. These resulting feedback ions are accelerated by the electric field back toward the input side of the MCP. If not suppressed, they may gain enough energy to strike the channel wall and release secondary electrons, initiating a second, unwanted cascade. These false after-pulses interfere with measurements and may lead to a sustained glow discharge, potentially damaging the MCP.

The chevron (V-shaped) configuration helps mitigate this effect by trapping feedback ions at the interface between the two plates. It is important to note that MCPs must be operated under high-vacuum conditions and well below their maximum voltage rating to prevent electrical breakdown. In the current SIMS system, the detector operates at a pressure of approximately 10^{-8} mbar.

3.4.4 Fast scintillator

After the MCPs, the electron signals need to be converted into detectable light signals for the camera and photomultiplier. A phosphor screen emits photons when impacted by electrons with high kinetic energy.

The Jablonski diagram illustrates the electronic states and vibrational levels of a molecule[164], as well as the transitions between them. The first subscript denotes the electronic states—singlet (S) or triplet (T)—while the second subscript indicates the vibrational level. In organic scintillators, the energy gap between the electronic ground state and the first excited singlet state typically ranges from 3 to 4 eV, with vibrational levels spaced by approximately 0.15 eV.

When a charged particle impacts the scintillator, its kinetic energy is absorbed, exciting scintillator molecules to vibronic levels within the manifold of higher electronic states,

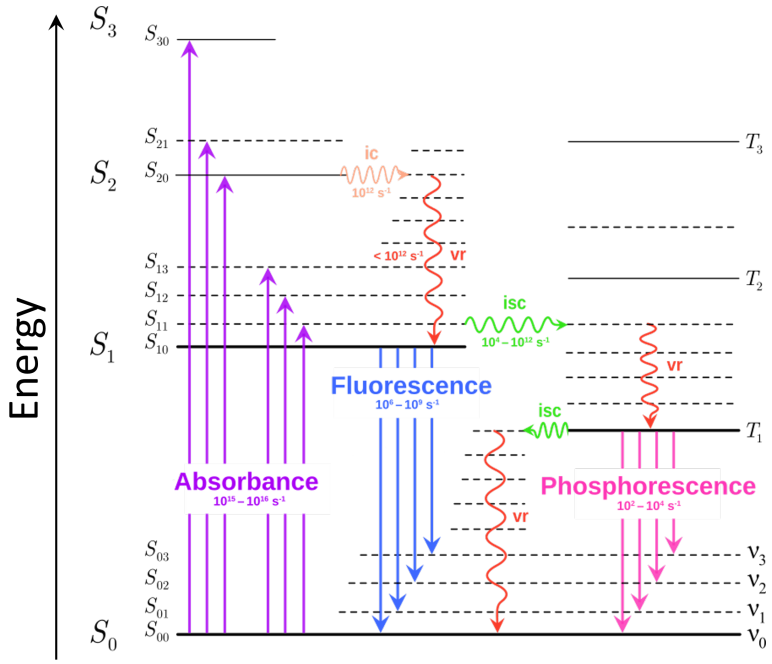


Figure 3.10: A Jablonski diagram illustrating the vibrational energy levels of a molecule. The diagram depicts the key photophysical processes including absorption, non-radiative decay (internal conversion and intersystem crossing), fluorescence, and phosphorescence. Associated rate constants for each transition process are also indicated. The singlet (S) and triplet (T) electronic states are shown with their respective vibrational sub-levels.

as indicated by the purple arrows in Figure 3.10. The excited molecules typically relax within a few picoseconds via radiationless internal conversion to the ground vibrational level, denoted as S_{10} and symbolized by the upper left orange arrow.

The scintillation process itself arises from fluorescence, specifically the transition from the S_{10} level to various vibrationally excited states within the electronic ground state manifold. The number and population of these final vibrational states largely determine the width of the emission spectrum observed for the organic scintillator in use. A second possible relaxation mechanism is indicated by the pink arrows in Figure 3.10, which occurs via intersystem crossing to the lowest triplet state, T_1. The emission spectrum associated with phosphorescence is typically red-shifted and does not overlap with the fluorescence spectrum, as the triplet state generally lies energetically below the first excited singlet state. However, phosphorescence and other non-radiative relaxation mechanisms are undesirable because they can quench the fluorescence of the scintillator and reduce the overall light yield. Another observable photon emission process is

delayed fluorescence. In this case, molecules that have transitioned to the triplet state can be thermally re-excited back to the first excited singlet state (S_1). This leads to a delayed emission of photons from the S_1 state, resembling prompt fluorescence but occurring on a longer timescale.

In microscope mode MSI systems, light-sensitive detectors such as cameras and photomultipliers are used; therefore, the fluorescence lifetime and brightness are crucial factors affecting mass resolution and detection efficiency. Fluorescence lifetime is defined as the time a fluorophore spends in its excited state before decaying to its ground state via spontaneous emission. Lifetimes can range from picoseconds to hundreds of nanoseconds[122][165][166]. When a large number of fluorophores are excited—as is often the case in ion microscopy—the fluorescence lifetime (τ) is defined as the time it takes for the population of excited fluorophores to decay to $1/e$ of its initial value. In practical measurements, τ is typically determined by monitoring the fluorescence intensity and identifying the time at which it decreases to $1/e$ of its original level. This relationship is expressed mathematically as:

$$I = I_0 e^{-t/\tau} \tag{3.1}$$

where I represents the emission intensity at time t, and I_0 is the initial intensity.

The fluorescence lifetime (τ) is potentionally related to the mass resolution of time-of-flight mass spectrometry (ToF-MS), since mass resolution is proportional to the time resolution. Time resolution is defined as the ratio of the ion's time-of-flight (ToF) to the full width at half maximum (FWHM), denoted as Δt, of the corresponding ToF peak. However, if a conventional scintillator such as P 47, characterized by a fluorescence rise time of approximately 6.7 ± 0.2 ns and a decay time of 168 ± 2.3 ns [167], is used, the resulting FWHM of the ToF peak, after convolution with the fluorescence decay, would significantly exceed 10 ns. This broadening limits the achievable mass resolution to approximately 200 (m/Δm). To achieve higher mass resolution, it is therefore essential to use a fast scintillator screen with a short fluorescence lifetime, which minimizes signal broadening and enhances temporal precision. B. Winter *et al.* investigated Exalite 404 and reported a fluorescence rise time of 3.25 ± 0.2 ns and a decay time of 7.7 ± 0.3 ns [167].

In this project, two types of scintillator materials are utilised: P 47 and BC-408. P 47 is characterised by its high brightness, rendering it particularly suitable for microscope-mode mass spectrometry imaging applications where high signal intensity is advantageous. Conversely, BC-408 exhibits a fast rise time of approximately 1 ns, which enables improved temporal resolution. The selection between these scintillators is determined by the specific experimental requirements, including timing precision, signal intensity, and compatibility with the optical readout system of the detector.

3.4.5 Photomultiplier tube

Photomultiplier tubes (PMTs) are highly sensitive light detectors commonly used in mass spectrometry[168]. In time-of-flight mass spectrometers (ToF-MS), PMTs detect optical signals emitted from scintillator screens, convert these signals into electrical currents, and transmit them to external processing devices. They offer exceptional photon-detection sensitivity across a wide spectral range, from ultraviolet to near-infrared, and feature very fast response times, typically under 1 ns[169], making them well-suited for applications requiring high temporal resolution.

Structurally, a PMT is an evacuated glass tube that operates based on the photoelectric effect, converting incident photons into electrons and amplifying the resulting current by factors of up to 10^8[122].

A schematic of a photomultiplier tube (PMT) is presented in Figure3.11. Light enters the PMT through the input window and strikes the photocathode, which is typically coated on the inner surface of the window. The photocathode is composed of a photosensitive semiconductor material that emits photoelectrons into the vacuum tube upon exposure to incident photons. A negative voltage (approximately -1.2 kV in this setup) is applied to the photocathode to accelerate the emitted photoelectrons away from its surface. These electrons are then guided by a focusing electrode toward the first dynode.

The first dynode initiates the electron multiplication process via secondary emission—each incident electron striking the dynode releases multiple secondary electrons. The PMT contains a cascade of such dynodes, each positioned to receive and amplify

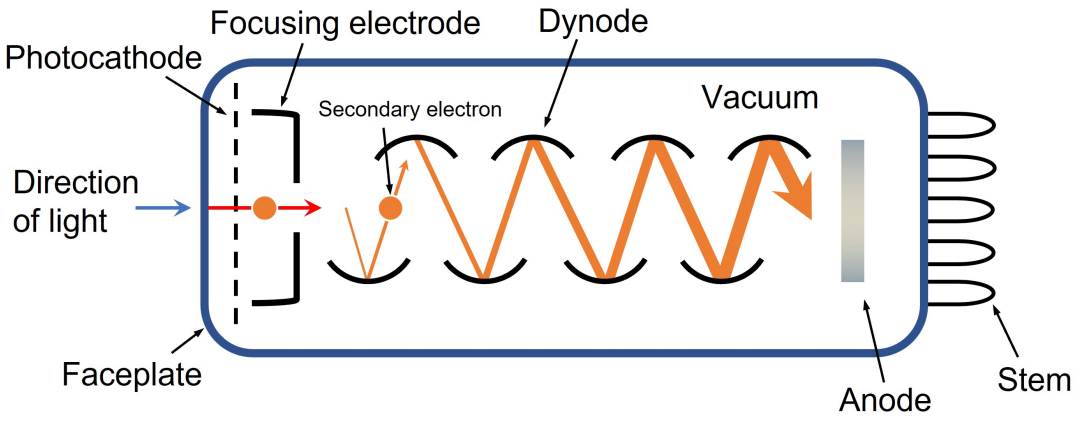


Figure 3.11: A schematic representation of a photomultiplier tube (PMT). Incident photons strike the photocathode, releasing photoelectrons via the photoelectric effect. These electrons are subsequently accelerated and multiplied through a series of dynodes, with each dynode stage producing additional secondary electrons. The amplified electron cascade is finally collected at the anode, generating a measurable output signal.

the electron stream from the previous stage. This cascade continues until the amplified electron pulse reaches the anode. The photocathode, dynodes, and anode are all interconnected through a resistor chain, which provides the appropriate voltage gradient to sustain electron multiplication across the dynode chain, as illustrated in Figure 3.11. This resistor chain functions as a voltage divider circuit, establishing a potential gradient across the PMT. Each dynode is maintained at a progressively more positive voltage than the preceding one. As a result, the secondary electrons emitted from the first dynode are accelerated by the potential difference and directed toward the second dynode, where they induce further secondary electron emission. This cascade process continues through successive dynodes, resulting in a rapid amplification of the electron signal as it travels down the tube.

The final output current of the PMT depends primarily on two factors: the number of dynodes and the accelerating potential between them. The number of dynodes determines how many stages of amplification the electron signal undergoes, while the inter-dynode potential difference influences the kinetic energy of the electrons at each stage, affecting the number of secondary electrons produced. At the end of the dynode chain, the electrons are collected by an anode, typically held near ground potential. The anode gathers the multiplied electron signal and converts it into a measurable current output, which is then

read by an external device such as an oscilloscope. Additionally, as shown in Figure 3.11, capacitors are connected in parallel with the final few dynodes. These capacitors serve to stabilize the voltage at these stages by supplying additional charge, thereby helping to maintain consistent dynode potentials during intense electron avalanches.

3.4.6 CCD and CMOS camera

The microscope mode MSI system uses position-sensitive detectors to record the spatial distribution of ions. Charged coupled device (CCD) and complementary metal-oxide-semiconductor (CMOS) cameras are commonly employed as imaging detectors to capture the photons emitted from the fast scintillator.

The schematic of the CCD camera is shown in Figure 3.12(a). CCD cameras consist of pixel arrays, with one column of pixels serving as the output register. When photon events incident on a pixel generate electron-hole pairs within the silicon, the resulting charge is stored by a capacitor within that pixel. During an experimental cycle, the charge generated in each pixel is first accumulated and then transferred across the pixel array by sequentially activating a series of gating electrodes on the pixel surface. These electrodes create a potential bias that enables controlled charge movement, forming a two-dimensional charge image where each pixel corresponds to a portion of the captured signal. At the end of each cycle, the charge from each pixel is shifted along the rows—one pixel at a time—ultimately transferring the charge from the final column into the output register. From there, the charge is moved pixel-by-pixel along the output register. An amplification stage converts this charge into a voltage signal, which is then read out by external electronics. This process is repeated for each column until the entire two-dimensional dataset has been read out from the camera.

The advent of complementary metal-oxide-semiconductor (CMOS) or active pixel sensors—such as the Pixel Imaging Mass Spectrometry (PImMS) camera and Timepix sensors—has provided a powerful alternative to traditional CCD technology. Like CCDs, CMOS sensors convert photons into charge and provide spatial information. However, they incorporate thresholding to suppress background noise and integrate most of their circuitry directly into the sensor. A schematic of the CMOS architecture is shown in

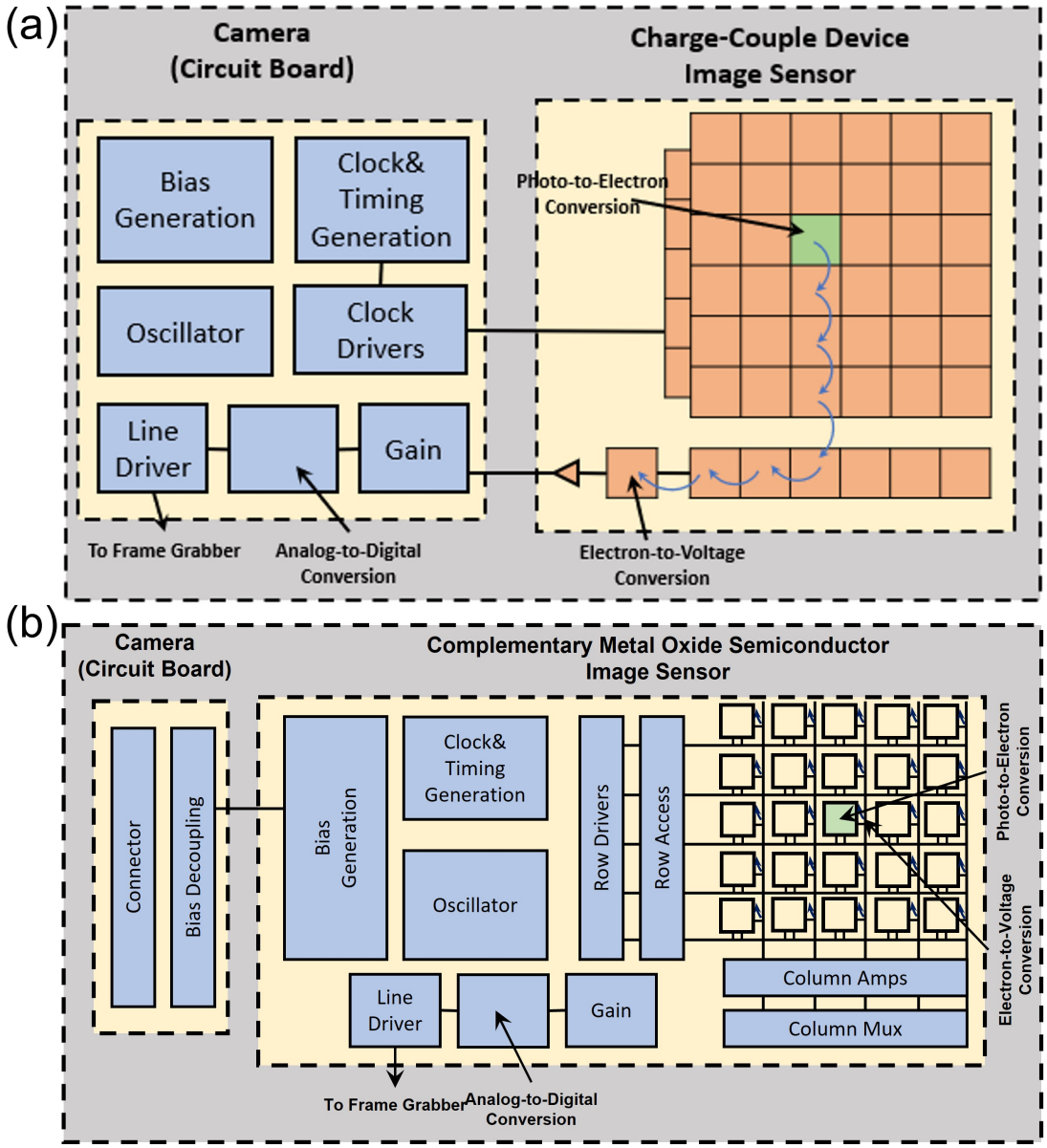


Figure 3.12: A schematic illustration of CCD (a) and CMOS (b) camera sensors. In both cases, incident photons strike the active sensor pixels (indicated in green), generating photoelectrons. In a CCD sensor, the photo-generated charge from all pixels is transferred sequentially across the array to a readout register, where it is converted into a voltage signal column by column. In contrast, a CMOS sensor performs the photon-to-electron conversion and subsequent charge-to-voltage conversion within each individual pixel, enabling parallel readout and potentially faster acquisition.

Figure 3.12(b). Unlike CCDs, CMOS sensors contain multiple transistors within each pixel, enabling local logic functions and time-stamping capabilities. As a result, each pixel acts as an independent sensor capable of recording events during a single experimental cycle. For example, the PImMS camera includes four memory registers per pixel, allowing

up to four events to be time-stamped and stored per cycle. After acquisition, each pixel outputs its data as a three-column matrix (x, y, t), representing spatial coordinates and time-of-arrival. In contrast, the TimePix3 sensor continuously records events relative to an external trigger, keeping all pixels active at all times. This capability to record and time-stamp multiple events per pixel within a single cycle enables multi-mass imaging in time-of-flight mass spectrometry (ToF-MS), capturing the full spectrum simultaneously. Consequently, it eliminates the need for sequential ion imaging, significantly enhancing throughput. CMOS technology has been applied across a range of imaging experiments, including velocity-map imaging, TRIFT ion microscopy, linear ToF-MS, and neutron detection. The integration of CMOS sensors with high-resolution ion microscope imaging enables simultaneous spatial and temporal detection of all ions in a mass spectrum within a single acquisition, fully leveraging the throughput potential of the instrument.

3.4.7 The Pixel Imaging Mass Spectrometry Sensor (PImMS)

The Pixel Imaging Mass Spectrometry (PImMS) camera is an event-triggered image sensor capable of recording ion events as a sequence of timestamps within each pixel. The sensor was developed in collaboration with the CMOS Sensor Design Group at Rutherford Appleton Laboratory (RAL), specifically to overcome the limitations associated with conventional detectors used in Imaging Mass Spectrometry (IMS) [170]. A key advantage of the PImMS approach is its ability to record multi-mass ions simultaneously, thereby enabling efficient time-resolved ion imaging across a broad mass range.

To date, two prototypes of the PImMS camera have been developed, as shown in Figure 3.13: PImMS 1, which consists of a 72×72 pixel array, and PImMS 2, featuring a significantly enhanced 324×324 pixel array. The maximum clock frequencies of these two generations are 80 MHz and 40 MHz, corresponding to timing precisions of 12.5 ns and 25 ns, respectively. Consequently, in PImMS 1, mass spectral peaks can be resolved provided that they are separated by more than 12.5 ns, while in PImMS 2 the minimum resolvable separation is 25 ns.

The pixel size of the PImMS camera is $70\,\mu\text{m} \times 70\,\mu\text{m}$. Ion impacts are recorded and time-stamped by one of four diodes whenever the signal in a pixel exceeds a predefined

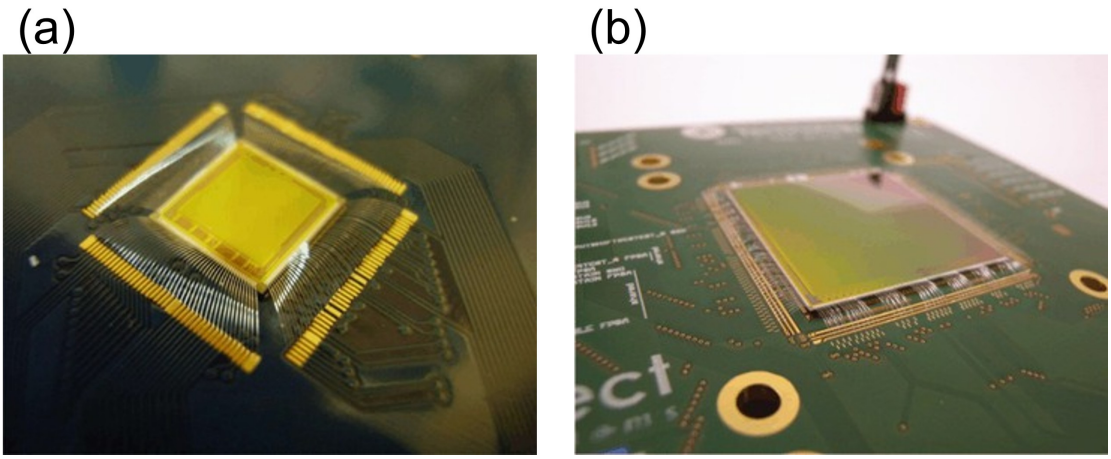


Figure 3.13: Pictures of the sensors of PImMS 1 (a) and PImMS 2 (b). Adapted from Ref [171].

threshold. The camera can operate continuously for up to 50 μs, ensuring that a typical experimental cycle can be fully captured and analysed. The primary readout method relies on the digital timestamp registers of each pixel, which provide the experimental information in the format: (x, y, t, n_{frame}, m_{register}). Here, x and y denote the two-dimensional spatial coordinates of the ion event, t corresponds to the time bin in which the event occurs (relative to an external trigger), n_{frame} represents the sequential number of the experimental iteration, and m_{register} indicates the register index (1–4). During an experimental cycle, the majority of pixels are not expected to detect any signal. Importantly, only ion events are recorded, in contrast to a conventional framing camera where every pixel stores data for a fixed acquisition period. This event-driven strategy substantially reduces the data storage requirements. Following each laser shot, the coordinates of ion impact voxels are transferred to a computer for subsequent processing.

The PImMS (versions 1 and 2) sensor is connected to a computer via USB, where it is controlled through the PImMS software suite. This software provides functionality for sensor configuration, calibration, data readout, as well as online and offline data visualisation. In addition, a dedicated post-processing package, the PImMS analysis software, is employed for advanced data handling. Its features include mass spectrum visualisation, temporal windowing, noisy-pixel filtering, and centroiding of ion clusters. The centroiding procedure reduces each detected cluster to a single representative pixel

and corresponding timestamp. Clusters are identified using an 8-fold connectivity algorithm, which is described in detail in the centroiding section.

With the power to resolve multiple masses at once, PImMS camera has been applied in many chemical systems, including spatial imaging [113]and velocity map imaging [115]. In the reaction dynamic field, the PImMS sensor has also been employed as a detector in time-resolved velocity-map imaging studies into gas-phase [115] and surface [172] photochemistry. Configured as an optical sensor, the camera is mounted outside the vacuum in place of the CCD camera in a conventional VMI detection setup. In the spatial imaging mass spectrometry field, it has been demonstrated the possibility to couple with fast Exalite 404 [167] or BC-408 [173] scintillators. The PImMS 1 camera, when coupled with a commercial mass spectrometer, enables multi-mass imaging with a mass resolution exceeding the isotopic limit ($\Delta m_{50\%} = 1$ m/z unit) across the range of $200 < m/z < 800$, while simultaneously achieving an optimum spatial resolution of 25 µm.

3.4.8 TimePix3-based camera

The TimePix3-based camera, a type of CMOS sensor, is capable of simultaneously acquiring time-of-flight (ToF) spectra and imaging data. A photograph of the TimePix3 sensor is shown in Figure 3.14(c). The sensor chip features a 256×256 pixel array spanning an area of 14 mm$\times$14 mm, with each pixel measuring 55 µm$\times$55 µm [174]. This high-resolution sensor can detect multiple ion events within each experimental cycle and offers a timing precision of 1.562 ns [174]. Each pixel hit is independently read out, and the chip is capable of sustaining a throughput of up to 40 MHits s^{-1} m^{-2} [175]. Unlike frame-based cameras, the TimePix3 outputs a continuous stream of data, necessitating a USB 3.0 connection to handle the required data transfer rates.

A key distinguishing feature of the TimePix3 chip, compared to conventional CCD cameras, is its ability to simultaneously record both the signal amplitude and the time-of-arrival of each detected event. The amplitude is recorded in the form of the time-over-threshold (ToT), which reflects the duration for which the signal remains above a predefined threshold.

Data readout from the sensor is managed by the USB 3.0-based AdvaDAQ system. Two software platforms were employed to control and acquire data from the TimePix3-based camera during the experiments described in this thesis: PiXet-Pro and a custom-developed Python-based application. PiXet-Pro provides real-time visualisation in multiple display modes and facilitates chip calibration to ensure consistent pixel thresholds and uniform response to photon events across the array. It records the acquired TimePix3 data in a '.t3pa' file format, which contains five key columns: matrix index, time-of-arrival (ToA), time-over-threshold (ToT), fine time-of-arrival (fToA), and overflow flags. These data are acquired and stored via a USB connection to a host computer.

The custom Python software provides an alternative acquisition method, storing data in the '.h5' format. Unlike PiXet-Pro, this tool records only those pixels which are triggered during an event, significantly reducing the file size and improving data handling efficiency during subsequent analysis.

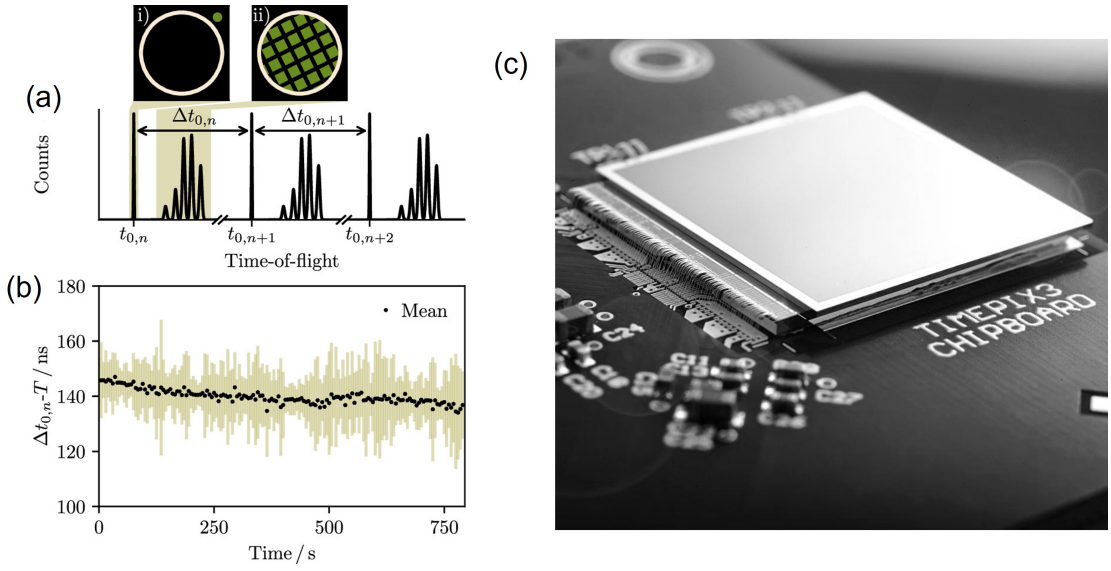


Figure 3.14: (a) Schematic of the external trigger strategy employed by the TimePix3-based camera system; (b) measured trigger time jitter, adapted from ref. [116]; (c) photograph of the TimePix3 sensor chip, adapted from ref. [174].

Conventionally, the TimePix3 camera operates using an internal trigger. However, in this thesis, a more cost-effective and efficient external triggering method is employed. A laser or LED source is used to illuminate the TimePix3 chip at a defined repetition rate, which is controlled by a programmable delay generator. The intensity of the laser or

LED signal is significantly higher than that of the scintillation signals typically detected by the chip. This strong signal can be selectively filtered by applying a high threshold, effectively distinguishing it from lower-intensity scintillation events.

The arrival time of this high-intensity trigger signal is designated as the reference time, t_0, for each experimental cycle, as illustrated in Figure 3.14(a). The temporal jitter associated with t_0 is shown in Figure 3.14(b), and is approximately 20 ns.

3.4.9 Data processing

In this project, both a CCD camera and a TimePix3-based camera are employed. Each camera collects single ion events and accumulates them to form ion images. Larger ion cluster sizes for each single ion event typically limit the spatial resolution of the images. To address this, an algorithm called *centroiding* is applied to reduce each large single ion event to a single camera pixel. The working mechanism of the 2D centroiding algorithm is illustrated in Figure 3.15.

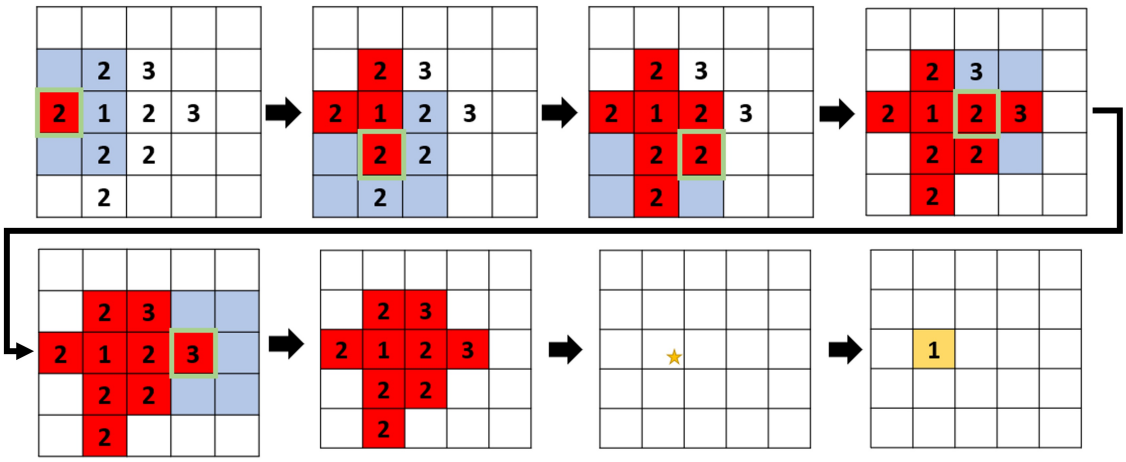


Figure 3.15: Illustration of the single-ion event centroiding strategy. Red pixels indicate counted pixels, the processed pixel is highlighted with a green square, and blue pixels represent surrounding pixels awaiting processing. The intensity of each pixel is annotated within its corresponding grid cell.

The CCD camera records only position information; therefore, the centroiding algorithm operates solely in 2D on the detector plane. The position of each single ion event is recorded by the camera as a cluster of multiple pixels (x, y). For each ion event within a single camera frame, the algorithm identifies an initial single-pixel

event and then searches the eight nearest neighboring pixels to group them into the same ion event cluster. This process is repeated for every pixel added to the cluster until no more adjacent pixels are found.

Once all N pixels constituting a cluster have been identified, the centroid positions c_x and c_y are calculated as the intensity-weighted averages of the coordinates of each pixel in the cluster:

$$\begin{aligned} c_x &= (\sum_{i=1}^{N} x_i \cdot I_i) / \sum_{i=1}^{N} I_i, \\ c_y &= (\sum_{i=1}^{N} y_i \cdot I_i) / \sum_{i=1}^{N} I_i. \end{aligned} \tag{3.2}$$

Here, x_i and y_i represent the spatial coordinates of the ith pixel within the cluster, while I_i denotes the corresponding signal intensity.

In the CCD camera system, the signal data are recorded with their intensity and position information, but without centroiding. Therefore, centroiding is performed after image acquisition, although the algorithm can also be integrated into the camera driver software. A comparison between the centroided and raw images—both single-frame and accumulated over multiple frames—is shown in Figure 3.16. It is evident that the centroided image exhibits significantly improved spatial resolution compared to the raw image.

TimePix3-based camera not only records the spatial coordinates (x, y), but also captures the Time-of-Arrival (*ToA*) and Time-over-Threshold (*ToT*) [176][177]. Therefore, centroiding and *ToT* correction are performed in three dimensions. The fundamental centroiding approach of TimePix3 is similar to that of a CCD sensor; however, the algorithm processes events in ascending order of time bins rather than within a single image frame, including all events occurring within a specified timing window. The weight of each pixel is evaluated based on *ToA* rather than intensity, as given by:

$$\begin{aligned} c_x &= \sum_{i=1}^{N} \frac{x_i}{t_i'} / \sum_{i=1}^{N} \frac{1}{t_i'}, \\ c_y &= \sum_{i=1}^{N} \frac{y_i}{t_i'} / \sum_{i=1}^{N} \frac{1}{t_i'}. \end{aligned} \tag{3.3}$$

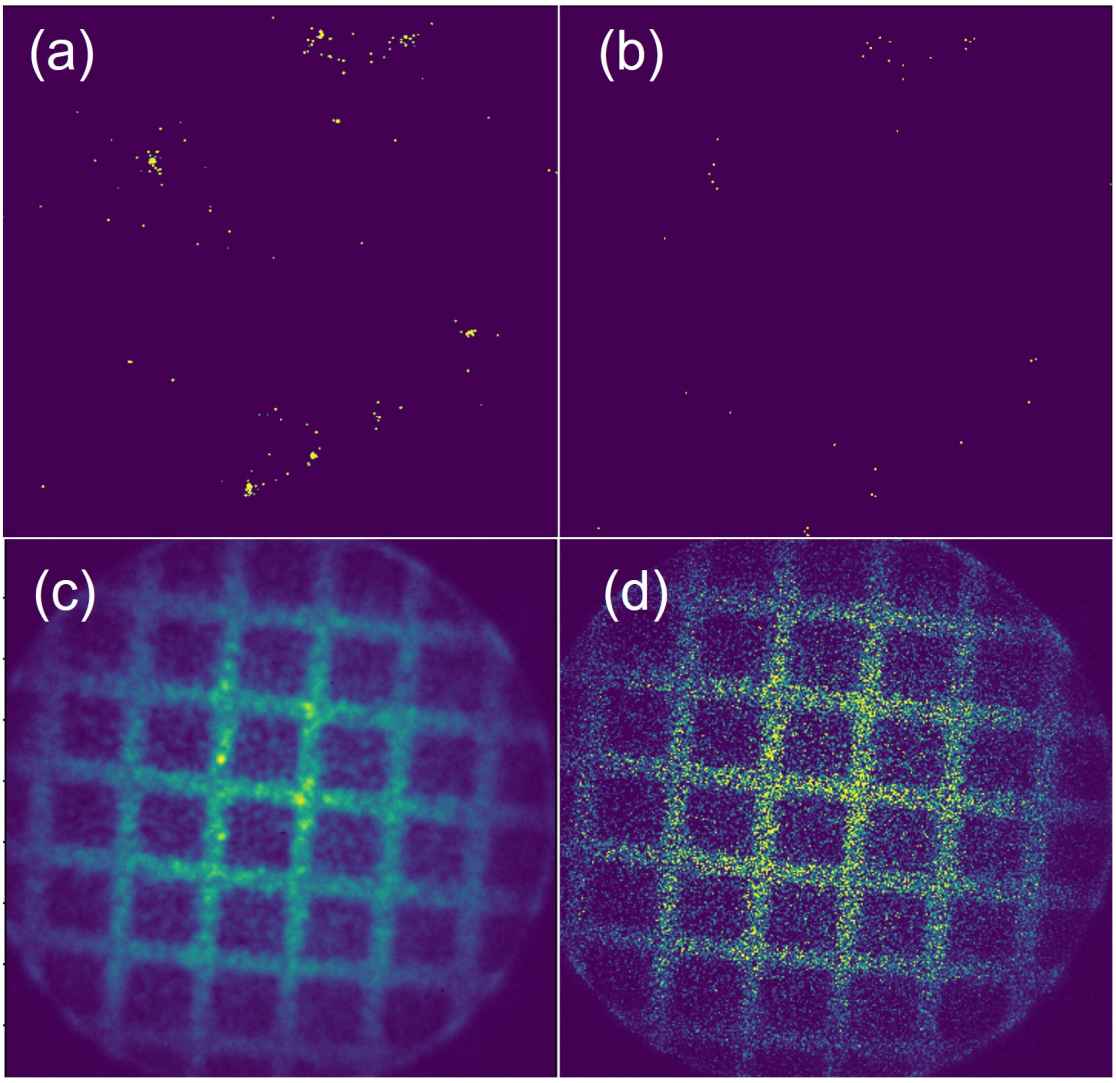


Figure 3.16: Ion images of a grid pattern of Rhodamine B : (a) and (c) represent the single-frame and accumulated raw images without centroiding, respectively, while (b) and (d) show the corresponding images processed with centroiding. The centroided images are noticeably sharper and better defined, demonstrating that the centroiding algorithm significantly enhances the spatial resolution of the microscope-mode MSI system.

Where x_i and y_i represent the spatial position of the ith event, while t_i' represents its timebin, relative to the earliest event timebin t_0:

$$t_i' = t_i - t_0 + 1. \tag{3.4}$$

To enhance the time resolution of TimePix3 spectra, *ToT Correction* or *Range-Walk Correction* [178][177] is applied using the *ToT* values. When an ion event hits the TimePix3 sensor, it generates a time-of-flight (ToF) signal that depends on both the

arrival time and the signal amplitude.

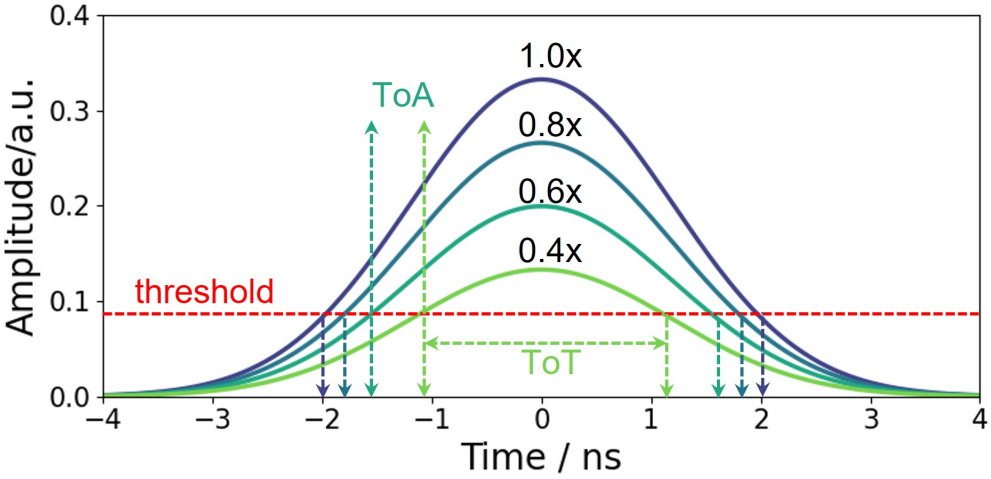


Figure 3.17: A simulated dataset illustrates the relationship between ToT and ToA. The threshold level is indicated by a red dashed line. Signals with varying amplitudes are shown in different colors, where a deeper (darker) color represents a higher signal amplitude. ToT corresponds to the duration for which a signal remains above the threshold, while ToA is defined as the start time of the ToT window.

Using a centroiding algorithm, the accuracy of the *ToA* is positively correlated with the ToF accuracy and the overall time resolution of a single event. As illustrated in Figure 3.17, a fixed threshold is applied (indicated by the red dashed line), and signals with higher amplitudes tend to produce larger *ToT* values and earlier *ToA* values. This relationship can be expressed as:

$$ToA = f(ToT)$$

By determining this functional relationship and correcting the *ToA* values accordingly, the corresponding ToF peaks can be aligned more accurately. This results in improved peak sharpness and enhanced time resolution in the final spectrum.

3.5 Sample Preparation

To evaluate the spatial resolution, mass resolution, and optimised mass range of the system, a variety of test samples were employed, including metal targets and laser dyes. The dye molecules enable the fabrication of high-quality, square-patterned samples through the use of a custom-built electrospray deposition device in conjunction with a metal

mesh mask. These thin and uniform patterned dye films are particularly well-suited for assessing both mass resolution and spatial imaging performance, offering a precise and reproducible method for characterising the system's capabilities.

Electrospraying is a technique that employs a high voltage applied to a liquid to generate a fine aerosol at the emitter tip [179]. Ideally, the liquid forms a Taylor cone at the emitter, from which a thin jet emerges. Surface instabilities on the jet lead to the formation of small, highly charged droplets. These droplets are subsequently dispersed radially due to Coulombic repulsion. The process of electrospray-based sample deposition is schematically illustrated in Figure 3.18(a).

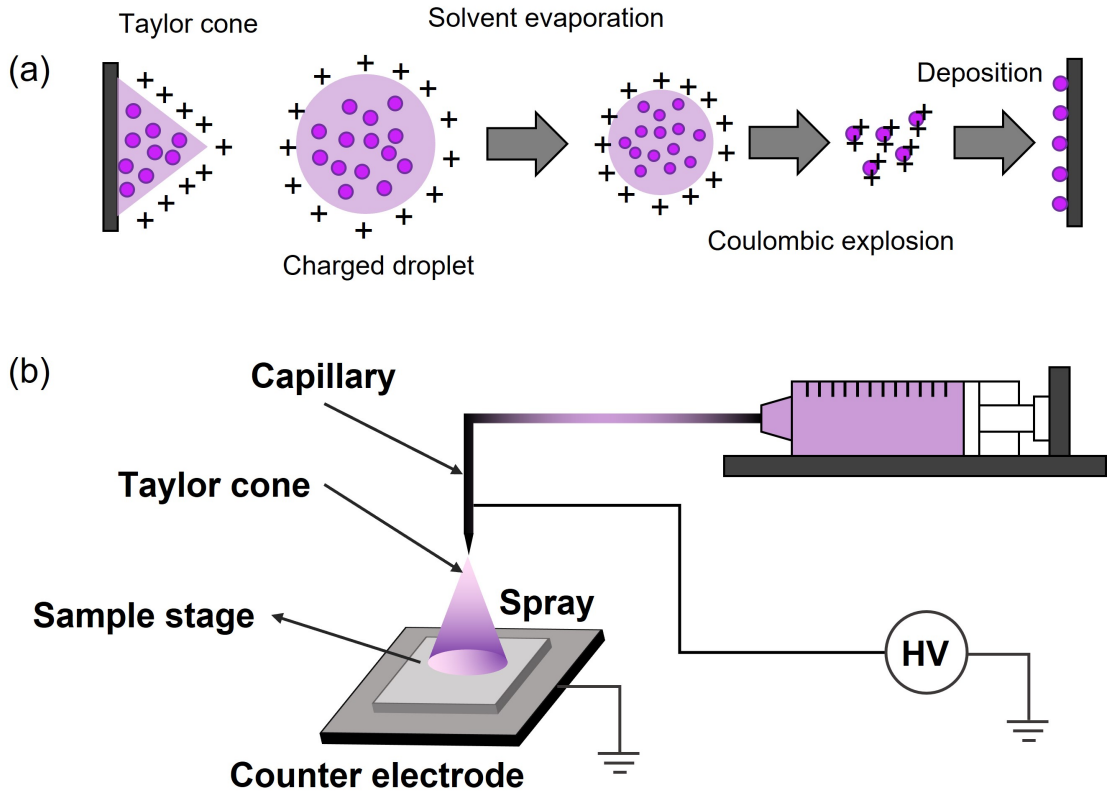


Figure 3.18: (a) illustrates the schematic of electrospray sample deposition. Under a high voltage, a Taylor cone is formed by the liquid. As the solvent in the droplets gradually evaporates, a Coulomb explosion occurs, resulting in the formation of sample ions that are subsequently deposited onto the sample surface. (b) shows the schematic diagram of the custom-built electrosprayer.

A home-built electrosprayer was used to prepare all of the dye samples in this thesis. The device consists of an injection needle (BD Microlance 3, filed flat) suspended above a

grounded plate. The needle has an outer diameter of 0.81 mm, a length of approximately 30 mm, and is held at a high potential ranging from 5.2 to 6 kV. It is connected to a capillary tube with an internal diameter typically less than 1 mm. The capillary is attached to a syringe containing the analyte mounted on a syringe pump (Legato 100, KD Scientific Inc.) operating at a flow rate of 20 µL/h. Indium tin oxide (ITO) coated glass slides ($25 \times 25 \times 1.1\,\mathrm{mm}^3$, Sigma-Aldrich) and silicon wafers were used as sample substrates. The ITO slides were placed with the conductive side facing up on the grounded plate, serving as the counter electrode positioned 1–3 cm below the tip of the needle. A small metal arm is connected to the top surface of the ITO slide to prevent charge buildup, which could otherwise negatively affect both the spatial and the mass resolution.

An analyte grid pattern is formed by using an electroformed nickel mesh as a stencil on the ITO slide. Two different mesh sizes were used to characterise the magnification and spatial resolution of: Industrial Netting BM0400-49 with a pitch of 63 µm and a wire width of 14.2 µm, and Industrial Netting BM0181-01 with a pitch of 101 µm and a wire width of 38.1 µm. Transmission electron microscopy (TEM) gold grids (Agar Scientific, 50/100 mesh) were also used to demonstrate spatial resolution.

3.6 Experiment Workflow

Figure 3.19 illustrates the complete workflow of data collection and post-processing used in this study. Following secondary ion generation from the sample surface, the ions are accelerated and focused by the ion optics assembly. These ions subsequently strike a microchannel plate (MCP) coupled to a P 47 phosphor screen, which converts the incident ion signal into a burst of photons. This photon output is then detected by a combination of instruments: a photomultiplier tube (PMT), a CCD camera, and a TimePix3 camera. In this work, different detection systems (PMT/CCD, PImMS2 camera and TimePix3-based camera) are employed for distinct purposes, each offering specific advantages in terms of temporal or spatial resolution, depending on the experimental requirements. Consequently, separate post-processing workflows are implemented to accommodate their respective data formats and resolutions.

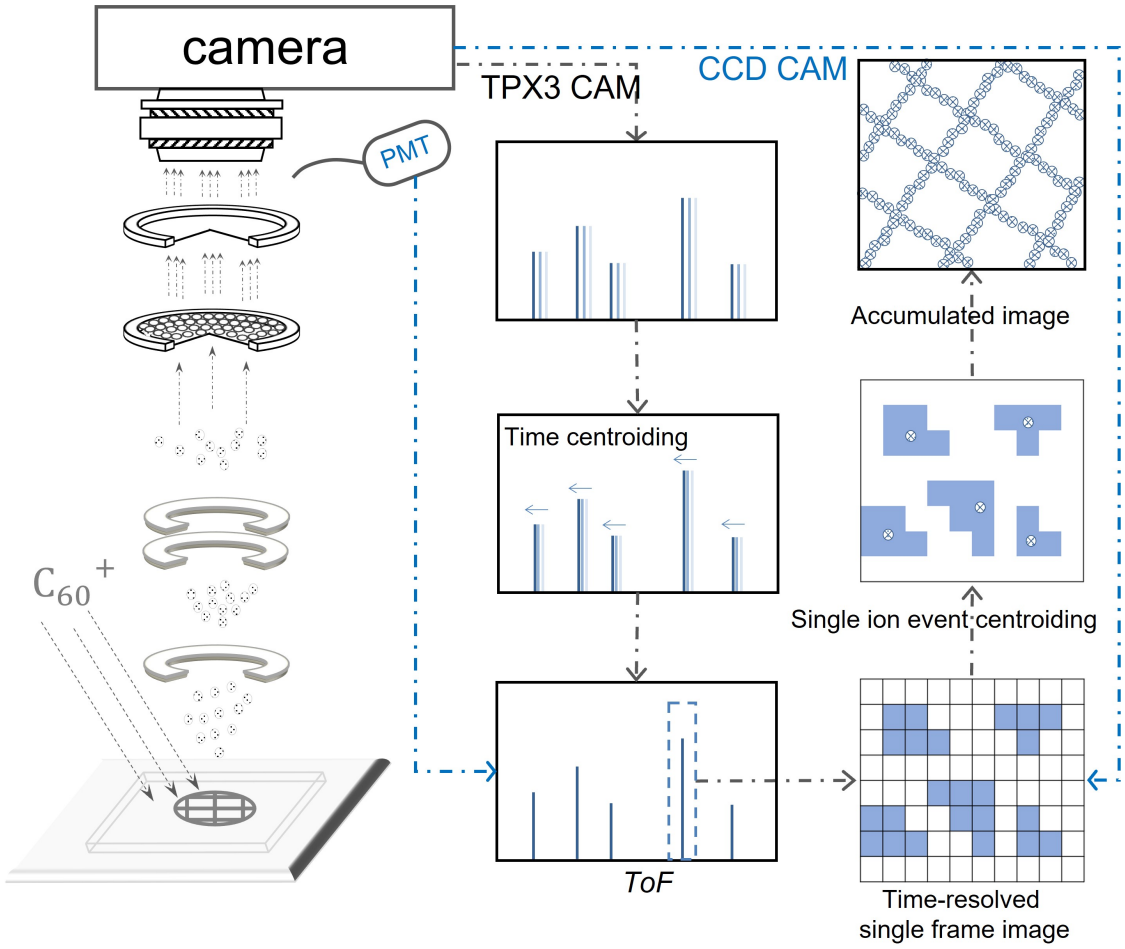


Figure 3.19: Workflow of SIMS data acquisition and processing. The sample is coated onto an ITO slide or Si wafer and bombarded with a C_{60}^+ primary ion beam. Secondary ion clusters are extracted and focused by the ion optics assembly. After travelling through the time-of-flight (ToF) tube, the ions impact the detector assembly. The PMT, CCD camera, and TimePix3-based camera are used to collect time and position-resolved data.

The PMT is directly connected to a high-speed oscilloscope, which converts the photon signals into electronic signals. These signals, recorded over multiple (typically 1000) single-shot acquisition cycles, are averaged to generate high signal-to-noise ratio time-of-flight spectra. This method provides precise timing information and is particularly effective for acquiring high-resolution mass spectra, especially when combined with PEDA. The CCD camera is usually coupled with the photomultiplier tube (PMT) to capture spatial distributions of ions. While the CCD offers spatial imaging capabilities, it lacks intrinsic time-stamping functionality. To address this, a pulse from the delay generator is used to trigger the CCD exposure window. Temporal synchronisation with

the PMT is therefore essential to correlate the spatial information acquired by the CCD with the corresponding time-of-flight (ToF) or mass spectral data obtained via the PMT. In contrast, the PImMS and TimePix3-based camera provides both spatial and temporal information by directly recording the x, y coordinates and the time-of-arrival (ToA) of each detected event. This enables single-ion event detection and is particularly advantageous for multi-mass ion imaging applications. The resulting datasets are processed using centroiding algorithms and range-walk correction techniques to extract accurate ToF values and spatial maps simultaneously. Together, all these detection strategies and processing pipelines enable a flexible approach to generating mass spectra and ion images.

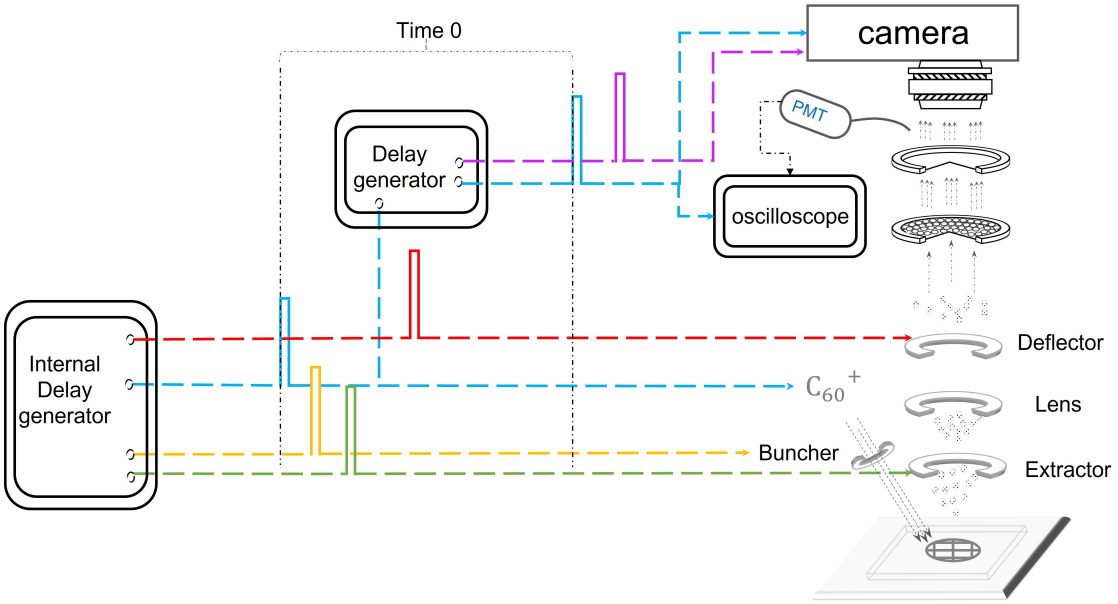


Figure 3.20: Trigger system of the instrument. Time zero (t_0) is defined by the rising edge of the blue pulse. Note that the relative delays between trigger pulses are not shown to scale.

The instrument is equipped with four internal trigger channels, which are used to control: (1) the primary ion (PI) beam; (2) the PI beam buncher; (3) the secondary ion deflector; and (4) the extractor pulse. The pulse used to trigger the PI beam is used to define the start of the experimental time window, referred to as time zero (t_0) of the entire experiment cycles.

To ensure full temporal synchronisation across the system, additional trigger outputs are provided for external devices, such as the oscilloscope and CCD camera. An external delay generator, triggered by the C_{60}^+ beam pulse, is employed to define t_0. Consequently,

the CCD exposure window and oscilloscope acquisition timing are precisely triggered by the external delay generator. Figure 3.20 illustrates this trigger timing scheme, with pulse delays configured according to specific experimental requirements. It should be noted that the delay intervals shown are illustrative and not to scale. This synchronised triggering setup enables reproducible and temporally resolved measurements by coordinating the active components of the beamline and detection system, forming the foundation for time-sensitive imaging mass spectrometry experiments.

3.7 *m/z* Calibration

ToF-MS distinguishes ion species by recording their time-of-flight (ToF); thus, the PMT and TimePix3-based camera data need to be converted from ToF to m/z. The conversion equation is highly dependent on the experimental setup, such as the voltage settings, so calibration must be performed each time the instrument parameters are changed.

In ToF-MS the relationship between m/z and an ion's time-of-flight, t, is given by:

$$t = k\sqrt{m/z} \tag{3.5}$$

Here, k is a linear parameter relating m/z and t, and the function between them can be approximated by a linear equation:

$$y = ax + b \tag{3.6}$$

In this equation, y and x correspond to t and $\sqrt{m/z}$, respectively. The slope a represents the linear relationship between t and $\sqrt{m/z}$, while the intercept b accounts for factors that may shift the entire ToF spectrum, such as the time delay between the C_{60}^+ ion firing and the moment it reaches the sample surface.

In the SIMS system, metallic samples are selected for calibration. The main peaks are identified from the spectra, four of which correspond to metals: Na^+ (23 Da), K^+ (39 Da), Al^+ (27 Da), and Cu^+ (63.5 Da). The first peak is identified as H^+ (1 Da). The approximate location of each peak is determined, after which each ToF peak is assigned

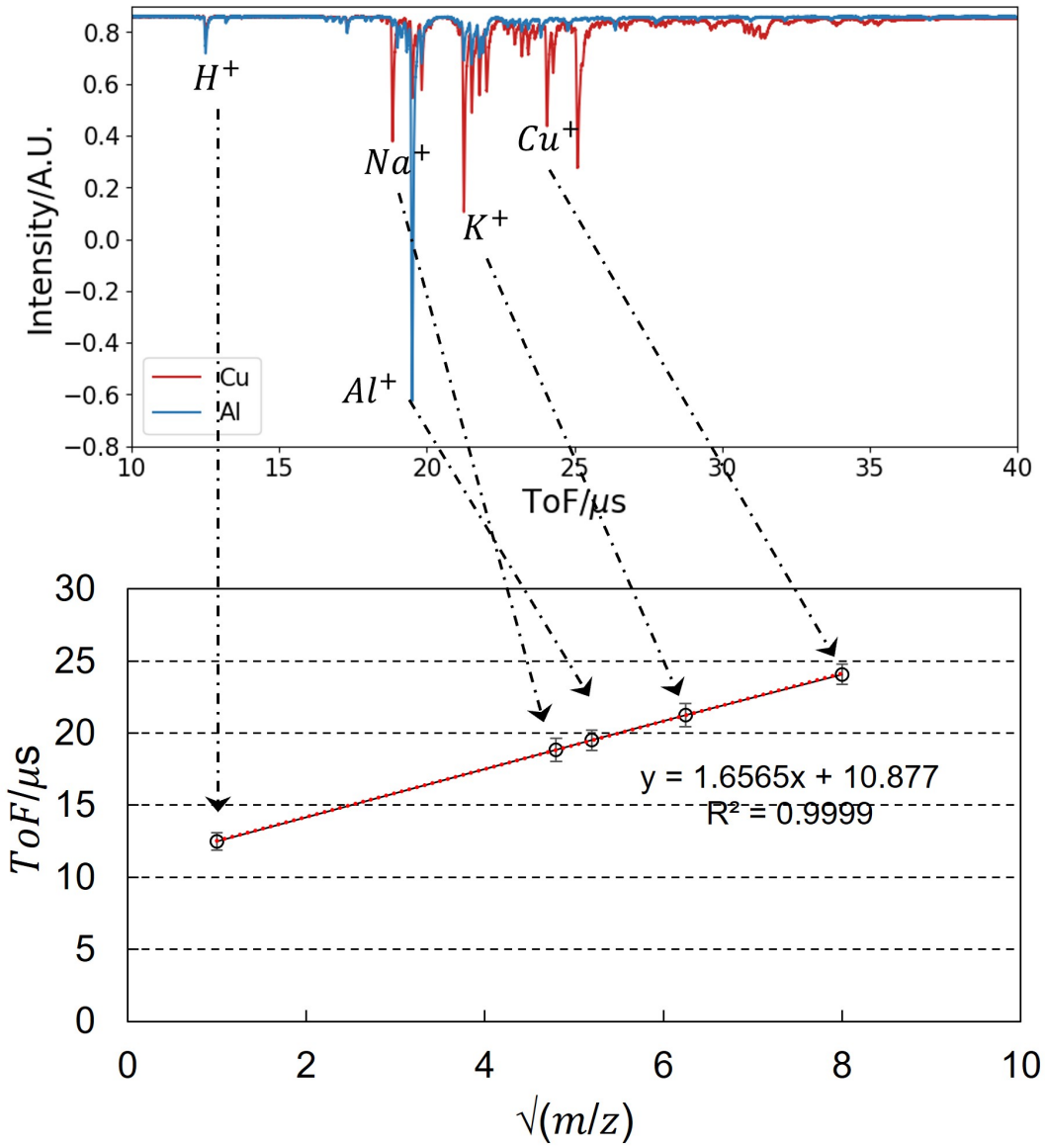


Figure 3.21: Converting a ToF spectrum to a mass spectrum. The top plane shows reference ToF spectra for Cu and Al, with key mass peaks are lablled. The below plane shows the calibration line obtained from known peaks.

to the corresponding expected mass, and a regression line is plotted. The calibration plot is shown in Figure 3.21, while the regression line for the calibration is:

$$y = 1.6565x + 10.877, \quad R^2 = 0.9999 \tag{3.7}$$

This method can be applied to any spectrum obtained under the same experimental conditions to determine the mass of any peak within the calibrated range. However, if applied outside this range, the accuracy cannot be guaranteed, as the relationship

may no longer remain linear.

3.8 Spatial Resolution Definition

Spatial resolution is a critical parameter in mass spectrometry imaging (MSI), as it defines the minimum distance at which two distinct features can be distinguished. In the spatial resolution measurement experiments presented in this thesis, grid-patterned samples are used. The variation in signal intensity across the edges of the grid provides a reliable means of assessing the system's spatial resolution.

Two spatial resolution measurement methods are applied in this study. The conventional approach involves drawing a line profile across a selected region of the image, ideally spanning both the background and a high-intensity feature. The signal intensity along this line is then plotted, and the spatial resolution is determined by analysing the sharpness of the transition. Specifically, the resolution is defined as the distance over which the signal intensity rises from 20% to 80% (or alternatively, from 30% to 90%) of the maximum value [180][181]. This method provides a quantitative measure of edge sharpness and spatial resolving power, as illustrated in Figure 3.22.

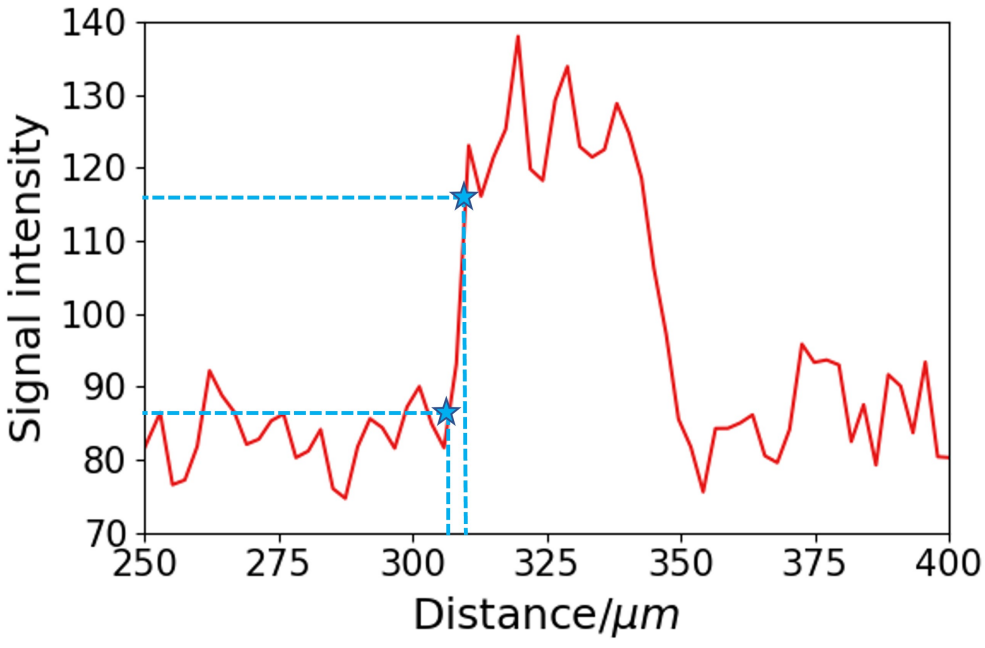


Figure 3.22: Measurement of spatial resolution using the 20%–80% rise distance method. The spatial resolution in this example is determined to be 3.3 µm.

To accurately model the spatial resolution and observed edge response of the imaging system, the signal profile $f(x)$ of an ideal grid feature can be described as a trapezoidal function with a sloped top:

$$f(x) = \begin{cases} 0 & x < a \\ p(x-a)+h & a \le x \le b \\ 0 & x > b \end{cases}$$

where:

- $[a,b]$ defines the spatial extent of the grid feature,
- $p \neq 0$ is the slope of the top (allowing for gradual intensity change),
- h is the height offset or baseline intensity.

To account for the spatial resolution of the system, this idealised signal is convolved with a Gaussian point spread function (PSF), defined as:

$$g(x) = \frac{1}{\sqrt{2\pi}\sigma} \exp\left(-\frac{x^2}{2\sigma^2}\right)$$

The resulting observed signal $y(x)$, which includes both the sample structure and the instrumental blurring, is given by the convolution:

$$y(x) = \int_a^b f(t) \cdot g(x-t)\, dt$$

This integral captures the smoothing effect of the imaging system on the sharp transitions in the grid pattern. By fitting experimental edge profiles with this model, the system's spatial resolution (quantified by the standard deviation σ of the Gaussian) can be accurately estimated, as shown in Figure 3.23. To estimate the spatial resolution, the key parameter is the standard deviation σ of the Gaussian point spread function, as the spatial resolution is defined by the full width at half maximum (FWHM), given by $\text{FWHM} = 2\sqrt{2\ln 2}\,\sigma \approx 2.355\,\sigma$.

In addition to the methods used in this thesis, several other approaches are conventionally employed to define spatial resolution, such as the modulation transfer function (MTF) and the point spread function (PSF).

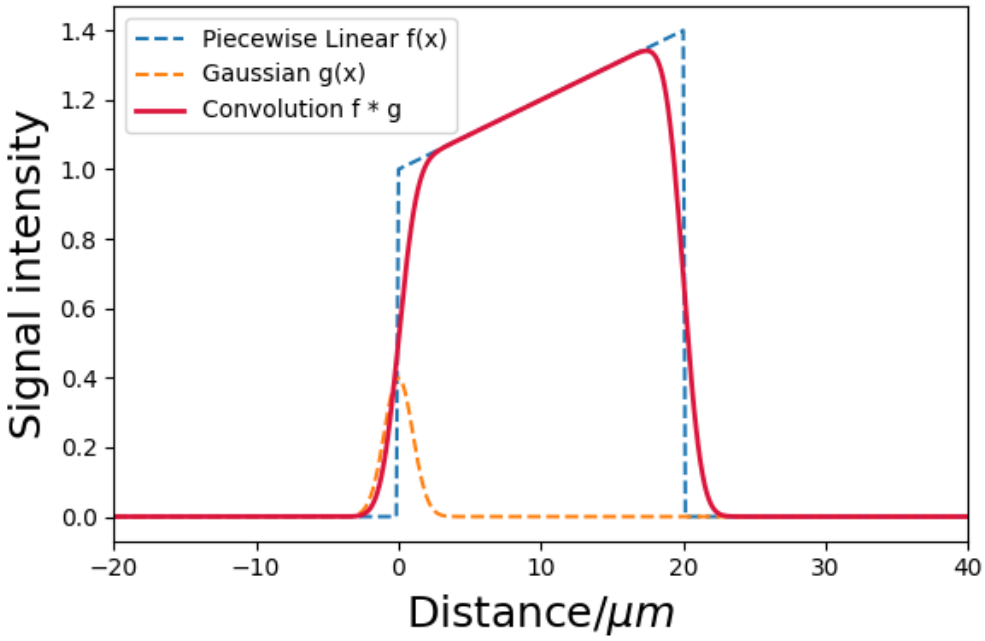


Figure 3.23: The observed signal profile across the grid edge can be modelled as the convolution between a normal distribution $g(x)$, representing the system's point spread function (PSF), and a piecewise linear function $f(x)$ that reflects the idealised structure of the grid pattern. This approach captures both the intrinsic resolution limit of the system and the geometric characteristics of the sample.

The modulation transfer function (MTF) is commonly used to evaluate the performance of optical systems. Spatial resolution describes an imaging system's ability to distinguish fine structural details. It is often characterised using line pairs, which consist of alternating black and white lines. The number of line pairs per millimetre (lp/mm) defines the spatial frequency, and the inverse of this frequency corresponds to the spacing (in millimetres) between two resolved lines. High-resolution images exhibit a large amount of fine detail due to minimal blurring, as shown in Figure 3.24(a). Conversely, low-resolution images lack fine detail, as illustrated in Figure 3.24(c).

The object resolution is calculated from the camera resolution and the primary magnification (PMAG) of the imaging lens (see equations below). It is important to note that these equations assume that the imaging lens introduces no additional resolution loss.

$$\text{Object Resolution } (\mu\text{m}) = \frac{\text{Camera Resolution } (\mu\text{m})}{\text{PMAG}}$$

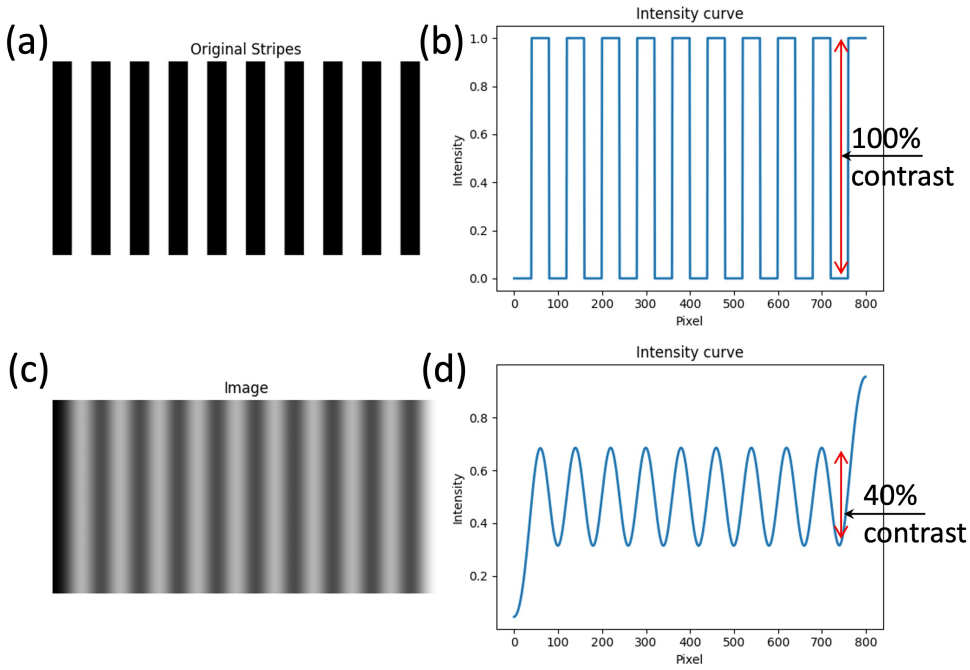


Figure 3.24: (a) and (c) present the original black strips image (with 100% contrast) and blurry image (with 40% contrast) respectively. (b) and (d) are the image intensity curve plot of (a) and (c).

$$\text{Object Resolution (lp/mm)} = \text{Camera Resolution (lp/mm)} \times \text{PMAG}$$

Another important parameter for evaluating image quality is the contrast:

$$\%\text{Contrast} = \frac{I_{\max} - I_{\min}}{I_{\max} + I_{\min}},$$

where I represents the image intensity. Contrast describes how faithfully the maximum and minimum intensity values are transferred from the object plane to the image plane. Figure 3.24(b) and (d) present image contrasts of 100% and 40%, respectively, illustrating that as the spatial frequency of the line pairs increases, the image contrast decreases. This behaviour is inherent to imaging systems with finite resolution. For an image to appear well defined, black regions must remain truly black and white regions truly white, with minimal intermediate grayscale.

Another method for evaluating image quality is the point spread function (PSF). The PSF describes the response of a focused optical imaging system to an idealised point source of light. In simple terms, for a given camera, it corresponds to the blurred spot

obtained when imaging a single point source. The extent of spreading (blurring) in the image of a point object provides a quantitative measure of the imaging system's performance. In incoherent imaging systems, image formation is linear in intensity and can be described using linear systems theory. Consequently, when two objects, A and B, are imaged simultaneously in an incoherent system, the resulting image is equal to the sum of the images that would be obtained from each object independently.

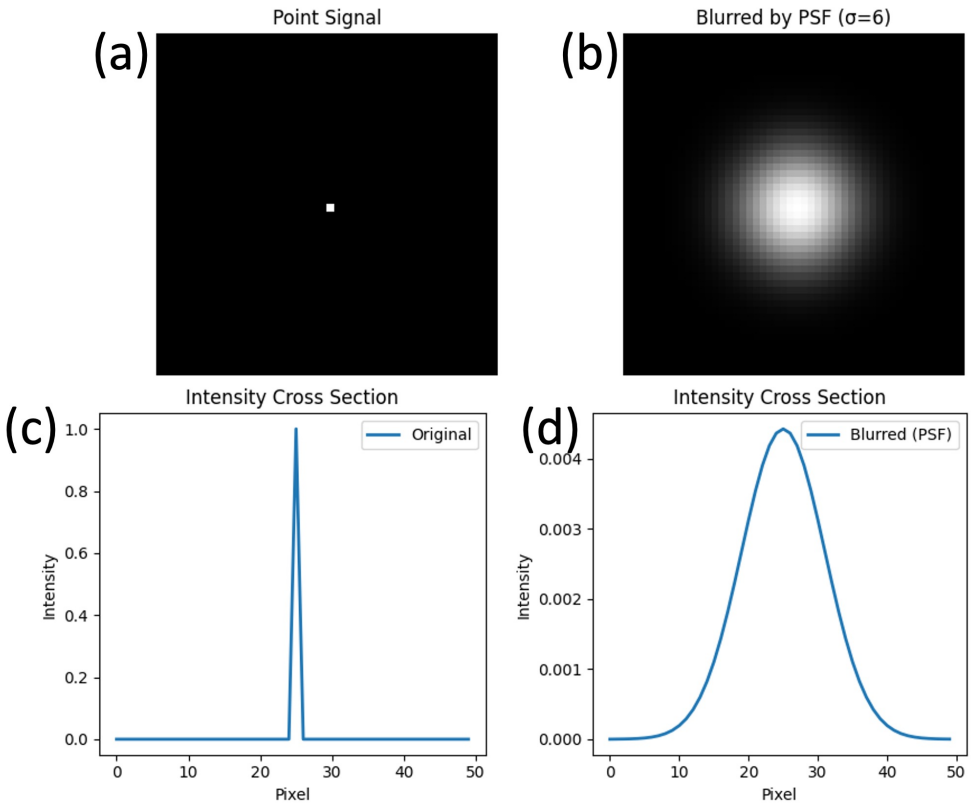


Figure 3.25: (a) and (c) present the original single point signal and blurred image with PSF respectively. (b) and (d) are the image intensity curve plot of (a) and (c).

As shown in Figure 3.25(c) and (d), line profiles (cross-sections) taken through the centre of the imaged point source are analysed. The spatial resolution is determined from the PSF by imaging a sub-resolution point source and measuring the full width at half maximum (FWHM) of its intensity profile. A narrower FWHM corresponds to higher spatial resolution.

3.9 Summary and aims

This chapter has detailed the individual components of the complex microscope-mode SIMS imaging system, outlining the experimental setup and data processing workflow. The system was described following the trajectory of the ions: beginning with the primary ion gun, continuing through the ion optics assembly, and culminating at the detector system. Subsequently, the procedures for data acquisition and processing were presented, including a discussion of the synchronised control system that ensures temporal coordination across the instrument. The chapter concluded with an overview of the calibration strategies employed to convert time-of-flight (ToF) data into mass spectra, alongside an examination of potential sources of mass measurement error.

The main results of this thesis are presented in Chapters 4, 5, and 6. Each chapter addresses distinct research aims.

The aim of Chapter 4 is to investigate the feasibility of direct multi-mass three-dimensional (3D) velocity map imaging (VMI) from surfaces and to develop a method for accurately calibrating the full 3D velocity distribution. The velocities of selected organic ions, such as Auramine O, are measured and subsequently used as input parameters for the SIMION modelling presented in Chapter 5.

The aim of Chapter 5 is to optimise the instrument's performance limits, including mass resolution, spatial resolution, and accessible mass range, with the goal of establishing it as one of the fastest microscope-mode MSI instruments. The optimised system is then applied to practical studies, with tissue imaging selected as the first demonstration.

The aim of Chapter 6 is to explore the feasibility of depth profiling and the instrument's potential for three-dimensional (3D) imaging. In addition, dedicated software is developed to automatically process and analyse the complex frame-based data.

4

Three Dimensional Mass Spectrometry-Velocity Map Imaging

This chapter presents a surface-scattering study employing a multi-mass, three-dimensional velocity map imaging (VMI) technique using the instrumentation described in the previous chapters. The sample is mounted on the repeller plate of the ion optical system and secondary ions are extracted and detected along the surface normal. By recording both the positions and arrival times of ions at the detector using a fast imaging camera, the half-Newton spheres of multiple ions can be directly measured, allowing determination of the complete three-dimensional velocity distributions of the species of interest. This approach is applied to investigate the sputtering and ionisation processes occurring in secondary ion mass spectrometry (SIMS) experiments following impact by a kilo-electron-volt C_{60}^{+} primary ion beam. The resulting three-dimensional velocity distributions of secondary ions provide detailed insight into the mechanisms of ion formation and ejection. The methodology developed here is broadly applicable to a wide range of surface dynamical studies in which ions are generated or extracted in a pulsed manner, enabling precise time-of-flight (ToF) detection and analysis. This chapter is based on the work reported in the paper *'Multi-mass three-dimensional velocity map imaging from surfaces'* [182].

4.1 Introduction

Velocity map [133] ion imaging [183] (VMI) is a well-established technique for determining the velocity distribution of ions generated by laser-introduced methods in the gas phase. The method has been applied widely, particularly to study molecular photodissociation and inelastic and reactive scattering [184]. Ion detection in VMI generally employs multichannel plates (MCPs) coupled with a phosphor screen and CCD camera. A variety of constraints on the latter means that VMI is most commonly used in a crushed or projected imaging mode in which the component of the ion velocity along the time-of-flight (ToF) axis is unresolved [185]. To obtain more precise measurements with higher velocity resolution, slice ion imaging methods have been developed [134, 186, 187], in which the ion Newton sphere is expanded along the ToF direction to enable a central slice to be obtained, for example, by pulsing the MCP detector or the intensified CCD camera employed, as described in the Chapter 1. In principle, slice imaging ion optics allow for the recording of the full three-dimensional (3D) Newton sphere of ions, provided the data rate and timing precision of the detector are sufficiently fast. For that reason, 3D VMI usually requires MCPs to be coupled with phosphor screens and fast CMOS-based detectors, such as the PImMS [115, 135, 188, 189] and TimePix-based cameras [116, 176, 190–193], with delay line detectors [194, 195], or using fast MCP readout [196]. Pulsed extraction methods can also be employed, for example, post-extraction inversion slice imaging, to stretch the ion clouds still further, thereby increasing the number of slices achieved with moderate timing requirements [192, 197].

In the last decade, VMI has shifted focus from gas-phase measurements to surface (photo-)reactions [138, 139, 172, 198–201] and surface scattering [138–142]. Because of the limited time resolution of conventional VMI detection systems, such measurements typically involve ion extraction in a direction parallel to the plane of the surface [140, 141], so that the scattering angle from the surface normal can be more readily determined. In the present work, we show how 3D VMI allows the extraction of multiple ions along the surface normal using a simple ion optical arrangement in which the sample is directly mounted on the repeller plate of the instrument. Whilst some previous studies, particularly

in surface photochemistry, have employed a similar geometry [172, 200–203], namely ion extraction along the surface normal, full three-dimensional velocity information has either been inaccessible due to insufficient detector time resolution [172] or has been inferred indirectly from the ion signal as a function of the time delay between surface photoexcitation and subsequent ionisation by a probe laser, analogous to slice imaging [200–203]. By contrast, the multi-mass three-dimensional VMI approach employed here allows the half-Newton spheres of ions to be measured directly at the detector. This provides a significant advantage in studies where it is desirable to interrogate multiple ionic species of different masses simultaneously, as exemplified in the present work.

The present work shows how 3D VMI allows the extraction of multiple ions along the surface normal using a simple ion optical arrangement in which the sample is directly mounted on the repeller plate of the instrument. In these proof-of-principle experiments, a sample comprising a thin film of organic dye is used and electrosprayed onto an indium tin oxide (ITO) cover slide, as previously employed in imaging mass spectrometry measurements [105, 106, 120, 158]. A modified secondary ion mass spectrometry (SIMS) instrument [158], coupled with 3D VMI using a TimePix3-based camera [116], is employed to record 3D velocity distributions of multiple metallic and organic secondary ions generated at a surface following sputtering with a kilo-electron-volt (keV) C_{60}^+ primary ion beam.

4.2 Experimental Methods

The experimental arrangement is shown schematically in Fig. 4.1(a) and (b). The mass spectrometer utilised is the same as outlined above but with modified ion optical settings to enable VMI instead of microscope mode imaging MS [158]. In these experiments, a 20 keV or 40 keV C_{60}^+ primary ion beam was employed, incident on the sample surface at an angle of 40° relative to the surface normal. A simplified ion optical configuration was used, consisting of a repeller plate (on which the specimen was mounted), an extractor, and an ion lens assembly. This arrangement enabled the mapping of secondary ions in either spatial or velocity mapping modes, as illustrated in Fig. 1(b). Switching between

spatial and velocity mapping conditions was achieved by tuning the relative voltage ratios applied to the repeller, extractor, and lens electrodes.

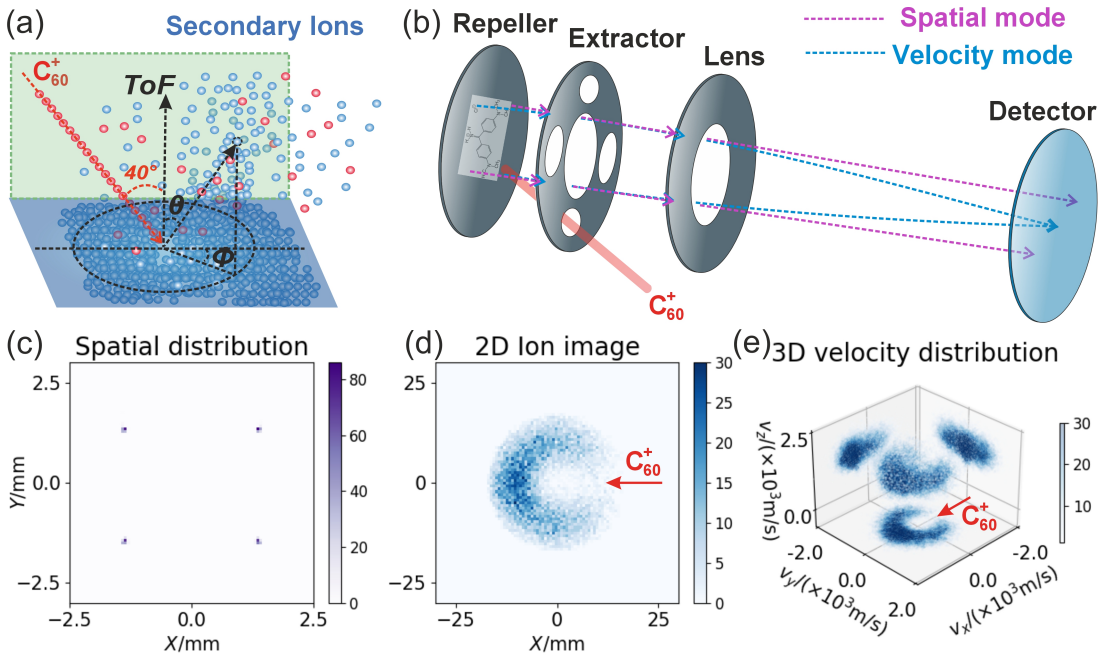


Figure 4.1: (a) Collisional process in SIMS: a 20 or 40 keV C_{60}^+ ion beam is used as the primary ion source. Upon bombardment of the target surface, the sample's chemical components undergo fragmentation and ionization. (b) After ionization, the secondary ions are extracted, accelerated, and focused using a conventional VMI ion-optical lens assembly. By adjusting the electrode voltages, the ion image can be switched between spatial mapping mode (purple dashed line) and velocity mapping mode (blue dashed line). (c) Simulated spatial ion image showing four focused spots on the detector, corresponding to the spatially mapped initial ion positions. (d) Simulated 'crushed' 2D velocity map image showing detector events that reflect the initial velocity distribution of the ions. (e) Simulated 3D velocity map image showing ion velocity distributions. The ions have an assumed mass of 269 Da with kinetic energies ranging from 0 to 1.2 eV.

The detector system (Photonis 39042PS-P 47) comprised two 40 mm imaging-quality Chevron microchannel plates (MCPs), followed by a fibre-optically coupled P 47 phosphor screen mounted on a 6-inch vacuum flange. The MCP assembly was operated with the front face of the first plate biased at -840 V, while the back of the first plate was electrically connected to the front of the second plate (held at ground potential). The back face of the second plate was set to +840 V. The coupled phosphor screen was maintained at a potential between 4.0 kV and 4.6 kV to ensure efficient electron-to-photon conversion. The resulting optical emission was subsequently detected and recorded for analysis using one of three detection systems: an intensified CCD camera, a TimePix3-based

camera [116], or a photomultiplier tube (PMT).

For velocity map imaging (VMI) experiments, data acquisition was performed using the TimePix3-based detector at a C_{60}^+ repetition rate of 100 Hz over a duration of approximately 15 minutes. The primary ion beam current was maintained in the range of 850–900 pA. Under these conditions, it is estimated that approximately 550 C_{60}^+ ions impinge on the sample surface during each ion-gun pulse. At a primary beam energy of 20 keV, this resulted in the detection of roughly 100 secondary ions per pulse, increasing to around 300 ions per pulse at 40 keV.

Samples of different laser dyes, specifically Rhodamine 640 and Auramine O, were deposited via electrospray using a custom-built electrosprayer. The substrates comprised standard indium tin oxide (ITO)-coated cover slips, which were mounted directly onto the repeller plate of the ion optical system (Fig. 4.1(b)). In addition, electrosprayed samples were deposited onto a nickel mesh; the resulting square ion image pattern, observed under spatial mapping mode, was employed to calibrate the ion image magnification and alignment.

Atomic force microscopy (AFM) measurements, supported by calculations based on the electrospray flow rate and solution concentration, indicated that the dye layers had a thickness of approximately 90 nm ($\pm$30 nm), as shown in Figure 4.2. For the three-dimensional velocity map imaging (3D VMI) experiments, the Auramine O mass peak at 269 m/z was selected, together with the Na^+ and K^+ ion signals. Additional calibration data also employed the Rhodamine 640 mass peak at 491 m/z.

The 3D VMI technique employed in this work is illustrated schematically in Figure 4.1. Following sputtering of the sample with the C_{60}^+ primary ion beam (Figure 4.1(a)), secondary ions were extracted along the surface normal using a simple ion-optical arrangement (Figure 4.1(b)). By adjusting the voltage ratios between the repeller, extractor, and lens, ion trajectories could be focused either according to their spatial origin on the surface (Figure 4.1(c)) or according to their initial velocity at the moment of emission (Figure 4.1(d) and (e)). The ability to switch readily between spatial and velocity mapping of the secondary ions generated at the surface, in principle on alternate primary beam pulses and in a multi-mass fashion, provides a powerful means of characterising

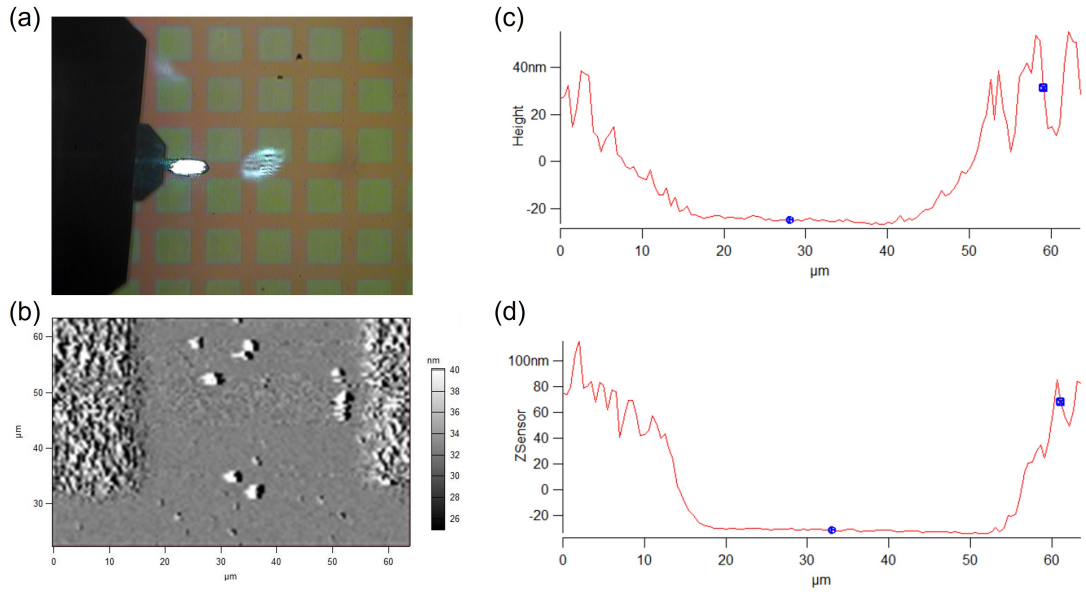


Figure 4.2: (a) presents the optical image of the Auramine O grid sample acquired using AFM, while (b) shows the corresponding AFM topographical scan, where brighter contrast corresponds to greater surface height. Panels (c) and (d) display the height profiles across selected regions of the scanned area, with measured thicknesses of 56.14 µm and 99.94 µm, respectively.

the dynamics within specific regions of the surface. Notably, the primary ion beam can be deliberately focused or defocused on alternate pulses: a defocused beam may be employed in spatial mapping mode to survey a wider area and identify regions of interest, whilst a focused beam can subsequently be applied in velocity map imaging mode to probe those regions with high spatial precision. In this way, spatial mapping serves to locate areas of significance, after which velocity map imaging can yield detailed three-dimensional velocity distributions of the secondary ions emitted from precisely those regions. Such an approach offers a highly versatile platform for investigating localised surface dynamics in a site-specific manner.

In the spatial map image, the signal reflects the molecular positions on the surface, appearing as four distinct circular spots. In contrast, in velocity map imaging (VMI) mode, the detector response is relatively insensitive to the initial spatial position of the molecule, but is instead governed by its initial velocity. Consequently, ions originating from different spatial positions but sharing identical velocities are focused onto the same detector location. Additional simulations using the Simion model outlined in chapter 2, assuming ion generation within a 100 µm region on the surface (consistent with

experimental conditions), indicate that ions are velocity-mapped onto the detector with a resolution ultimately limited by the pixel count of the camera.

To obtain accurate three-dimensional velocity distributions, high temporal precision in ion detection is required to ensure that the velocity components along the x, y, and z axes are sampled as uniformly as possible. In this work, the sample surface is defined as lying in the xy plane, with the time-of-flight (ToF) axis taken as the z direction. Ions were detected using a standard dual-MCP/P 47 imaging detector, coupled either to a conventional CCD camera or to a TimePix3-based camera [116]. The TimePix3 detector records ion impact positions with a ToF timing precision of 1.56 ns, corresponding to approximately 60 discrete time slices for every 100 ns interval of the ToF spectrum. For the organic ion at 269 m/z (see below), the total width of the ToF peak was approximately 180 ns, with a full width at half maximum (FWHM) of $\sim$75 ns. The number of available time bins, which is directly related to the resolution of the velocity component along the z-axis, may be compared with the number of pixels in the TimePix3 detector array. The array consists of 256×256 pixels, of which at most 128 are used to characterise the image radius, corresponding to the speed component along a chosen axis in the xy plane.

The TimePix3-based camera provides ToF data in the form (x_i, y_i, t_i), where (x_i, y_i) are the detector plane coordinates (pixel numbers), and t_i is the arrival time (timestamp) of ion i. For each detected ion, these data must be transformed into $(v_{x,i}, v_{y,i}, v_{z,i})$, where the z axis is defined as the ToF axis and the $+x$ axis corresponds to the direction of the C_{60}^{+} primary beam. In most VMI experiments, velocity calibration is performed by photodissociation of a gas-phase molecule that produces fragments with a well-characterized velocity distribution. In the present work, however, we adopted an alternative approach: combining ion-trajectory simulations with calibration against experimental spatial mapping and time-focusing measurements.

4.3 Velocity Focus

In conventional gas-phase experiments, velocity focusing and calibration in velocity map imaging (VMI) are readily achieved through the photodissociation of molecules, which generates fragments with well-defined and predictable velocities. In principle, the same

approach could be applied to the present experiments. However, such a calibration method was not feasible with the instrument employed in this study. Consequently, alternative strategies were developed, based on a combination of ion-trajectory simulations using SIMION [153] and carefully designed calibration experiments. These methods allowed us to establish the appropriate mapping conditions and velocity calibration without relying on molecular photodissociation processes.

Unlike velocity calibration in VMI, determining the spatial focus and calibration within the secondary ion mass spectrometry (SIMS) instrument is relatively straightforward. This was accomplished by systematically adjusting the ratio of the extractor to repeller voltages until a sharp and well-resolved image of a calibration grid, of known pitch, was obtained, as illustrated in Figure 4.3. The resulting spatial calibration provided a direct means of validating the experimental imaging conditions. Furthermore, the optimised experimental voltage settings were found to be in excellent agreement with the outcomes of ion trajectory simulations, thereby reinforcing confidence in the reliability of the simulations as a guide for the surface VMI experiments. This agreement also highlights the robustness of the experimental methodology, ensuring that the calibration procedure is both reproducible and transferable across different measurement conditions.

In the simulations, the spatial focus was quantified in terms of the spatial resolution, with a smaller value corresponding to a better focus. To determine the spatial resolution, three groups of ions are initialised at distinct positions on the repeller, each separated by a distance d_1. When these ions reach the detector, their final positions are recorded, yielding a new separation distance d_2. The ratio, $M = d_2/d_1$, defines the magnification of the instrument. Each ion group forms a spot on the detector with a spatial spread characterised by a standard deviation, from which the full width at half maximum (FWHM) of the signal intensity can be calculated. The spatial resolution is then obtained as the ratio of the FWHM of the detector spot to the magnification, Resolution $=$ FWHM$/M$. The dependence of the spatial resolution on the voltage ratios between the extractor and repeller (V_E/V_R) and between the lens and repeller (V_L/V_R) is shown in Figure 4.3(a). The darkest blue regions correspond to the optimum performance, indicating a spatial

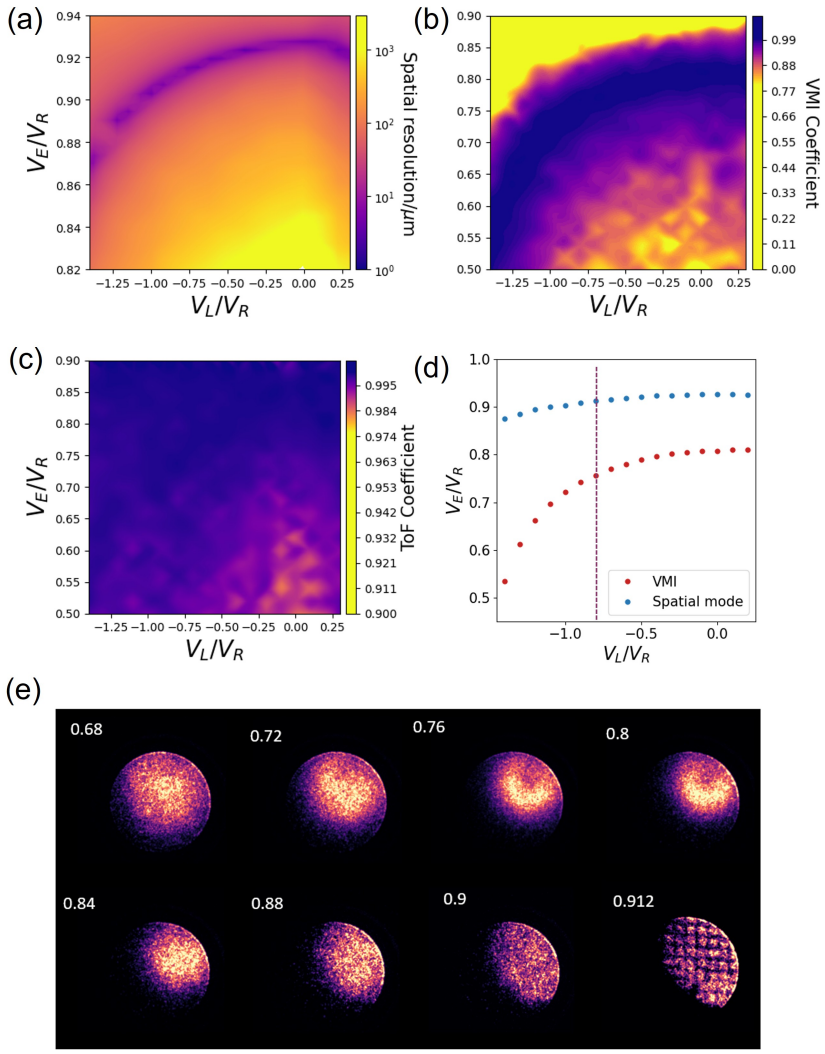


Figure 4.3: Simulation results demonstrating the optimisation of the lens/repeller (V_L/V_R) and extractor/repeller (V_E/V_R) voltage ratios. In panels (a) and (b), darker blue regions indicate improved performance in terms of (a) spatial resolution, (b) velocity mapping and (c) ToF coefficient, as quantified by the Pearson correlation coefficient, ρ_x. (Note that non-linear colour scales are employed in both panels to highlight regions of optimal performance.) Panel (d) compares the optimised V_E/V_R ratios for spatial mapping (blue data points) and velocity mapping (red data points), underscoring the distinct operating conditions required for each mode. Panel (e) presents experimental ion images of a Rhodamine 640 sample acquired at a repeller voltage of 10 kV and a lens voltage of -8 kV, with the extractor-to-repeller ratio systematically varied. The extractor-to-repeller ratio is given at the top of each image in the panel. Under these conditions, a defocused C_{60}^+ beam produces a spatial image of the calibration grid pattern at a ratio of 0.912. The simulations predict an optimum velocity-focusing ratio of 0.76, in excellent agreement with the experimental ion images, thereby validating the predictive accuracy of the ion-trajectory simulations.

resolution below 5 μm. The voltage ratios associated with the optimum spatial resolution are plotted as blue data points in Figure 4.3(d).

The velocity focus in the simulations was quantified using Pearson correlation coefficients, ρ_{ToF} and $\rho_{x/y}$. Here, the surface normal is defined along the ToF direction (the z-axis), with the surface lying in the (x,y) plane. The coefficient ρ_{ToF} refers to the correlation between the measured time-of-flight (t_{ToF}) and the corresponding velocity component along the ToF axis (v_{ToF}). It is defined as:

$$\rho_{\mathrm{ToF}} = \frac{\mathrm{cov}(t_{\mathrm{ToF}}, v_{\mathrm{ToF}})}{\sigma_{t_{\mathrm{ToF}}}\,\sigma_{v_{\mathrm{ToF}}}}, \tag{4.1}$$

where $\mathrm{cov}(\cdot)$ denotes the covariance between t_{ToF} and v_{ToF}, while $\sigma_{t_{\mathrm{ToF}}}$ and $\sigma_{v_{\mathrm{ToF}}}$ represent their respective standard deviations. Similarly, the velocity focus along the x-axis in the detector plane was quantified using the Pearson correlation coefficient, ρ_x, defined as

$$\rho_x = \frac{\mathrm{cov}(x, v_x)}{\sigma_x\,\sigma_{v_x}}, \tag{4.2}$$

where σ_x and σ_{v_x} represent the standard deviations of the detector coordinate x and the corresponding velocity component v_x, respectively. An analogous definition applies for the y coordinate in the image plane. To achieve optimal velocity focusing, both ρ_{ToF} and $\rho_{x/y}$ should be considered. However, in practice, the ρ_{ToF} coefficient is found to exhibit a considerably larger tolerance than $\rho_{x/y}$. Simulations in Figure 4.3(c) also demonstrate this, showing that most voltage settings yield a coefficient greater than 0.995. This behaviour indicates that velocity focusing along the ToF axis is inherently more readily achieved than in the detector plane.

A Pearson correlation coefficient close to +1 or -1 indicates a strong linear relationship, whereas values near 0 imply only a weak correlation. Since the detector coordinate (x or y) and the corresponding velocity component (v_x or v_y) are directly related under velocity mapping conditions, the quality of the mapping is best when ρ_x or ρ_y approaches +1. This behaviour is clearly illustrated by the blue stripe in Figure 4.3(b), which highlights the region of optimal velocity correlation. For each lens/repeller voltage ratio ($V_{\mathrm{L}}/V_{\mathrm{R}}$), the corresponding optimal extractor/repeller voltage ratio ($V_{\mathrm{E}}/V_{\mathrm{R}}$) is shown in Figure 4.3(d). The comparison of the optimal ratios for spatial mapping (blue data points) and velocity mapping (red data points) demonstrates the distinct operating regimes required for the two modes. These data provide a practical guide when it comes to the experimental setup.

Simulations were conducted to quantify the image spatial resolution and velocity resolution under the spatial/VMI imaging mode. For instance, in the simulation the repeller voltage was fixed at 10 kV, while the lens-to-repeller voltage ratio (V_L/V_R) was set to -0.8 in order to obtain a reasonable magnification. A distribution of 269 Da ions was generated with an initial spatial separation of 50 µm, a single velocity of 1000 m/s, and a cone-shaped angular distribution of 30°.

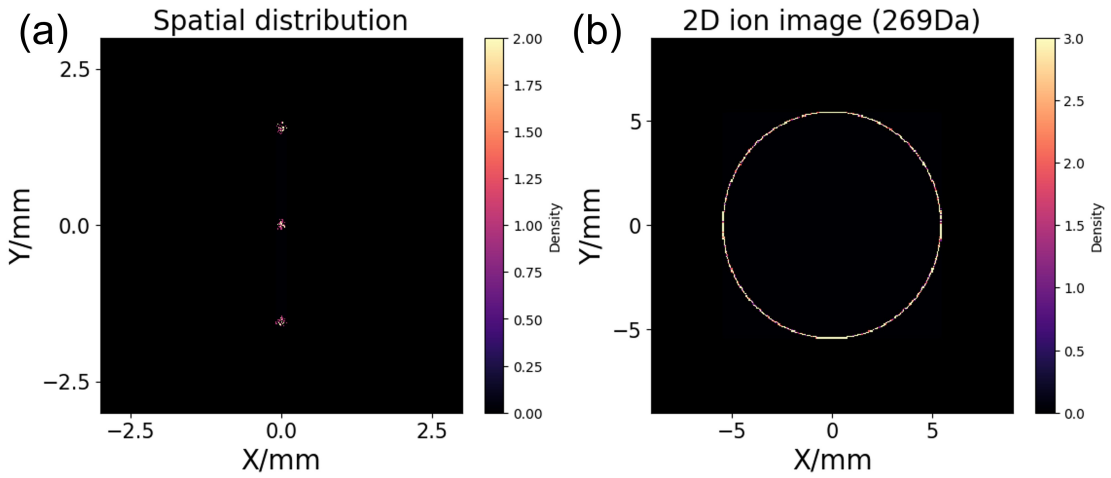


Figure 4.4: SIMION simulation of 269 Da ion distributions under different extraction conditions. Panel (a) shows the spatial image on the detector, which reflects the initial positions of the ions. Panel (b) shows the corresponding velocity-mapped image, in which the distribution is determined by the ions' initial velocities. The transition between these two imaging modes is achieved by tuning the extractor-to-repeller voltage ratio (V_E/V_R).

In velocity mapping mode, the extractor-to-repeller ratio was adjusted to $V_E/V_R = 0.76$, whereas in spatial mapping mode it was tuned to $V_E/V_R = 0.912$. As illustrated in Figure 4.4, the adjustment of this voltage ratio enables the ion image to be switched from spatial mode (a), where the image reflects the initial positions of the ions, to velocity mode (b), where the image reflects their velocity distribution. This tunability provides a direct and practical means of correlating spatial and velocity information, which is essential for calibrating velocity-map imaging in systems where a conventional molecular beam reference is not available.

It is worth emphasising that the mass spectrometry velocity map imaging (MS-VMI) technique is broadly applicable to multiple ion species. Under optimised VMI voltage

conditions, ions of different masses were tested through trajectory simulations. Specifically, ions of 500, 269, 150, and 23 Da were each assigned an identical initial kinetic energy corresponding to a speed of 1000 m/s with a 30 ° conical angular distribution. The resulting ion images are presented in Figure 4.5 (a)-(d). It should be noted that these images have not been transformed into velocity space, in order to illustrate the relative signal intensities of different masses on the detector. In all cases, the ions are successfully mapped into well-focused circular patterns, demonstrating the mass-independent focusing capability of the VMI configuration.

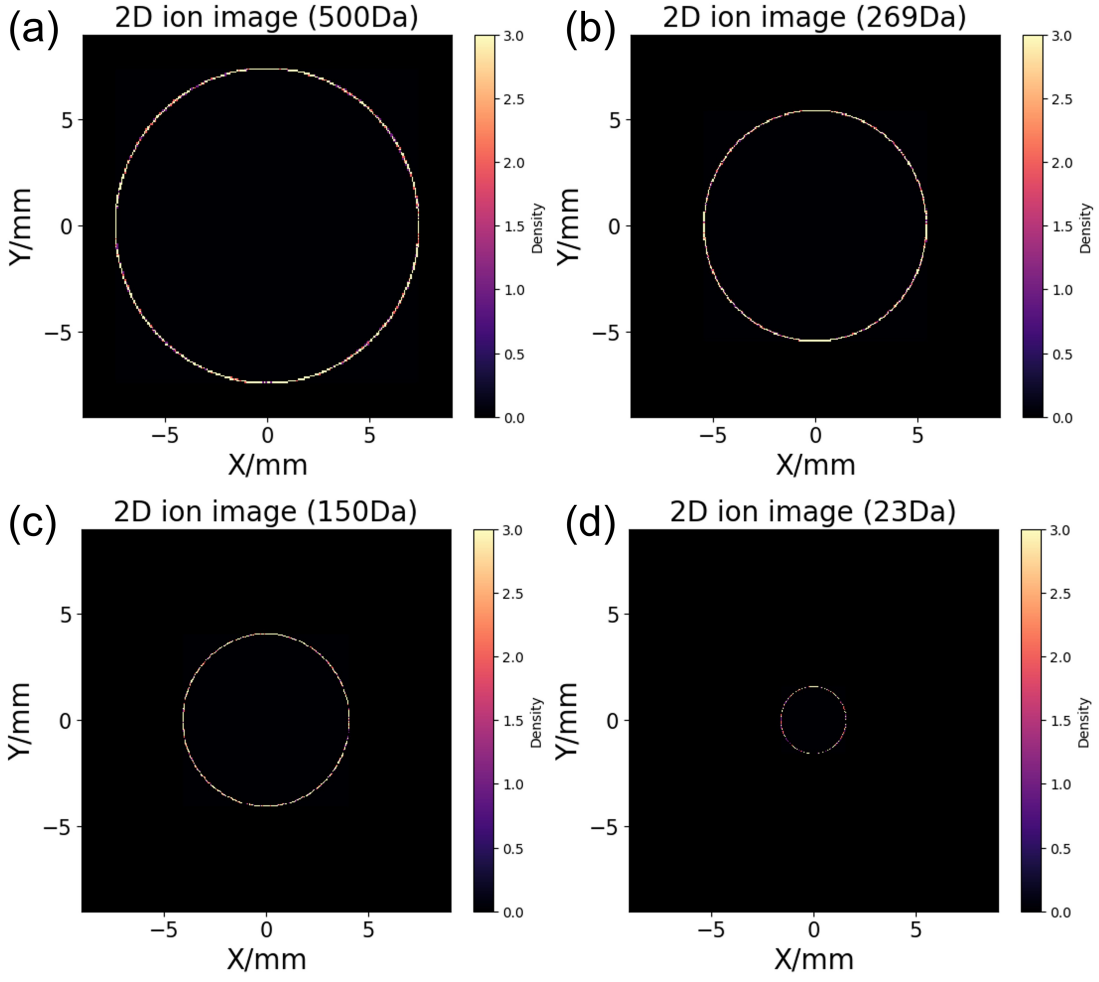


Figure 4.5: Simulated velocity map images of ions with different masses under identical VMI conditions. Panels (a)–(d) correspond to 500, 269, 150, and 23 Da ions, respectively. All distributions are obtained assuming a single velocity of 1000 m/s and a 30 ° conical angular spread. The circular distributions highlight the ability of VMI to focus ions of different masses into well-defined images.

An alternative way to verify the imaging quality is calculating the velocity resolution.

Analogous to the spatial resolution that characterises the quality of spatial imaging, the performance of velocity map imaging can be quantitatively assessed through its velocity resolution. The velocity resolution is defined as the ratio of the mean velocity to the spread of the velocity distribution, and can be expressed as:

$$\frac{v}{\Delta v} = \frac{\bar{v}}{\mathrm{FWHM}} = \frac{\bar{v}}{2\sqrt{2\ln 2}\cdot\sigma_{\mathrm{v}}} \approx \frac{\bar{v}}{2.35\,\sigma_{\mathrm{v}}}, \tag{4.3}$$

where $\bar{v}$ denotes the mean ion velocity, σ_{v} represents the standard deviation of the velocity distribution, and FWHM is the full width at half maximum of the corresponding Gaussian distribution. This formulation allows direct comparison between experimental and simulated velocity distributions, thereby providing a robust metric for evaluating the focusing performance of the VMI configuration.

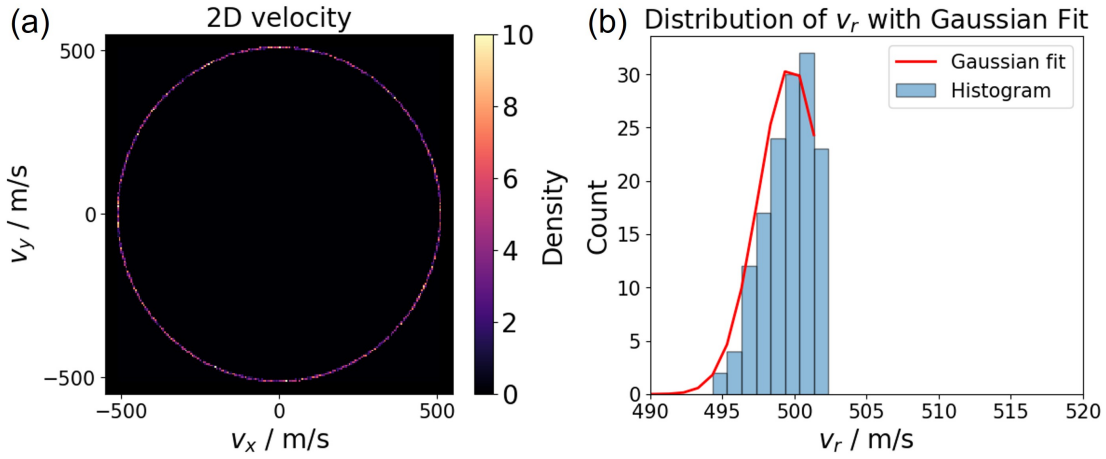


Figure 4.6: (a) Calibrated 2D velocity map image (VMI) for ions with a single speed of 1000 m/s and a 30 ° cone distribution. (b) Corresponding v_r velocity distribution within the amplified region.

v_r is the radial velocity on the detector panel, and its distribution within the selected velocity region is shown in Figure 4.6 (d). The distribution was fitted with a Gaussian function, yielding a standard deviation of $\sigma = 2.29$ m/s and a full width at half maximum (FWHM) of 5.392 m/s. Accordingly, the velocity resolution is calculated as

$$\frac{\Delta v}{v} = \frac{\mathrm{FWHM}}{\bar{v}} = \frac{5.392}{500} \approx 1.078\%.$$

In the experimental configuration, to achieve velocity focus in the image plane, a defocused 40 keV C_{60}^{+} primary ion beam was employed to bombard a meshed grid (pitch

140 μm) electrosprayed with a laser dye of Rhodamine 640. The repeller voltage was maintained at 10 kV, while the V_L/V_R ratio was fixed at -0.8 to provide an appropriate magnification; this setting is indicated by the dashed vertical line in Figure 4.3(c). As the V_E/V_R ratio was varied from approximately 0.6 to 0.95, the spatial mapping condition was clearly observed at $V_E/V_R = 0.912$, where a well-resolved grid pattern is detected, in agreement with the predictions from the ion trajectory simulations in Figure 4.3(c). Upon decreasing V_E/V_R, the image progressively blurs, eventually forming a half-ring pattern at $V_E/V_R = 0.76$, which corresponds closely to the velocity focus ratio of 0.758 suggested by the simulations. Further reduction of the ratio results in the image becoming increasingly diffuse and ultimately disappearing, indicative of the loss of velocity focus. These observations demonstrate excellent agreement between experimental measurements and the simulated voltage optimisation, providing confidence in the use of the simulations to guide experimental settings for both spatial and velocity mapping modes.

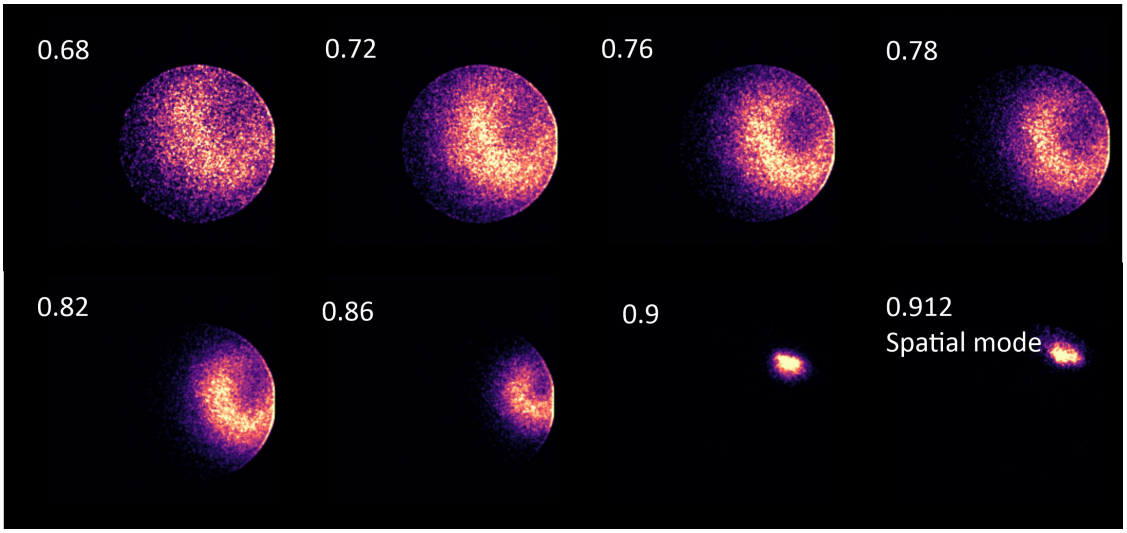


Figure 4.7: shows ion images of the Rhodamine 640 sample obtained using a focused primary ion beam with a diameter of approximately 100 µm, while systematically varying the extractor-to-repeller voltage ratio, V_E/V_R. The repeller voltage was maintained at $V_R = 10$ kV, and the lens voltage was set to $V_L = -8$ kV.

For the defocused primary ion beam employed in Figure 4.3(d), the velocity focus is inherently limited due to the finite size of the ionisation source region on the sample surface. Ions generated further from the centre of the extraction optics experience variations in flight path, leading to a reduction in velocity focusing. To mitigate this

effect, subsequent experiments were conducted using a focused C_{60}^{+} primary beam with an approximate spot size of 100 µm. As illustrated in Figure 4.7, the secondary ion image in spatial mode is now concentrated into a well-defined spot rather than a broad circular distribution. Panel Figure 4.7 presents the results of a voltage ratio scan (V_E/V_R) using the focused beam. The tolerance of the velocity focus to variations in V_E/V_R was significantly improved compared to the defocused beam experiments. Importantly, the optimal voltage ratio remained close to 0.76, in excellent agreement with the predictions from ion trajectory simulations, confirming the reliability of the simulation-guided calibration.

4.4 Imaging Centering

To determine the absolute velocity values of the secondary ions, it is first necessary to establish the centre of the velocity map image, (x_0, y_0), as well as the origin along the time-of-flight (ToF) axis, t_0. These parameters effectively define the laboratory reference point within the three-dimensional velocity map, serving as the origin of the 3D coordinate system. A schematic representation of this laboratory frame origin is shown in Figure 4.8(a), where (x_0, y_0) denotes the spatial centre on the detector plane and t_0 corresponds to the ToF of ions with zero initial velocity along the z-axis.

The origin of the ion image corresponds to the position on the detector that a secondary ion would hit if it has no angular component to its velocity, as illustrated in Figure 4.8(a), *i.e.* when $\theta = 0$, such that the ion travels directly along the time-of-flight (ToF) z-axis. This point therefore defines the velocity origin in the (x, y) plane of the image. In practice, when the primary ion impacts the sample surface, secondary ions are generally ejected with a non-zero polar angle, θ, and those with larger θ values, for a given speed, are mapped further from the centre of the ion image. As demonstrated in Figure 4.3(d) and 4.7, the resulting two-dimensional velocity distribution is not necessarily cylindrically symmetric, complicating the direct identification of the central point as the centroid of the image. To address this challenge, a signal magnification procedure was introduced to facilitate an accurate determination of the image centre.

By adjusting the lens and extractor voltages, the magnification of the ion signal on the detector can be modulated. In the simulations presented in Figure 4.8(b), secondary

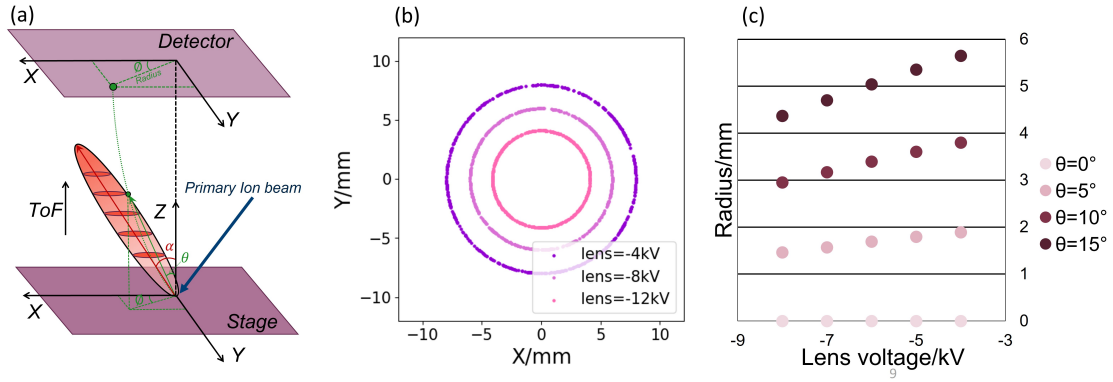


Figure 4.8: Panel (a) illustrates the transformation strategy from camera measurements to ion velocity components. A single ion is represented as a green dot, with its azimuthal angle ϕ and polar angle θ recorded by the camera as a set of spatial coordinates (x,y) and time-of-arrival. The ion cluster or plume is depicted in orange, with an average polar angle α indicating the overall scattering direction. Panel (b) shows a scatter plot of the secondary ion velocity distribution, measured using the same repeller potential and lens voltages of -4, -8, and -12 kV, with $\theta = 30°$. The plot visualises the velocity distribution of ions at varying scattering angles. Panel (c) shows the ion positions on the detector relative to the central axis and the lens voltage for ions with different scattering angles.

ions of 269 m/z with a single kinetic energy of 1.7 eV and a polar cone angle distribution of $\theta = 30°$ were considered. The repeller voltage was held constant at 10 kV, while the lens voltage was varied between -4 kV, -8 kV, and -12 kV. For a given polar angle θ, an increase in the lens voltage results in a reduction of the signal magnification, as illustrated in Figure 4.8(c). The simulations further indicate that ions with larger polar angles are increasingly sensitive to changes in the lens potential, whereas the ion signal corresponding to $\theta = 0°$, *i.e.*, the central axis of the velocity map, remains essentially invariant. Consequently, by systematically varying the lens voltage and monitoring the resulting changes in signal magnification, it is possible to identify the origin of the ion image in the (x,y) plane. This approach exploits the fact that only ions emitted along the surface normal (with $\theta = 0°$) exhibit a signal position that is independent of lens voltage, whereas ions emitted at larger angles experience progressively greater shifts in response to lens potential changes.

Figure 4.9(a) presents ion images recorded at varying magnifications for Rhodamine 640 ([M-ClO_4^-]$^+$) (top row) and Na^+ (bottom row) ions. In these experiments, the repeller voltage was maintained at 10 kV, while the lens voltage was systematically varied from

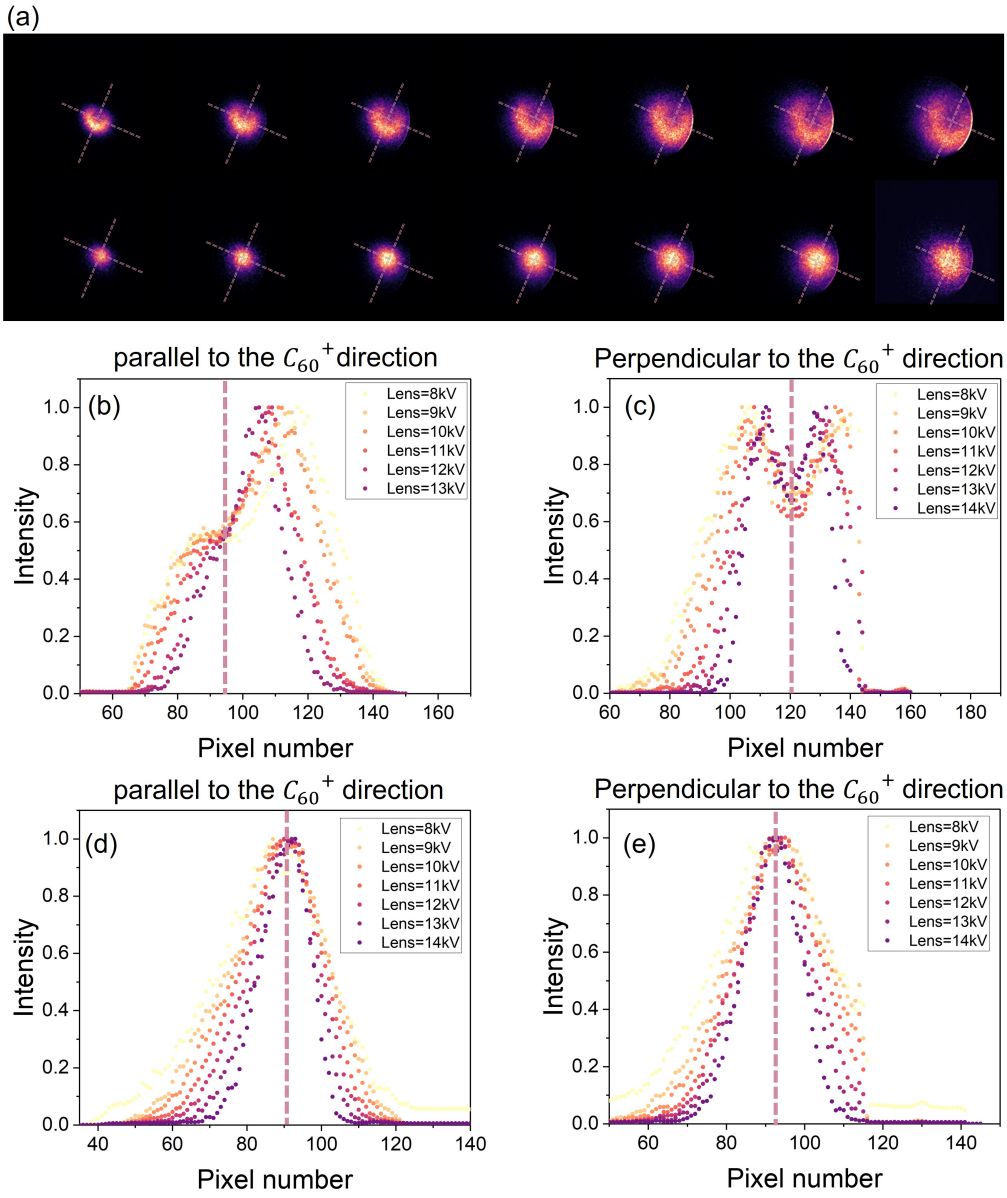


Figure 4.9: Panel (a): Ion images of Rhodamine 640 (top) and Na^+ (bottom) acquired at varying lens voltages, ranging from 14 kV to 4 kV in decrements of 2 kV. Panels (b) and (c): Signal intensity profiles for the Rhodamine 640 images, measured parallel (b) and perpendicular (c) to the C_{60}^+ primary ion beam direction. Panels (d) and (e): Signal intensity profiles for the Na^+ images, measured parallel (d) and perpendicular (e) to the C_{60}^+ primary ion beam direction. These profiles illustrate the shift in the apparent ion impact positions on the detector as a function of lens voltage, which is used to determine the centre of the velocity map image and define the laboratory origin in the (x, y) plane.

-8 kV to -14 kV in 1.0 kV increments. All images were captured using an intensified CCD camera. Two dashed lines are overlaid on each image to indicate directions parallel and perpendicular to the C_{60}^+ primary ion beam. Panels (b) and (c) of Figure 4.9 show

the normalized signal intensity profiles along these two orthogonal directions for the Rhodamine 640 ions, whereas panels (d) and (e) present the corresponding profiles for the Na^+ ions. As the signal magnification increases, the width of the intensity distribution broadens due to the magnification effect; however, the central point of the image remains fixed, as highlighted by the purple dashed lines. This observation demonstrates that, by varying the lens voltage and monitoring the signal profiles, the central origin of the VMI image can be accurately determined in the (x, y) plane, providing a reliable reference for subsequent velocity calibration.

4.5 Determining the ToF origin

Because velocity is inherently three-dimensional, accurate calibration of the velocity component along the time-of-flight (ToF) axis is critical, as it directly affects the derived ion speeds and angular distributions. Accordingly, the definition of the origin along the ToF axis, t_0, is essential. Here, t_0 corresponds to the arrival time at the detector of an ion ejected from the surface with zero initial velocity along the surface normal, *i.e.* parallel to the ToF axis.

In the present experiments, t_0 was determined using a calibration approach based on the post-extraction differential acceleration (PEDA) and post-extraction inversion slice imaging (PEISI) techniques [105, 106, 135], which have previously been employed to focus or defocus ToF peaks by applying a voltage pulse to the extractor electrode. Specifically, by applying a precisely timed pulsed voltage to the extractor and varying the pulse trigger time, a given mass peak can be observed to time-focus at two distinct trigger times. This behaviour arises because, at the moment the extractor pulse is applied, the ion cloud may either have passed the extractor plate or not yet reached it. Consequently, ions are either accelerated or decelerated along the ToF direction depending on their position relative to the extractor.

We denote the arrival times of these two time-focused peaks as t_1 and t_2. Since t_1 and t_2 can be measured accurately in the experiment, the value of t_0 can be determined with the assistance of ion trajectory simulations. Importantly, t_0 corresponds to the ToF

arrival time in the absence of any extractor pulse, thus defining the intrinsic temporal origin of the system.

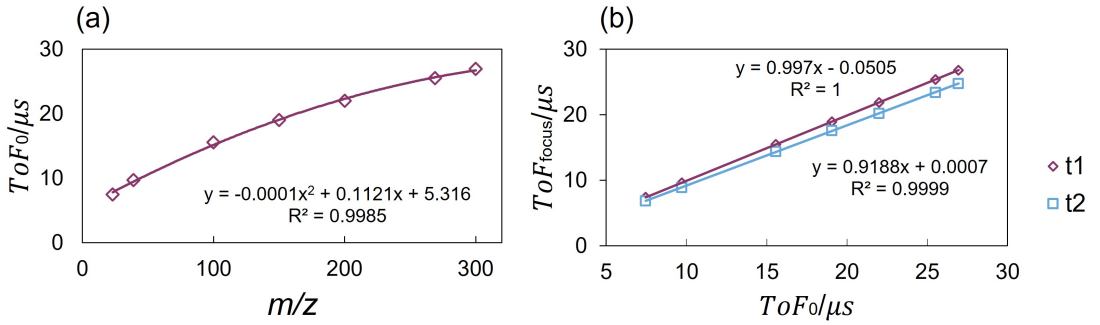


Figure 4.10: Panel (a) illustrates the relationship between different ion masses and their corresponding t_0 values. Panel (b) shows the relationship between the two time-focused peaks (t_1 and t_2) and t_0. All data were obtained from SIMION simulations of the experimental setup, providing a computational reference for the determination of t_0.

In the SIMION simulations (Figure 4.10), a series of ions with different masses were initially considered, and their ToF was recorded under the condition that their velocity along the ToF axis was zero. As expected, a quadratic dependence of t_0 on ion mass was observed, as shown in Figure 4.10(a). Subsequently, the pulse trigger time applied to the extractor was varied to determine the corresponding time-focused peaks, t_1 and t_2. Analysis of the simulated data, presented in Figure 4.10(b), reveals that both t_1 and t_2 exhibit an approximately linear relationship with t_0. This relationship provides a straightforward means to calibrate t_0 experimentally, by matching the measured time-focused peaks to the simulation predictions. Such a calibration is essential for accurate determination of the secondary ion velocities and polar angles in the 3D velocity map imaging experiments.

In the experiments (see Figure 4.11), the initial voltages of the repeller, extractor, and lens were set to 3 kV, 2.79 kV, and 2.4 kV, respectively. At the trigger time, indicated in Figure 4.11(b), the extractor voltage was pulsed to 3.79 kV, with a response time of less than 100 ns. The time-focusing of the secondary ions was determined by monitoring the variation in the full-width-at-half-maximum (FWHM) of the targeted ion peak as a function of the trigger delay time, which was varied in 10 ns increments. Both a photomultiplier tube and a TimePix3-based camera were employed to record the FWHM.

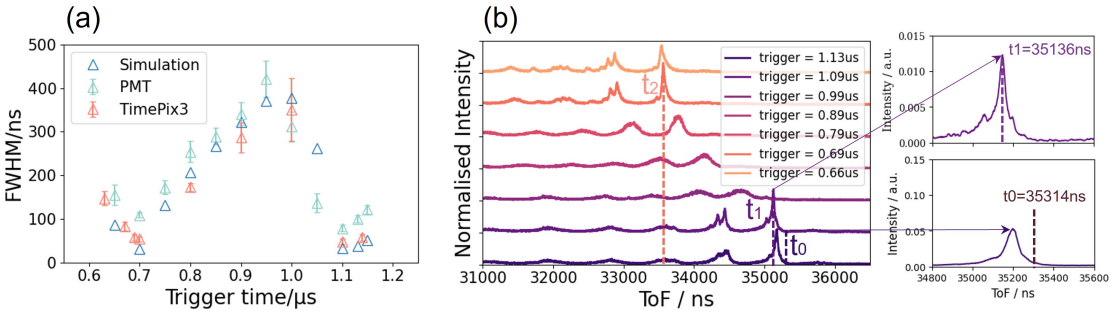


Figure 4.11: Panel (a) compares the full-width-at-half-maximum (FWHM) of the post-extraction calibration peaks obtained experimentally using both a TimePix3-based camera and a photomultiplier tube (PMT) detector, alongside the corresponding simulation results. This comparison serves to validate the accuracy and reliability of the experimental setup. Panel (b) illustrates the ToF peak focusing achieved by varying the pulse trigger time applied to the extractor. The two time-focused arrival times (t_1 and t_2) are indicated, demonstrating the influence of the pulsed trigger on the ToF distribution. Auramine O was used as the sample in these experiments.

The two focused arrival times, t_1 and t_2, identified from the minimum FWHM values, were found to be in excellent agreement with those predicted by ion trajectory simulations (Figure 4.11(a)). It should be noted that the FWHM measured using the PMT is slightly larger than that obtained from the TimePix3-based camera and simulations. This difference arises because the TimePix3 pixels are triggered on the leading edge of the phosphor emission, whereas the PMT measurements are limited by the response time of the P 47 phosphor screen employed on the MCP detector. Representative experimental ToF data are shown in Figure 4.11(b), highlighting the two time-focusing conditions obtained by varying the trigger delay, which yield the time-focused mass peaks at t_1 and t_2. The relationship of these focused times with the origin time, t_0, obtained in the absence of a trigger pulse, is also indicated in the right-hand panel.

4.6 3D velocity calibration

Once the image centre, (x_0, y_0), and the time-of-flight origin, t_0, have been established, the transformation strategy illustrated in Figure 4.8(a) can be applied. The three-dimensional velocity distribution is obtained using the transformation equations (*e.g.*, Eqs (4.4)(4.5)(4.6)), which map each measured ion event, (x_i, y_i, t_i), from the detector frame into the laboratory-frame velocity components, $(v_{x,i}, v_{y,i}, v_{z,i})$. The specific

scaling factors relating the detector positions, (x,y), and the time-of-flight, t_{ToF}, to the corresponding 3D velocities were derived from SIMION ion trajectory simulations, which were calibrated against the experimental data as described above.

In the simulations, ions were initially distributed over a circular region of 100 µm diameter, and assigned linear velocity distributions along both the ToF axis and the detector plane. Under the velocity map imaging (VMI) conditions employed, SIMION was used to calculate the ToF of each ion and its corresponding impact position on the detector. The resulting data were subsequently used to fit the calibration equations in the in-plane directions (x,y) as well as along the ToF axis (z). Specifically, for the Na^+ ions under the experimental conditions described, this procedure yields the following calibration equations:

The calibrated 3D velocity components for the Na^+ ions are expressed as follows:

$$v_x = \left[-0.3056\cdot(x-x_0)-0.0221\right]\times 10^3\ \mathrm{m\,s^{-1}}, \tag{4.4}$$

$$v_y = \left[-0.3056\cdot(y-y_0)-0.0221\right]\times 10^3\ \mathrm{m\,s^{-1}}, \tag{4.5}$$

$$v_z = \left[-710.24\cdot(t_{\mathrm{ToF}}-t_0)^2-191.04\cdot(t_{\mathrm{ToF}}-t_0)+0.008\right]\times 10^3\ \mathrm{m\,s^{-1}}, \tag{4.6}$$

where x and y are the ion positions on the detector in millimeters, and t_{ToF} is the measured ToF in microseconds. Equation (4.4) represents the velocity component along the x-direction, while Eq. (4.5) corresponds to the y-direction in the image plane. The velocity along the time-of-flight axis, z, is given by Eq. (4.6). Here, t_0 defines the laboratory origin along the ToF axis, as discussed in **Determining the ToF origin Section**, whereas x_0 and y_0 define the laboratory origin in the detector plane, as outlined in **Imaging centering Section**. Equivalent calibration equations can be readily derived for ions of different masses, allowing the determination of their full 3D velocity distributions.

Some noise is present in the simulation results used to define the calibration equations, primarily arising from the finite spatial extent of the primary ion beam. However, this noise is minimal, and the velocity map imaging (VMI) focusing is excellent, with correlation coefficients exceeding 0.99. For example, in a simulation of a 23 Da ion with a velocity of $600\,\mathrm{m\,s^{-1}}$ in the detector plane and a 100 µm spatial spread, the resulting detector radius in VMI mode was 1.970 ± 0.012 mm. This corresponds to

a standard deviation in the velocity calibration of less than 1%, confirming the high robustness and reliability of the velocity mapping simulations.

4.7 VMI with TimePix3-based camera

4.7.1 multi-mass VMI

An example time-of-flight (ToF) mass spectrum optimised for velocity map imaging as outlined above and obtained using a C_{60}^{+} primary beam at 20 keV and recorded with the TimePix3-based camera, is presented in Figure 4.12(a) for an Auramine O laser dye sample (see Experimental Methods Section). The three-dimensional (3D) velocity distributions for this sample were determined for Na^{+}, K^{+}, and $[M\text{-}Cl^{-}]^{+}$ (the parent ion of Auramine O), with these peaks identified in the mass spectrum. Enlarged views of the corresponding ToF peaks are shown in the lower panels of Figure 4.12(a). The bottom row of panels, Figure 4.12(b)-(d), displays the two-dimensional (2D) projected velocity map images. The centres of the images are marked with cyan dots, as shown, and all three images share the same C_{60}^{+} primary beam injection direction, which is indicated only in the $[M\text{-}Cl^{-}]^{+}$ image in Figure 4.12(d). The images shown are raw outputs from the TimePix3-based camera, without velocity transformation, and therefore the image size does not directly reflect the ion speeds. As demonstrated by the simulations in Figure 4.5, ions of lower mass exhibit smaller velocity spreads on the detector at a given speed. This arises because they are more strongly accelerated in the ToF tube and possess shorter flight times. Consequently, their distributions on the detector are less expanded compared with those of higher-mass ions. It is notable that the organic ions exhibit markedly different projected ion images compared with the metallic ions, reflecting fundamental differences in the sputtering and ionization mechanisms underlying their formation.

Additional examples of 2D projected velocity map images for both parent and fragment ions are provided in the Figure 4.13. These data show that fragment ions with masses close to that of the Auramine O parent ion exhibit similar anisotropic 2D projected velocity distributions, whereas lower mass fragments display nearly isotropic velocity maps, more closely resembling those of the metallic ions. This effect is strongly

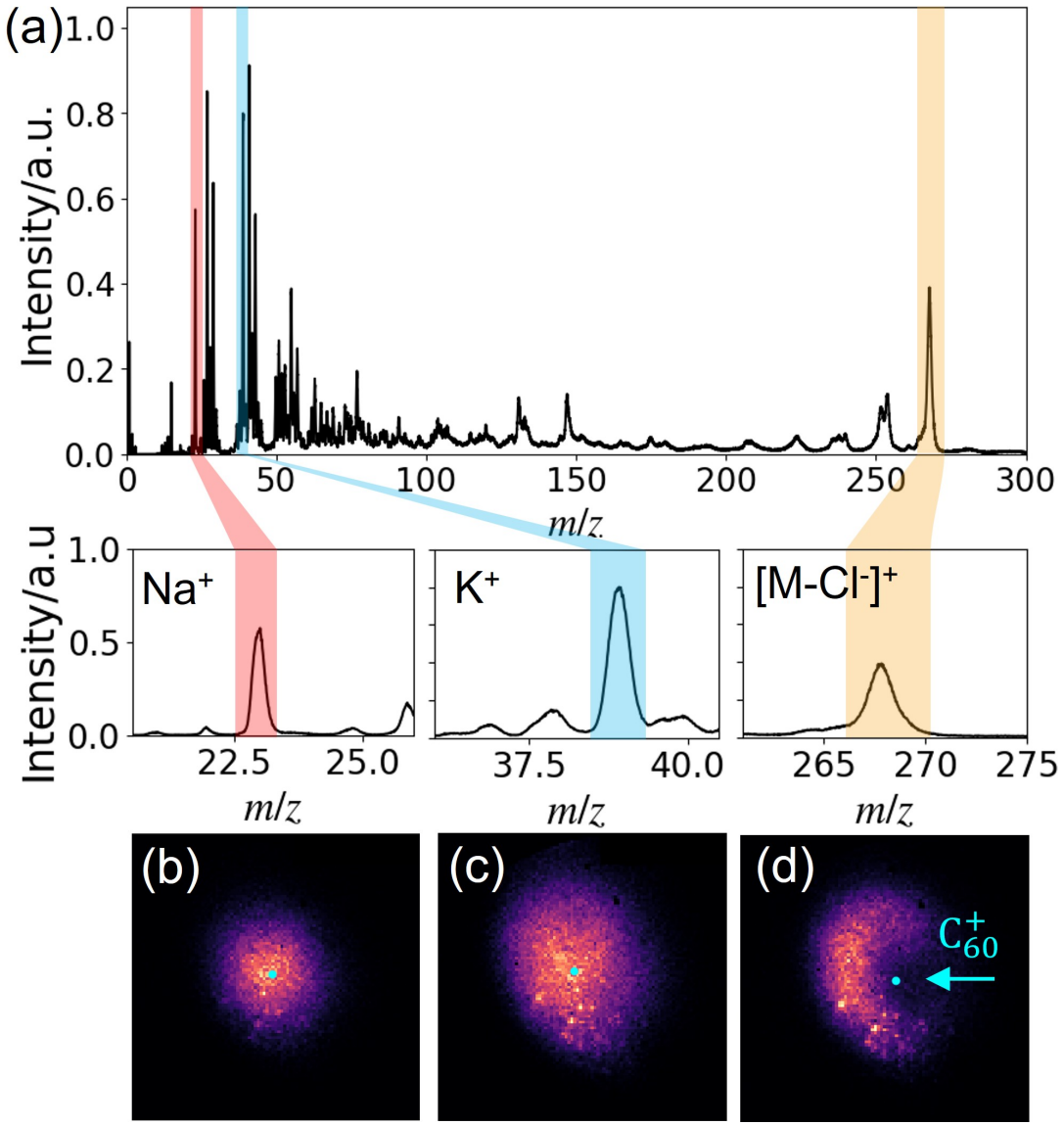


Figure 4.12: Top panel: ToF mass spectrum of Auramine O, measured with the TimePix3-based camera using a C_{60}^+ primary beam at 20 keV. Middle panels: Expanded views of the ToF spectra for three secondary ions, Na^+ (left), K^+ (center), and $[M\text{-}Cl^-]^+$ (right), obtained under velocity mapping conditions. Bottom panels: Corresponding two-dimensional (2D) velocity map images for (b) Na^+, (c) K^+, and (d) $[M\text{-}Cl^-]^+$ ions. The cyan dot indicates the centre of the velocity map images. All experiments were performed with repeller, extractor, and ion lens voltages of 3.0 kV, 2.79 kV, and 2.4 kV, respectively.

influenced by fragmentation processes. Lower-mass fragments arise not only from direct collision-induced sputtering but also from subsequent dissociation processes, therefore the direction of momentum of the incoming PI beam is not reflected in the velocity distribution. The observed differences between the velocity distributions of high-mass

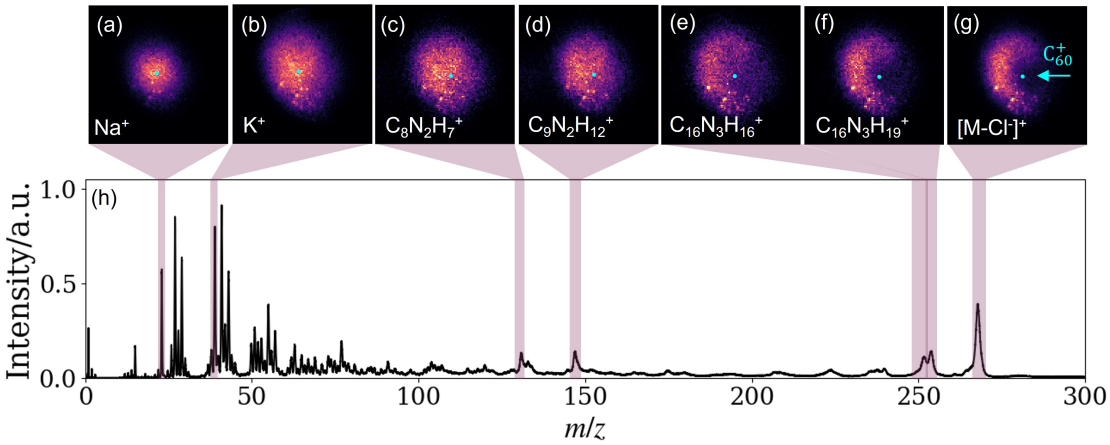


Figure 4.13: Top panels (a)-(g): Example two-dimensional projected velocity-map images are presented for a range of ions, including Na^+, K^+, and $[M\text{-}Cl^-]^+$ (the Auramine O (AO) parent ion) as shown in the main text, together with several AO fragment ions. The centre of each velocity map image is indicated by the cyan dot. The experiments were performed using repeller, extractor, and ion lens voltage settings of 3.0 kV, 2.79 kV, and 2.4 kV, respectively. Bottom panel (h): The associated ToF mass spectrum of AO, measured with the TimePix3-based camera at a C_{60}^+ primary beam energy of 20 keV.

and low-mass fragments therefore suggest that high-mass fragments, including the parent ions, are predominantly governed by momentum transfer dynamics, whereas low-mass fragments involve a greater contribution from dissociation pathways, since the velocity distribution is directly effected by the direction of momentum of the incoming PI beam.

An Auramine O dye layer was deposited onto a standard indium tin oxide (ITO) cover slide and subsequently bombarded with C_{60}^+ primary ions at energies of 20 keV and 40 keV. Figure 4.13 presents an example ToF spectrum of Auramine O obtained at the lower sputtering energy, together with a more complete set of two-dimensional projected velocity map images for both the parent ions and several of their fragments, as well as for Na^+ and K^+. Notably, as the degree of fragmentation of the parent ion increases, the corresponding velocity map images evolve from being highly anisotropic around the image center to more isotropic in character, with those of the smaller fragment ions closely resembling the two-dimensional images of the metallic ions.

4.7.2 3D VMI with TimePix3-based camera

Figure 4.14 presents the full three-dimensional velocity and angular distributions derived from the three-dimensional velocity map images of Na^+, K^+, and $[M\text{-}Cl^-]^+$ ions,

bombarded by a 20 keV C_{60}^+ primary beam, and the 2D velocity distributions are shown in the (x,y), (x,z), (y,z) panels. It is worth noting that the 3D VMI plots are not in the same scale.

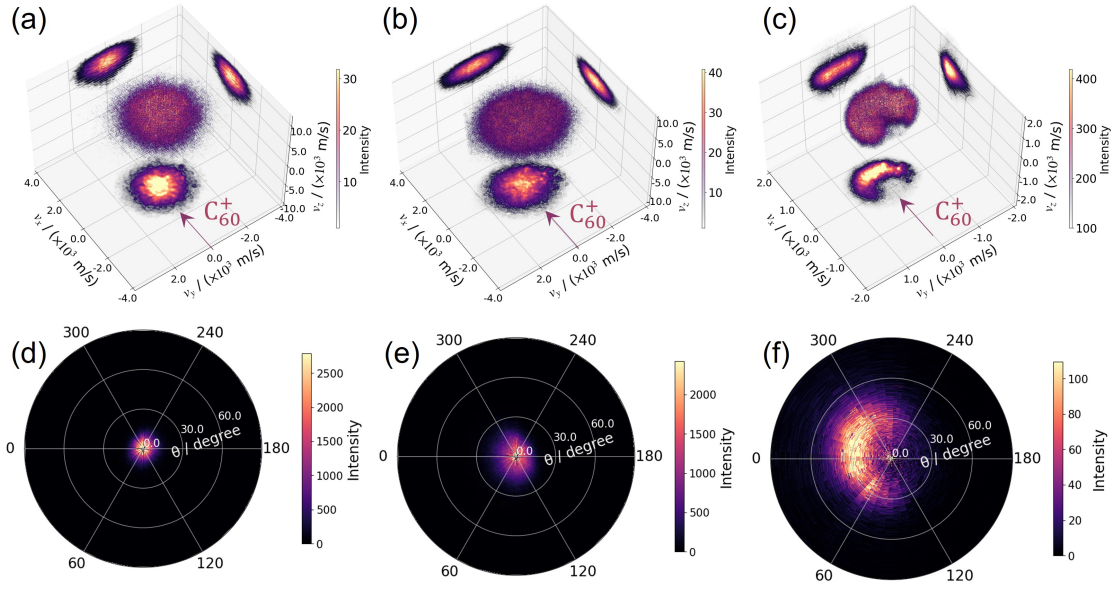


Figure 4.14: Panels (a)-(c) present the three-dimensional velocity distributions obtained for Na^+ (left), K^+ (centre), and $[M–Cl^-]^+$ (right) ions following C_{60}^+ sputtering of an Auramine O sample at 20 keV. The experiments were conducted with repeller, extractor, and ion lens voltage settings of 3.0 kV, 2.79 kV, and 2.4 kV, respectively. Panels (d)-(f) show the corresponding $P(\theta,\phi)$ angular distributions for each ion (Na^+, left; K^+, centre; and $[M\text{-}Cl^-]^+$, right).

For an incident C_{60}^+ injection angle of 40° with respect to the surface normal, the organic parent ions exhibit an azimuthal angle distribution, $P(\phi)$, that peaks around $\phi = 0°$ but extends over a broad range of approximately 155°. More notably, the organic $[M\text{-}Cl^-]^+$ ion distribution peaks away from the surface normal at $\theta \approx 20°$, whereas the metallic ions, Na^+ and K^+, peak close to the surface normal at $\theta = 0°$.

The velocity distribution data can be further analysed to obtain the polar angle, momentum, and kinetic energy distributions of Na^+, K^+, and $[M\text{-}Cl^-]^+$ ions, as shown in Figure 4.15, using a 20 keV C_{60}^+ primary beam. For the polar angle and momentum distributions, a Gaussian fit function is applied, whereas a Maxwell-Boltzmann fit function is employed for the kinetic energy distribution. The mean values and full widths at half maximum (FWHM) of these distributions are summarised in Table 4.1.

Table 4.1: Kinetic energy, momentum, and angular spread characteristics of selected ion species with 20 keV C_{60}^{+}.

Ion Species	Mean KE (eV)	FWHM KE (eV)	Mean Momentum (10^{-22} kg·m/s)	FWHM Momentum (10^{-22} kg·m/s)	Mean θ (°)	FWHM θ (°)
Na	8.29 ± 0.08	10.85 ± 0.15	3.33 ± 0.02	2.01 ± 0.04	0.56 ± 0.16	17.14 ± 0.17
K	4.87 ± 0.06	8.35 ± 0.11	3.35 ± 0.01	2.60 ± 0.03	0.96 ± 0.19	26.39 ± 0.27
AO	1.51 ± 0.04	2.81 ± 0.07	4.90 ± 0.02	4.22 ± 0.04	22.12 ± 0.25	36.86 ± 0.67

The results confirm that the polar angle distributions, $P(\theta)$, for Na^{+} and K^{+} peak close to $\theta = 0°$, while the $[M\text{-}Cl^{-}]^{+}$ organic ions exhibit a broader distribution with a mean around $\theta \approx 22°$. Furthermore, the momentum distributions of the two metallic ions are nearly identical and display substantially lower mean momenta than those of the organic species.

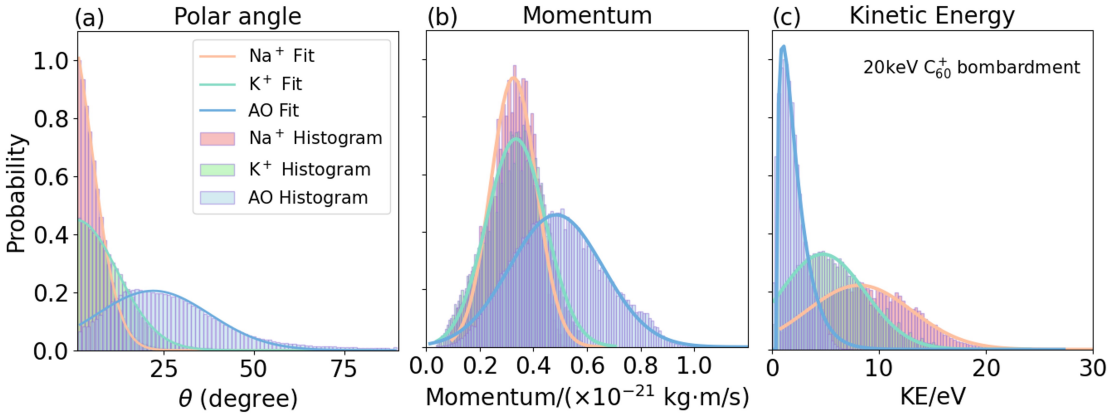


Figure 4.15: Panels (a)-(c) present the polar angle, momentum, and kinetic energy distributions for Na^{+} (red), K^{+} (green), and $[M\text{-}Cl^{-}]^{+}$ (blue) ions following C_{60}^{+} sputtering of an Auramine O (AO) sample at 20 keV.

A key factor in explaining the observed behaviour is likely to be the location of the ions at the point of their generation. Given that the surface of the sample is electrosprayed with the organic dye, it is reasonable to assume that the organic ions originate from the topmost layer of the sample. Na^{+} and K^{+} ions are ubiquitous contaminants and are readily ionised in mass spectrometry. However, the fact that increasing the primary ion beam energy results in a substantially larger increase in Na^{+} and K^{+} signals compared with the organic ions suggests that the metallic ions are more concentrated deeper within the sample, closer to the ITO-coated substrate, as accessed by the higher-energy C_{60}^{+} beam. It should be noted that, due to the manufacturing process of ITO slides, the presence

of sodium and potassium ions is unsurprising [204, 205]. This phenomenon becomes evident when the C_{60}^+ beam energy is doubled, as shown in Figure 4.16. The mass spectra obtained at sputtering energies of 20 and 40 keV are overlapped and normalised by aligning the Auramine O peak. With increasing sputtering energy, the intensities of Na^+ and K^+ ions rise markedly, particularly for Na^+, suggesting that these metallic ions originate from deeper layers within the sample, and they have higher ionisation efficiency than the organic ions.

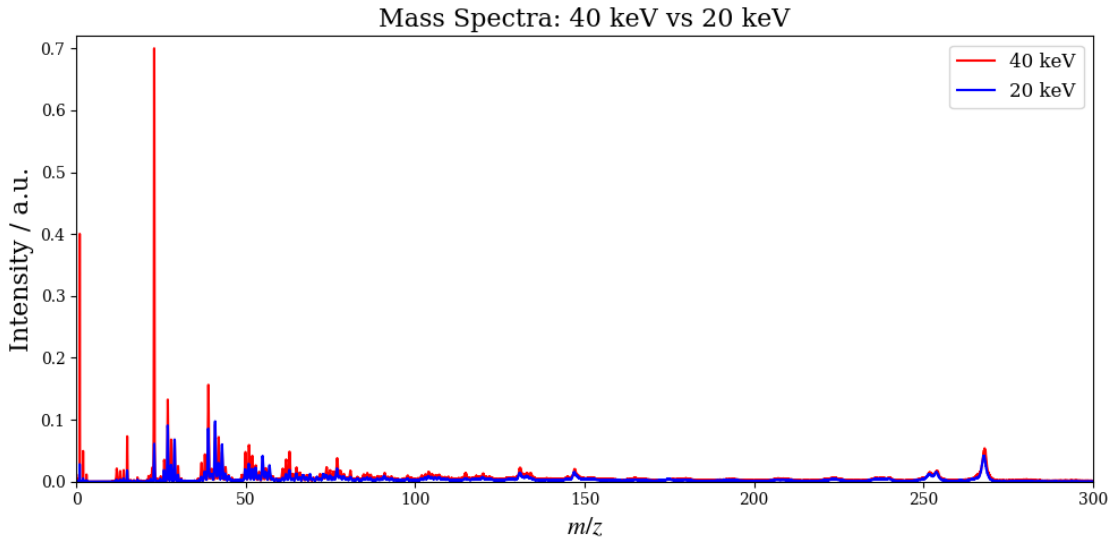


Figure 4.16: The spectra collected under different C_{60}^+ beam energies, 20 keV (blue) and 40 keV (red), are compared.

Given that the organic layer is only approximately 100 nm thick (see Experimental Methods), and that the typical penetration depth of a C_{60}^+ ion ranges between 20 nm and 50 nm [206], it is likely that the higher-energy C_{60}^+ ions release a greater number of Na^+ and K^+ ions, which are concentrated closer to the ITO surface. In contrast, the organic ions, originating from the top surface, are expected to result from a more direct sputtering process, producing an anisotropic angular distribution and relatively high momentum transfer from the primary ion, compared with the more readily ionised metallic species, which originate from regions nearer the ITO-coated substrate.

4.7.3 Primary ion beam energy impact

To gain further insight into the sputtering and ionisation processes, the secondary-ion velocity distributions were also measured using a 40 keV primary ion beam. For comparison with the 20 keV data presented in Figure 4.12, the full three-dimensional velocity distributions of Na^+, K^+, and $[M\text{-}Cl^-]^+$ ions at both 20 keV and 40 keV primary beam energies are presented in Figure 4.17. Comparisons of the resulting polar angle, momentum, and kinetic energy distributions for each of these ions at both sputtering energies are presented in Figure 5, with the mean values and full widths at half maximum (FWHM) of these distributions also summarised in Table 4.2.

Table 4.2: Kinetic energy, momentum, and angular spread characteristics of selected ion species with 40 keV C_{60}^+.

Ion Species	Mean KE (eV)	FWHM KE (eV)	Mean Momentum (10^{-22} kg·m/s)	FWHM Momentum (10^{-22} kg·m/s)	Mean θ (°)	FWHM θ (°)
Na	18.17 ± 0.98	7.00 ± 2.36	4.76 ± 0.01	0.90 ± 0.02	0.91 ± 0.10	14.51 ± 0.12
K	9.90 ± 0.98	8.67 ± 2.36	4.76 ± 0.01	1.92 ± 0.02	0.61 ± 0.19	20.59 ± 0.26
AO	3.25 ± 0.03	4.60 ± 0.06	7.06 ± 0.04	4.69 ± 0.07	17.05 ± 0.11	25.9 ± 0.28

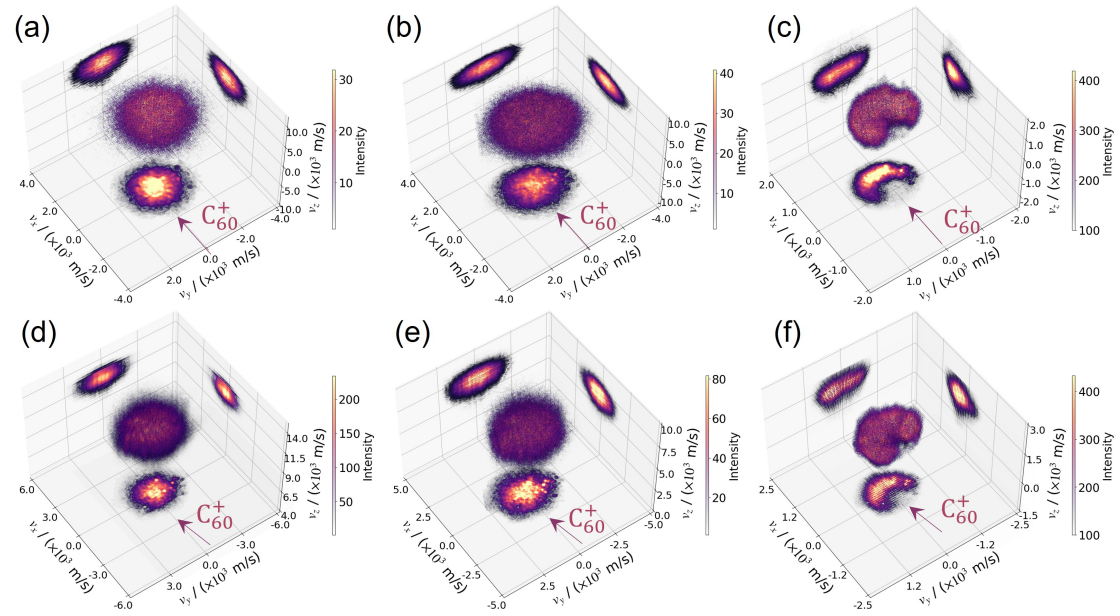


Figure 4.17: Panels (a)–(c) show the 3D velocity distributions of Na^+, K^+, and $[M\text{–}Cl^-]^+$ ions following C_{60}^+ sputtering of an Auramine O (AO) sample at 20 keV, while panels (d)–(f) present the corresponding velocity distributions obtained under 40 keV C_{60}^+ sputtering.

The general patterns observed for Na^+, K^+, and $[M\text{-}Cl^-]^+$ ions at a 20 keV primary beam energy are largely reproduced at 40 keV (see Figure 4.18), which suggests that the

ionization processes don't change a lot by varying the collision energy. The metallic ions remain distributed very close to the surface normal, exhibiting near-cylindrical symmetry. In contrast, the organic ion scatters significantly away from the surface normal and displays pronounced non-axial symmetry. The momentum distributions of the two metallic ions are almost identical at both sputtering energies, whereas the organic $[M\text{-}Cl^-]^+$ ion carries considerably higher momentum, suggesting that Na^+ and K^+ are generated via a similar ionisation mechanism, while distinct dynamics govern the organic ion. Furthermore, when the primary ion beam energy is doubled, the mean kinetic energies of the secondary ions approximately double, and the mean momentum increases by a factor of $\sqrt{2}$ (see Figure 4.18 and Table 4.14.2).

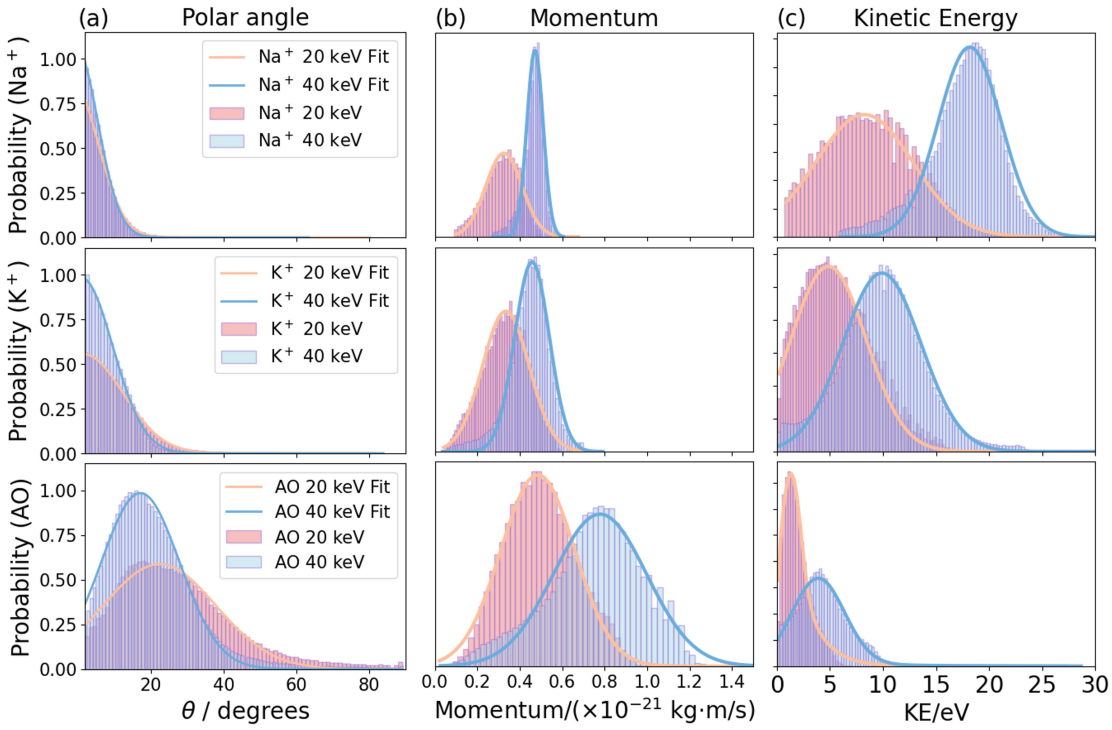


Figure 4.18: Panels (a)-(c) present comparisons of the polar angle, momentum, and kinetic energy distributions for Na^+ (top row), K^+ (middle row), and $[M\text{-}Cl^-]^+$ (bottom row) ions generated following C_{60}^+ sputtering of an Auramine O (AO) sample at 20 keV and 40 keV. In each plot, the effect of the primary ion beam energy is indicated, with 20 keV shown in red and 40 keV in blue.

The momentum distributions of the metallic and organic ions support a model in which incoming C_{60}^+ ions transfer significantly more momentum to the surface organic ions than to the underlying metallic ions. As noted above, the momentum of both the metallic and organic secondary ions increases by approximately a factor of $\sqrt{2}$ when

the primary ion beam energy is doubled. This observation indicates that a constant fraction of the incoming C_{60}^{+} ion momentum is transferred to the secondary ions during the sputtering process, with this fraction being smaller for the metallic ions than for the surface organic ions. Consistent with this increase in secondary ion momentum with increasing primary ion beam momentum, the mean kinetic energies of the three types of secondary ions roughly double when the primary beam kinetic energy is doubled. This mechanism of momentum transfer is in agreement with previous studies by Kelner and Markey [207], and Magee [208].

The polar-angle distributions provide further insight into the secondary ion dynamics, with higher primary ion beam energies resulting in somewhat smaller θ angles and sharper polar-angle distributions, as shown in Figure 4.18(a). This effect is more pronounced for the organic ions than for the metallic ions (see Table 4.14.2), which may be attributed to the increased penetration depth of the primary ions at higher energies. A deeper injection allows the crater edge and the depth of ion scattering to influence the secondary ion trajectories, directing them closer to the surface normal, thereby reducing θ angles and sharpening the angular distributions. It is also noteworthy that the momentum distributions of the organic ions become somewhat broader at higher primary ion beam energies, whereas the metallic ions exhibit sharper distributions (see Figure 4.18(b) and Table 4.14.2). This behaviour is likely related to the deeper penetration of the primary ions and the resulting secondary ion scattering dynamics.

As noted in the Introduction, the sputtering process in SIMS is relatively well understood for metallic ions ejected by monoatomic primary ions, where a 'linear collision cascade' occurs, leading to the ejection of atoms from the surface [209–211] and to beam-induced evaporation [211].

In condensed-matter physics, a collision cascade (also referred to as a displacement cascade or displacement spike) describes a series of adjacent, energetic atomic collisions induced by the impact of a high-energy particle in a solid or liquid [212, 213]. If the maximum kinetic energies of atoms or ions within the cascade exceed the material's threshold displacement energy (typically on the order of tens of eV), atoms can be permanently displaced from their lattice sites, thereby generating defects. The initial

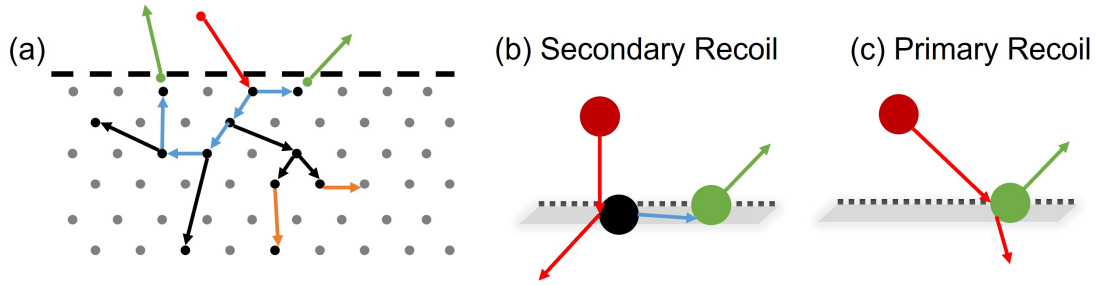


Figure 4.19: (b) illustrates the models commonly utilized to describe the linear collision cascade, adapted from Ref. [125].

energetic atom may originate from various sources, such as an incident ion from a particle accelerator, an atomic recoil produced by a passing high-energy neutron, electron, or photon, or from the recoil energy imparted during the decay of a radioactive nucleus. In the linear collision cascade sputtering process, information about the impact angle and direction of the primary ion is largely lost (see Figure 4.19, where primary ions are shown in red, secondary ions in green, and a representative collision cascade in blue). As a result, the ejection of secondary particles becomes mostly independent of the primary ion incidence angle, except at very shallow (glancing) angles. The emitted species exhibit no azimuthal preference, and their angular distribution is rotationally symmetric with respect to the surface normal.

However, for cluster primary ions, it has been shown that the linear collision cascade model no longer applies, and additional mechanisms must be considered to explain the observed sputtering. The sputtering of Ag with C_{60}^{+} has been investigated, with the corresponding schematic models shown in Figure 4.20(a) and (c), and the resulting secondary ion polar angular distributions presented in Figure 4.20(b) and (d). This indicates that, under C_{60}^{+} bombardment, the ejection direction of secondary ions is strongly influenced by the incidence angle of the primary ion beam.

These sputtering mechanisms involve the collective motion arising from multiple low-energy atoms impacting the surface at the same location simultaneously, resulting in a collective transfer of kinetic energy and subsequent thermal desorption [211]. This process is sometimes subdivided into two distinct sputtering mechanisms: ions located at the centre of the collision region, which yield higher kinetic energy secondary ions [131, 214,

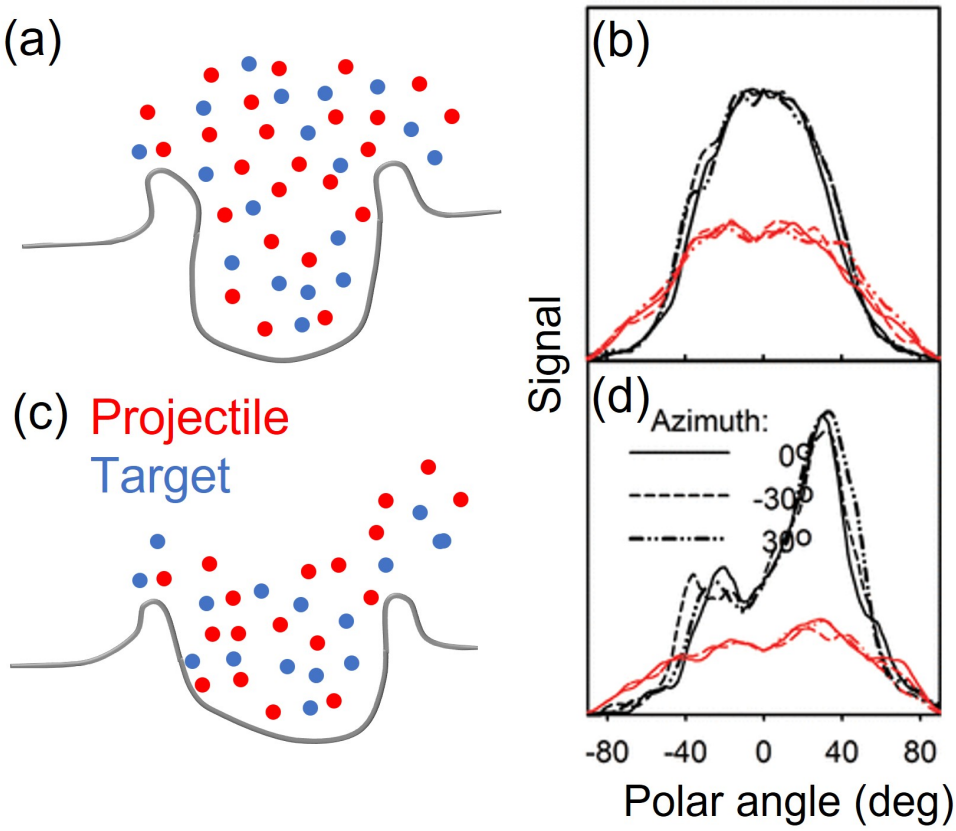


Figure 4.20: Panels (a) and (c) illustrate models commonly used to describe the sputtering process with a C_{60}^+ beam at different incidence angles: normal and 70 °, adapted from Ref. [125]. Panels (b) and (d) show the corresponding polar angle distributions of Ag atoms sputtered with a 20 keV C_{60}^+ beam at normal incidence and 70 ° impact angles, adapted from Ref. [126].

215], and ions desorbed from the edges of the collision area, which result in secondary ions with lower kinetic energies [130]. Although various terms have been used to describe these mechanisms, we will here refer to them as the linear and thermal mechanisms, respectively. The linear collision cascade mechanism typically produces sputtered ions after a series of collisions, resulting in secondary ions with relatively uniform angular distributions about the surface normal and higher kinetic energies than those generated by the thermal mechanism. This behaviour is similar to that observed for the underlying metallic ions, Na^+ and K^+, in the present study. In contrast, thermal sputtering occurs at or near the sample surface and is usually anisotropic; the ballistic collision process is strongly influenced by the primary ion injection angle, so that the angular distributions reflect the asymmetry of the primary ion motion. This behaviour is analogous to the scattering observed for the organic surface ions.

The dynamical information presented here indicates that the location and nature of the secondary ions are of key importance. Surface organic ions undergo more direct sputtering and acquire higher momenta than the metallic ions. In contrast, the metallic ions, Na^+ and K^+, which are likely to originate from regions beneath the surface, closer to the ITO substrate, exhibit more isotropic sputtering patterns and lower momentum than the surface organic ions. This behaviour may reflect both the multiple collisions experienced by the incoming C_{60}^+ primary ion beam and the increased likelihood of secondary ions originating from deeper layers undergoing additional collisions within the organic dye.

4.8 Summary

In summary, this work has demonstrated the measurement of three-dimensional velocity distributions of multiple ions generated in a surface-scattering experiment using a simple velocity-map imaging (VMI) ion optical system coupled to a TimePix3-based camera. A key aspect of the experiment is the extraction of multiple ions along the surface normal, enabled by the high time resolution in the time-of-flight (ToF) coordinate provided by the TimePix3-based camera. The method developed here should be applicable to other surface scattering experiments, provided the detected ions are produced in a pulsed manner to allow for ToF mass spectrometry analysis. We directly measure the full three-dimensional velocity distributions, or half-Newton spheres, of multiple ions following their extraction along the surface normal. This is made possible by the high temporal resolution in the ToF coordinate afforded by the TimePix3-based camera. The methods developed here are expected to be applicable to a wide range of other surface photo-initiated processes, including laser desorption ionisation (LDI) and matrix-assisted laser desorption ionisation (MALDI), as well as to surface scattering experiments, provided that the detected ions are generated in a pulsed manner to enable ToF mass spectrometric analysis. Importantly, these approaches can be implemented in both positive and negative ion modes. In particular, for surface scattering experiments, we envisage that multiple species of interest could be simultaneously detected using universal femtosecond near-infrared non-resonant ionisation [137, 199], coupled with the three-dimensional VMI methods described here. Furthermore, the time delay between the photo-initiation or scattering event and the

ionisation pulse could be varied or scanned systematically, thereby ensuring that the full velocity range of the species of interest is recorded.

This work has exemplified the approach by measuring the 3D velocity distributions of multiple secondary ions generated in a SIMS sputtering process, using a C_{60}^{+} primary ion beam impacting a meshed Auramine O dye sample. The data provide insights into the effect of primary ion beam energy on secondary ion angular and momentum distributions. Furthermore, we observe significant differences in the 3D velocity distributions, both in angle and momentum, between organic and metallic ions, which can be attributed to distinct sputtering and ionisation mechanisms depending on the depth within the surface at which the secondary ions are formed and extracted.

This work highlights the complexity of SIMS sputtering and ionisation in determining secondary ion momentum distributions and suggests that further simulation studies would be valuable to fully understand these processes.

5

High-resolution Secondary Ion Mass Spectrometry Imaging

This chapter is based on the work presented in the paper *'High-resolution microscope-mode secondary ion mass spectrometry imaging'* [216].

For this chapter, the experimental design, data collection and analysis, as well as the principal simulations and subsequent interpretation, were carried out by myself. I would like to express my sincere thanks to Kieran Cheung for his assistance in the development of the TimePix3 camera software and the LED trigger methodology, which formed the foundation of the **PEDA with TimePix3** section. I am also grateful to Yuting Su for her support with the simulations used to extend the optimised mass range of the PEDA by varying the distances within the ion optics, as illustrated in Figure 5.8.

5.1 Introduction

Probing the molecular complexity of tissues and organs at the cellular level offers immense potential. As a label-free technique, mass spectrometry plays a vital role in the qualitative and quantitative analysis of biological chemical composition. By integrating imaging capability, mass spectrometry imaging (MSI) enables precise visualisation of the spatial distribution of chemical compounds within samples, enabling breakthroughs in material sciences [217–220] and biology [221–224].

Mass spectrometry imaging (MSI) strategies can broadly be categorised into two principal modes: microprobe mode and microscope mode [64]. At present, microprobe mode MSI remains the most widely adopted approach. The most commonly employed microprobe mode techniques include matrix-assisted laser desorption/ionisation (MALDI), secondary ion mass spectrometry (SIMS), and desorption electrospray ionisation (DESI) [225], each offering distinct advantages in terms of spatial resolution, ionisation efficiency, and molecular coverage. In this configuration, a focused primary beam sequentially scans the sample surface, and ion signals are recorded pixel-by-pixel. Thus, microprobe mode MSI is typically time-consuming and can cost hours when acquiring large-area images at spatial resolutions below 10 µm [226].

Microscope mode Mass Spectrometry Imaging (MSI) represents a significant evolution in the field, offering a promising combination of high mass and spatial resolution with markedly improved throughput. Unlike microprobe mode, this approach enables imaging over larger areas by employing defocused primary ion beams and position-sensitive detectors, such as Delay line detectors [227, 228], pixel imaging mass spectrometry sensor (PImMS) [113, 173], and TimePix camera [116, 118, 229]. Demonstrating this potential, Green *et al.* has shown that it is now possible to defocus the primary beam to cover an area with a diameter of about 1.8 mm while maintaining a spatial resolution of 23 µm [158]. However, this remains less precise than the spatial resolution typically achieved in microprobe mode. To enhance the suitability of microscope mode for rapid clinical diagnosis, a key challenge lies in balancing the demand for high throughput with the need for spatial accuracy.

Microscope mode MSI requires the preservation of the original spatial information of secondary ions, making the Time-of-Flight (ToF) analyser the preferred option. However, ToF analysers still fall short of delivering the mass resolution offered by orbitrap [81, 230, 231] and Fourier Transform Ion Cyclotron Resonance (FT-ICR) [56, 232, 233] systems. The principal obstacle to the broader adoption of microscope mode MSI is therefore its limited mass resolution. Earlier efforts, such as those by Korber et al., achieved an m/z resolution of approximately 100 at 395 m/z, with the slow response of the phosphor screen identified as a limiting factor[118]. Nonetheless, progress in

ion extraction techniques, initially developed by Aoki *et al.* [197] and later adapted to MALDI MSI by Guo *et al.* [105, 106], and coupled with reflectron [120] point to promising avenues for overcoming these constraints.

This research reports the development of a high-throughput microscope-mode Secondary Ion Mass Spectrometry (SIMS) instrument that significantly enhances both mass and spatial resolution while maintaining acquisition speed suitable for biological and clinical applications. To address the inherent mass resolution limitations of linear time-of-flight (ToF) analysers, we introduce a time-dependent PEDA scheme. Through optimised pulsing strategies and Genetic Algorithm-based parameter tuning with SIMION as outlined in Chapter 2, mass resolution is improved from approximately $500\,m/\Delta m$ to over $2000\,m/\Delta m$ across wide mass ranges. Further enhancement to $6890 \pm 401\,m/\Delta m$ is achieved by replacing conventional P 47 phosphor screens with fast-rise-time BC-408 scintillators, thereby enabling isotopic peak resolution. Spatial resolution is improved through electrostatic lens refinement and controlled magnification using an Einzel lens, reducing detector pixel influence. Under optimised conditions, a spatial resolution of 3.56 ± 2.12 µm is attained. High-speed centroiding and use of a TimePix3-based detector allow simultaneous acquisition of time-of-flight spectra and ion images without repetition rate limitation. We demonstrate the platform's capability by imaging molecular species in rat brain tissue sections, capturing biologically relevant ions such as K^+, Na^+, and neurotransmitter fragments over millimetre-scale regions within 10 minutes. These results highlight the instrument's potential for rapid, high-resolution imaging in spatial omics and clinical diagnostics.

5.2 Post-Extraction Differential Acceleration (PEDA)

5.2.1 Theory of Time-Variable PEDA

The theoretical schematic of the time-variable PEDA [106] is illustrated in Figure 5.1. Consider an ion of mass (m) and velocity (v). Under a static and uniform electric field, the ion successfully traverses the extractor. The time (t_1) spent in region (L_1), along with the temporary velocity (v_t) and acceleration a, are described by the following equations:

$$v_t = \sqrt{v^2 + \frac{2qV_E}{m}}, \tag{5.1}$$

$$t_1 = \frac{v_t - v}{a}, \tag{5.2}$$

$$t_1 = \frac{qV_E}{L_1 m}\left(\sqrt{v^2 + \frac{2qV_E}{m}} - v\right). \tag{5.3}$$

Upon exiting the extractor, the ion enters a region with a dynamic electric field. The voltage settings, including the repeller voltage ($V_A + V_E$), extractor voltage (V_A), pulse jump voltage (ΔV_{Jump}), step voltage (ΔV_{step}), and pulse trigger time (τ), are optimised using a genetic algorithm.

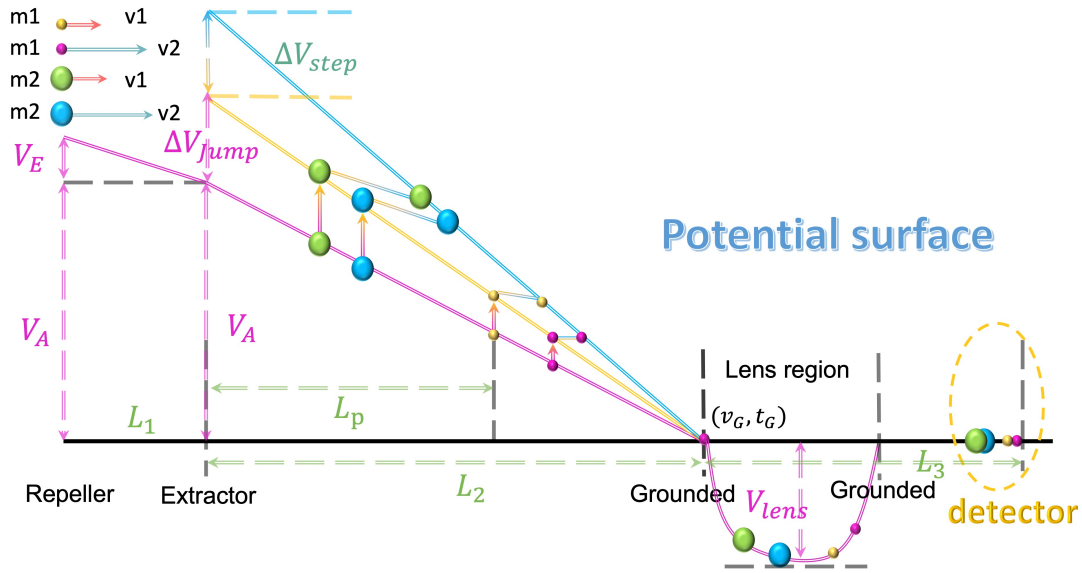


Figure 5.1: Theoretical diagram shows how time-variable PEDA work for ions with different mass and velocity values. Yellow particle is the light ion with low initial velocity, red particle is the light ion with high initial velocity, green particle is the heavy ion with low initial velocity, while the blue one is the heavy ion with high initial velocity. For the ions with same mass, but different initial velocities, the slower ion is closer to the extractor plate at the trigger time. Thus, it will gain more extra potential than the faster one, and it is possible to compel the ions with different initial velocities timely focus on the detector.
For the ions with different masses, the heavier ones are slower to pass the extractor plate, and they need more increased potentials. By precise calculation and voltage regulation, ions with different masses will have the same focal length.

Due to hardware limitations, the pulse shape is modelled as an instantaneous voltage jump followed by an exponential rise. The distance travelled after extraction (L_P),

the velocity at trigger time (v_P), and the velocity at the end of the acceleration region (v_G) are defined by:

$$L_P = v_t(\tau - t_1) + \frac{qV_A}{2mL_2}(\tau - t_1)^2, \tag{5.4}$$

$$v_P = \sqrt{v^2 + \frac{2q}{m}\left(V_E + \frac{V_A L_P}{L_2}\right)}. \tag{5.5}$$

The pulsed voltage is governed by an RC circuit. The voltage difference of the step and the total dynamic voltage at time t are:

$$V_{\text{dif_step}} = 1 - \exp\left(\frac{\tau - t}{R_{\text{step}} \cdot C \cdot 10^6}\right), \tag{5.6}$$

$$V_D = V_A + \Delta V_{\text{Jump}} + \Delta V_{\text{step}} \cdot V_{\text{dif_step}}. \tag{5.7}$$

Lighter ions are typically focused using the initial voltage jump, whereas heavier ions benefit from the gradually increasing step voltage. The final velocity v_G at time t_G is:

$$v_G = v_P + \frac{q}{mL_2}\int_{\tau}^{t_G}(V_A + V_D)\,dt. \tag{5.8}$$

Since the lens is electrostatically neutral for acceleration, ion motion beyond the grounded plate is considered uniform. The total time-of-flight (ToF) is:

$$t_f = t_G + \frac{L_3}{v_G}, \tag{5.9}$$

$$t_d = t_f(v_0, m/z) - t_f(\bar{v}_0, m/z), \tag{5.10}$$

where $\bar{v}_0$ is the average initial velocity. A smaller time deviation t_d indicates improved mass resolution.

5.2.2 Ion Trajectory Simulation

SIMION 2020 was employed to simulate ion trajectories and compute both mass and spatial resolutions, as introduced in Chapter 2. A custom `LUA` script automated the electrode control and ion source configuration. The system comprises three electrodes, one of which operates dynamically. Minor voltage fluctuations across these electrodes

significantly affect ion behaviour; hence, a multi-parameter genetic algorithm (GA) optimisation strategy was adopted.

The GA was executed over 10,000 iterations (100 generations $\times$ 100 populations). Ions were launched from three spatial origins, each separated by 0.1 mm, with a mean kinetic energy of 3.32 eV and an angular spread of 30°. The input velocity distribution is a critical factor in determining the appropriate voltage settings, particularly as the angular distribution is one of the key parameters influencing the ability of the Einzel lens to achieve spatial focusing of the ion images. Therefore, the ion velocity distributions measured in Chapter 4 have been applied in this study. Three reference masses (e.g., 200, 400, 600 m/z) were used to span a target mass window (200-600 m/z. Each run comprised 111 ions per mass-position pair, totalling 999 ions.

In this study, both simulations and experiments were carried out in positive ion mode, with the stage voltage maintained at +8 kV. To determine the spatial resolution, three groups of ions were initialised at distinct positions on the repeller, separated by a distance d_1. After propagation through the ion optics, their final positions on the detector were recorded, yielding a separation d_2. The instrument magnification, M, was defined as

$$M = d_2/d_1.$$

Each ion group produced a spot on the detector with a spatial spread characterised by a standard deviation, from which the full width at half maximum (FWHM) of the signal intensity was determined. The spatial resolution, R, was then calculated as the ratio of the detector spot FWHM to the magnification,

$$R = \mathrm{FWHM}/M.$$

The calculated spatial resolution as a function of the ion optic voltage setting is presented in Figure 4.3(a) in Chapter 4, illustrating the dependence of the instrument's performance on the applied extraction conditions.

Five parameters are subject to optimisation: the lens voltage, extractor baseline voltage, first pulse voltage, second pulse voltage, which is reached using a time dependent exponential voltage ramp, and the trigger time of the first pulse. Optimisation is carried

out using a Genetic Algorithm (GA), which searches for parameter combinations that optimise a figure of merit and hence maximise instrument performance. The fitness function, $F = SR/MR$, combines spatial resolution (SR) and mass resolution (MR), where a lower spatial resolution and higher mass resolution are desired. Consequently, optimal voltage settings are selected when the GA yields a minimum value of the fitness parameter F, corresponding to a configuration that simultaneously enhances both spatial resolution and mass resolving power. Following optimisation using the Genetic Algorithm, the voltage configuration in positive ion mode was set as follows: +8 kV on the stage, +5.53 kV on the extractor, and -14.3 kV on the lens. When the PEDA is triggered, the extractor voltage is pulsed from its baseline of +5.53 kV to +5.87 kV, then exponentially ramped to +6.87 kV. The beam trigger time t_0 is defined as the firing time of the primary C_{60}^+ ion beam. Two trigger delays, 380 ns and 450 ns, are used to optimise the mass resolution across different m/z ranges. The simulated voltage settings were verified experimentally by fixing the stage and lens voltages and scanning the extractor voltage in 10 V steps under static conditions. The voltage at which the grid-pattern ion image came into focus was defined as the optimised setting. The experiments indicate that the inaccuracy of the simulation is less than 20 V, confirming the reliability of the ion trajectory simulation, as Figure 5.2 shows.

5.2.3 Experimental method

Instrument and Measurement Procedure

The instrument, based on linear ToF SIMS (Ionoptika, Chandler's Ford, UK), featured a C_{60}^+ ion beam (IOG C60-20S). Further setup details are provided in Figure 3.19. Briefly, the detector assembly comprised microchannel plates (MCPs), BC-408 scintillator/P 47 phosphor screen, and TimePix3-based/intensified CCD camera. Vacuum pressures were monitored, and analyses were conducted at pressures $\leq 2\times10^{-8}$ mbar. The C_{60}^+ ion beam, defocused to 2.5 mm, was optimized for a continuous ion beam current of 700-800 pA at a source temperature of 380 °C.

The experimental process is illustrated in Figure 3.19. The sample is mounted on either a silicon chip or an indium tin oxide (ITO) substrate and is bombarded by a

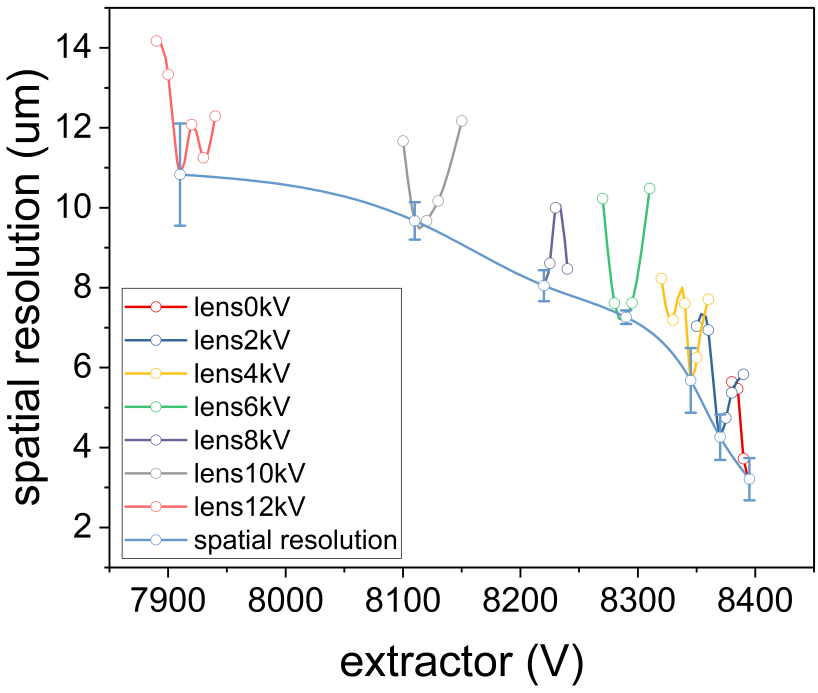


Figure 5.2: presents the spatial resolution obtained under a range of extractor and lens voltage settings. The black line represents the results of the ion trajectory simulations performed in SIMION, whereas the coloured data points correspond to the experimental measurements. The close agreement between the simulated and experimental results provides confidence in the accuracy of the calibration and the predictive capability of the simulations.

defocused C_{60}^{+} primary ion beam (Ionoptika). The primary ion beam is operated at 40 keV, with a typical experimental current ranging between 700–800 pA. The initial pulse width of the primary ion beam is 100 ns, and is bunched to a duration of less than 6 ns.

Secondary ions (SIs) generated from the sample surface are extracted and focused using an ion lens assembly. These ions are detected after time-of-flight (ToF) separation by a microchannel plate (MCP)-phosphor screen assembly, which converts the ion signal into photons. The gain voltages for the detector are configured as $-820\,\mathrm{V}/+820\,\mathrm{V}/+4200\,\mathrm{V}$ for the front MCP, back MCP, and P 47 phosphor screen, respectively. In the MCP–BC-408 assembly, the gain voltages for the detector are applied as $0\,\mathrm{V}/+1600\,\mathrm{V}/+5600\,\mathrm{V}$ for the front MCP, back MCP, and scintillator, respectively.

Different detection and data acquisition systems are employed, including a photo-

multiplier tube (PMT) and Charge-Coupled Device (CCD) or TimePix3-based camera, depending on the application. The photomultiplier tube (PMT) and CCD camera are used in tandem as a detection assembly. The PMT is employed for the acquisition of time-of-flight (ToF) spectra, with each spectrum averaged over 1,000 laser shots to enhance the signal-to-noise ratio. Simultaneously, the CCD camera is used to acquire gated, mass-resolved images, providing two-dimensional spatial distributions corresponding to selected ion masses. In parallel, the TimePix3-based camera is independently employed to record both the spatial distribution and ToF information of individual ions. This enables simultaneous acquisition of ion images and ToF spectra with single-ion sensitivity and high temporal resolution, without the need for signal averaging.

During data processing for both spectra and imaging, time-of-flight values and single-shot ion images are centroided to improve mass and spatial resolution. For CCD-based imaging, each individual ion impact is centroided to enhance spatial accuracy. In the case of the TimePix3-based camera, which records both spectra and images simultaneously, centroiding is applied not only to the spatial data but also to the ToF data. Corrections are made using the time-of-arrival (ToA) and time-over-threshold (ToT) information to process ToT correction [177, 178] further refining both temporal and spatial resolution.

5.2.4 Triggering

A primary ion beam pulse with a 100 ns initial pulse width was fired at time 0 (t_0). The C_{60}^+ triggered the delay generator, marking t_0 as the C_{60}^+ ion beam fire time. Other trigger pulses are applied to trigger the buncher, PEDA voltage box, secondary ion deflector, PMT, TimePix3-based/CCD camera within the recognizing time of the fire of the ion beam C_{60}^+ as t_0.

5.2.5 Post-extraction differential acceleration (PEDA)

The ion optical configuration has been previously described in Ref.[158]. In this setup, an electrodynamic PEDA was employed, wherein the voltage pulse was applied to the extractor plate. Spatial resolution and magnification are controlled via an Einzel lens, which focuses the ion trajectories. The current spatial separation between the stage and

the extractor is 5.5 mm, while the distance from the extractor to the grounded plate of the Einzel lens is 12 mm. The stage voltage was fixed at +8 kV. The amplitude of the PEDA pulse controls the velocity-focusing capability for secondary ions, whereas its trigger time determines the mass range that is temporally focused. The voltage applied to the Einzel lens is correspondingly adjusted in relation to the PEDA pulse to optimise spatial focusing of the secondary ion beam.

5.2.6 Sample preparation

To evaluate the performance of the SIMS system, dye samples with grid pattern were employed. For the characterization of mass resolution and spatial resolution, a series of laser dyes (Auramine O, Rhodamine B, Rhodamine 640, Exalite 404, Exalite 428) and Irganox 1010 (chemical information is provided in Table 5.1) were uniformly deposited using a home-built electrospray setup. The electrospray parameters were set to a voltage of 5.6 kV, a flow rate of 20 µL/s, and a spraying duration of 20 minutes. The laser dye solution was electro-sprayed onto 25 mm × 25 mm indium tin oxide (ITO) coated glass slides or silicon wafers (chips $10\times10\times0.5$ mm) overlaid with nickel meshes (140 µm pitch) and TEM support grids with 50/100 mesh sizes (corresponding to 250-500 µm pitch) to generate well-defined grid patterns.

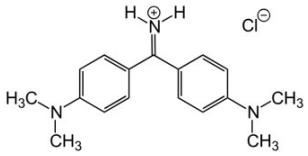
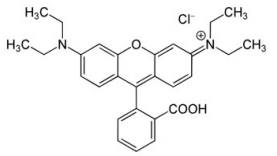
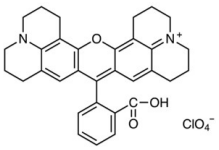
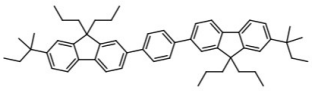
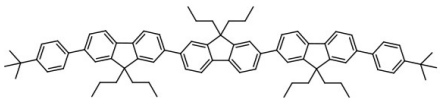
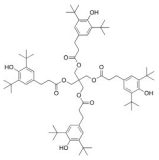
For biological validation, wild type mouse brain tissue (Mary Lyons Centre) was cryo-sectioned to a thickness of 10 µm using a cryo-microtome onto silicon wafers. The tissue sections were stored at -80 °C and dehydrated before analysis.

5.2.7 Data Processing

Intensified CCD camera images were acquired at a frame rate of 5 Hz. The TimePix3-based camera was operated at a repetition rate of 100 Hz for a total acquisition time of 10 minutes per dataset.

All data processing was conducted using Python (version 3.11.9). Images were generated in both raw and centroided formats. Spatial resolution analysis was performed by extracting intensity profiles across selected grid regions. The spatial resolution was quantified using two methods: one based on curve fitting, and the other employing the

Table 5.1: Chemical compounds with their molecular weights and structures.

Chemical Name	Molecular Weight (g/mol)	Structure
Auramine O	303.83	
Rhodamine B	479.02	
Rhodamine 640	591.05	
Exalite 404	658	
Exalite 428	1011.51	
Irganox 1010	1177.6	

standard 20%-80% criterion, which measures the width across the rising edge of each intensity peak corresponding to the grid features.

5.3 Results and discussion

5.3.1 Post-extraction differential acceleration

To ensure affordability and maximize spatial information and throughput, we employed a linear ToF mass analyser. The entire imaging area can achieve up to 2 mm, as shown in the top Panel images in Figure5.3(a). The pitch size of the grids is 250 µm. However, the inherent low mass resolution of the linear ToF presents a significant drawback. In addressing this limitation, we introduced an electrodynamic PEDA to enhance the mass

resolution across wide mass ranges by focusing the secondary ion velocity distribution along the ToF axis.

In the current instrument configuration, a three-electrode ion lens assembly, comprising the stage, extractor, and lens, is employed to extract and focus secondary ions (SIs). Details of this configuration have been previously described in Ref [158]. The voltage ratios between these components are critical for preserving and accurately focusing the spatial information of the ions. An electrodynamic PEDA is applied to the extractor electrode; both the amplitude and timing of the PEDA pulses play a crucial role in determining the achievable mass resolution and the optimised mass range. Following optimisation using the Genetic Algorithm, the voltage configuration in positive ion mode was set as follows: +8 kV on the stage, +5.53 kV on the extractor, and −14.3 kV on the lens. When the PEDA is triggered, the extractor voltage is pulsed from its baseline of +5.53 kV to +5.87 kV and then exponentially ramped to +6.87 kV. The beam trigger time t_0 is defined as the firing time of the primary C_{60}^+ ion beam. Two trigger delays, 380 ns and 450 ns, were used to optimise the mass resolution across different m/z ranges.

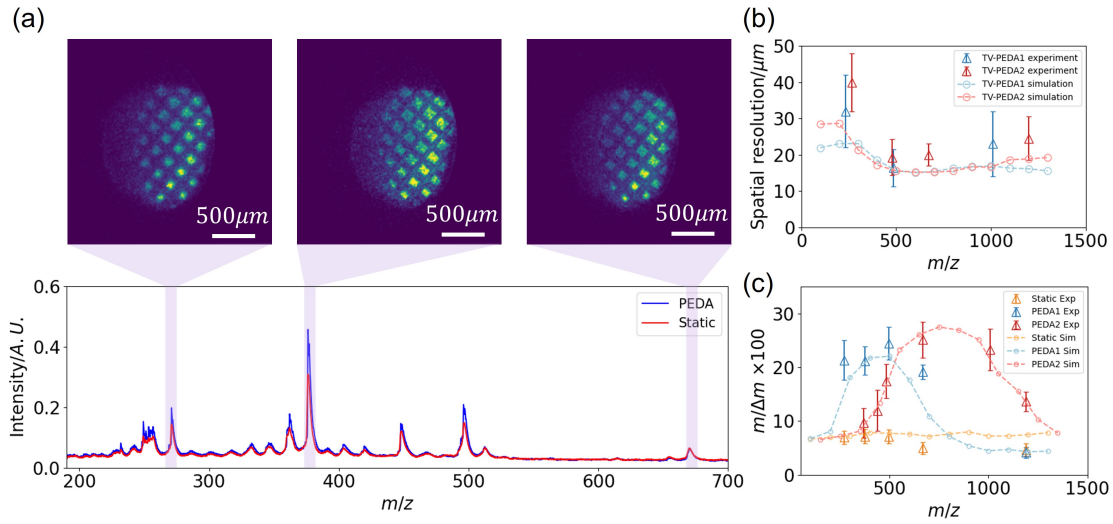


Figure 5.3: (a) shows the ion image (top panel) and spectrum (blue) with time-dependent PEDA, while the spectrum is compared with the one applied static electric field. (b) is the simulation and experiment spatial resolutions with 380 ns (light red and light blue) and 450 ns (dark red and dark red) trigger time PEDA. (c) shows the simulation and experiment spatial resolutions with 380 ns (blue) and 450 ns (red) trigger time PEDA, and static electric field (yellow).

The PEDA pulse is effective when the secondary ions (SIs) are located in the region between the extractor and the lens. Consequently, the trigger delay and the spatial

separation between the extractor and lens predominantly determine the optimised mass range. Figure 5.3(a) presents the mass spectra and corresponding ion images for two cases: one using a static electric field and the other employing PEDA with a 380 ns trigger delay. Under static extractor conditions, the mass resolution is approximately $500\,m/\Delta m$. When PEDA is applied with optimised timing (e.g., a 380 ns trigger delay), the mass resolution improves significantly, exceeding $2000\,m/\Delta m$. As an electrodynamic method, PEDA is capable of enhancing mass resolution across a broad mass range. For a trigger delay of 380 ns, the optimised mass range spans from approximately $250\,m/z$ to $600\,m/z$, covering a mass window of around $350\,m/z$, as shown by the blue curve (simulation) and dots (experiments) in Figure 5.3(c). Another important parameter for MSI, the spatial resolution, is maintained between 12 and 25 µm within the optimised mass range, as demonstrated by the blue curve (simulation) and data points (experiment) in Figure 5.3(b).

Currently, the mass resolution is limited by the detector response time. The scintillator employed in this study is a P 47 layer, which exhibits an emission peak with a rise time of 6.7 ± 0.2 ns and a decay time of 168 ± 2.3 ns [167]. This relatively long decay time can limit the accuracy of FWHM measurements of individual mass peaks, which are commonly used to calculate the mass resolving power of the instrument. To reduce the influence of the phosphor time response, we instead utilise the leading edge of the peak (20–80%) to estimate the peak width for calculating the mass resolution, in agreement with the method in previous work [158]. Alternatively, to mitigate the effects of the decay tail, the mass peaks can be analysed using derivative mode: in this representation, the leading edge of an original mass peak appears as a positive signal in the derivative spectrum, while the trailing edge generates a negative signal, as illustrated in Figure 5.4(a). Experimental Rhodamine B ToF spectra are presented in Figure 5.4(b), comparing the raw spectrum (orange) with the corresponding derivative spectrum (blue). With the application of PEDA, the ToF peaks are temporally focused; however, the achievable time resolution remains constrained by the response time of the P 47 detector. By applying the derivative approach to the spectrum, the effective ToF peak width becomes equivalent to the rise time of the P 47 detector. The corresponding transformed mass spectrum is presented in Figure 5.5.

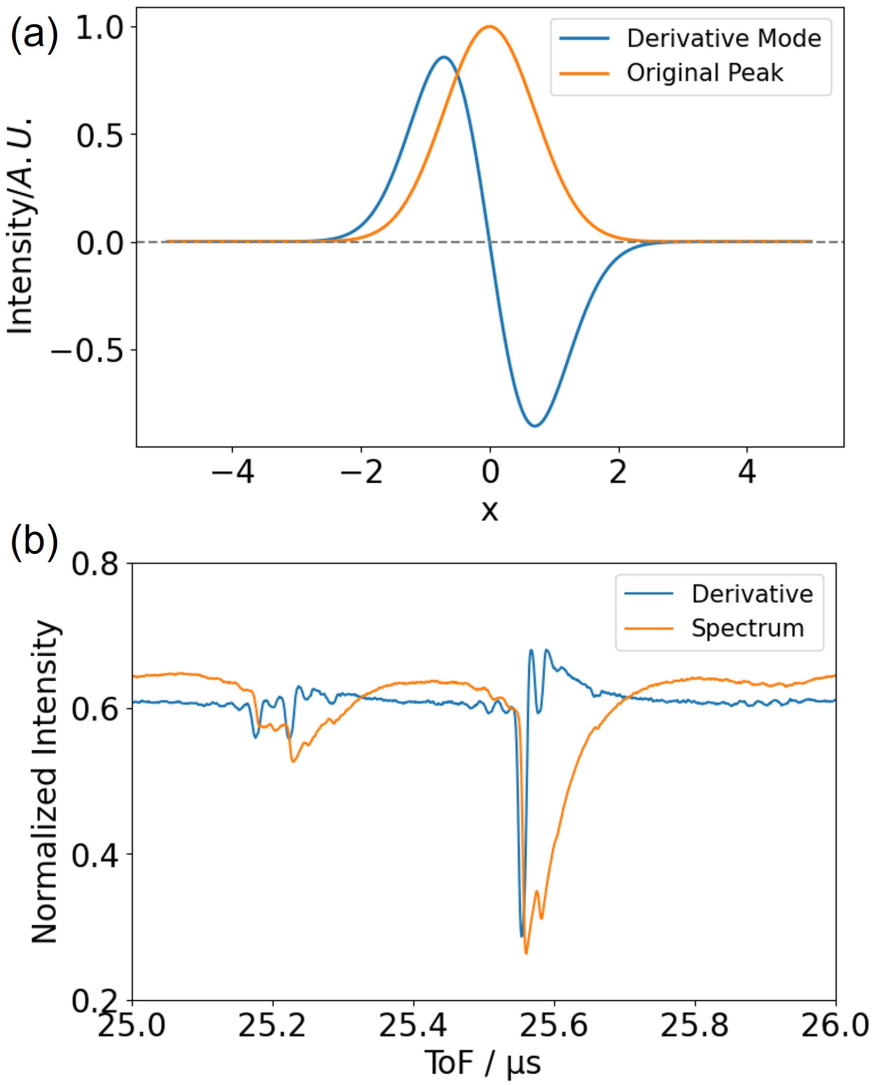


Figure 5.4: (a) Schematic of the derivative strategy. The orange curve represents a simulated Gaussian-distributed peak, while the blue curve shows its derivative. The rising edge of the original peak corresponds to the positive derivative peak, whereas the falling edge is transformed into a negative peak. (b) Experimental ToF peak shown as an example.

The derivative strategy can be implemented either during data acquisition using the oscilloscope or post-analysis using a derivative algorithm. The oscilloscope can record the derivative ToF spectrum of a single frame and average, for example, 1000 frames to produce a well-defined averaged derivative spectrum. Alternatively, in post-analysis, a derivative algorithm can be applied to an averaged raw spectrum to generate a similarly well-defined averaged derivative spectrum.

Figure 5.5 shows a derivative spectrum collected using the oscilloscope, comparing

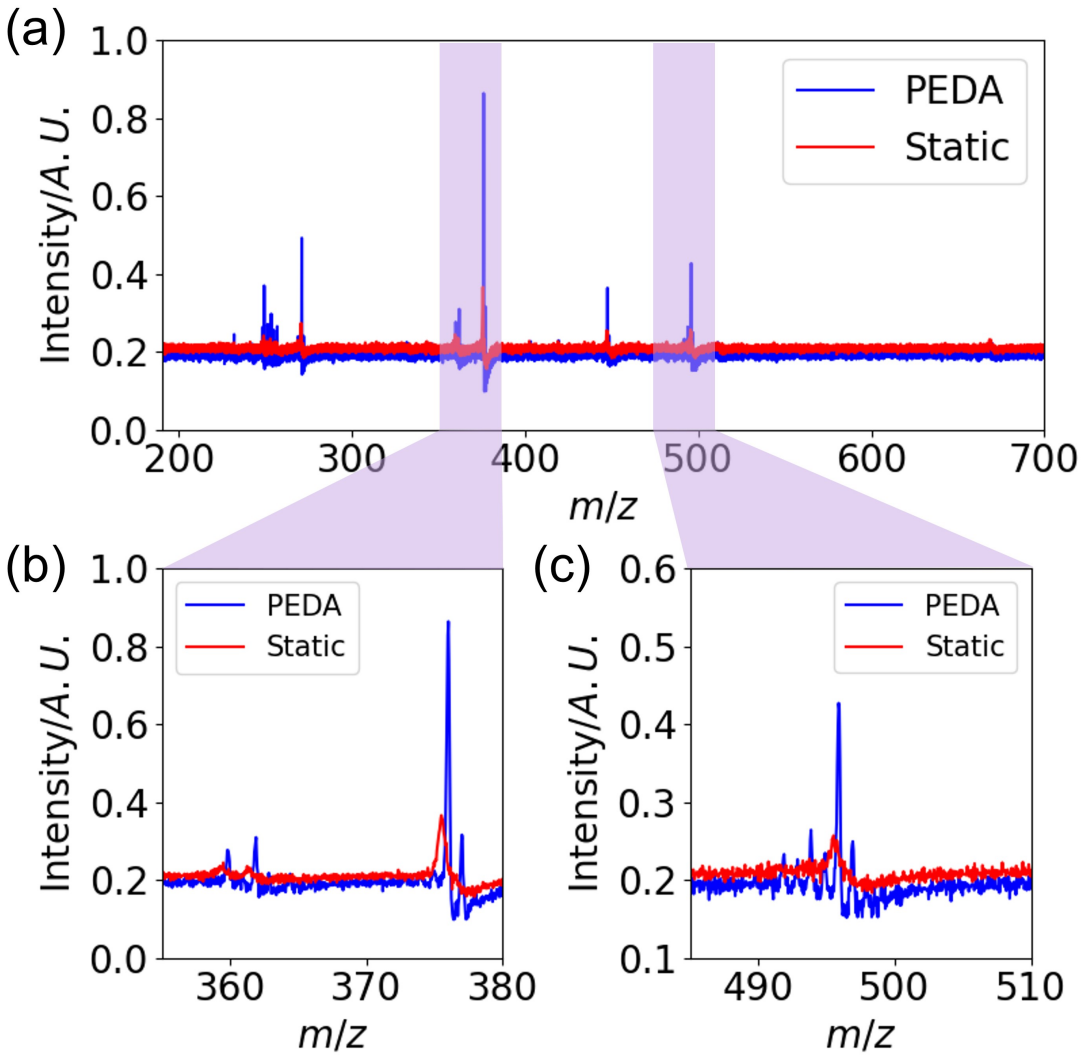


Figure 5.5: Derivative mass spectrum of the PEDA, optimised in the mass window between 250–600 m/z.

peaks recorded with (blue) and without (red) the PEDA, which applies a 380 ns delay. In the derivative spectrum, the leading edge of each original mass peak appears as a positive signal, while the trailing edge appears as a negative signal. This approach mitigates the negative impact of the long decay time of the P 47 phosphor screen. As shown in Figure 5.3(a), the raw Rhodamine B mass peak at 375 m/z can be distinguished using PEDA, but the adjacent peaks are not fully resolved. By applying the derivative procedure, however, the adjacent mass peaks become clearly resolved, as illustrated by the blue curve in Figure 5.5(b).

This enhancement enables the resolution of small mass differences, such as those

arising from a single hydrogen atom, as evidenced by the blue traces in Figure 5.3(a) and Figure 5.5. The PEDA system is effective only within a limited mass range. As shown in Figure 5.6, the lower mass range (250–600 m/z) has been successfully optimised. To extend the optimisation to higher masses, a mixture of dyes, including Rhodamine 640, Rhodamine B, Auramine O, and Exalite 428, was prepared and sprayed in a grid pattern onto the ITO-coated slide. By delaying the PEDA trigger time from 380 ns to 450 ns, the optimised mass range was shifted to cover 500–1200 m/z. As shown in Figure 5.6(a) and (d), the Exalite 428 peak exhibited improved focus when PEDA was applied to higher masses, yielding a mass resolution of 2332.7 ± 385.8 m/Δm at 1010.5 m/z. The corresponding Exalite 428 ion image also displayed enhanced focus, achieving a spatial resolution of 23 ± 9 µm.

To further demonstrate the robustness of PEDA, another organic sample, Irganox 1010, was tested. A uniformly coated Irganox 1010 layer was covered with a TEM support grid (mixed mesh with a pitch size of 62–125 µm). Its mass spectra acquired with (blue) and without (red) PEDA (480 ns trigger delay) are shown in Figure 5.7(a), while the corresponding ion image obtained with PEDA is shown in Figure 5.7(b). Analysis of the rising edge of the mass peaks yielded a mass resolution of 1364.7 ± 180.7 m/Δm at 1189 m/z. The spatial resolution measurement is presented in Figure 5.7(c). A Gaussian fit was applied to determine the spatial resolution, which was 20.38 µm for the selected peak, with the average spatial resolution maintained at 24.5 ± 6 µm.

The optimised mass range corresponds to the range of ion masses that can be effectively stored and accelerated within the region between the extractor and the Einzel lens. This range is fundamentally constrained by the physical distances between the repeller, extractor, and lens electrodes. As shown in Figure 5.8, simulations illustrate the influence of these inter-electrode gaps on the optimised mass range.

A straightforward means of extending the optimised mass range is to increase the distance between the extractor and the lens, thereby allowing a broader spectrum of ions to be accommodated. More significantly, reducing the distance between the repeller and the extractor leads to a notable enhancement in the mass range. This effect arises because the gap between the repeller and extractor is inherently smaller than that between the extractor

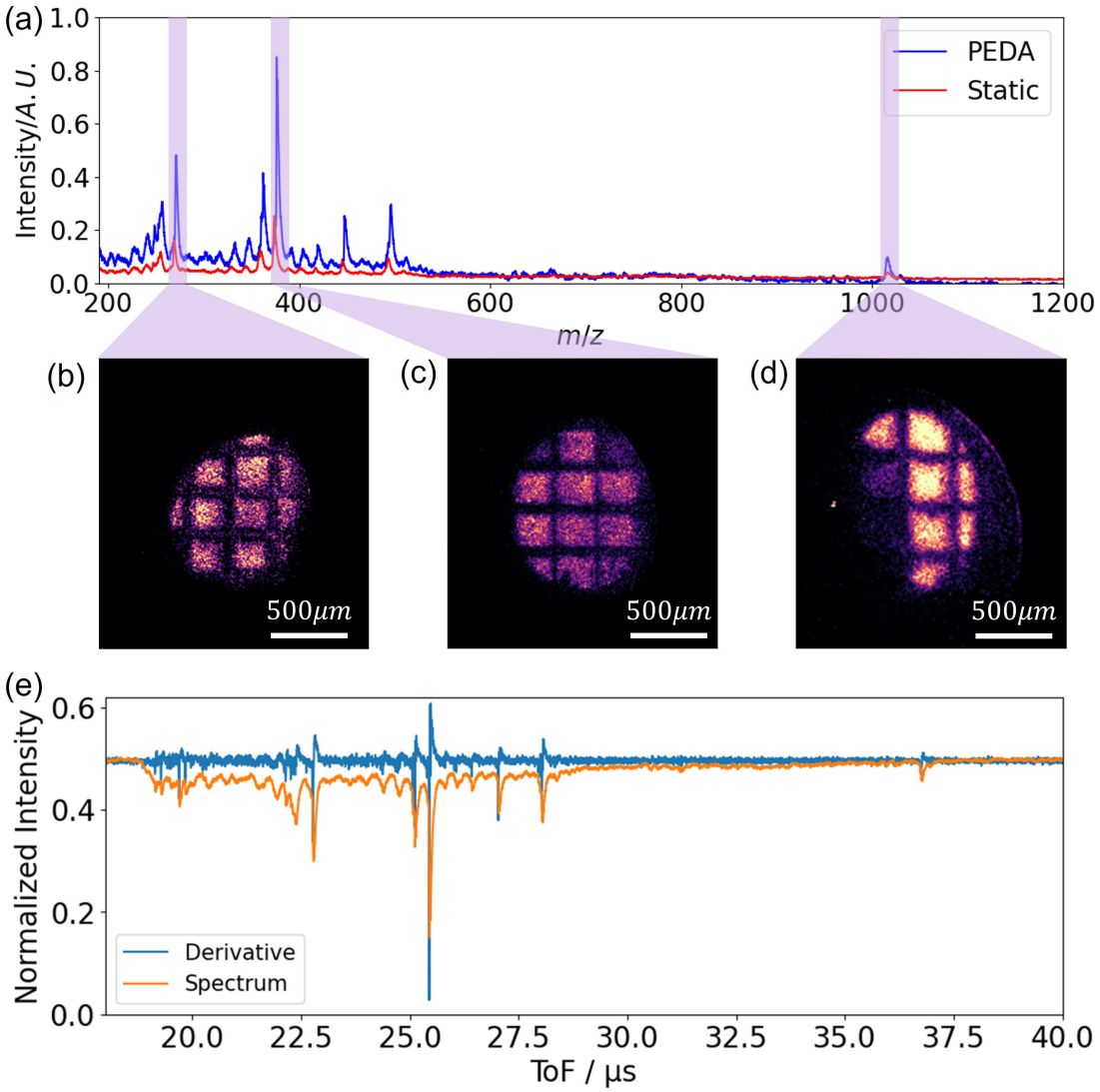


Figure 5.6: (a) Mass spectrum of the mixed dyes, including Rhodamine B, Rhodamine 640, Auramine O, and Exalite 428. (b)–(d) Spatial ion distributions of Auramine O, Rhodamine B, and Exalite 428 grids acquired under PEDA conditions with a 480 ns trigger delay. (e) Comparison of the raw ToF spectrum (orange) and the corresponding derivative ToF spectrum (blue) derived from panel (a).

and the lens, and primary ion acceleration predominantly occurs within this shorter region. A reduced acceleration distance compresses the spread in ion velocities and consequently narrows the mass dispersion at the point of extraction. As a result, increasing the gap between the extractor and the lens allows a greater number of distinct ion masses to be optimally focused, thereby broadening the effective mass range of the system.

In the current configuration, the distance between the repeller and extractor (L_1) is 5.5 mm, and the distance between the repeller and ion lens (L_2) is 12 mm, as shown in

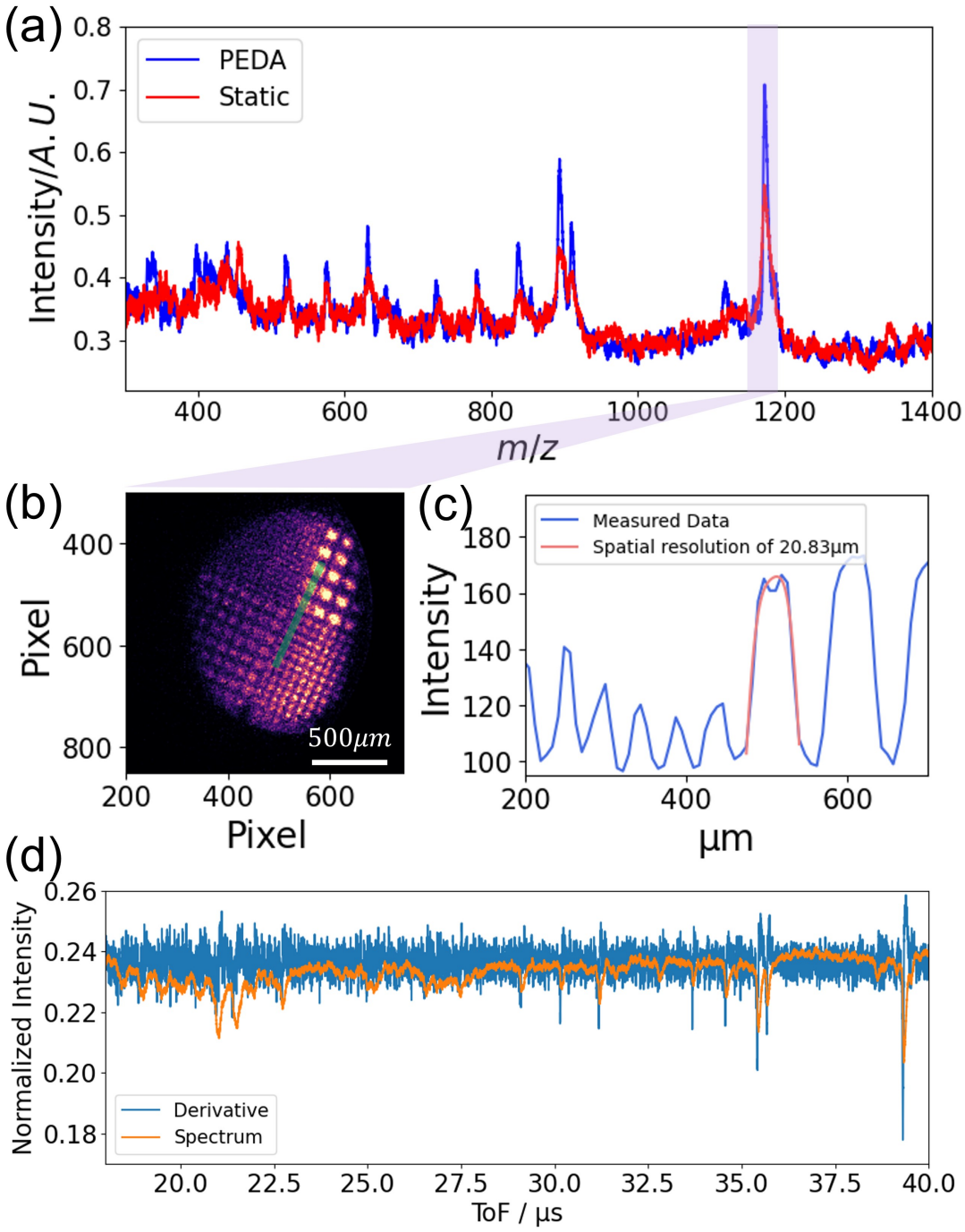


Figure 5.7: (a) Comparison of Irganox 1010 mass spectra acquired with (blue) and without (red) PEDA. (b) Irganox 1010 parent ion image obtained with PEDA. (c) Signal intensity profile of the selected region in (b), indicated by the green square. (d) presents a comparison of the raw ToF spectrum (orange) and the corresponding derivative ToF spectrum (blue) derived from panel (a).

Figure 5.8(a). Initially, the ion lens assembly was repositioned further from the extractor, increasing the repeller-to-lens distance to 17 mm. This modification broadened the

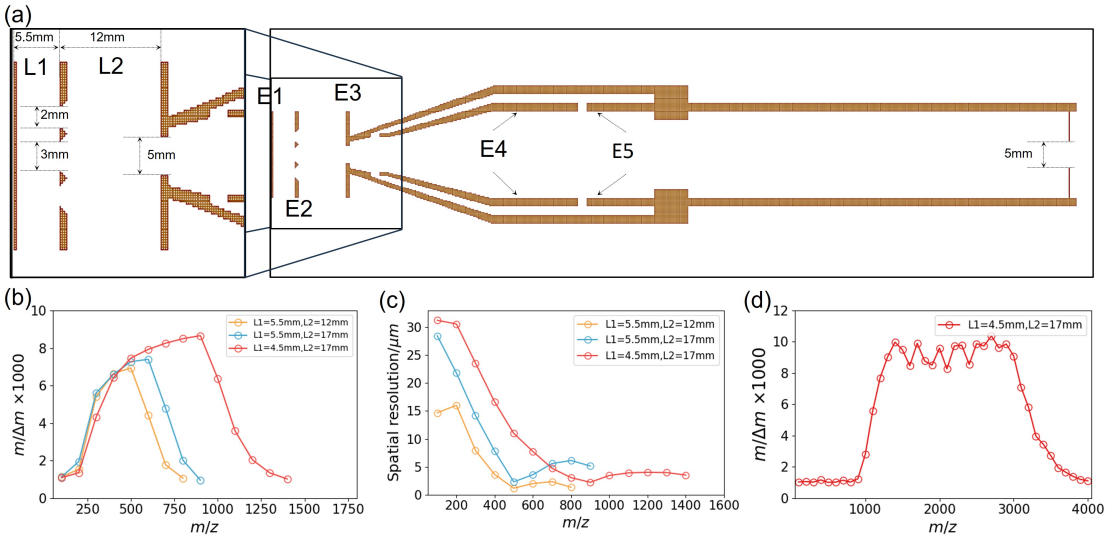


Figure 5.8: (a) SIMION ion optics model of the current design, with a 5.5 mm repeller–extractor gap and a 12 mm repeller–lens distance. (b) and (c) show the simulated optimal mass resolution and spatial resolution over the optimised mass range after modifying the electrode distances (L_1 and L_2), as shown in the legends. (d) Simulation of mass resolution for optimised detection above 1000 m/z.

optimised mass range from 250–600 m/z to 250–750 m/z, due to an expanded region for ion storage between the extractor and lens.

Subsequently, by maintaining the increased extractor–lens distance (L_2) at 17 mm and reducing the repeller–extractor gap (L_1) from 5.5 mm to 4.5 mm, the optimised mass range was further extended to 250–1100 m/z, nearly doubling that achieved with the original configuration, as shown by the red line in Figure 5.8(b). This enhancement arises from the ions being accelerated more rapidly, which compresses the mass clusters and reduces their spatial dispersion before entering the extractor–lens region, thereby improving the overall performance of the PEDA.

For even higher mass species ($m/z > 1000$), simulations indicate that the optimised mass range can reach up to approximately 2200 m/z by changing the PEDA trigger time from 420 ns to 800 ns in the simulation, as shown in Figure 5.8(d).

5.3.2 The impact of scintillator rise time on the mass resolution

Currently, the mass resolution is limited by the rise time of the P 47 phosphor screen, which is approximately 6.7 ns[167]. To address this limitation, we investigated an

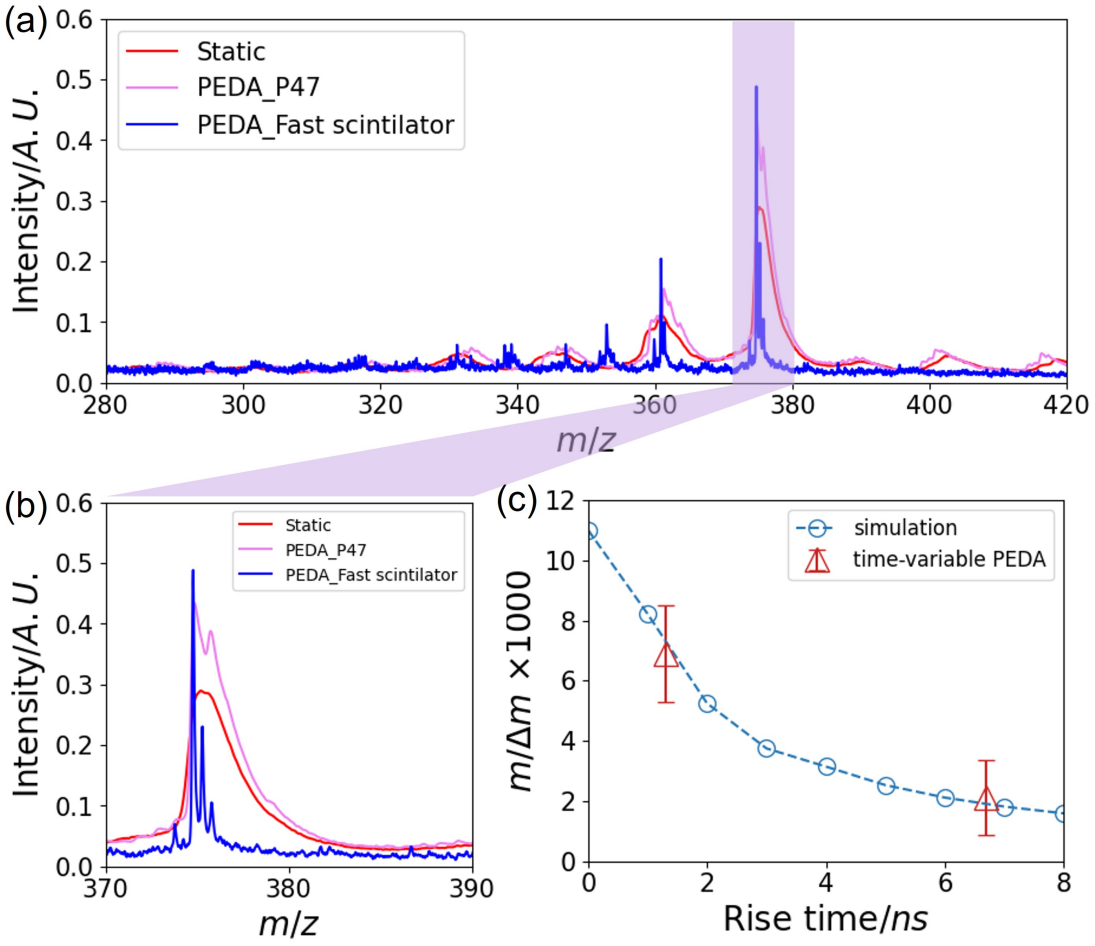


Figure 5.9: (a) shows the Rhodamine B mass peaks with static extractor voltage and P 47 screen (red), the peaks with PEDA and P 47 screen (purple) or BC-408 scintillator (blue). (b) shows the SIMION simulation and calculation on the rising time impact on the mass resolution.

alternative scintillator (BC-408) with a rise time of approximately 1 ns[234]. As shown in Figure 5.9(A), the red peak corresponds to the Rhodamine B signal acquired using P 47 under static conditions, while the purple peak represents the same ion under PEDA conditions. Although PEDA significantly sharpens the peak, the signal remains broadened, primarily due to the long decay time of the P 47 screen. In contrast, the blue peak illustrates the Rhodamine B signal obtained using the BC-408 scintillator under PEDA conditions. Compared to P 47, the BC-408 enables full resolution of individual isotopic peaks corresponding to different numbers of hydrogen atoms, with the mass resolution improving from $2120 \pm 315\, m/\Delta m$ (P 47) to $6890 \pm 401\, m/\Delta m$ (BC-408).

Since mass resolution is measured from the rise edge of the signal peak, the rise time

of the phosphor screen directly affects resolution performance. Figure 5.9(B) presents a simulation of the influence of scintillator rise time on achievable mass resolution. In the ideal case of zero rise time, the simulated mass resolution reaches up to 18,014 $m/\Delta m$. As the rise time increases, the resolution degrades accordingly, consistent with the experimental observations.

5.3.3 Spatial resolution enhancement

To advance the spatial resolution limits of the system, our experimental approach was guided by SIMION trajectory simulations. We systematically investigated a range of electrostatic lens configurations to identify an optimal setting that maximizes spatial resolution. Previous collaborative work, led by Felicia and colleagues, achieved a spatial resolution of 23 µm by compiling cumulative, in-mass-gated images[158]. However, our trajectory simulations reveal the potential to attain spatial resolutions below 2 µm under ideal conditions, *e.g.,* Figure 5.8(c). Achieving such high resolution depends critically on several factors, including the intrinsic pixel size of the detector, the size of the ion event clusters registered per imaging frame, and the contributions of optical aberrations, each of which plays a significant role in determining the ultimate spatial resolving power.

Currently, image magnification within the ion optical assembly is controlled by an Einzel lens, which allows dynamic adjustment through modulation of the applied voltage. In the present experiment, the stage voltage was held constant at +8 kV, while the magnification was varied from 11.2 × to 44.8 × by tuning the Einzel lens voltage from −16 kV to 0 kV. The extractor voltage was correspondingly adjusted to match the varying lens voltage settings. This configuration enables the examination of ion images across multiple spatial scales with enhanced flexibility. As illustrated in Figure 5.10(a) and (c), an increase in magnification corresponds to the enhancement in spatial resolution. This improvement arises from the fact that higher magnification enables the ion signal to be distributed across a greater number of detector pixels. Effectively, this reduces the projected pixel size on the image plane, thereby mimicking an increase in sensor resolution, as observed in digital imaging systems. Consequently, the spatial fidelity of the captured image is enhanced, enabling a more accurate representation of fine structural

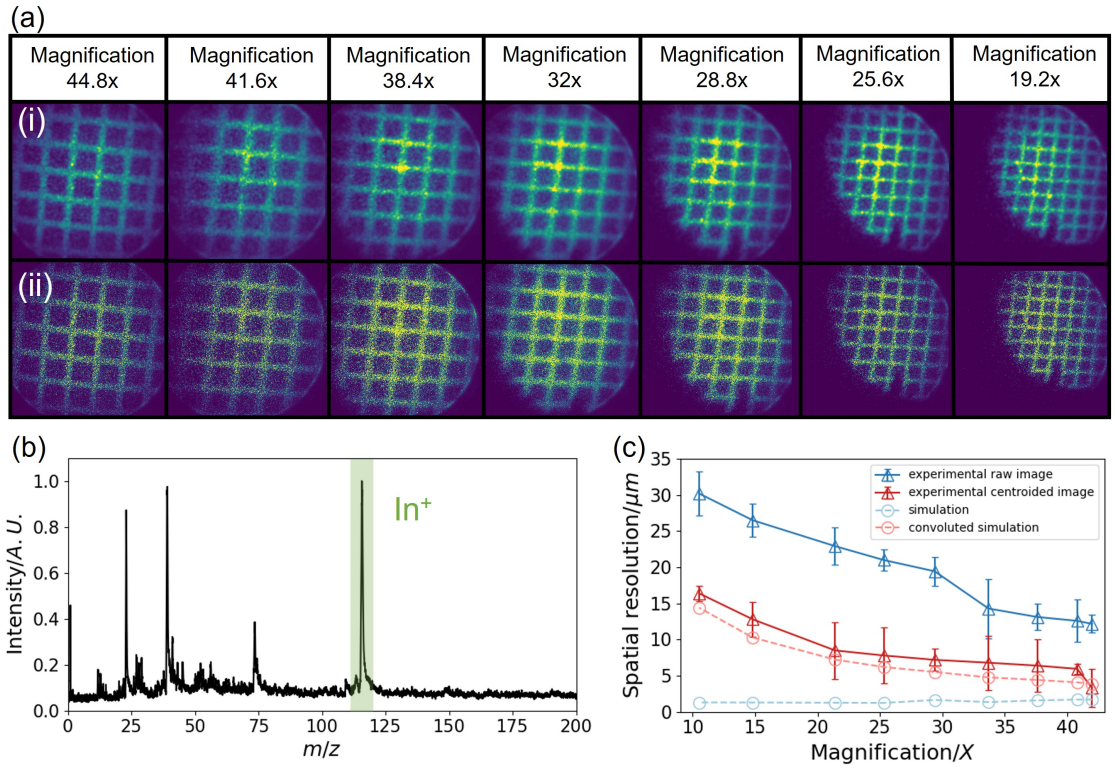


Figure 5.10: (a) Raw (i) and centroided (ii) In^+ Images at Different Magnifications. (b) Corresponding Mass Spectrum: The mass spectrum corresponding to the experiments in (a). The gated mass window is highlighted with a green square. (c) Magnification Impact on Spatial Resolution: This panel illustrates the effect of magnification on spatial resolution. The solid lines correspond to the experimental data from Panels (i) (dark blue) and (ii) (dark red) in Panel (a), representing the raw and centroided spatial resolutions, respectively. The dashed curves show simulation results: the raw simulated spatial resolution (light blue) and the simulated spatial resolution convoluted with the detector pixel size (light red).

features. Under optimised conditions, +8 kV applied to the repeller, +7.38 kV to the extractor, and 0 kV to the lens, a mean raw spatial resolution of 12.17 ± 1.24 µm was achieved at the highest applied magnification of $44.8\times$.

Another factor limiting the spatial resolution is the size of the individual ion detection clusters. When a single ion event spans multiple detector pixels, the resulting signal becomes spatially broadened, which can blur fine image details. This effect is particularly pronounced when the cluster size is large relative to the detector pixel pitch. To mitigate this, a centroiding algorithm is applied to compress the spatial distribution of each ion event by calculating its centre of intensity and reassigning it to a single representative pixel. The process of imaging centroiding, as illustrated in Figure 3.15, serves to eliminate

background signals and condense target ion events into a single pixel. This mitigation of overlap among adjacent ion events is crucial for improving the overall image quality. A comparison of the images before (Figure 5.10(a)(i)) and after (Figure 5.10(a)(ii)) the centroiding process clearly shows that the centroided images are sharper and exhibit enhanced contrast. The corresponding spatial resolutions are compared in Figure 5.10(c), where the blue and red solid lines represent the non-centroided and centroided data, respectively. The spatial resolution of the centroided images is improved by approximately a factor of two.

Conventionally, spatial resolution is assessed by analysing the intensity profile across a grid image. A bold grid line is selected, and the spatial resolution is defined as the distance across the intensity profile between the 20% and 80% levels. Additionally, a Gaussian fitting function is applied to the rising and falling edges of the intensity curve. The spatial resolution is then calculated using the full width at half maximum (FWHM), which has been discussed in Chapter 3.

As shown in Figure 5.11, a grid image was acquired using a CCD camera with a magnification of about 44.8 $\times$. Using the conventional 20%–80% intensity method, the measured spatial resolution is $12\,\mu m \pm 1.56\,\mu m$ (Figure 5.11(b) inset). Using the Gaussian fitting method, the calculated spatial resolution is $12.96\,\mu m \pm 1.35\,\mu m$ (Figure 5.11(b) red line fit).

As discussed in Figure 5.10, one of the limitations to spatial resolution is the size of the ion event clusters. After applying centroiding to the raw image, the processed image is shown in Figure 5.11(c). Using the conventional method on the centroided image, the spatial resolution improves to $3.5\,\mu m \pm 0.75\,\mu m$ (Figure 5.11(d) inset), while the Gaussian fitting yields a result of $3.36\,\mu m \pm 1.65\,\mu m$ (Figure 5.11(d) red line fit). The good agreement between both measurement approaches validates the spatial resolution analysis. Moreover, the centroiding process enhances the spatial resolution by approximately a factor of four. Panel (ii) in Figure 5.10 (a) showcases the ion images after the centroiding process, revealing a notably sharper image with a 2-3 times improvement in resolution. With the largest image magnification, the achieved spatial resolution reaches approximately $3.56 \pm 2.12\,\mu m$.

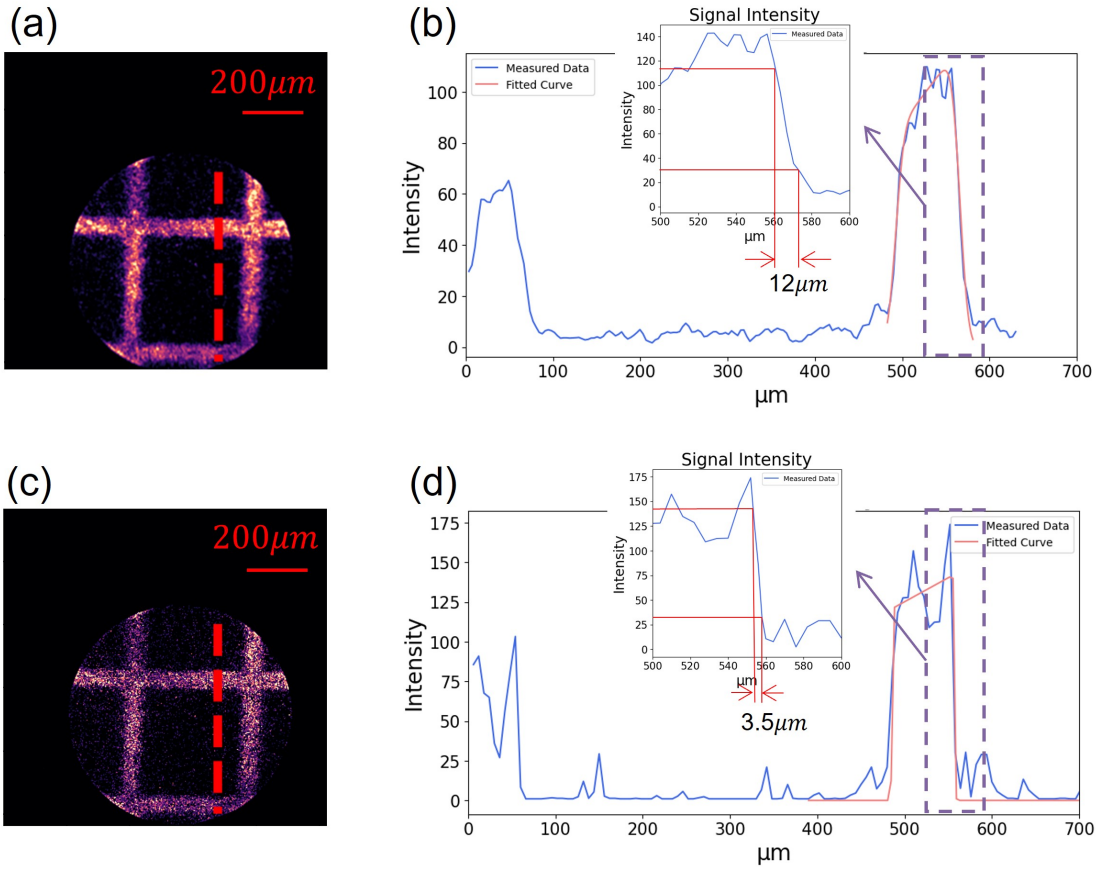


Figure 5.11: (a) and (c) show the raw and centroided grid images, respectively. (b) and (d) display the corresponding intensity profiles, with Gaussian fitting applied to the edges of the peaks.

However, the experimental spatial resolution remains slightly inferior to the simulated values, primarily due to aberrations in the ion optics. The extraction electrode features a 2 mm central aperture, and the edge effects of the extraction electric field at this edge induce spherical aberration, which leads to image distortion. As illustrated in Figure 5.12, the optimal spatial resolution is achieved at the centre of the extractor. The resolution gradually deteriorates as the radial distance of the detected ions from the extractor centre increases, a behaviour characteristic of aberrations in the ion optics system. Figures 5.12 (a) and (b) present centroided images obtained at magnifications of 11.8× and 44.8×, respectively, where the grid pitch is 140 µm. Owing to a misalignment of the central aperture of the extractor, the peak signal position does not coincide precisely with the geometric centre of the extractor. Figure 5.12 (c) shows the spatial resolution measured at each grid position, with alignment to panel (b) indicated by the grey arrow.

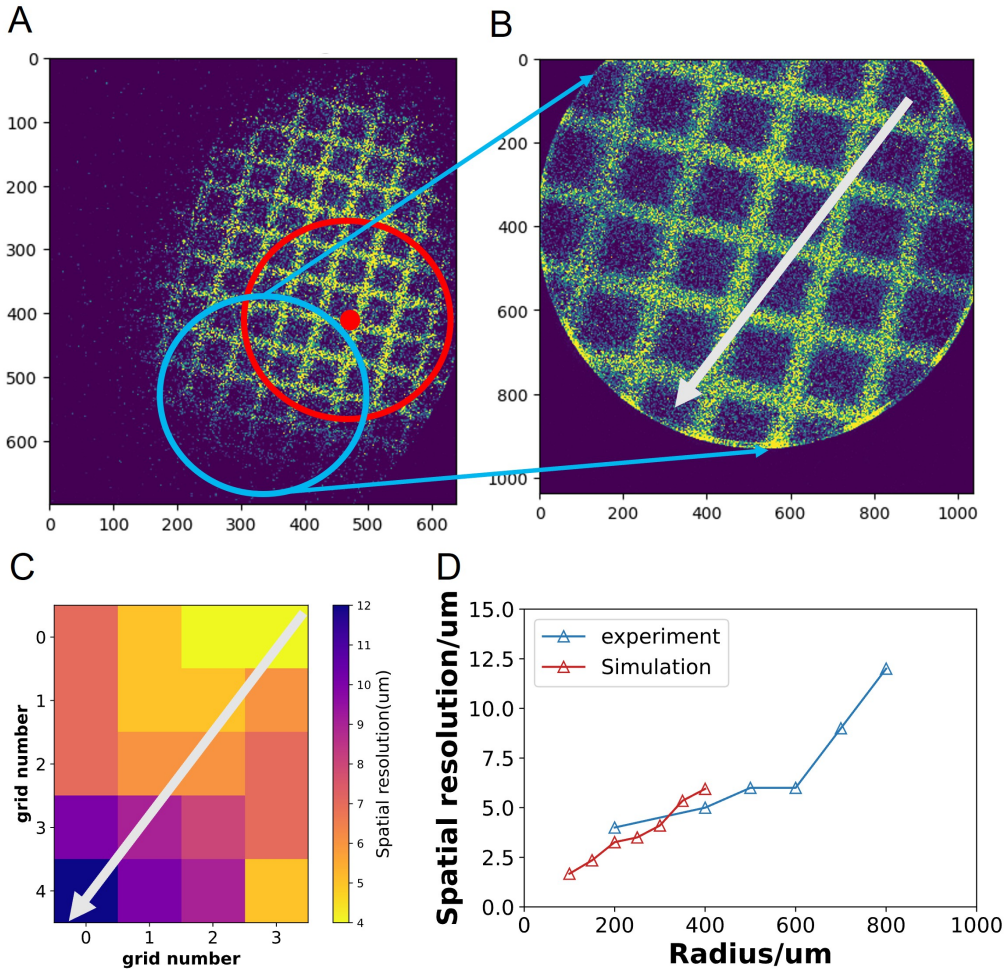


Figure 5.12: (a) and (b) present centroided images acquired at magnifications of 11.8× and 44.8×, respectively, with a grid pitch of 140 µm. Owing to a slight misalignment of the extractor's central aperture, the peak signal position does not coincide with the geometric centre of the extractor. (c) shows the spatial resolution measured at each grid position, aligned with panel (b) as indicated by the grey arrow. (d) illustrates the variation in spatial resolution as a function of radial distance from the extractor centre, demonstrating a clear deterioration in resolution towards the periphery.

Panel (d) depicts the measured spatial resolution as a function of the radial position from the extractor centre, confirming the degradation in resolution towards the periphery. This provides a quantitative measure of the spherical aberration in the current ion optics. The overlap between the experimental and simulated results is good, indicating that a 200 µm radius contributes to a reduction in spatial resolution of approximately 2 µm. This deterioration is primarily caused by the limited diameters of the extractor and lens central apertures. To mitigate this effect, the ion optics should be redesigned to enlarge the open areas of these central apertures.

5.3.4 PEDA with TimePix3

Although the CCD camera can produce high spatial resolution images due to its greater number of sensor pixels, it suffers from low acquisition efficiency, as it is only capable of capturing a single ion image per exposure. In contrast, the TimePix3-based camera enables the simultaneous detection of multiple ions, capturing both their spatial and temporal information in real time.

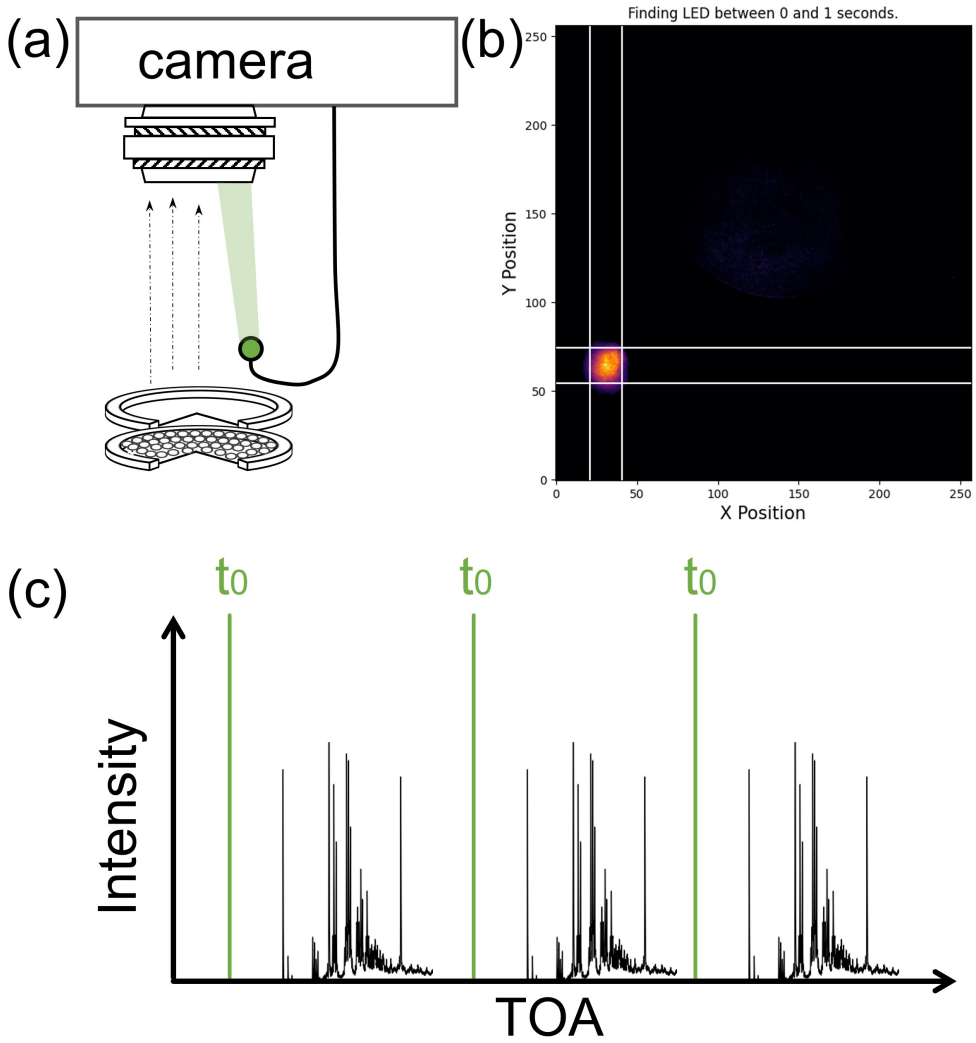


Figure 5.13: (a) Schematic of the LED trigger system, in which an LED is externally fixed to the camera and positioned in front of the phosphor screen. (b) Accumulated image of the LED signal recorded during the first second. (c) Strategy for defining the ToF cycle for the TimePix3-based camera. The green peaks correspond to the LED pulses, which exhibit the highest intensity. The first instance above the threshold is identified as t_0.

Conventionally, a TimePix3-based camera employs an external time-to-digital con-

verter (TDC) to define the precise t_0. However, this approach increases hardware costs. To address this limitation, Wood *et al.* introduced a novel triggering technique that enables a commercially available readout system. In MALDI systems, the laser can be readily split, with part of the beam focused onto a few pixels of the camera and used as a trigger. In the present SIMS instrument, however, the sample is ionised by an ion beam rather than a laser, and the beam cannot be used to trigger the camera. Instead, an external LED is employed to replace the laser and provide a trigger for the TimePix3-based camera [235].

In the current setup, the LED is connected via a flexible, plastic-insulated copper wire and secured by screwing it into the camera housing. The instrument is equipped with a 40 mm MCP/phosphor screen. Increasing the distance between the phosphor screen and the camera reduces the effective number of camera pixels utilised and thereby decreases the spatial resolution of the image. However, as illustrated schematically in Figure 5.13(a), in order to fit the LED signal within the camera field of view (FoV), the LED is mounted slightly above the phosphor rather than on the same horizontal line. Consequently, when the camera is positioned too close to the phosphor screen, it becomes difficult to focus simultaneously on both the detector signal and the LED signal. To achieve a compromise between FoV and LED focusing, the camera is therefore mounted approximately 25 cm away from the phosphor screen. As shown in Figure 5.13(b), the LED signal is not perfectly focused and appears as an intensified spot, which introduces greater jitter compared with the laser-triggered MALDI system. The LED trigger exhibits greater temporal instability than the laser, with standard deviations in the range of 2-10 ns.

In this study, Rhodamine B was electrosprayed onto an ITO-coated slide using a mesh grid with a spacing of 140 µm. The resulting mass spectrum is presented in Figure S4. Several ions, including m/z 23, 39, 141, and 269, which are tentatively assigned as Na^+, K^+, In^+, and the Auramine O parent ion ($[AO\text{-}Cl^-]^+$), were selected to demonstrate the imaging capabilities of the system. To enhance the time resolution of the ToF spectrum, a ToT correction is applied to adjust the ToA. As shown in Figure 5.15(a), ToF spectra corresponding to different ToT values exhibit distinct initial times. The functional relationship between ToT and the corresponding initial ToA, measured just above the selected threshold, and all ToAs are subsequently corrected according to the

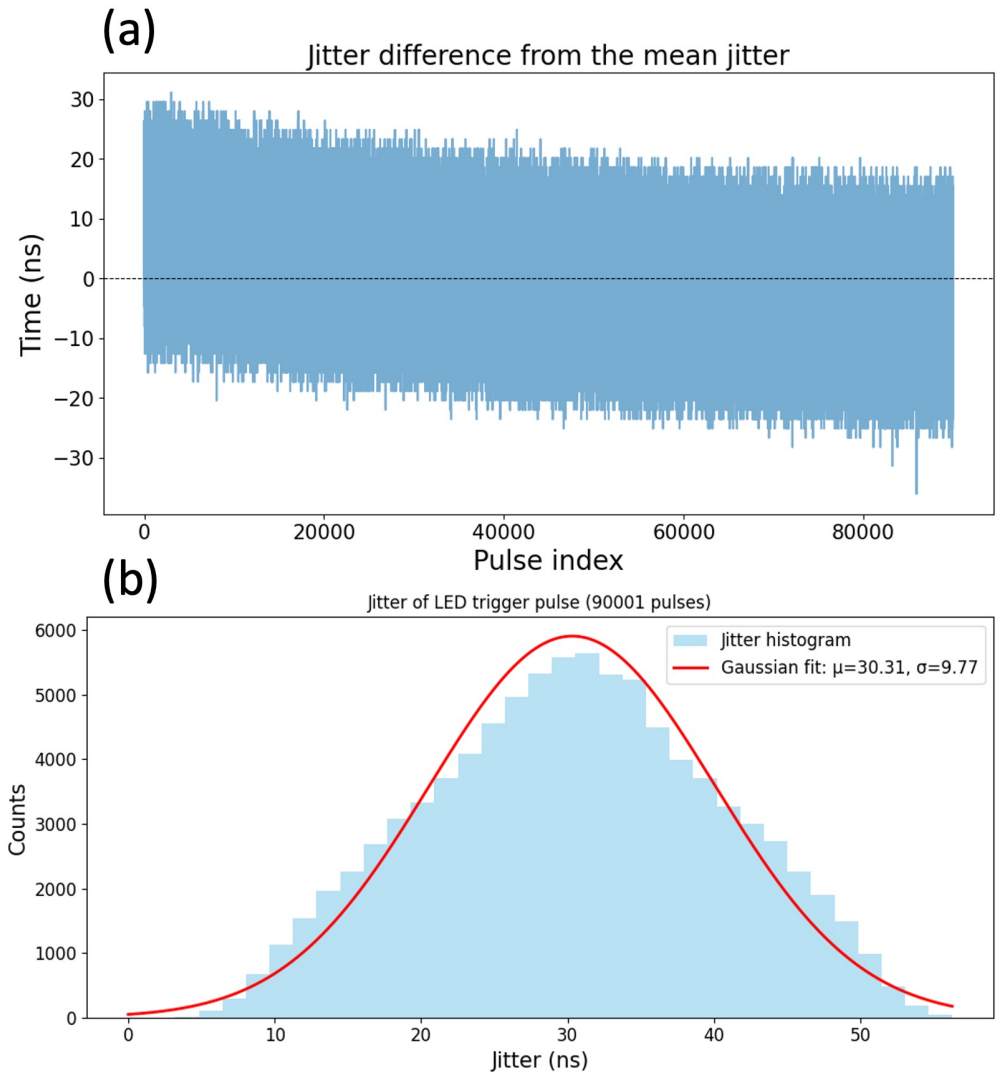


Figure 5.14: Panels (a) and (b) illustrate the timing jitter analysis. Panel (a) shows the deviation of the jitter from the mean value for each data shot, while panel (b) presents the statistical distribution of the jitter. A Gaussian fit function was applied to the distribution to estimate the full width at half maximum (FWHM) of the jitter.

fitted curve. After applying the ToT correction, the peak full width at half maximum (FWHM) is reduced from 90 ns (Figure 5.15(b)) to 43 ns (Figure 5.15(c)), representing an improvement of almost a factor of two.

The optimised spectrum and images were collected under the PEDA condition with a 380 ns trigger delay, as indicated by the blue line in Figure 5.16. Compared with the static voltage setting, the application of PEDA produces sharper and more distinguishable mass peaks. Using the leading edge of the peak, the measured mass resolution under

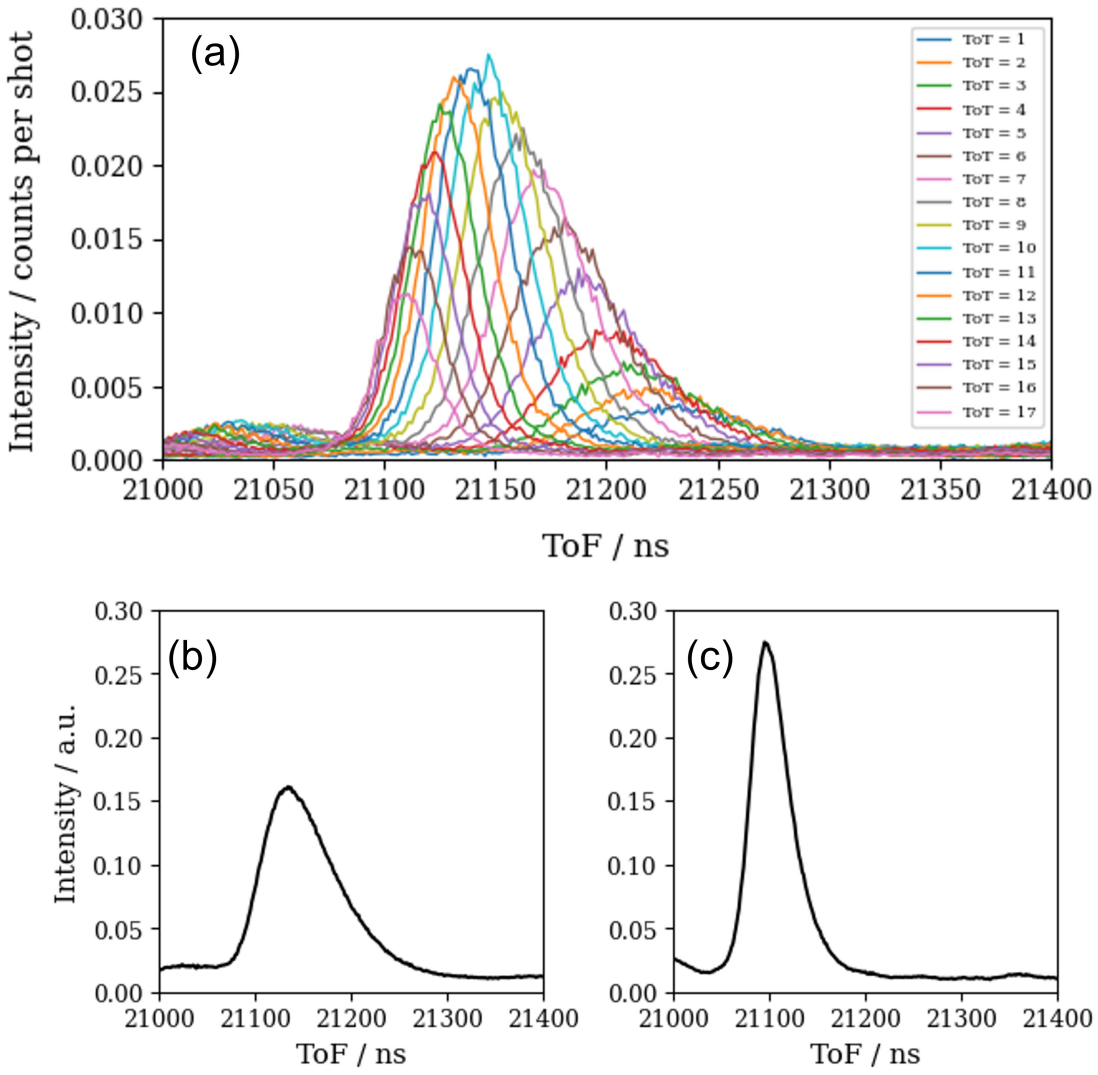


Figure 5.15: (a) ToF spectra of In^+ ions for different ToT values. (b) Full In^+ ToF peak prior to ToT correction. (c) Full In^+ ToF peak after ToT correction.

PEDA was $913.6 \pm 57.1\, m/\Delta m$ at $367\, m/z$. The TimePix3-based camera operates with a nominal time resolution of 1.5625 ns (corresponding to a repetition rate of 640 MHz)[176], but the time precision is limited by the trigger jitter [116]. In the experiment shown in Figure 5.16, the TimePix3-based camera was triggered by an LED, which introduced a jitter with a standard deviation of 9.77 ns, corresponding to a FWHM of 23 ns, as shown in Figure 5.14(b). This constraint could be mitigated by employing a stable commercial internal trigger system.

Unlike CCD-based detection systems, the TimePix3 does not require synchronisation with a fixed repetition rate, thereby allowing experiments to be conducted at rates of up

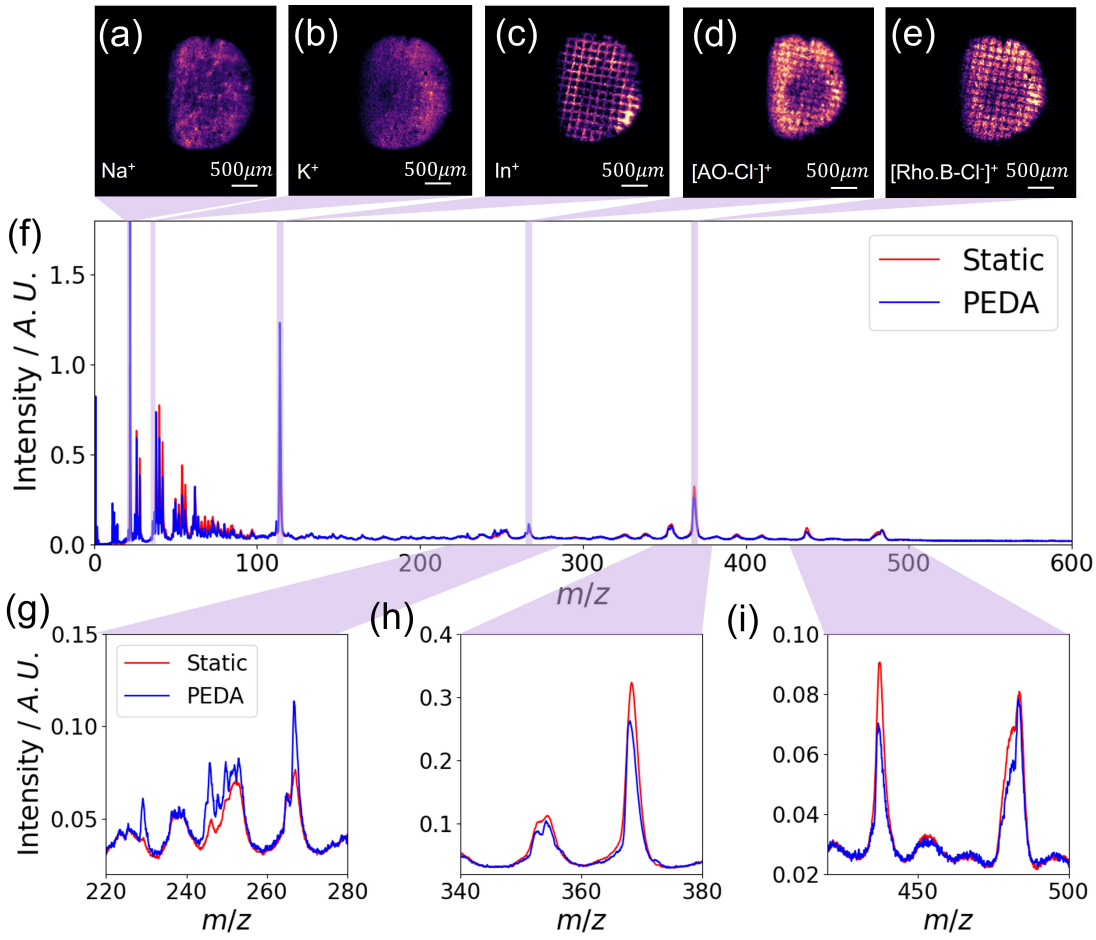


Figure 5.16: Top: Spatial ion images of Na^+ (a), K^+ (b), In^+ (c), $[AO\text{-}Cl^-]^+$ (d) and $[Rho.B\text{-}Cl^-]^+$ (e) under PEDA condition, demonstrating the imaging capability of the TimePix3-based camera. Panel (f) shows the mass spectrum obtained from dye sample on an ITO substrate, with different amplified mass ranges (220-280 m/z, 340-380 m/z, and 420-500 m/z), with static (red) and PEDA (blue) conditions.

to 1 kHz, which is limited by the PEDA pulsed power supplier. In this example, images were acquired over a 15 minute period at a repetition rate of 100 Hz. The resulting ion images exhibit well-defined grid patterns and demonstrate a spatial resolution of approximately 25 µm $\pm$ 3.2 µm. This resolution is primarily limited by the pixel count of the camera (256 $\times$ 256 pixels), with the effective signal area covering only about 80 $\times$ 80 pixels. These results highlight the potential of the TimePix3-based system for rapid and high-resolution mass spectrometry imaging, with acquisition times reduced to the minute timescale.

5.3.5 High-throughput rat brain tissue mass imaging

With the time-dependent PEDA, the mass resolution has been optimized over a wide m/z range while retaining spatial resolution between 12–20 µm. A critical next step is to extend microscope mode SIMS imaging to real biological samples. Using C_{60}^+ primary ion beams, SIMS imaging has already been widely applied in tissue imaging [75, 76, 221] and lipidomics [8, 222]. In particular, C_{60}^+ Secondary Ion Mass Spectrometry (SIMS) has been employed to map the spatial distribution of key ions in mouse brain tissue sections, enabling high-resolution molecular imaging [162, 221, 236–238].

To validate the capability of the microscope mode SIMS instrument for lipid distribution imaging in tissue, a mouse brain tissue section was analyzed as a cross-verification experiment. The mouse brain tissue is taken at the infundibulum (IF) and/or median eminence, and the imaging section is chosen the region crossing the fronto-parietal cortex (FrPT) and hippocampus (Hipp)[239], whose optical image and PMT mass spectrum are shown in Figure 5.17(a) and (b) respectively. Figure 5.17(a) illustrates the region of interest (a diameter of about 2 mm) within the brain, overlaid with an optical image to provide anatomical context. (b) presents the corresponding mass spectrum (0–700 m/z), acquired under an electrodynamic PEDA configuration. In this setting, the stage was held at +8 kV, the extractor at a baseline of +5.53 kV, and the lens at -14.3 kV. Upon PEDA triggering, the extractor voltage was pulsed from +5.53 kV to +5.87 kV at a trigger time of 180 ns, followed by an exponential ramp to +6.87 kV. The resulting spectrum exhibits distinct ion peaks corresponding to biologically relevant species, including potassium (39 Da, K^+), sodium (23 Da, Na^+), and various lipid fragments (e.g., 55 Da, $C_4H_7{}^+$ or $C_2H_5N^+$). Because Na^+ and K^+ ions are much more easily ionized than lipid molecules, their mass peak intensities are significantly higher. To account for this difference, the spectra were scaled by different amplification factors in distinct mass regions: peaks in the 50–200 m/z range were amplified 33-fold, while those in the 350–600 m/z range were amplified 50-fold. Selected ion masses are indicated with orange markers, and their corresponding spatial distributions are presented in Figure 5.18.

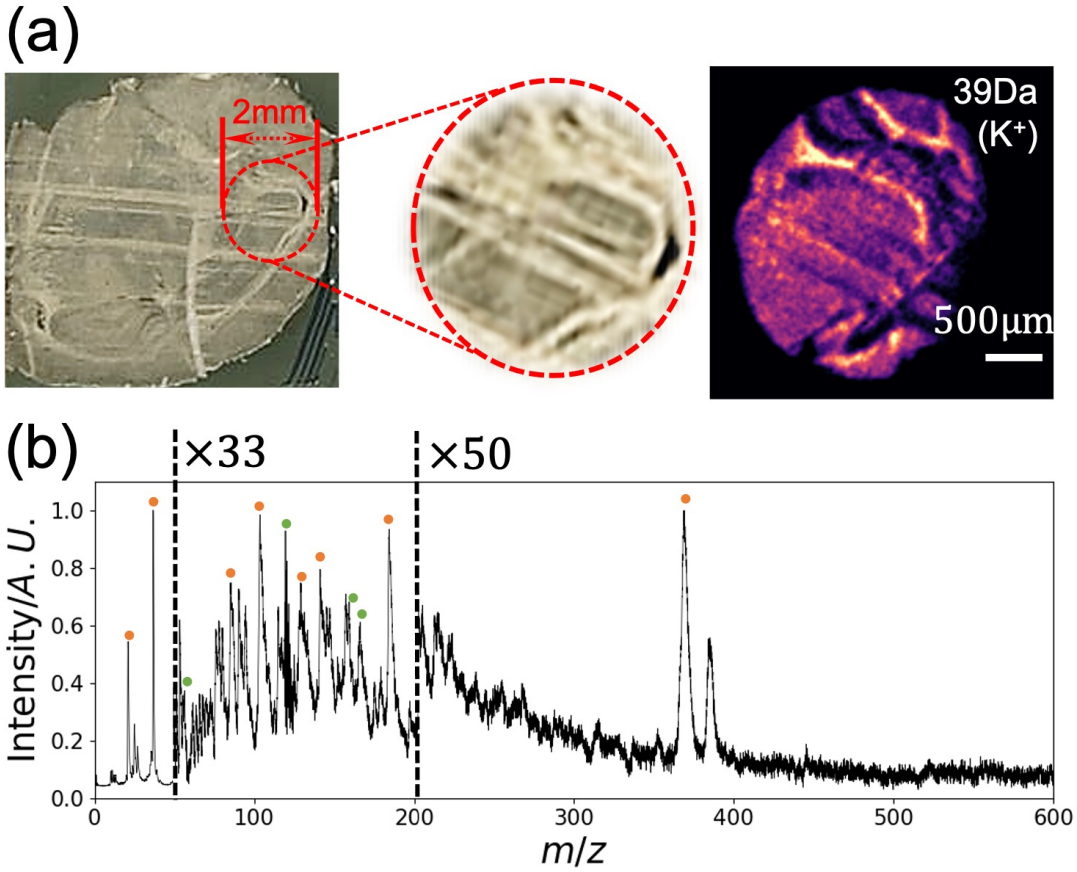


Figure 5.17: Panel (a) shows the optical image (left and middle panels) of the mouse brain tissue coronal section spanning the fronto-parietal cortex (FrPT) and hippocampus (Hipp). The zoomed in optical image is compared with the K^+ ion image shown in the right panel. Panel (b) shows the ToF mass spectrum of the mouse brain, collected using a MCP-P47-PMT system. Selected ion masses are indicated with orange markers and labeled in red in Table 5.2; their corresponding spatial distributions are presented in Figure 5.18 of the main text. Ion masses indicated with green dots correspond to tryptophan fragment peaks at m/z 60, 120, and 159, while the peak at m/z 166 represents an additional phosphocholine fragment. The data were acquired using PEDA with a 180 ns trigger delay.

Figure 5.18(a) presents K^+ ion images of the selected region acquired at different magnifications (14.7×, 19.8×, and 44.8×). As the magnification increases, an improvement in spatial resolution is observed, resulting in enhanced clarity of the labeled isolated region and greater definition of its textural features. Panel (b)-(j) display ion-specific images at about 12 µm resolution, highlighting heterogeneous distributions. Some representative organic ions are selected and labelled in Table 5.2, including fragments derived from phospholipids and amino acids. $C_5H_{14}NO^+$ (104 Da) is assigned to choline [82, 241], a key headgroup component of sphingomyelin, which is a major class of sphin-

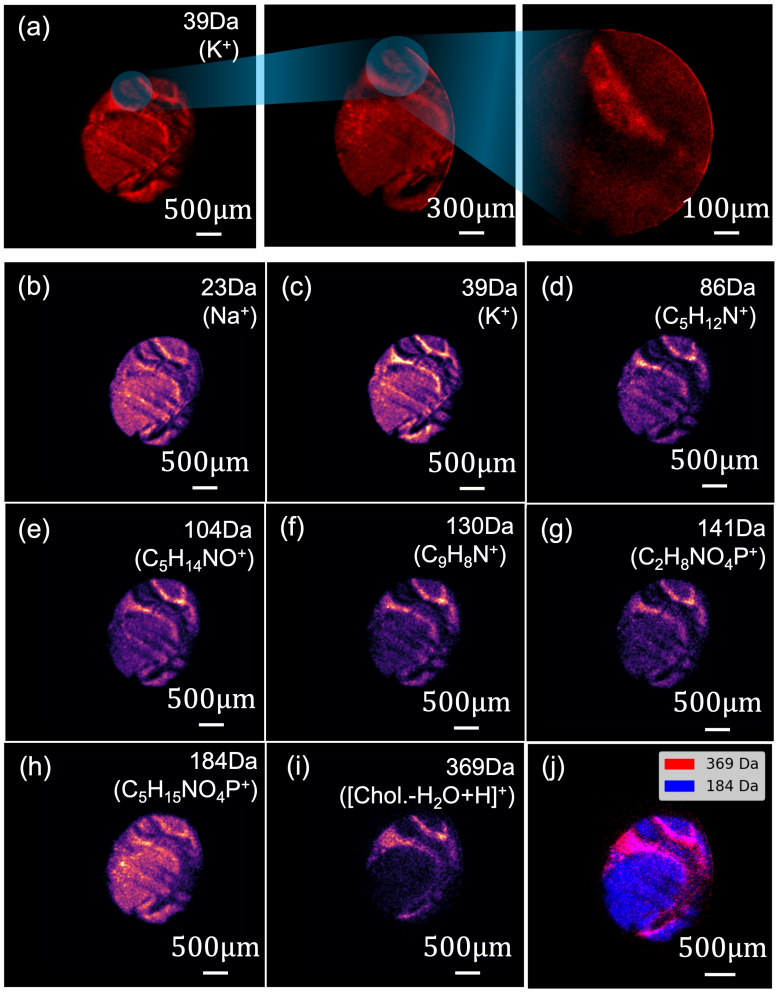


Figure 5.18: Panel (a): Microscope-mode SIMS CCD images of a mouse brain section acquired over 5, 10, and 20 minutes at low, medium, and high image magnifications, respectively. Due to the different magnifications employed, the spatial resolutions of the K^+ ion images range from approximately 3 to 12 µm. The low-magnification (×11.2) 5-minute MSI data are shown in panels (b)–(i) for different inorganic and organic ions, demonstrating the capability for rapid tissue imaging. Panel (j) shows an overlay of the m/z 184 and 369 peaks, highlighting that these species are associated with different regions of the brain (grey and white matter, respectively).

golipids. The ion $C_2H_8NO_4P^+$ (141 Da) is widely used as a diagnostic fragment for phosphatidylethanolamine (PE) in positive mode [242, 243].The ions $C_5H_{13}NO_3P^+$ (166 Da) and $C_5H_{15}NO_4P^+$ (184 Da) are characteristic fragments of phosphocholine-containing lipids, particularly phosphatidylcholine (PC) [82]. These CHNOP-containing ions are commonly observed in positive-ion mode; notably, the 184 Da fragment is especially prominent and is frequently associated with membrane lipid chemistry, including that of M0 macrophages. In addition, $C_{27}H_{45}^+$ (369 Da) is well established as the dehydrated

Chemical formulae	Mass (Da)	Parent molecule	Relevant to parent molecule
$C_2H_6NO^+$	60	Tryptophan	$[M–C_9H_6NO]^+$
$C_5H_{12}N^+$	86	Leucine	$[M–CHO_2]^+$
$C_5H_{14}NO^+$	104	Choline	M^+
$C_8H_{10}N^+$	120	Tryptophan	$[M–C_3H_2NO_2]^+$
$C_9H_8N^+$	130	Tryptophan	$[M–C_2H_4NO_2]^+$
$C_2H_8NO_4P^+$	141	Phosphatidylethanolamine (PE)	$[M–C_{37}H_{68}O_4]^+$
$C_{10}H_{11}N_2^+$	159	Tryptophan	$[M–CHO_2]^+$
$C_5H_{13}NO_3P^+$	166	Phosphocholine (PC)	$[M–H_2O]^+$
$C_5H_{15}NO_4P^+$	184	Phosphocholine (PC)	M^+
$C_{27}H_{45}^+$	369	Cholesterol	$[M–OH]^+$

Table 5.2: Assignment of characteristic lipid fragment ions and their relation to parent molecules [82, 240–245].

fragment of cholesterol ($[M-OH]^+$) [240, 244]. Cholesterol is strongly localised to tissue regions corresponding to white matter, whereas phosphocholine are primarily localised to gray matter regions, in qualitative agreement with the reported lipid compositions of brain tissue [240, 245–247]. These are putative assignments; however, the observed distributions of phosphocholine and cholesterol are broadly consistent with previous ToF-SIMS studies [162, 246–250]. Amino acid fragments can also be detected; for example, $C_5H_{12}N^+$ (86 Da) is assigned to leucine [82]. Tryptophan is another widely distributed amino acid. Characteristic fragments of tryptophan include $C_2H_6NO^+$ (60 Da), $C_8H_{10}N^+$ (120 Da), $C_9H_8N^+$ (130 Da), and $C_{10}H_{11}N_2^+$ (159 Da) [82]. Tryptophan metabolism may provide therapeutic targets for the treatment of age-related diseases associated with inflammation and could contribute to the extension of healthspan and lifespan.

These results underscore C_{60}^+-SIMS's capability to resolve molecular heterogeneity in brain tissue, offering insights for spatial omics studies. This complements our ongoing development of a high-speed MSI platform for proteomic analysis, providing a foundation for mapping complex bio-molecular landscapes in neurological disease research.

5.4 Conclusion

This work presents a new-generation microscope-mode SIMS imaging system that, to a considerable extent, addresses the traditional trade-offs between spatial resolution, mass resolution, and acquisition throughput. Through the implementation of an electrodynamic

PEDA scheme, mass resolutions exceeding 2000 and up to $6800\,m/\Delta m$ have been achieved using a P 47 phosphor screen and a fast BC-408 scintillator, respectively. By dynamically tuning the Einzel lens voltage, signal magnification can be increased up to $44.8\times$, yielding a spatial resolution of $3.56 \pm 2.12\,\mu$m. The use of a genetic algorithm for optimisation of ion optical parameters enables compatibility with a wide mass range while maintaining robust spatial and mass resolutions.

The system's capacity for wide-field, high-resolution mass imaging within minutes is further enhanced by the integration of a TimePix3-based camera, which enables simultaneous acquisition of ion images and time-of-flight (TOF) spectra without constraints imposed by repetition rate. This capability is exemplified through applications such as the spatial mapping of neurotransmitters and inorganic ions in rat brain tissue, with both mass specificity and fine spatial detail.

Taken together, this instrument represents a significant advancement in microscope-mode mass spectrometry imaging, offering a practical and scalable solution for high-throughput spatial omics, clinical diagnostics, and large-area tissue-based studies. The demonstrated performance improvements and operational versatility support its potential for broader adoption in biomedical and translational research.

6
Depth Profile

6.1 Statement of Contributions

This work was carried out in collaboration with Anya Eyres at the National Physical Laboratory (NPL). To ensure transparency regarding contributions: the overall project concept was proposed by Anya Eyres. The experimental methodology was developed jointly, with primary leadership from Anya Eyres. I undertook the initial instrument commissioning and contributed to data collection, while the majority of the experimental data were acquired by Anya Eyres. Together, we defined the requirements and capabilities of the analysis software; my principal role was the development of the TimePix3 and PImMS2 depth profile analysis tools. I also participated in aspects of data analysis, including mass calibration, sputtering frame selection, and the plotting of spectra and images, though the majority of the analysis was performed by Anya Eyres.

In summary, my primary contributions involved the development of the analysis algorithms, along with participation in the experimental design and data acquisition. To avoid any potential conflict, this chapter, therefore, concentrates on the analytical strategy and presents a selection of preliminary results.

6.2 Introduction

As discussed in Chapter 1, Secondary Ion Mass Spectrometry (SIMS) enables three-dimensional (3D) chemical analysis, owing to its ability to sequentially sputter and analyse only the uppermost atomic or molecular layers, typically just a few nanometres thick, under low primary ion fluence conditions. In this context, microprobe mode SIMS has been successfully applied to 3D imaging of biological specimens, including single cells [81, 82] and tissue sections [83], offering molecular-level insights into spatial organisation and biochemical composition.

Despite these advantages, a key limitation of the microprobe mode in mass spectrometry imaging (MSI) is its relatively slow acquisition speed, which becomes particularly pronounced in 3D imaging applications. Given the demonstrated high-throughput capabilities of microscope mode MSI, it is therefore compelling to investigate the feasibility of integrating 3D imaging functionality within the framework of microscope mode SIMS. Such an approach could potentially combine the volumetric analytical depth of conventional SIMS with the rapid image acquisition speed and spatial resolution advantages inherent in the microscope mode.

6.3 Experimental Methods

6.3.1 Instrument setup

The instrument, based on a linear time-of-flight (ToF) SIMS system (Ionoptika, Chandler's Ford, UK), was equipped with a C_{60}^+ ion beam source (IOG C60-20S). The experimental setup details are illustrated in Chapter 3and 5. The detector assembly comprised microchannel plates (MCPs), a P 47 phosphor screen, and one of the following camera systems: PImMS2, TimePix3, or an intensified CCD.

The C_{60}^+ primary ion beam was operated at a source temperature of 380 °C. For sputtering, the beam was semi-focused using a primary ion lens 2 voltage of 23.5–24 kV and run in continuous mode. To minimise surface damage while maximising the number of analysable data points, a low primary ion beam current of 100 pA was initially employed. The current was regulated by adjusting the ion gun grid current, with 100 pA

obtained at a grid setting of 2 mA. The maximum achievable current was approximately 950 pA at 10 mA. For the majority of experiments, a stable current of 750 pA was maintained by setting the grid current to 8 mA. It should be noted that, due to current measurement limitations, all currents were measured in direct current (DC) mode rather than under analytical operating conditions.

During imaging, the primary ion beam was operated in a fully defocused, pulsed mode at repetition rates of 100 Hz (TimePix3-based camera) and 20 Hz (PimMS2 camera), with lens 2 held at 15 kV and a typical beam current of approximately 750 pA. For sputtering, lens 2 was set to 23.5–24 kV to semi-focus the C_{60}^{+} beam, while the beam current was reduced to 100 pA in order to improve depth resolution.

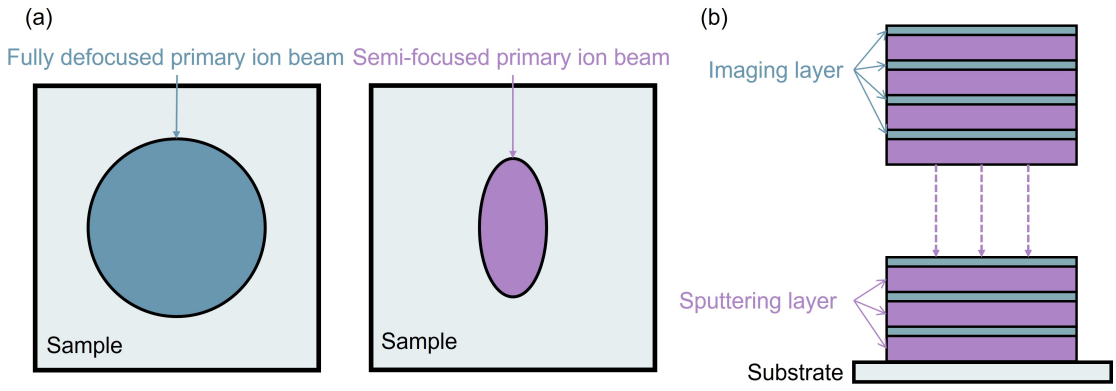


Figure 6.1: Schematic representation of the depth profiling experiment. Different primary ion beam sizes are used for imaging (fully defocused) and sputtering (semi-focused), as shown in (a). Panel (b) illustrates the working principle: imaging and sputtering are performed alternately, with a 2D image acquired after each sputtering cycle, continuing until the substrate is reached.

The working principle of the depth profiling experiment is illustrated in Figure 6.1. As shown in Figure 6.1(a), a fully defocused primary ion beam with a current of 750 pA is employed for imaging, while a semi-focused beam with a lower current of 100 pA is used for sputtering. These two modes operate in an alternating sequence to facilitate layer-by-layer material removal and analysis.

Each complete cycle, comprising one imaging event followed by one sputtering event, constitutes a single data point in the depth profile. At each data point, both a mass spectrum and a 2D molecular image are acquired, enabling the construction of a three-dimensional chemical map of the sample, as illustrated in Figure 6.1(b).

To accurately calculate the profile depth of each cycle, the area of the sputtering needs to be calibrated and calculated carefully. An SED, which is described in Chapter 3, is utilized to image and measure the area of the sputtered crater before and after the depth profile experiment.

6.3.2 Samples

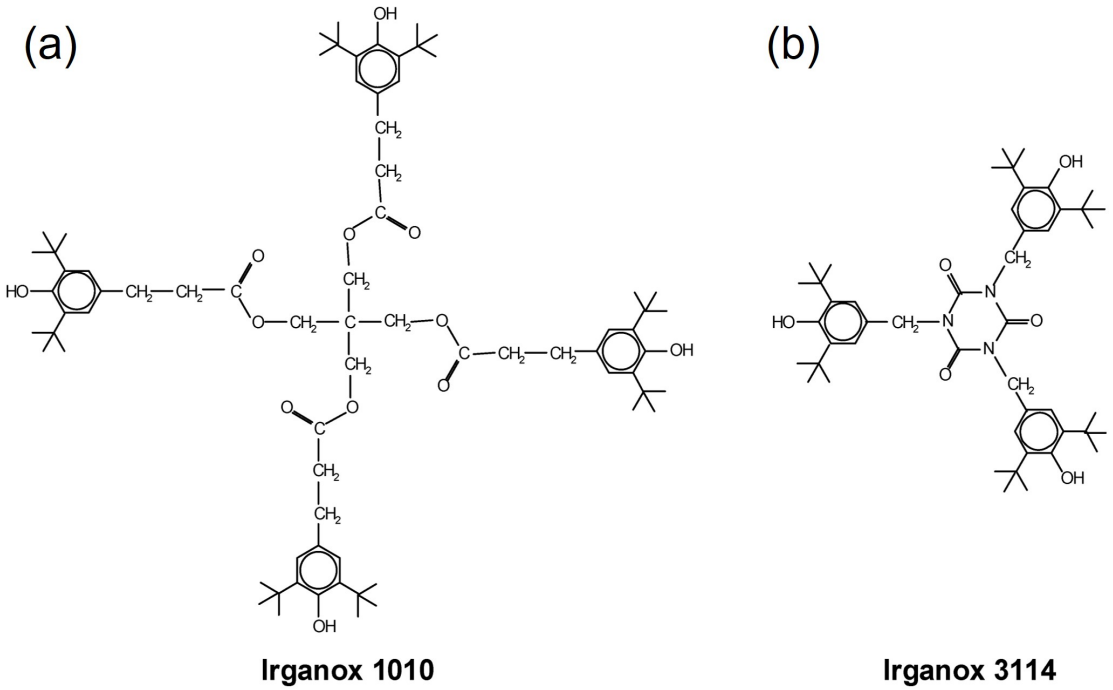


Figure 6.2: Molecular structures of Irganox 1010 (a) and Irganox 3114 (b).

Various samples were selected to investigate depth profiling performance. Irganox 1010 [251, 252] and Irganox 3114 [253–256] have been extensively studied in microprobe mode SIMS in previous research, and their molecular structures are shown in Figure 6.2. The details of the sample preparation have been reported previously [257, 258]. In this study, Irganox 1010 films with thicknesses of 40 nm, 80 nm, and 1600 nm were prepared and used for single-layer depth profiling experiments.

6.4 Analysis Algorithm Software

The analysis algorithm software was custom-developed in Python to process the large-scale time-resolved and spatially-resolved data acquired during the experiments. The

software supports automated pre-processing, ion event clustering, centroiding, time-of-flight to mass-to-charge (m/z) conversion, and spatial image reconstruction. A modular design allows for flexible adaptation to different acquisition modes, including data sets from PImMS2/TimePix3-based systems. The implementation also includes performance optimisations to handle high-throughput data and streamline interactive visualisation for both spectral and image-based outputs.

6.4.1 Image frame number identification

During the experimental procedure, each data file corresponds to approximately 30 minutes of continuous acquisition, encompassing both imaging and sputtering periods. Within each file, multiple data points are recorded, where a data point is defined as a series of image frames collected at a single depth within the sample. Therefore, it is essential to use software capable of distinguishing each individual data point within a combined data file. Here, a software tool has been developed to identify and extract the image frame numbers.

Since the gate valve between the extraction and detector regions is close during the sputtering cycles, the imaging cycles can be readily distinguished from the sputtering cycles, with the former yielding significantly higher ion counts and corresponding signal intensities. To distinguish between imaging and sputtering frames, the signal intensity of each individual frame can be plotted and analysed. Figure 6.3 illustrates a representative plot of raw signal intensities per frame for an Irganox 1010 single layer sample acquired using the PImMS2 camera.

However, background noise is evident in the sputtering frames, resulting in non-zero signal values. This noise introduces ambiguity, as the highest signal values from sputtering frames can overlap with the lowest values from imaging frames. Consequently, the separation between sputtering and imaging frames becomes non-trivial, and a simple threshold-based segmentation may not be sufficient to fully resolve the frame regions with high accuracy.

In Figure 6.3, a red dashed line indicates a provisional signal threshold, while the green and orange dashed lines mark the estimated start and end points of the imaging frame

region. Despite the threshold approximation, some frames near the boundary remain difficult to classify definitively. This limitation motivates the development of a more refined frame classification algorithm, potentially incorporating temporal smoothing, noise filtering, or clustering-based approaches.

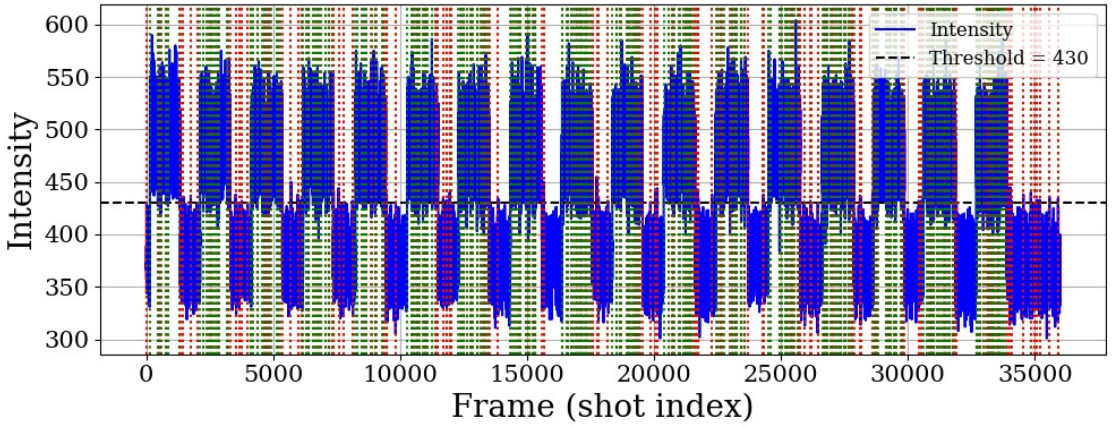


Figure 6.3: Raw signal intensity values per frame for an Irganox 1010 single layer sample, acquired using the PImMS2 camera. The black dashed line indicates a provisional signal threshold used to differentiate imaging frames from sputtering frames. Green and red dashed lines represent the estimated beginning and end of the imaging frame region, respectively.

To mitigate this classification uncertainty, a **Frame Intensity Smoothing Strategy** was applied to reduce shot-to-shot fluctuations and reveal underlying trends in ion detection intensity. Specifically, the total number of ion hits in each frame (also referred to as a "shot") was computed by grouping events according to their frame index. This raw intensity data was subsequently smoothed using a symmetric moving average (rolling average) technique.

A centred moving average with a window size of n frames was employed, whereby each smoothed value corresponds to the average intensity of the current frame and its two immediate neighbours before and after:

$$I_{\text{smooth}}(i) = \frac{1}{n} \sum_{j=i-2}^{i+2} I(j)$$

where $I(j)$ represents the intensity (i.e., the number of ion hits) in frame j, and i denotes the index of the current frame. This approach effectively suppresses high-frequency noise and enhances the visibility of significant transitions in the temporal signal profile. Frames

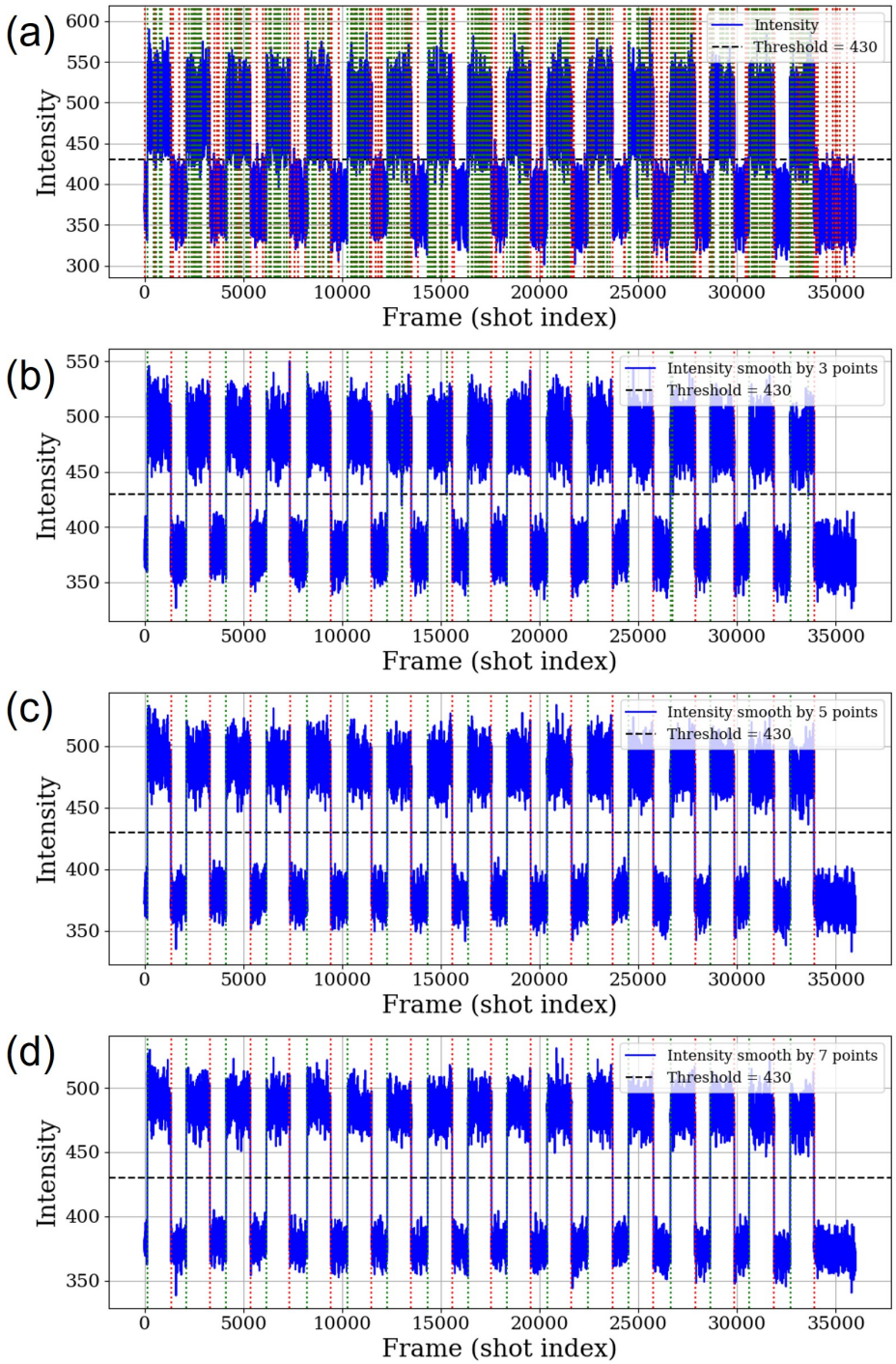


Figure 6.4: Different moving average window sizes were applied to smooth the frame intensity curves. From top to bottom, the corresponding window sizes are 1 (raw data), 3, 5, and 7, respectively.

located at the beginning and end of the dataset, for which a complete smoothing window is unavailable, yield undefined (`NaN`) values and are therefore excluded from further analysis.

By applying the **Frame Intensity Smoothing Strategy** to the dataset shown in Figure 6.3, using various window sizes (3, 5, and 7), the resulting smoothed frame intensities are presented in Figure 6.4. It can be observed that, following smoothing, the imaging frames become clearly distinguishable from the sputtering frames. As the window size increases, high-frequency noise is more effectively suppressed, and the boundary between imaging and sputtering regions becomes more apparent. This highlights the effectiveness of temporal smoothing in enhancing frame classification accuracy.

6.4.2 Region of Interest (ROI) capability

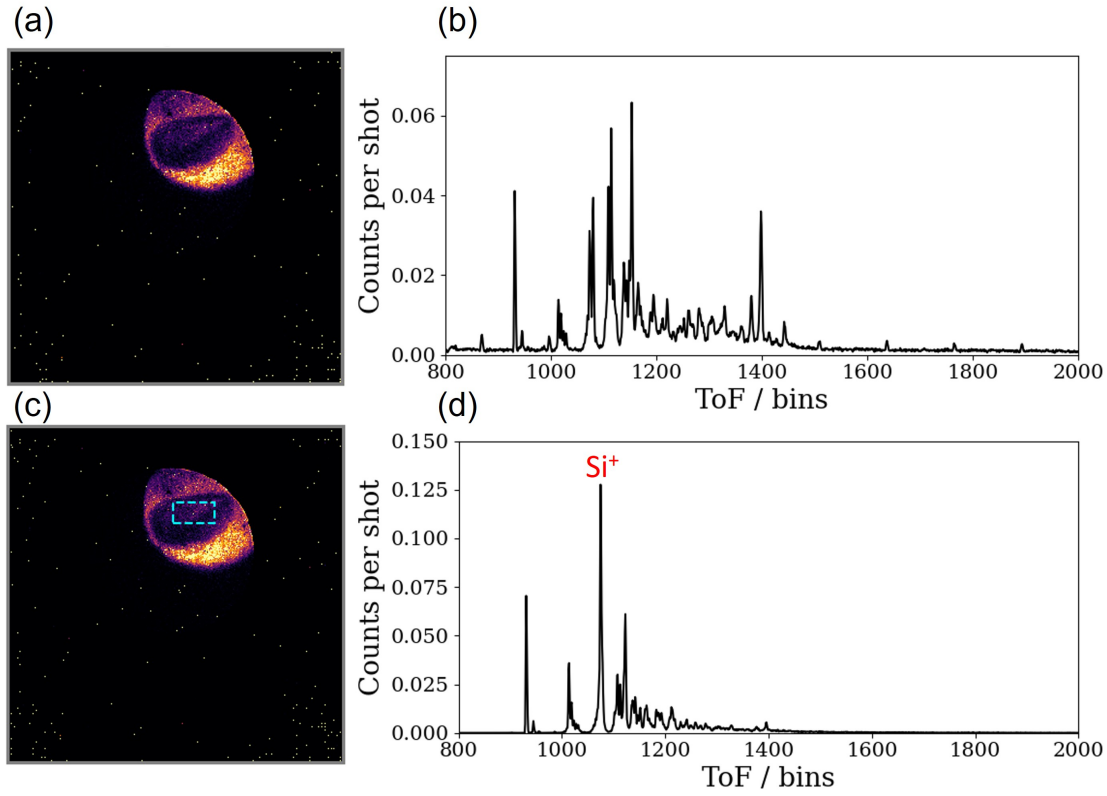


Figure 6.5: Panels (a) and (c) show the accumulated ion images across all masses. The full-field spectrum corresponding to the entire image area is presented in (b). A region of interest (ROI) is selected and highlighted with a cyan rectangle, and the corresponding time-of-flight (ToF) spectrum for the ROI is displayed in (d).

In the depth profiling experiment, the imaging area is deliberately chosen to be larger than the sputtered region to ensure complete coverage of the ablated surface. Consequently, the mass spectral information obtained varies significantly between the sputtered

and non-sputtered regions, particularly as the primary ion beam progressively drills through successive layers of the sample. This spatial variation in chemical composition renders it critical to selectively extract and analyse mass spectral data corresponding exclusively to the sputtered region to obtain accurate depth-resolved information.

As illustrated in Figure 6.5, when the C_{60}^{+} primary ion beam penetrates down to the silicon substrate, a crater or 'hole' is evident at the centre of the sputtered area. This crater should be characterised by a prominent Si^{+} signal in the time-of-flight (ToF) spectrum. However, due to the relatively large size of the overall imaging area compared to the sputtered crater, the Si^{+} signal is significantly diluted by signals from surrounding regions, which predominantly contain organic fragments such as $C_2H_4^{+}$ and $C_2H_3^{+}$. As a result, the Si^{+} peak appears less distinct in the full-field spectrum.

By restricting the spectral analysis to a region of interest (ROI) that is spatially confined to the sputtered crater, as indicated by the cyan rectangle in Figure 6.5 (a) and (c), the corresponding ToF spectrum (Figure 6.5 (d)) reveals a substantially enhanced Si^{+} peak relative to the organic fragments. This targeted approach significantly improves the fidelity of the mass spectral data, enabling more precise characterisation of the chemical composition within the sputtered region and thereby enhancing the reliability of the depth profile analysis.

6.5 Results and Discussions

6.5.1 Single layer depth profile

The single-layer Irganox 1010 depth profiling experiment was conducted using the TimePix3-based camera. Each experimental batch lasted approximately 30 minutes and comprised multiple data points. Within the TimePix3 data set, it is essential to distinguish imaging frames from sputtering frames to ensure correct data segmentation. To facilitate this, the data array values for each frame were plotted, as shown in Figure 6.6.

Figure 6.6 represents a single 30-minute data set, where a blue dashed line indicates the threshold used to separate imaging frames from sputtering frames. By identifying

the initial and final frame numbers in each cycle whose values exceed this threshold, the imaging frames associated with each data cycle can be accurately filtered and isolated.

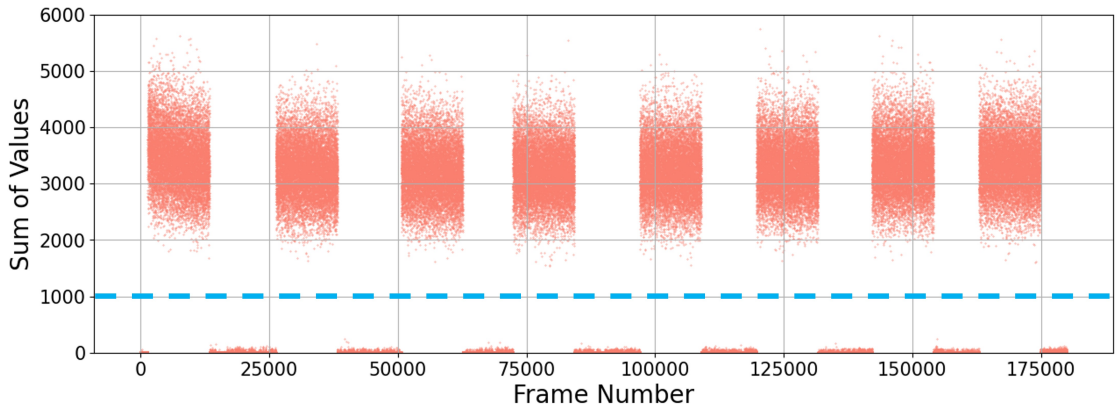


Figure 6.6: A representative TimePix3 data set showing frame value distribution. The blue line indicates the threshold used to differentiate imaging frames from sputtering frames.

Subsequently, the data from each imaging cycle were centroided separately to reduce memory usage and accelerate processing. The centroiding procedure, introduced in Chapter 3, is employed to enhance both mass and spatial resolution. Following centroiding, both the mass spectra for each experimental cycle and the corresponding ion images for individual masses were generated for analysis.

The spectra obtained from the first and last data points of the depth profiling experiment are compared in Figure 6.7. Two major fragment ions of Irganox 1010, $C_{15}H_{24}O^+$ (220 m/z) and $C_{17}H_{24}O_2^+$ (260 m/z), are clearly observed in both spectra. However, as the primary ion beam progressively sputters through the organic layer and reaches the substrate (silicon wafer), the Si^+ signal becomes prominent, as evidenced by its increased intensity in the red spectrum. This transition indicates the successful progression of the depth profiling experiment from the surface of the Irganox 1010 film down to the underlying substrate.

Images of $C_{15}H_{24}O^+$ (220 m/z) and Si^+ (28 m/z) at selected data points (1, 12, 23, and 34) are presented in Figure 6.8. At the beginning of the sputtering process (data point 1), the $C_{15}H_{24}O^+$ signal is uniformly distributed, while the Si^+ signal is not completely absent. This residual signal is attributed to background noise, likely caused by $C_2H_4^+$ fragments generated by the C_{60}^+ primary ion beam.

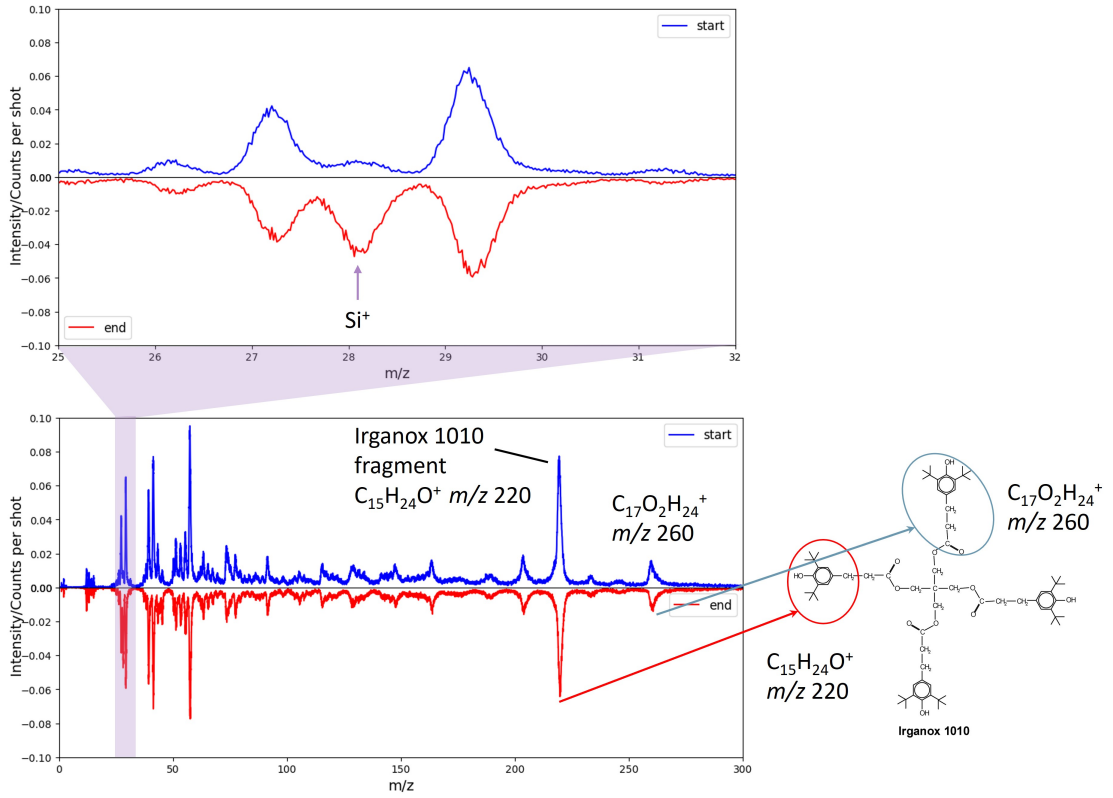


Figure 6.7: Comparison of spectra acquired at the first (blue) and last (red) data points of the depth profiling experiment. The mass region between 25–32 m/z is enlarged to highlight the silicon peak.

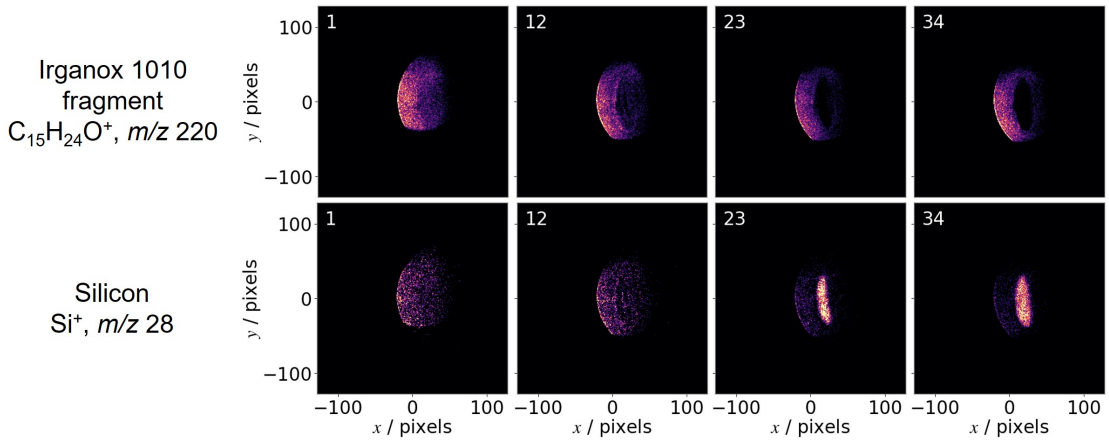


Figure 6.8: Ion images of an Irganox 1010 fragment (top panel) and silicon ion (bottom panel) at selected data points during the depth profile. The data point number is shown in the top-left corner of each image.

By data point 12, a central hollow appears in the $C_{15}H_{24}O^+$ image, indicating that the primary ion beam has begun to penetrate through the Irganox 1010 layer. Notably, the signal intensity at the crater edge becomes enhanced, which is a known effect caused by

the accumulation of material at the crater perimeter during sputtering [259]. At data point 23, the Si^+ signal begins to emerge prominently in the centre of the image, and by data point 34, this silicon-rich region has expanded further. This observation suggests that the crater formed by sputtering does not have vertical sidewalls but rather a sloped profile. As sputtering continues, the crater becomes more uniform and the exposed substrate area increases, consistent with the expected depth profiling progression.

6.6 Conclusion and Future Work

To date, the single-layer depth profiling experiments have demonstrated promising results, confirming the capability of a defocused C_{60}^+ ion beam to effectively sputter organic layers. The developed Analysis Software has proven effective in automatically identifying imaging frame regions, generating selected mass images, and analysing both mass spectral and spatial information within defined regions of interest (ROIs).

The depth profiling project remains ongoing, with several important tasks planned for future work. Foremost among these is the analysis of multilayer (delta layer) samples, where precise identification and differentiation of individual layers will be crucial. Following this, a rigorous determination of the depth resolution achievable with microscope mode C_{60}^+-SIMS imaging is required. This will provide essential quantitative metrics to assess the performance and spatial accuracy of the technique, thereby guiding optimisation for advanced three-dimensional chemical imaging applications.

To broaden the applicability of three-dimensional microscope mode MSI, it is necessary to analyse a diverse range of samples and materials, including, but not limited to, biological tissues, polymer films, multilayered organic devices, and inorganic substrates. Such studies will help to evaluate the versatility and limitations of the technique across various domains and provide valuable insights into sample-specific ionisation behaviours and depth profiling performance.

7
Conclusions and Outlooks

Chapters 4, 5, and 6 present the main results of this thesis. These chapters investigate the performance of the new-generation microscope-mode SIMS imaging instrument, demonstrate its initial application to tissue imaging, and preliminarily explore its potential for three-dimensional (3D) imaging.

In Chapter 4, the three-dimensional velocity distribution of secondary ions is measured using velocity map imaging (VMI). A new method based on a TimePix3 camera is developed to achieve direct 3D VMI along the time-of-flight (ToF) axis. The velocities of inorganic ions (Na^+ and K^+) and organic ions (Auramine O) are measured, providing fundamental input parameters for the SIMION simulations used in Chapter 5. These measurements are essential for accurately modelling secondary ion trajectories and improving instrument performance. This study is highly novel, as conventional velocity map imaging (VMI) of surface-emitted species is not truly three-dimensional. Typically, the detector is positioned off the time-of-flight (ToF) axis, which compromises velocity accuracy and makes it challenging to achieve genuine 3D VMI for multiple masses simultaneously. In contrast, the method developed in this work enables multi-mass 3D VMI directly along the ToF axis. This approach provides a fundamental methodological advance for VMI, with broad implications for chemical dynamics and surface scattering studies.

In Chapter 5, three key performance characteristics of the microscope-mode SIMS imaging instrument are optimised. Guided by SIMION simulations, the PEDA tech-

nique is modelled and implemented to enhance the instrument's mass resolution. A magnification-tuning method is then developed to improve the spatial resolution to below 5 µm. Finally, different PEDA settings are applied to extend the mass resolution across a wider mass range. Simulation results suggest that an optimised configuration could achieve a mass resolving power exceeding 2000 at higher m/z values. This section would be the most impact part of this thesis. Currently, no microscope-mode instrument can simultaneously achieve high imaging speed, high mass resolution, and high spatial resolution; trade-offs between these performance parameters are inevitable. This study provides the mass spectrometry community with a potential high-throughput MSI solution that seeks to balance these competing requirements.

Finally, in Chapter 6, the depth profiling performance of the instrument is investigated. This study provides a preliminary demonstration of the instrument's potential for three-dimensional (3D) imaging.

Secondary ion mass spectrometry (SIMS) imaging is a powerful technique for analysing the chemical composition and spatial distribution of species on a sample surface. Although it is challenging to directly detect large biological molecules, SIMS offers unique capabilities for depth profiling, enabling the reconstruction of a full three-dimensional image. Conventionally, SIMS imaging employs a well-focused primary ion beam to raster the sample surface pixel by pixel; the secondary ions are then analysed using a conventional mass spectrometer and reconstructed into images corresponding to each mass peak. In this mode, the spatial resolution is limited by the focusing ability of the primary ion beam, and data acquisition is relatively slow.

Alternatively, as discussed in this thesis, SIMS imaging can operate in microscope mode, in which ions produced simultaneously across the entire sample surface are spatially mapped by projecting their positional information onto a two-dimensional detector using an appropriate ion optical design. By employing a defocused primary ion beam, the spatial resolution becomes decoupled from the primary beam spot size and instead depends on the secondary ion angular distribution and the focusing performance of the ion optics. In principle, the spatial resolution achievable in microscope mode can surpass that of microprobe mode, and the analysis time can be significantly shorter.

However, to preserve the positional information of secondary ions, a ToF mass analyser is coupled with SIMS in the microscope-mode instrument. Compared with other mass analysers, such as Orbitrap or FTICR, the ToF mass analyser provides relatively low mass resolution, since it is not uncoupled from the initial velocity of the ion. To address this limitation, a time-variable PEDA is applied to enhance the mass resolution across a wide range of masses. The PEDA settings are optimised using SIMION ion trajectory simulations, which require accurate input of secondary ion velocities. To obtain these velocities, a novel three-dimensional velocity-map imaging (VMI) approach is employed to measure the precise secondary ion velocity distributions.

The TimePix3-based camera and the PEISI technique are employed to acquire and calibrate the secondary ion velocity distributions. Notably, the organic parent ions exhibit markedly different velocity distributions—particularly in their angular distributions—compared with the metallic ions, as discussed in detail in Chapter 4. To obtain more comprehensive information about the sputtering process, primary ions with different initial energies (20 and 40 keV) are used. By doubling the initial collision energy, the kinetic energy of the secondary ions approximately doubles as well, suggesting that the sputtering process is primarily governed by momentum transfer. Furthermore, increasing the initial collision energy reduces the angular spread of the secondary ions, indicating that deeper penetration associated with higher-energy collisions can partially align the angular distributions toward the surface normal. This technique not only facilitates analysis of secondary ion velocities but also provides a novel approach to studying molecular and reaction dynamics in both surface and gas-phase systems.

Within the measured three-dimensional secondary ion velocity distribution, the PEDA voltage settings are optimised using a genetic algorithm. By employing a time-variable PEDA, the mass resolution is enhanced from approximately 500 to over 2000 $m/\Delta m$ across a wide mass range (600–1200 m/z) with a PEDA delay time of 450 ns. Simultaneously, a spatial resolution of approximately 20 µm is achieved. To further improve both mass and spatial resolution, a BC-408 scintillator is employed to measure the ToF peak, benefiting from a detector response time of approximately 1 ns. With this modification, the mass resolution is enhanced to about 6700 $m/\Delta m$ at 375 m/z. To

enhance spatial resolution, the signal magnification is increased to overcome camera pixel number limitations by tuning the Einzel lens voltage. Under the current ion optical settings, the maximum magnification reaches 44.8 ×, resulting in a measured spatial resolution of $3.56 \pm 2.12\,\mu m$. This technique has also been applied to mouse brain tissue, enabling clear imaging of neurotransmitters, lipids, Na^+, and K^+ ions.

Finally, the depth profiling capability of the microscope-mode SIMS imaging system is also investigated, as demonstrated using a single layer of Irganox 1010. Using the analysis software, the instrument is capable of performing three-dimensional imaging on selected samples. Further work on depth resolution calculations and delta-layer measurements is being carried out by Anya Eyres.

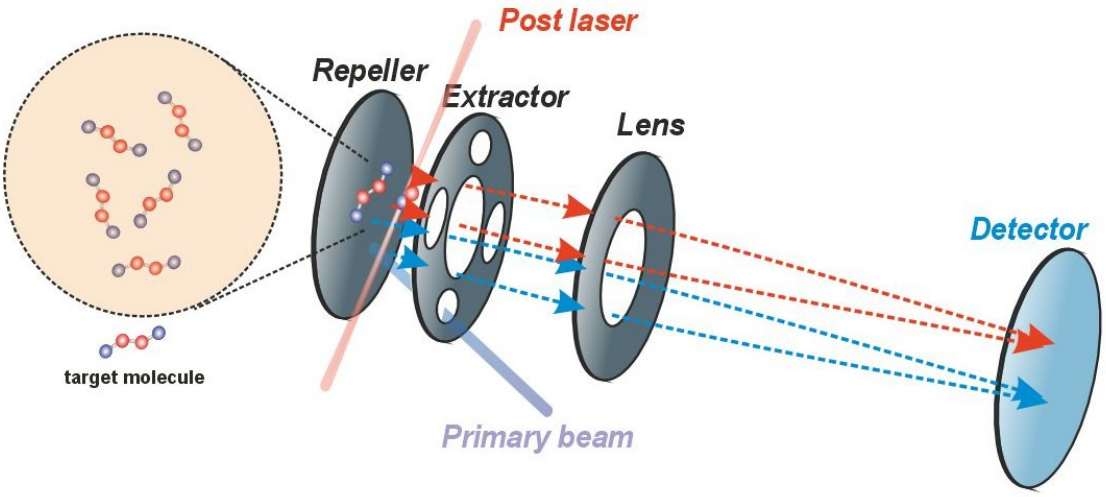


Figure 7.1: illustrates the instrument setup for velocity map imaging. Using a primary beam, the parent molecule primarily generates singly charged ions (blue ion trajectories) and neutral co-fragments. Upon applying the post-laser, the neutral co-fragments are further ionized (red ion trajectories). All ions are extracted into the time-of-flight tube and detected by the MCP-phosphor-TimePix3 camera assembly.

The work presented in this thesis can be extended in several directions to explore a range of applications. Firstly, the newly developed 3D VMI methodology enables the measurement of the velocity of secondary ions generated by MALDI, addressing the currently insufficiently understood ionisation process. By comparing ion velocity distributions with and without the matrix, the so-called matrix effect could be further clarified. For SIMS-VMI, investigating different primary ion beams and sample surfaces

would provide additional insights into the sputtering process. Understanding the velocity distributions of secondary ions is also critical for the development of next-generation SIMS instruments. Moreover, a second picosecond laser can be integrated into the SIMS instrument to enable post-ionisation, as illustrated in Figure 7.1. This approach not only enhances the secondary ion yield but also facilitates detailed studies of fragmentation and ionisation processes in SIMS. By applying covariance analysis, fragment ions originating from the same parent species can be identified, thereby allowing the determination of fragmentation pathways.

This thesis demonstrates that microscope-mode secondary ion mass spectrometry (SIMS) imaging can achieve spatial resolutions of approximately 3 µm within 10 minutes while maintaining sufficient mass resolving power to distinguish isotopes. The technique also shows potential for spatially resolved lipidomic analysis of mouse brain tissue. To broaden its applications and enhance throughput, future work could explore integration with microarray platforms and extend its use to additional sample types, such as various tissues and blood. Owing to the high-throughput advantage of microscope mode MSI and the rapid advancement of artificial intelligence (AI), combining fast MSI with machine learning presents a significant opportunity for accelerated and sophisticated spatial omics analysis. Such integration could greatly facilitate rapid clinical diagnosis and biomarker discovery. Furthermore, by improving the spatial resolution, microscope mode MSI could be extended to single-cell imaging, thereby enabling its application to more fundamental biological studies. This would open new possibilities for investigating cell–cell interactions and elucidating how biomarkers or proteins regulate cellular behaviour.

Furthermore, preliminary results indicate that microscope-mode SIMS can achieve depth profiling, highlighting the potential for 3D imaging in the future. It would be of interest to systematically measure the instrument's depth resolution on different surface materials and to explore applications in semiconductor and tissue imaging.

Microscope mode SIMS and MALDI are expected to evolve along distinct developmental directions. In the future, the primary advantages of microscope mode MSI are likely to lie in its speed and label-free imaging capability, particularly when compared with microprobe mode MSI and conventional microscopy techniques. As genomics and

proteomics continue to dominate biological and medical research, these strengths will become increasingly valuable. Microscope mode MALDI is anticipated to focus on further improving spatial resolution, with the potential to achieve resolutions of 1 µm or even sub-micrometre levels. Conversely, microscope mode SIMS instruments should aim to advance their three-dimensional imaging capabilities, thereby complementing the limitations of MALDI MSI and expanding the overall applicability of microscope mode mass spectrometry imaging.

Appendices

A
Appendices

As introduced in Chapter 1, the mass analyser that can be adapted for microscope-mode MSI is the time-of-flight (ToF) analyser, with the addition of a reflectron stage to significantly increase mass resolution. The equations describing the ion trajectories in the ToF analyser with a reflectron are detailed below:

As Figure 1.9 shows, the total time-of-flight, t_f, can be related to the mass-to-charge ratio through the following equations:

The relationship between an ion's potential energy and its velocity in a Time-of-Flight (ToF) mass spectrometer can be derived as follows. When an ion of charge z and elementary charge e is accelerated by a repelling potential V_{rep}, its electric potential energy (P) is given by:

$$P = qV_{\text{rep}} = zeV_{\text{rep}} \tag{A.1}$$

where q is the ion charge and V_{rep} is the high voltage applied to the sample holder.

This potential energy is fully converted into kinetic energy (K) as the ion exits the acceleration region and enters the field-free drift tube:

$$K = \frac{1}{2}mv^2 \tag{A.2}$$

where m is the mass of the ion and v is its velocity.

Equating Equations A.1 and A.2 gives the expression for the ion velocity:

$$v = \sqrt{2zeV_{\text{rep}}/m} \tag{A.3}$$

In the field-free drift region, the ion travels at constant velocity v over a known distance L. The time-of-flight t is therefore:

$$t = \frac{L}{v} \tag{A.4}$$

Substituting Equation A.3 into Equation A.4 yields:

$$t = \frac{L}{\sqrt{2zeV_{\text{rep}}/m}} = \sqrt{mL^2/2zeV_{\text{rep}}} \tag{A.5}$$

Rearranging for the mass-to-charge ratio m/z gives:

$$m/z = 2eV_{\text{rep}}t^2/L^2 \tag{A.6}$$

This equation forms the basis for determining the m/z values of ions in a ToF mass spectrometer.

As shown in Figure 1.12, the extraction potential is denoted as V_s, while the reflectron is set to a potential V_R and has an effective length D. This results in a uniform electric field within the reflectron given by $E = V_R/D$. An ion with charge q and kinetic energy E_k enters the reflectron with an initial velocity v_x and penetrates to a depth d, which is derived from energy conservation:

$$d = \frac{E_k}{qE} = \frac{qV_s}{q(V_R/D)} = \frac{DV_s}{V_R} \tag{A.7}$$

Since the ion decelerates, reverses direction, and exits the reflectron, the total time spent in the reflectron is:

$$t_0 = \frac{4d}{v_x} \tag{A.8}$$

assuming symmetric entry and exit paths. The total flight time in the mass analyser (including both linear and reflectron paths) is then:

$$t = \frac{L_1 + L_2 + 4d}{v_x} \tag{A.9}$$

where L_1 and L_2 represent the lengths of the field-free drift regions before and after the reflectron, respectively.

The initial velocity v_x is derived from the acceleration due to the extraction voltage V_s:

$$v_x = \sqrt{\frac{2zeV_s}{m}}. \tag{A.10}$$

Substituting Equation (A.10) into Equation (A.9), the total time-of-flight squared becomes:

$$t_{\mathrm{ToF}}^2 = \frac{m(L_1 + L_2 + 4d)^2}{2zeV_s} \tag{A.11}$$

To evaluate the reflectron's compensation effect on ions with the same m/z but different kinetic energies, we define a dimensionless energy ratio a^2 between a higher kinetic energy E_k' and the nominal energy E_k:

$$a^2 = \frac{E_k'}{E_k} \tag{A.12}$$

The corresponding velocity of the ion with E_k' is:

$$v_x' = \sqrt{\frac{2E_k'}{m}} = av_x \tag{A.13}$$

and the time required to traverse the linear drift region (excluding the reflectron) is:

$$t' = \frac{L_1 + L_2}{v_x'} = \frac{L_1 + L_2}{av_x} = \frac{t_{\mathrm{drift}}}{a} \tag{A.14}$$

In the reflectron region, an ion with a random kinetic energy E_k' will penetrate to a greater depth d', given by:

$$d' = \frac{E_k'}{qE} = \frac{a^2 E_k}{qE} = a^2 d, \tag{A.15}$$

where $a^2 = E_k'/E_k$ and d is the penetration depth of the ion with nominal kinetic energy E_k.

The corresponding time spent in the reflectron by the ion with energy E_k' is:

$$t'_r = \frac{4d'}{v'_x} = \frac{4a^2 d}{a v_x} = a t_r, \tag{A.16}$$

where t_r is the time spent in the reflectron by the reference ion with energy E_k.

Thus, the total time-of-flight for the ideal ion (t_{ToF}) and the ion with excess kinetic energy (t'_{ToF}) can be expressed as:

$$t_{\mathrm{ToF}} = t + t_r, \qquad t'_{\mathrm{ToF}} = \frac{t}{a} + a t_r, \tag{A.17}$$

where t is the time the ion spends outside the reflectron. By appropriately adjusting the reflectron length and potential, one can achieve time-focusing such that $t'_{\mathrm{ToF}} \approx t_{\mathrm{ToF}}$, thus compensating for the initial kinetic energy spread and improving mass resolution.

References

(1) Murphy, R. C.; Gaskell, S. J. *Journal of Biological Chemistry* **2011**, *286*, 25427–25433.

(2) Ridenour, W. B.; Kliman, M.; McLean, J. A.; Caprioli, R. M. *Analytical Chemistry* **2010**, *82*, 1881–1889.

(3) Chen, Y.; Allegood, J.; Liu, Y.; Wang, E.; Cachón-González, B.; Cox, T. M.; H., M. A.; Sullards, M. C. *Analytical Chemistry* **2008**, *80*, 2780–2788.

(4) Murphy, R. C.; Axelsen, P. H. *Mass Spectrometry Reviews* **2011**, *30*, 579–599.

(5) Griffiths, W. J. *Mass Spectrometry Reviews* **2003**, *22*, 81–152.

(6) Han, X.; Gross, R. W. *Mass Spectrometry Reviews* **2005**, *24*, 367–412.

(7) Thomas, M. C.; Mitchell, T. W.; Harman, D. G.; Deeley, J. M.; Murphy, R. C.; Blanksby, S. J. *Analytical Chemistry* **2007**, *79*, 5013–5022.

(8) Masoodi, M.; Eiden, M.; Koulman, A.; Spaner, D.; Volmer, D. A. *Analytical Chemistry* **2010**, *82*, 8176–8185.

(9) Hardesty, W. M.; Caprioli, R. M. *Analytical and Bioanalytical Chemistry* **2008**, *391*, 899–903.

(10) Domon, B.; Aebersold, R. *Science* **2006**, *312*, 212–217.

(11) Zhang, G.; Annan, R. S.; Carr, S. A.; Neubert, T. A. *Current Protocols in Protein Science* **2010**, *62*, 16.1.1–16.1.30.

(12) Brancia, F. L. *Expert Review of Proteomics* **2006**, *3*, doi: 10.1586/14789450.3.1.143, 143–151.

(13) LENNON, J. J.; WALSH, K. A. *Protein Science* **1999**, *8*, 2487–2493.

(14) Link, A. J.; Eng, J.; Schieltz, D. M.; Carmack, E.; Mize, G. J.; Morris, D. R.; Garvik, B. M.; Yates, J. R. *Nature Biotechnology* **1999**, *17*, 676–682.

(15) Villas-Bôas, S. G.; Mas, S.; Åkesson, M.; Smedsgaard, J.; Nielsen, J. *Mass Spectrometry Reviews* **2005**, *24*, 613–646.

(16) Demyttenaere, J. C. R.; Moriña, R. M.; Sandra, P. *Journal of Chromatography A* **2003**, *985*, 127–135.

(17) Wen, B.; Mingshe; Zhu *Drug Metabolism Reviews* **2015**, *47*, doi: 10.3109/03602532.2014.1001029, 71–87.

(18) Ma, S.; K, S.; Chowdhury *Bioanalysis* **2013**, *5*, 1285–1297.

(19) Pohl, L. R.; Nelson, S. D.; Garland, W. A.; Trager, W. F. *Biomedical Mass Spectrometry* **1975**, *2*, 23–30.

(20) Cuyckens, F. *Rapid Communications in Mass Spectrometry* **2019**, *33*, 90–95.

(21) Lappin, G.; Lloyd; Stevens *Expert Opinion on Drug Metabolism & Toxicology* **2008**, *4*, doi: 10.1517/17425255.4.8.1021, 1021–1033.

(22) Meyer, M. R.; Maurer, H. H. *Analytical and Bioanalytical Chemistry* **2012**, *403*, 1221–1231.

(23) Zhang, A.; Sun, H.; Wang, X. *Mass Spectrometry Reviews* **2018**, *37*, 307–320.

(24) Meissner, F.; Geddes-McAlister, J.; Mann, M.; Bantscheff, M. *Nature Reviews Drug Discovery* **2022**, *21*, 637–654.

(25) Dueñas, M. E.; Peltier-Heap, R. E.; Leveridge, M.; Annan, R. S.; Büttner, F. H.; Trost, M. *EMBO Molecular Medicine* **2023**, *15*, e14850.

(26) Scholz, S.; Walzer, K.; Leo, K. *Advanced Functional Materials* **2008**, *18*, 2541–2547.

(27) Verlinden, J.; Gijbels, R.; Adams, F. *Journal of Analytical Atomic Spectrometry* **1986**, *1*, 411–419.

(28) Richardson, S. D. *Chemical Reviews* **2001**, *101*, doi: 10.1021/cr990090u, 211–254.

(29) Gronert, S. *Chemical Reviews* **2001**, *101*, doi: 10.1021/cr9900836, 329–360.

(30) Armentrout, P. B.; Baer, T. *The Journal of Physical Chemistry* **1996**, *100*, doi: 10.1021/jp953329t, 12866–12877.

(31) Gülbakan, B.; Barylyuk, K.; Zenobi, R. *Current Opinion in Biotechnology* **2015**, *31*, 65–72.

(32) Armentrout, P. B. *Journal of the American Society for Mass Spectrometry* **2002**, *13*, 419–434.

(33) De Laeter, J. R. *Mass Spectrometry Reviews* **1998**, *17*, 97–125.

(34) Roberts, N. M. W.; Drost, K.; Horstwood, M. S. A.; Condon, D. J.; Chew, D.; Drake, H.; Milodowski, A. E.; McLean, N. M.; Smye, A. J.; Walker, R. J.; Haslam, R.; Hodson, K.; Imber, J.; Beaudoin, N.; Lee, J. K. *Geochronology* **2020**, *2*, 33–61.

(35) Goldstein, E. *Berlin Akademie Monatsberichte* **1876**, 279.

(36) Spear, B. *World Patent Information* **2006**, *28*, 330–335.

(37) Wikisource Rays of Positive Electricity and Their Application to Chemical Analyses/Wien's Proof of the Magnetic and Electric Deflection of the Rays — Wikisource, [Online; accessed 26-June-2025], 2022.

(38) Kaufmann, W. *Dieterich (in commission)* **1901**, 143–155.

(39) Millikan, R. A. *Science* **1910**, *32*, 436–448.

(40) Fletcher, H. *Physics Today* **1982**, *35*, 43–47.

(41) R., W. *Nature* **1914**, *92*, 549–550.

(42) Aston, F. W. *The London, Edinburgh, and Dublin Philosophical Magazine and Journal of Science* **1919**, *38*, 707–714.

(43) Meyerson, S. *Organic Mass Spectrometry* **1986**, *21*, 197–208.

(44) Fjeldsted, J. C. In *Comprehensive Analytical Chemistry*, Pérez, S., Eichhorn, P., Barceló, D., Eds.; Elsevier: 2016, pp 19–49.

(45) Cameron, A. E.; Jr., D. F. E. *Review of Scientific Instruments* **1948**, *19*, 605–607.

(46) Marcus, R. A. *The Journal of Chemical Physics* **1966**, *45*, 2138–2144.

(47) Giacomo, F. D. *Journal of Chemical Education* **2015**, *92*, 476–481.

(48) Paul, W. *Rev. Mod. Phys.* **1990**, *62*, 531–540.

(49) Gohlke, R. S.; McLafferty, F. W. *Journal of the American Society for Mass Spectrometry* **1993**, *4*, 367–371.

(50) Munson, M. S. B.; Field, F. H. *Journal of the American Chemical Society* **1966**, *88*, doi: 10.1021/ja00964a001, 2621–2630.

(51) McLafferty, F.; Bente, P.; Kornfeld, R.; Tsai, S.-C.; Howe, I. *Journal of the American Chemical Society* **1973**, *95*, 2120–2129.

(52) Jennings, K. R. *International Journal of Mass Spectrometry and Ion Physics* **1968**, *1*, 227–235.

(53) Mamyrin, B. A.; Karataev, V. I.; Shmikk, D. V.; Zagulin, V. A. *Soviet Journal of Experimental and Theoretical Physics* **1973**, *37*, 45.

(54) Carroll, D. I.; Dzidic, I.; Stillwell, R. N.; Horning, M. G.; Horning, E. C. *Analytical Chemistry* **1974**, *46*, 706–710.

(55) Arpino, P.; Baldwin, M. A.; McLafferty, F. W. *Biomedical Mass Spectrometry* **1974**, *1*, 80–82.

(56) Marshall, A. G.; Hendrickson, C. L.; Jackson, G. S. *Mass Spectrometry Reviews* **1998**, *17*, 1–35.

(57) Burlingame, A. L.; Boyd, R. K.; Gaskell, S. J. *Analytical Chemistry* **1996**, *68*, 599–652.

(58) Barber, M.; Bordoli, R. S.; Sedgwick, R. D.; Tyler, A. N. *J. Chem. Soc., Chem. Commun.* **1981**, 325–327.

(59) Karas, M.; Bachmann, D.; Hillenkamp, F. *Analytical Chemistry* **1985**, *57*, 2935–2939.

(60) Yamashita, M.; Fenn, J. B. *The Journal of Physical Chemistry* **1984**, *88*, 4451–4459.

(61) Kaufmann, R.; Chaurand, P.; Kirsch, D.; Spengler, B. *Rapid Communications in Mass Spectrometry* **1996**, *10*, 1199–1208.

(62) Hu, Q.; Noll, R. J.; Li, H.; Makarov, A.; Hardman, M.; Cooks, R. G. *Journal of Mass Spectrometry* **2005**, *40*, 430–443.

(63) Badman, E. R.; Graham Cooks, R. *Journal of Mass Spectrometry* **2000**, *35*, 659–671.

(64) Luxembourg, S. L.; Mize, T. H.; McDonnell, L. A.; Heeren, R. M. A. *Analytical Chemistry* **2004**, *76*, 5339–5344.

(65) Dodds, J. N.; Baker, E. S. *Journal of the American Society for Mass Spectrometry* **2019**, *30*, 2185–2195.

(66) Pringle, S. D.; Giles, K.; Wildgoose, J. L.; Williams, J. P.; Slade, S. E.; Thalassinos, K.; Bateman, R. H.; Bowers, M. T.; Scrivens, J. H. *International Journal of Mass Spectrometry* **2007**, *261*, 1–12.

(67) Cooks, R. G.; Ouyang, Z.; Takats, Z.; Wiseman, J. M. *Science* **2006**, *311*, 1566–1570.

(68) Graham, A. W. G.; Ray, S. J.; Enke, C. G.; Barinaga, C. J.; Koppenaal, D. W.; Hieftje, G. M. *Journal of the American Society for Mass Spectrometry* **2011**, *22*, 110–117.

(69) Leo, G.; Altucci, C.; Bourgoin-Voillard, S.; Gravagnuolo, A. M.; Esposito, R.; Marino, G.; Costello, C. E.; Velotta, R.; Birolo, L. *Rapid Communications in Mass Spectrometry* **2013**, *27*, 1660–1668.

(70) Walton, B. L.; Hoffmann, W. D.; Verbeck, G. F. *International Journal of Mass Spectrometry* **2014**, *370*, 66–74.

(71) Zhou, S.; Fatma, Z.; Xue, P.; Mishra, S.; Cao, M.; Zhao, H.; Sweedler, J. V. *Analytical Chemistry* **2023**, *95*, 4067–4076.

(72) Lockyer, N. P.; Aoyagi, S.; Fletcher, J. S.; Gilmore, I. S.; van der Heide, P. A. W.; Moore, K. L.; Tyler, B. J.; Weng, L.-T. *Nature Reviews Methods Primers* **2024**, *4*, 32.

(73) Weibel, D.; Wong, S.; Lockyer, N.; Blenkinsopp, P.; Hill, R.; Vickerman, J. C. *Analytical Chemistry* **2003**, *75*, 1754–1764.

(74) Fletcher, J. S.; Conlan, X. A.; Jones, E. A.; Biddulph, G.; Lockyer, N. P.; Vickerman, J. C. *Analytical Chemistry* **2006**, *78*, 1827–1831.

(75) Tian, H.; née Rabbani, S. S.; Vickerman, J. C.; Winograd, N. *Analytical Chemistry* **2021**, *93*, 7808–7814.

(76) Tian, H.; Sparvero, L. J.; Anthonymuthu, T. S.; Sun, W.-Y.; Amoscato, A. A.; He, R.-R.; Bayır, H.; Kagan, V. E.; Winograd, N. *Analytical Chemistry* **2021**, *93*, doi: 10.1021/acs.analchem.0c05311, 8143–8151.

(77) Svensson, B. G.; Linnarsson, M. K.; Mohadjeri, B.; Petravić, M.; Williams, J. S. *Nuclear Instruments and Methods in Physics Research Section B: Beam Interactions with Materials and Atoms* **1994**, *85*, 363–369.

(78) Ekar, J.; Panjan, P.; Drev, S.; Kovač, J. *Journal of the American Society for Mass Spectrometry* **2022**, *33*, 31–44.

(79) Clark, P. A.; Hagenhoff, B.; Kersting, R.; Tallarek, E. *Journal of Vacuum Science & Technology B* **2016**, *34*, 03H135.

(80) Bailey, J.; Havelund, R.; Shard, A. G.; Gilmore, I. S.; Alexander, M. R.; Sharp, J. S.; Scurr, D. J. *ACS Applied Materials & Interfaces* **2015**, *7*, 2654–2659.

(81) Passarelli, M. K. et al. *Nature Methods* **2017**, *14*, 1175–1183.

(82) Suvannapruk, W.; Edney, M. K.; Kim, D.-H.; Scurr, D. J.; Ghaemmaghami, A. M.; Alexander, M. R. *Analytical Chemistry* **2022**, *94*, 9389–9398.

(83) Suvannapruk, W.; Fisher, L. E.; Luckett, J. C.; Edney, M. K.; Kotowska, A. M.; Kim, D.-H.; Scurr, D. J.; Ghaemmaghami, A. M.; Alexander, M. R. *Advanced Science* **2024**, *11*, 2306000.

(84) Karas, M.; Bachmann, D.; Bahr, U.; Hillenkamp, F. *International Journal of Mass Spectrometry and Ion Processes* **1987**, *78*, 53–68.

(85) Ehring, H.; Karas, M.; Hillenkamp, F. *Organic Mass Spectrometry* **1992**, *27*, 472–480.

(86) Lu, I.-C.; Lee, C.; Lee, Y.-T.; Ni, C.-K. *Annual Review of Analytical Chemistry* **2015**, *8*, 21–39.

(87) Karas, M.; Glückmann, M.; Schäfer, J. *Journal of Mass Spectrometry* **2000**, *35*, 1–12.

(88) Allwood, D. A.; Dyer, P. E.; Dreyfus, R. W.; Perera, I. K. *Applied Surface Science* **1997**, *109-110*, 616–620.

(89) Allwood, D. A.; Dyer, P. E.; Dreyfus, R. W. *Rapid Communications in Mass Spectrometry* **1997**, *11*, 499–503.

(90) Lai, Y.-H.; Wang, C.-C.; Lin, S.-H.; Lee, Y. T.; Wang, Y.-S. *The Journal of Physical Chemistry B* **2010**, *114*, 13847–13852.

(91) Ahn, S. H.; Park, K. M.; Bae, Y. J.; Kim, M. S. *Journal of Mass Spectrometry* **2013**, *48*, 299–305.

(92) Fenn, J. B.; Mann, M.; Meng, C. K.; Wong, S. F.; Whitehouse, C. M. *Science* **1989**, *246*, 64–71.

(93) Banerjee, S.; Mazumdar, S. *International Journal of Analytical Chemistry* **2012**, *2012*, 282574.

(94) Takáts, Z.; Wiseman, J. M.; Gologan, B.; Cooks, R. G. *Science* **2004**, *306*, 471–473.

(95) De Hoffmann, E.; Stroobant, V., *Mass spectrometry: principles and applications*; John Wiley & Sons: 2007.

(96) D'Agostino, P. A.; Hancock, J. R.; Provost, L. R.; Semchuk, P. D.; Hodges, R. S. *Rapid Communications in Mass Spectrometry* **1995**, *9*, 597–603.

(97) Haag, A. M. In *Modern Proteomics – Sample Preparation, Analysis and Practical Applications*, Mirzaei, H., Carrasco, M., Eds.; Springer International Publishing: Cham, 2016, pp 157–169.

(98) Xian, F.; Hendrickson, C. L.; Marshall, A. G. *Analytical Chemistry* **2012**, *84*, 708–719.

(99) Lai, Y.-H.; Wang, Y.-S. *Mass Spectrometry Reviews* **2023**, *42*, 2426–2445.

(100) Bowman, A. P.; Blakney, G. T.; Hendrickson, C. L.; Ellis, S. R.; Heeren, R. M. A.; Smith, D. F. *Analytical Chemistry* **2020**, *92*, 3133–3142.

(101) Cochran, D.; Powers, R. *Biomedicines* **2024**, *12*, DOI: 10.3390/biomedicines12081786.

(102) Wolff, M. M.; Stephens, W. E. *Review of Scientific Instruments* **1953**, *24*, 616–617.

(103) Wiley, W. C.; McLaren, I. H. *Review of Scientific Instruments* **1955**, *26*, 1150–1157.

(104) Gatlin-Bunai, C. L.; Cazares, L. H.; Cooke, W. E.; Semmes, O. J.; Malyarenko, D. I. *Journal of Proteome Research* **2007**, *6*, 4517–4524.

(105) Guo, A.; Burt, M.; Brouard, M. *International Journal of Mass Spectrometry* **2018**, *429*, 121–126.

(106) Guo, A.; Burleigh, R. J.; Smith, N.; Brouard, M.; Burt, M. *Journal of the American Society for Mass Spectrometry* **2020**, *31*, 1903–1909.

(107) Buchberger, A. R.; DeLaney, K.; Johnson, J.; Li, L. *Analytical Chemistry* **2018**, *90*, 240–265.

(108) Holst, S.; Heijs, B.; de Haan, N.; van Zeijl, R. J. M.; Bruijn, I. H. B.-d.; van Pelt, G. W.; Mehta, A. S.; Angel, P. M.; Mesker, W. E.; Tollenaar, R. A.; Drake, R. R.; Bovée, J. V. M. G.; McDonnell, L. A.; Wuhrer, M. *Analytical Chemistry* **2016**, *88*, 5904–5913.

(109) Bodzon-Kulakowska, A.; Suder, P. *Mass Spectrometry Reviews* **2016**, *35*, 147–169.

(110) Keren, L. et al. *Science Advances* **2025**, *5*, eaax5851.

(111) Angelo, M.; Bendall, S. C.; Finck, R.; Hale, M. B.; Hitzman, C.; Borowsky, A. D.; Levenson, R. M.; Lowe, J. B.; Liu, S. D.; Zhao, S.; Natkunam, Y.; Nolan, G. P. *Nature Medicine* **2014**, *20*, 436–442.

(112) Dong, Y.; Li, B.; Aharoni, A. *Trends in Plant Science* **2016**, *21*, 686–698.

(113) Brouard, M. et al. *Review of Scientific Instruments* **2012**, *83*, 114101.

(114) Jungmann, J. H.; MacAleese, L.; Buijs, R.; Giskes, F.; de Snaijer, A.; Visser, J.; Visschers, J.; Vrakking, M. J. J.; Heeren, R. M. A. *Journal of the American Society for Mass Spectrometry* **2010**, *21*, 2023–2030.

(115) Clark, A. T. et al. *Journal of Physical Chemistry A* **2012**, *116*, 10897–10903.

(116) Wood, D.; Burleigh, R. J.; Smith, N.; Bortoletto, D.; Brouard, M.; Burt, M.; Nomerotski, A.; Plackett, R.; Shipsey, I. *Journal of the American Society for Mass Spectrometry* **2022**, *33*, 2328–2332.

(117) Schueler, B. W. *Microsc. Microanal. Microstruct.* **1992**, *3*, 119–139.

(118) Körber, A.; Keelor, J. D.; Claes, B. S. R.; Heeren, R. M. A.; Anthony, I. G. M. *Analytical Chemistry* **2022**, *94*, 14652–14658.

(119) Hazama, H.; Aoki, J.; Nagao, H.; Suzuki, R.; Tashima, T.; Fujii, K.-i.; Masuda, K.; Awazu, K.; Toyoda, M.; Naito, Y. *Applied Surface Science* **2008**, *255*, 1257–1263.

(120) Burleigh, R. J.; Guo, A.; Smith, N.; Green, A.; Thompson, S.; Burt, M.; Brouard, M. *Review of Scientific Instruments* **2020**, *91*, 023306.

(121) Riedl, M. J., *Optical design fundamentals for infrared systems*; SPIE press: 2001; Vol. 48.

(122) Guo, A. Improving the performance of microscope mass spectrometry imaging, Ph.D. Thesis, University of Oxford, 2018.

(123) Seah, M. P. *The Journal of Physical Chemistry C* **2013**, *117*, 12622–12632.

(124) Delcorte, A.; Garrison, B. J. *Nuclear Instruments and Methods in Physics Research Section B: Beam Interactions with Materials and Atoms* **2011**, *269*, 1572–1577.

(125) Lorenz, M.; Shard, A. G.; Counsell, J. D. P.; Hutton, S.; Gilmore, I. S. *The Journal of Physical Chemistry C* **2016**, *120*, 25317–25327.

(126) Paruch, R.; Rzeznik, L.; Russo, M. F.; Garrison, B. J.; Postawa, Z. *The Journal of Physical Chemistry C* **2010**, *114*, 5532–5539.

(127) Delcorte, A.; Poleunis, C.; Bertrand, P. *Applied Surface Science* **2006**, *252*, 6542–6546.

(128) Postawa, Z.; Czerwinski, B.; Winograd, N.; Garrison, B. J. *The Journal of Physical Chemistry B* **2005**, *109*, 11973–11979.

(129) Toyoda, N.; Kitani, H.; Hagiwara, N.; Aoki, T.; Matsuo, J.; Yamada, I. *Materials Chemistry and Physics* **1998**, *54*, 262–265.

(130) Colla, T. J.; Urbassek, H. M. *Nuclear Instruments and Methods in Physics Research Section B: Beam Interactions with Materials and Atoms* **2000**, *164-165*, 687–696.

(131) Brenes, D. A.; Garrison, B. J.; Winograd, N.; Postawa, Z.; Wucher, A.; Blenkinsopp, P. *The Journal of Physical Chemistry Letters* **2011**, *2*, 2009–2014.

(132) Sharma, S.; Gahan, D.; Scullin, P.; Daniels, S.; Hopkins, M. B. *Review of Scientific Instruments* **2015**, *86*, 113501.

(133) Eppink, A. T. J. B.; Parker, D. H. *Review of Scientific Instruments* **1997**, *68*, 3477–3484.

(134) Townsend, D.; Minitti, M. P.; Suits, A. G. *Review of scientific instruments* **2003**, *74*, 2530–2539.

(135) Allum, F.; Mason, R.; Burt, M.; Slater, C.; Squires, E.; Winter, B.; Brouard, M. *Molecular Physics* **2020**, *119*.

(136) Brouard, M.; Chadwick, H.; Gordon, S. D. S.; Hornung, B.; Nichols, B.; Aoiz, F. J.; Stolte, S. *The Journal of Chemical Physics* **2016**, *144*, 224301.

(137) Lam, C.-S.; Chou, T.-C.; McManus, J.; Hodgkinson, C.; Burt, M.; Brouard, M. *Communications Chemistry* **2025**, *8*, 268.

(138) Harding, D. J.; Neugebohren, J.; Hahn, H.; Auerbach, D. J.; Kitsopoulos, T. N.; Wodtke, A. M. *The Journal of Chemical Physics* **2017**, *147*, 013939.

(139) Reid, M.; Koehler, S. P. K. *Review of Scientific Instruments* **2013**, *84*, 044101.

(140) Hadden, D. J.; Messider, T. M.; Leng, J. G.; Greaves, S. J. *Review of Scientific Instruments* **2016**, *87*, 106104.

(141) Greenwood, T.; Koehler, S. P. K. *The Journal of Physical Chemistry C* **2021**, *125*, doi: 10.1021/acs.jpcc.1c05014, 17853–17860.

(142) Borodin, D.; Hertl, N.; Park, G. B.; Schwarzer, M.; Fingerhut, J.; Wang, Y.; Zuo, J.; Nitz, F.; Skoulatakis, G.; Kandratsenka, A.; Auerbach, D. J.; Schwarzer, D.; Guo, H.; Kitsopoulos, T. N.; Wodtke, A. M. *Science* **2022**, *377*, doi: 10.1126/science.abq1414, 394–398.

(143) Roman, M. J.; Knight, A. G.; Moon, D. R.; Lane, P. D.; Greaves, S. J.; Costen, M. L.; McKendrick, K. G. *The Journal of Chemical Physics* **2023**, *158*, 244704.

(144) Nesbitt, D. J.; Zolot, A. M.; Roscioli, J. R.; Ryazanov, M. *Accounts of Chemical Research* **2023**, *56*, doi: 10.1021/acs.accounts.2c00823, 700–711.

(145) Bünermann, O.; Jiang, H.; Dorenkamp, Y.; Kandratsenka, A.; Janke, S. M.; Auerbach, D. J.; Wodtke, A. M. *Science* **2015**, *350*, 1346–1349.

(146) Rettner, C. T.; Fabre, F.; Kimman, J.; Auerbach, D. J. *Physical Review Letters* **1985**, *55*, 1904–1907.

(147) Werdecker, J.; Shirhatti, P. R.; Golibrzuch, K.; Bartels, C.; Wodtke, A. M.; Harding, D. J. *The Journal of Physical Chemistry C* **2015**, *119*, 14722–14727.

(148) Golibrzuch, K.; Shirhatti, P. R.; Geweke, J.; Werdecker, J.; Kandratsenka, A.; Auerbach, D. J.; Wodtke, A. M.; Bartels, C. *Journal of the American Chemical Society* **2015**, *137*, 1465–1475.

(149) Bisson, R.; Sacchi, M.; Beck, R. D. *Physical Review B* **2010**, *82*, 121404.

(150) Shirhatti, P. R.; Geweke, J.; Steinsiek, C.; Bartels, C.; Rahinov, I.; Auerbach, D. J.; Wodtke, A. M. *The Journal of Physical Chemistry Letters* **2016**, *7*, 1346–1350.

(151) Rettner, C. T.; Michelsen, H. A.; Auerbach, D. J. *The Journal of Chemical Physics* **1995**, *102*, 4625–4641.

(152) Dahl, D. A. *International Journal of Mass Spectrometry* **2000**, *200*, 3–25.

(153) SIMION `https://simion.com/`.

(154) Brenes, D. A.; Postawa, Z.; Wucher, A.; Blenkinsopp, P.; Garrison, B. J.; Winograd, N. *Surface and Interface Analysis* **2013**, *45*, 50–53.

(155) Petrowski, A.; Ben Hamida, S., *Evolutionary Algorithms*; Wiley: 2016.

(156) Gerges, F.; Zouein, G.; Azar, D. In *Proceedings of the 2018 International Conference on Computing and Artificial Intelligence*, Association for Computing Machinery: Chengdu, China, 2018, pp 19–22.

(157) Burkhart, M. C.; Ruiz, G. *Journal of Computational Science* **2023**, *71*, 102054.

(158) Green, F. M.; Castellani, M. E.; Jia, Y.; Eyres, A.; Smith, N.; Thompson, S.; Blenkinsopp, P.; Burt, M.; Vallance, C.; Bunch, J.; Takats, Z.; Brouard, M. *Journal of the American Society for Mass Spectrometry* **2023**, *34*, 1272–1282.

(159) Golunski, M.; Postawa, Z. *Journal of Vacuum Science & Technology B* **2018**, *36*, 03F112.

(160) Schiffmann, K. I. *Surface and Interface Analysis* **2019**, *51*, 703–711.

(161) Czerwinski, B.; Rzeznik, L.; Paruch, R.; Garrison, B. J.; Postawa, Z. *Nuclear Instruments and Methods in Physics Research Section B: Beam Interactions with Materials and Atoms* **2011**, *269*, 1578–1581.

(162) Hill, R.; Blenkinsopp, P.; Barber, A.; Everest, C. *Applied Surface Science* **2006**, *252*, 7304–7307.

(163) Plies, E.; Marianowski, K.; Ohnweiler, T. *Nuclear Instruments and Methods in Physics Research Section A: Accelerators, Spectrometers, Detectors and Associated Equipment* **2011**, *645*, 7–11.

(164) Frackowiak, D. *Journal of Photochemistry and Photobiology B: Biology* **1988**, *2*, 399.

(165) Winter, B. Novel methods in imaging mass spectrometry and ion time-of-flight detection, Oxford University, UK, 2014.

(166) Knoll, G. E., *Radiation Detection and Measurement*; John Wiley & Sons, University of Michigan, Ann Arbor, Michigan, 2010.

(167) Winter, B.; King, S. J.; Brouard, M.; Vallance, C. *Review of Scientific Instruments* **2014**, *85*, 023306.

(168) Rajawat, J.; Jhingan, G. In *Data Processing Handbook for Complex Biological Data Sources*, Misra, G., Ed.; Academic Press: 2019, pp 1–20.

(169) Burgess, C. In *Encyclopedia of Analytical Science (Second Edition)*, Worsfold, P., Townshend, A., Poole, C., Eds., Second Edition; Elsevier: Oxford, 2005, pp 438–443.

(170) Wilman, E. S.; Gardiner, S. H.; Nomerotski, A.; Turchetta, R.; Brouard, M.; Vallance, C. *Review of Scientific Instruments* **2012**, *83*, 013304.

(171) PImMS `https://pimms.chem.ox.ac.uk/pimms2.php`.

(172) Kershis, M. D.; Wilson, D. P.; White, M. G.; John, J. J.; Nomerotski, A.; Brouard, M.; Lee, J. W. L.; Vallance, C.; Turchetta, R. *The Journal of Chemical Physics* **2013**, *139*, 084202.

(173) Halford, E.; Winter, B.; Mills, M. D.; Thompson, S. P.; Parr, V.; John, J. J.; Nomerotski, A.; Vallance, C.; Turchetta, R.; Brouard, M. *Rapid Communications in Mass Spectrometry* **2014**, *28*, 1649–1657.

(174) CERN Accelerating science `https://kt.cern/technologies/timepix3`.

(175) Turecek, D.; Jakubek, J.; Soukup, P. *Journal of Instrumentation* **2016**, *11*, C12065.

(176) Poikela, T.; Plosila, J.; Westerlund, T.; Campbell, M.; Gaspari, M. D.; Llopart, X.; Gromov, V.; Kluit, R.; van Beuzekom, M.; Zappon, F.; Zivkovic, V.; Brezina, C.; Desch, K.; Fu, Y.; Kruth, A. *Journal of Instrumentation* **2014**, *9*, C05013.

(177) Zhao, A.; van Beuzekom, M.; Bouwens, B.; Byelov, D.; Chakaberia, I.; Cheng, C.; Maddox, E.; Nomerotski, A.; Svihra, P.; Visser, J.; Vrba, V.; Weinacht, T. *Review of Scientific Instruments* **2017**, *88*, 113104.

(178) Yang, R.; Tang, Y.; Fu, Z.; Qiu, J.; Liu, K. *Photonics* **2022**, *9*.

(179) Kebarle, P.; Tang, L. *Analytical Chemistry* **1993**, *65*, 972A–986A.

(180) Winter, B.; Halford, E.; Brouard, M. *International Journal of Mass Spectrometry* **2013**, *356*, 14–23.

(181) Jin, S.; Beydoun, W. *Geophysical Prospecting* **2000**, *48*, 163–180.

(182) Jia, Y.; Green, F. M.; Cheung, K.; Castellani, M. E.; Brouard, M. *The Journal of Physical Chemistry Letters* **2025**, *16*, 11762–11769.

(183) Chandler, D. W.; Houston, P. L. *The Journal of Chemical Physics* **1987**, *87*, 1445–1447.

(184) Ashfold, M.; Parker, D. *Physical Chemistry Chemical Physics* **2013**, *16*, 381–382.

(185) Whitaker, B. J., *Imaging in molecular dynamics: technology and applications*; Cambridge university press: 2003.

(186) Gebhardt, C. R.; Rakitzis, T. P.; Samartzis, P. C.; Ladopoulos, V.; Kitsopoulos, T. N. *Review of Scientific Instruments* **2001**, *72*, 3848–3853.

(187) Lin, J. J.; Zhou, J.; Shiu, W.; Liu, K. *Review of Scientific Instruments* **2003**, *74*, 2495–2500.

(188) Nomerotski, A.; Brouard, M.; Campbell, E.; Clark, A.; Crooks, J.; Fopma, J.; John, J. J.; Johnsen, A. J.; Slater, C.; Turchetta, R.; Vallance, C.; Wilman, E.; Yuen, W. H. *Journal of Instrumentation* **2010**, *5*, C07007.

(189) Amini, K.; Blake, S.; Brouard, M.; Burt, M. B.; Halford, E.; Lauer, A.; Slater, C. S.; Lee, J. W. L.; Vallance, C. *Review of Scientific Instruments* **2015**, *86*, 103113.

(190) Fisher-Levine, M.; Nomerotski, A. *Journal of Instrumentation* **2016**, *11*, C03016.

(191) Nomerotski, A.; Chakaberia, I.; Fisher-Levine, M.; Janoska, Z.; Takacs, P.; Tsang, T. *Journal of Instrumentation* **2017**, *12*, C01017.

(192) Allum, F.; Cheng, C.; Howard, A. J.; Bucksbaum, P. H.; Brouard, M.; Weinacht, T.; Forbes, R. *The Journal of Physical Chemistry Letters* **2021**, *12*, doi: 10.1021/acs.jpclett.1c02481, 8302–8308.

(193) Cheng, C.; Frasinski, L. J.; Moǧol, G.; Allum, F.; Howard, A. J.; Rolles, D.; Bucksbaum, P. H.; Brouard, M.; Forbes, R.; Weinacht, T. *Physical Review Letters* **2023**, *130*, 93001.

(194) Chichinin, A. I.; Einfeld, T.; Maul, C.; Gericke, K.-H. *Review of Scientific Instruments* **2002**, *73*, 1856–1865.

(195) Pitzer, M. et al. *ChemPhysChem* **2016**, *17*, 2465–2472.

(196) Basnayake, G.; Ranathunga, Y.; Lee, S. K.; Li, W. *Journal of Physics B: Atomic, Molecular and Optical Physics* **2022**, *55*, 023001.

(197) AOKI, J.; HAZAMA, H.; TOYODA, M. *Journal of the Mass Spectrometry Society of Japan* **2011**, *59*, 57–61.

(198) Scheidsbach, R. J. A.; Parker, D. H. *Physical Chemistry Chemical Physics* **2019**, *21*, 14278–14283.

(199) Dorst, A. C.; Dissanayake, R. E. A.; Schauermann, D.; Knies, S.; Wodtke, A. M.; Killelea, D. R.; Schäfer, T. *Frontiers in Chemistry* **2023**, *11*, DOI: `10.3389/fchem.2023.1248456`.

(200) Koehler, S. P. K.; Ji, Y.; Auerbach, D. J.; Wodtke, A. M. *Physical Chemistry Chemical Physics* **2009**, *11*, 7540.

(201) Ji, Y.; Koehler, S. P. K.; Auerbach, D. J.; Wodtke, A. M. *Journal of Vacuum Science & Technology A: Vacuum, Surfaces, and Films* **2010**, *28*, 807–813.

(202) Abujarada, S.; AlSalem, H.; Chohan, U. K.; Draper, G. L.; Koehler, S. P. K. *The Journal of Chemical Physics* **2016**, *145*, DOI: 10.1063/1.4967248.

(203) Abujarada, S.; Flathmann, C.; Koehler, S. P. K. *The Journal of Physical Chemistry C* **2017**, *121*, 19922–19929.

(204) Psuja, P.; Hreniak, D.; Strek, W. *Journal of Physics: Conference Series* **2009**, *146*, 012033.

(205) Preeti; Majhi, T.; Singh, R. K.; Kumar, S. *Next Materials* **2025**, *6*, 100495.

(206) Zheng, L.; Wucher, A.; Winograd, N. *Analytical Chemistry* **2008**, *80*, doi: 10.1021/ac801056f, 7363–7371.

(207) Kelner, L.; Markey, S. P. *International Journal of Mass Spectrometry and Ion Processes* **1984**, *59*, 157–167.

(208) Magee, C. W. *International Journal of Mass Spectrometry and Ion Physics* **1983**, *49*, 211–221.

(209) Morita, K. *Nuclear Instruments and Methods in Physics Research Section B: Beam Interactions with Materials and Atoms* **1993**, *78*, 171–180.

(210) Seshan, K., *Handbook of thin film deposition*; William Andrew: 2012.

(211) Schou, J. *CAS 2006 - CERN Accelerator School: Vacuum in Accelerators, Proceedings* **2007**.

(212) Smith, R., *Atomic and Ion Collisions in Solids and at Surfaces: Theory, Simulation and Applications*; Cambridge University Press: 1997.

(213) AVERBACK, R. S.; RUBIA, T. D. D. L. In *Solid State Physics*, Ehrenreich, H., Spaepen, F., Eds.; Academic Press: 1998, pp 281–402.

(214) Russo, M. F.; Garrison, B. J. *Analytical Chemistry* **2006**, *78*, doi: 10.1021/ac061180j, 7206–7210.

(215) Garrison, B. J.; Postawa, Z.; Ryan, K. E.; Vickerman, J. C.; Webb, R. P.; Winograd, N. *Analytical Chemistry* **2009**, *81*, doi: 10.1021/ac802399m, 2260–2267.

(216) Jia, Y.; Castellani, M. E.; Cheung, K.; Su, Y.; Burt, M.; Blenkinsopp, P.; Green, F. M.; Brouard, M. *Analytical Chemistry* **0000**, *0*, null.

(217) Gilmore, I. S. *Journal of Vacuum Science & Technology A* **2013**, *31*, 050819.

(218) McPhail, D. S. *Journal of Materials Science* **2006**, *41*, 873–903.

(219) Kollmer, F. *Applied Surface Science* **2004**, *231*, 153–158.

(220) Davies, N.; Weibel, D.; Blenkinsopp, P.; Lockyer, N.; Hill, R.; Vickerman, J. *Applied Surface Science* **2003**, *203*, 223–227.

(221) Benabdellah, F.; Seyer, A.; Quinton, L.; Touboul, D.; Brunelle, A.; Laprévote, O. *Analytical and bioanalytical chemistry* **2010**, *396*, 151–162.

(222) Brulet, M.; Seyer, A.; Edelman, A.; Brunelle, A.; Fritsch, J.; Ollero, M.; Laprévote, O. *Journal of lipid research* **2010**, *51*, 3034–3045.

(223) Dollery, C. *Clinical Pharmacology & Therapeutics* **2013**, *93*, 263–266.

(224) Fisher, G. L.; Belu, A. M.; Mahoney, C. M.; Wormuth, K.; Sanada, N. *Analytical chemistry* **2009**, *81*, 9930–9940.

(225) McDonnell, L. A.; Heeren, R. M. A. *Mass Spectrometry Reviews* **2007**, *26*, 606–643.

(226) Spraggins, J. M.; Rizzo, D. G.; Moore, J. L.; Noto, M. J.; Skaar, E. P.; Caprioli, R. M. *PROTEOMICS* **2016**, *16*, 1678–1689.

(227) Froesch, M.; Luxembourg, S. L.; Verheijde, D.; Heeren, R. M. *European Journal of Mass Spectrometry* **2010**, *16*, 35–45.

(228) Klerk, L. A.; Lockyer, N. P.; Kharchenko, A.; MacAleese, L.; Dankers, P. Y.; Vickerman, J. C.; Heeren, R. M. *Analytical chemistry* **2010**, *82*, 801–807.

(229) Kiss, A.; Jungmann, J. H.; Smith, D. F.; Heeren, R. M. A. *Review of Scientific Instruments* **2013**, *84*, 013704.

(230) Zubarev, R. A.; Makarov, A. *Analytical Chemistry* **2013**, *85*, doi: 10.1021/ac4001223, 5288–5296.

(231) Manicke, N. E.; Dill, A. L.; Ifa, D. R.; Cooks, R. G. *Journal of Mass Spectrometry* **2010**, *45*, 223–226.

(232) Tiquet, M.; Rocca, R. L.; Kirnbauer, S.; Zoratto, S.; Kruining, D. V.; Quinton, L.; Eppe, G.; Martinez-Martinez, P.; Marchetti-Deschmann, M.; Pauw, E. D.; Far, J. *Analytical Chemistry* **2022**, *94*, 9316–9326.

(233) Smith, D. F.; Kilgour, D. P. A.; Konijnenburg, M.; O'Connor, P. B.; Heeren, R. M. A. *Analytical Chemistry* **2013**, *85*, 11180–11184.

(234) Runtso, M. F.; Naumov, P. Y.; Naumov, P. P.; Maklyaev, E. F.; Kaplin, V. A.; Fomin, V. S.; Razzhivin, I. S.; Melikyan, Y. A. *Journal of Physics: Conference Series* **2017**, *798*, 012014.

(235) Cheung, K.; Jia, Y.; Wood, D.; Nomerotski, A.; Plackett, R.; Brouard, M. A Novel Triggered TimePix3-Based Camera with Time-of-Threshold Correction, Unpublished, 2025.

(236) Jones, E. A.; Lockyer, N. P.; Vickerman, J. C. *International Journal of Mass Spectrometry* **2007**, *260*, Imaging Mass Spectrometry Special Issue, 146–157.

(237) Berrueta Razo, I.; Sheraz (née Rabbani), S.; Henderson, A.; Lockyer, N. P.; Vickerman, J. C. *Rapid Communications in Mass Spectrometry* **2015**, *29*, 1851–1862.

(238) Jones, E. A.; Lockyer, N. P.; Vickerman, J. C. *Analytical Chemistry* **2008**, *80*, 2125–2132.

(239) Rao, D. B.; Little, P. B.; Sills, R. C. *Toxicologic Pathology* **2014**, *42*, 487–509.

(240) Sjövall, P.; Lausmaa, J.; Johansson, B. *Analytical Chemistry* **2004**, *76*, 4271–4278.

(241) Lanni, E. J.; Dunham, S. J. B.; Nemes, P.; Rubakhin, S. S.; Sweedler, J. V. *Journal of the American Society for Mass Spectrometry* **2014**, *25*, PMID: 25183225, 1897–1907.

(242) Xia, Y.-Q.; Jemal, M. *Rapid Communications in Mass Spectrometry* **2009**, *23*, 2125–2138.

(243) Pulfer, M.; Murphy, R. C. *Mass Spectrometry Reviews* **2003**, *22*, 332–364.

(244) Rakowska, P. D.; Seah, M. P.; Vorng, J.-L.; Havelund, R.; Gilmore, I. S. *Analyst* **2016**, *141*, 4893–4901.

(245) Clarke, D. D.; Sokoloff, L.; Siegel, G. *Lippincott-Raven, Philadelphia* **1999**.

(246) Sjövall, P.; Johansson, B.; Lausmaa, J. *Applied Surface Science* **2006**, *252*, 6966–6974.

(247) Razo, I. B.; Rabbani), S. S. (; Henderson, A.; Lockyer, N. P.; Vickerman, J. C. *Rapid Communications in Mass Spectrometry* **2015**, *29*, 1851–1862.

(248) Razo, I. B.; Sheraz, S.; Henderson, A.; Lockyer, N. P.; Vickerman, J. C. *Surface and Interface Analysis* **2014**, *46*, 136–139.

(249) Sjövall, P.; Lausmaa, J.; Johansson, B. *Analytical Chemistry* **2004**, *76*, doi: 10.1021/ac049389p, 4271–4278.

(250) Fletcher, J. S.; Lockyer, N. P.; Vickerman, J. C. *Surface and Interface Analysis* **2011**, *43*, 253–256.

(251) Seah, M. P.; Spencer, S. J.; Shard, A. G. *The Journal of Physical Chemistry B* **2013**, *117*, 11885–11892.

(252) Shard, A.; Gilmore, I.; Wucherb, A. *ToF-SIMS: Materials Analysis by Mass Spectrometry* **2013**, 311.

(253) Chakraborty, B.; Shard, A.; Dalai, M.; Sehgal, G. *Surface and Interface Analysis* **2014**, *46*, 36–41.

(254) Mao, D.; Wucher, A.; Brenes, D. A.; Lu, C.; Winograd, N. *Analytical Chemistry* **2012**, *84*, 3981–3989.

(255) Mao, D.; Wucher, A.; Winograd, N. *Analytical Chemistry* **2010**, *82*, 57–60.

(256) Lee, J. L. S.; Ninomiya, S.; Matsuo, J.; Gilmore, I. S.; Seah, M. P.; Shard, A. G. *Analytical Chemistry* **2010**, *82*, 98–105.

(257) Shard, A. G.; Green, F. M.; Brewer, P. J.; Seah, M. P.; Gilmore, I. S. *The Journal of Physical Chemistry B* **2008**, *112*, doi: 10.1021/jp077325n, 2596–2605.

(258) Shard, A. G.; Ray, S.; Seah, M. P.; Yang, L. *Surface and Interface Analysis* **2011**, *43*, 1240–1250.

(259) Galindo, R. E.; Forniés, E.; Albella, J. M. *Journal of Analytical Atomic Spectrometry* **2005**, *20*, 1108–1115.